27th edition

ISSN 1454 - 8003

Proceedings of International Conference on HYDRAULICS, PNEUMATICS, SEALING ELEMENTS, TOOLS, PRECISION MECHANICS, SPECIFIC ELECTRONIC EQUIPMENT & MECHATRONICS

HERVEX 2023

November 8-10 | Băile Govora, ROMANIA

HERVEX

November 2023
27th Edition

INTERNATIONAL CONFERENCE

HERVEX 2023

Hydraulics| Pneumatics|
Sealing Elements| Tools| Precision Mechanics|
Specific Electronic Equipment & Mechatronics

Baile Govora, ROMANIA | November 8 - 10, 2023

ORGANIZERS

HYDRAULICS AND PNEUMATICS RESEARCH INSTITUTE
BUCHAREST, ROMANIA

CHAMBER OF COMMERCE AND INDUSTRY VALCEA, ROMANIA

ORGANIZING PARTNERS

WROCLAW UNIVERSITY OF SCIENCE AND TECHNOLOGY, POLAND

KOMAG INSTITUTE OF MINING TECHNOLOGY, POLAND

TECHNICAL UNIVERSITY OF MOLDOVA IN CHISINAU, REPUBLIC OF MOLDOVA

NATIONAL INSTITUTE OF RESEARCH & DEVELOPMENT FOR MACHINES AND INSTALLATIONS DESIGNED TO AGRICULTURE AND FOOD INDUSTRY – INMA BUCHAREST, ROMANIA

“POLITEHNICA” UNIVERSITY OF BUCHAREST, ROMANIA

“POLITEHNICA” UNIVERSITY OF TIMISOARA, ROMANIA

TECHNICAL UNIVERSITY OF CLUJ-NAPOCA, ROMANIA

“DUNAREA DE JOS” UNIVERSITY OF GALATI, ROMANIA

MEDIA PARTNERS

HIDRAULICA
HYDRAULICS-PNEUMATICS-TRIBOLOGY-ECOLOGY-SENSORICS-MECHATRONICS

Partener European
CAMERA DE COMERȚ ȘI INDUSTRIE VÂLCEA

HERVEX 2023

INTERNATIONAL CONFERENCE

HERVEX 2023

HELD UNDER HONORARY AEGIS OF

Comité Européen des Transmissions Oléohydrauliques et Pneumatiques

SUPPORTED BY

Ministry of Research, Innovation and Digitalization in Romania (MCID)

National Professional Association of Hydraulics and Pneumatics in Romania - "FLUIDAS"

Conference Proceedings is **indexed by**

Published by Hydraulics and Pneumatics Research Institute, Bucharest, Romania

COMMITTEES

HONORARY COMMITTEE

PhD.Eng. Hubertus MURRENHOFF – Institute for Fluid Power Drives and Controls at Aachen University, Germany

Prof. PhD. Eng. Viorel BOSTAN – Rector of Technical University of Moldova, Republic of Moldova

PhD.Eng. Petrin DRUMEA – President of National Professional Association of Hydraulics and Pneumatics – FLUIDAS, Romania

Dipl.Eng. Valentin CISMARU – President of Chamber of Commerce and Industry Valcea, Romania

ORGANIZING COMMITTEE

Dipl. Eng. Gheorghe RIZOIU – General Manager of Chamber of Commerce and Industry Valcea, Romania

PhD. Eng. Gabriela MATACHE – Hydraulics and Pneumatics Research Institute in Bucharest, Romania

PhD. Eng. Krzysztof KEDZIA – Wroclaw University of Technology, Poland

Prof. PhD. Eng. Dan OPRUȚA – Technical University of Cluj-Napoca, Romania

Prof. PhD. Eng. Ilare BORDEAȘU – Politehnica University of Timisoara, Romania

Prof. PhD. Eng. Adrian CIOCĂNEA – Politehnica University of Bucharest, Romania

PhD. Phys. Mihai VARLAM - General Manager of National Research & Development Institute for Isotope & Cryogenics Technologies (ICSI) Râmnicu Vâlcea, Romania

PhD.Eng. Sergiu NICOLAIE – General Manager of R&D National Institute for Electrical Engineering ICPE-Advanced Researches, Bucharest, Romania

PhD.Eng. Nicolae-Valentin VLĂDUȚ – General Manager of National Institute of Research and Development for Machines and Installations Designed to Agriculture and Food Industry – INMA Bucharest, Romania

PhD.Eng. Ioan LEPĂDATU – Hydraulics and Pneumatics Research Institute in Bucharest, Romania

PhD.Eng. Cătălin DUMITRESCU – Director of Hydraulics and Pneumatics Research Institute in Bucharest, Romania

SCIENTIFIC PROGRAMME COMMITTEE

PhD.Eng. Zygmunt DOMAGALA – Wroclaw University of Technology, Poland

Prof. PhD.Eng. Valeriu DULGHERU – Technical University of Moldova, Republic of Moldova

PhD.Eng. Cătălin DUMITRESCU – Director of Hydraulics and Pneumatics Research Institute in Bucharest, Romania

D.Sc. Eng. Dariusz PROSTAŃSKI – KOMAG Institute of Mining Technology, Gliwice, Poland

Ph.D. Eng. Bartosz POLNIK – KOMAG Institute of Mining Technology, Gliwice, Poland

Ph.D. Eng. Krzysztof NIEŚPIAŁOWSKI – KOMAG Institute of Mining Technology, Gliwice, Poland

Ph.D. Eng. Artur DYCZKO – KOMAG Institute of Mining Technology, Gliwice, Poland

EXECUTIVE SECRETARIAT

SPECIALIZED REVIEWER COMMITTEE

EDITORIAL STAFF

CONTENTS

ISSN 1454 - 8003
Proceedings of 2023 International Conference on Hydraulics and Pneumatics - HERVEX
November 8-10, Băile Govora, Romania

COMPARATIVE ANALYSIS OF CURRENT APPROACHES TO DIGITAL TWINS OF ELECTRO-HYDRAULIC MECHATRONIC SYSTEMS CREATIONS

Alexander SKVORCHEVSKY[1,*]

[1] Research Center of Robotics, Mechatronics and Production Informatization, Kharkiv, Ukraine

* sircrmpi@gmail.com

Abstract: *The aim of this study is to identify approaches and principles for creating digital twins of electrohydraulic mechatronic systems. The aim of the study was achieved by bibliometric analysis and systematic review for identification approaches and principles of creating digital twins of various electro-hydraulic mechatronic systems in all stages of their life cycles. As a result of the research, publications were systematized in accordance with the approaches and methods proposed in them for creating digital twins of electrohydraulic mechatronic systems and their elements. Namely, which stages of the life cycles of electrohydraulic mechatronic systems are covered by the approaches and methods proposed in publications. During the bibliometric analysis, no publications were identified that would offer a systematic methodology for creating different types of digital twins of electrohydraulic mechatronic systems at all stages of their life cycles. Thus, the creation of such a systematic methodology is an important scientific and practical task.*

Keywords: *Electrohydraulic mechatronic systems, heavy-duty machines, digital twins, life cycles*

1. Introduction

Heavy-duty machines, such as excavators, mining, agricultural, and military vehicles, are often operated in hazardous and harmful environments. Electrohydraulic mechatronic drives continue to be important components of such machines. The transformation of heavy-duty machines into more autonomous and robotic ones requires the creation of digital twins of electro-hydraulic mechatronic drives that would reflect their functioning at all stages of their life cycles.

2. Literature review and problem statement

The current state of development of digital twins at various stages of product life cycles is covered in publications [1-2]. The principles and approaches outlined in [1-2] can partially be applied to electrohydraulic mechatronic systems. However, they need serious adaptation and addition.
The papers [3-10] present various aspects of creating digital twins of heavy-duty machines. The papers [3-10] pay insufficient attention to electrohydraulic mechatronic systems, as important components of heavy-duty machines. In the process of creating digital twins of electrohydraulic mechatronic systems, it is necessary to take into account research [3-10] results. This is due to the fact that digital twins of electrohydraulic mechatronic systems must be suitable for integration into digital twins of heavy-duty machines.
The papers [9-10] outline approaches to creating digital twins of electrohydraulic mechatronic systems of heavy-duty machines. However, the approaches outlined in [9-10] cannot be considered comprehensive and cover all stages of the life cycles of electrohydraulic mechatronic systems.
Papers [11-13] propose results of the creation of a simplified numerical model, based on a very compact semi-empirical formulation, able to simulate the fluid dynamics behaviours of an electrohydraulic servo valve taking into account several effects due to valve geometry and operating conditions. The results [11-13] are proposed to be used to create digital twins at the stages of development and detailed design of electrohydraulic servo valves. Despite the fact that the research [11-13] concerns only electrohydraulic servo valves, they can be used to create digital twins of electrohydraulic mechatronic systems.

The article [14] presents a model for counterbalance valves which are widely used in hydraulic and electro-hydraulic drives. The model consists of parameters that account for the internal geometry, inertia, and friction characteristics of the counterbalance valves. The proposed model of the counterbalance valve satisfies the main requirements of digital twins and thus, is a suitable candidate for the digital twin of the counterbalance valves and can easily be integrated into the digital twins of larger systems where the counterbalance valves are installed [14]. The model [14] and the principles of its creation can be used in digital twins of electrohydraulic mechatronic systems.
The paper [15] presents the construction technology of the digital twinning model for the erect-fold electromechanical-hydraulic system of radar based on co-simulation. The construction technology [15] can be generalized to other electrohydraulic mechatronic systems, but it should be added with other principles of digital twins' creation.
The literature review shows a lack of research in the field of creating digital twins of electrohydraulic mechatronic systems. Publications which outline the methodology for creating digital twins of various electro-hydraulic mechatronic systems in all stages of their life cycles have not been identified. Thus, development of a methodology for creating digital twins of electro-hydraulic mechatronic systems, which covers all stages of electro-hydraulic mechatronic systems life cycles is an important scientific task.

3. The aim of the study

The aim of this study is to identify approaches and principles for creating digital twins of electrohydraulic mechatronic systems. Such digital twins should cover all stages of the life cycles of electrohydraulic mechatronic systems.

4. The study materials and methods

This study adopts bibliometric analysis and systematic review for identification approaches and principles of creating digital twins of various electro-hydraulic mechatronic systems in all stages of their life cycles. The research materials included publications on the above-mentioned scientific direction and related areas.

5. Results of comparative analysis of current approaches to digital twins of electro-hydraulic mechatronic systems creations

According to the aim of the study, each of the publications in the field of digital twins of electrohydraulic mechatronic systems and their elements were analysed to identify the methods used for creating digital twins. Also, was identified which stage of the life cycles of electrohydraulic mechatronic systems or their elements cover some publications. The results of the review are systematised in Table 1.
The papers [9, 10] propose using pressure indication in hydraulic and electro-hydraulic systems to, directly and indirectly, determine their other characteristics. The data obtained in this way is proposed to be used to create digital twins of electrohydraulic mechatronic systems mainly at such stages of their life cycles as Deployment, Operation and technical support.
The paper [11] presents an overview of low-fidelity models of the hydrodynamic behaviour of an electrohydraulic servo valve. They are designed to operate in real-time as digital twins of a physical system to enable diagnostic and prognostic algorithms. The accuracy of the simulation is assessed by comparing its results to a detailed, physics-based, high-fidelity model that calculates the equipment response based on the pressure and flow characteristics of all internal passages of the electrohydraulic servo valve.
The article [12] proposes a new simplified numerical model, based on a very compact semi-empirical formulation, able to simulate the fluid dynamics behaviours of an electrohydraulic servo valve taking into account several effects due to valve geometry and operating conditions. Although the proposed model is still based on a simplified formulation with lower computational cost, it introduces a new nonlinear approach that, by approximating the dynamic pressure and fluid flow characteristics of a servo valve with reasonable accuracy, overcomes the shortcomings typical of such models [12].

Ideas and approaches for creating digital twins of electrohydraulic servo valves based on simplified models proposed in papers [11, 12] were further developed in the article [13]. This work proposes a new simplified lumped parameter numerical model that, despite a very compact formulation and lower computational cost, simulates the internal fluid dynamics of the valve, overcoming some critical problems typical of other models available in the literature. It evaluates valve performance based on spool position and environmental conditions (e.g., supply pressure), more accurately assessing flow feedback, internal leaks, and other operating conditions (e.g., fine spool adjustment, variable supply pressure, overpressure, or water hammer). The performance of this numerical model is evaluated in comparison with other simplified models published in the literature. In addition, this is confirmed using a high-precision digital twin that simulates valve behaviour taking into account spool geometry, hydraulic fluid properties and local internal fluid dynamics (laminar or turbulent conditions, cavitation). , etc.) [13].

Table 1: Results of publications systematic review according to proposed approaches to the creation of digital twins of electro-hydraulic mechatronic systems in different stages of their life cycles

Life cycles stages of electrohydraulic mechatronic systems	Publications
Identification and analysis of needs	No publications identified
Feasibility study	No publications identified
System layout	[11], [12], [13], [14]
Design and development	[11], [12], [13], [14], [15]
Production	[15]
Deployment	[9], [10], [14]
Operation and technical support	[9], [10], [14], [15]
Disposal	No publications identified

The studies presented in the papers [11-13] are pioneering in the direction of creating digital twins of electrohydraulic servo valves based on their simplified models. However, they do not completely close the issue of creating digital twins of electrohydraulic mechatronic systems for two main reasons:

- only the electrohydraulic servo valve is considered, not the electrohydraulic mechatronic system as a whole;

- only digital twins are considered at the stage of design and development, while they need to be filled with data at all stages of the life cycles of electrohydraulic mechatronic systems.

Like the papers [11, 12, 13], the article [14] is also devoted to the creation of digital twins of a specific type of valve - counterbalance valves. The article [14] presents such a model of counterbalance valves, which are often found in various hydraulic systems. The model consists of parameters that take into account the internal geometry, inertia and friction characteristics of the counterbalance valve. To illustrate the parameter identification strategy for this model, a test setup is designed and four sets of experiments are conducted. A subset of measured data is used to systematically identify parameters. The remaining data is used to validate the counterbalance valve model and parameter identification strategy. The results show that the model is able to successfully predict the behaviour of the counterbalance valve under various operating conditions, thereby validating the model.

The proposed counterbalance valve model satisfies the key requirements of digital twins and is thus a suitable candidate for a digital twin of counterbalance valves and can be easily integrated into digital twins of larger systems where counterbalance valves are installed.

Just like the scientific results presented in the papers [11, 12, 13], the scientific results [14] are applicable to one type of valve and are limited to the following stages of life cycles, namely System layout, Design and development, Deployment, and Operation and technical support.

The paper [15] presents a comprehensive approach to creating digital twins of complex electro-hydraulic mechatronic systems, which is applicable in many stages of their life cycles. Creating a digital twin is done using an example of the erect-fold electromechanical-hydraulic system of radar. The paper [15] utilizes radar electro-hydraulic system development and digital twin technology to enhance the design, manufacturing, and comprehensive support capabilities of the system. Key technologies such as co-simulation data output, training data cleaning, reduced-order ROM model establishment, and accuracy verification are employed. The construction of a digital twin model for the radar electro-hydraulic system enables virtual-real data fusion, facilitating iteration, optimization, and improvement of electromechanical hydraulic systems throughout their life cycle. Additionally, the digital twin model allows for real-time updates of visual simulations of the radar rack and removal system, enhancing system reliability and manoeuvrability. By developing the digital twin architecture of the electromechanical hydraulic radar system based on co-simulation, a digital twin system platform for the radar installation and removal system is established. Combined with the logical connections between the subsystems of the electromechanical hydraulic system, a final digital twin model of the electromechanical hydraulic system was built and executable program code with real-time response was generated. Finally, it was analyzed and calculated on the radar structure digital twin system platform and responded to in real-time. This enables easy implementation of the digital twin model in electromechanical hydraulic system simulation without the use of traditional modelling and analysis tools [15]. The approaches and principles propoused in the paper [15] can be used to create digital twins of other complex electrohydraulic mechatronic systems.

6. Discussion of comparative analysis of current approaches to digital twins of electro-hydraulic mechatronic systems creations

The principles of creating digital twins of high-tech engineering products covering all stages of their life cycles set out in the articles [16, 17], can be used for digital twins of electrohydraulic mechatronic systems. To increase the robustness of computer networks on which models and data of digital twins will be stored, it is recommended to use the topology proposed in the [18]. To create components of digital twins of electrohydraulic mechatronic systems that would cover the initial stage of their life cycle (Identification and analysis of needs), it is recommended to use the approaches outlined in [19].

7. Conclusions

It should be noted that there are very few publications in the direction of creating digital twins of electrohydraulic mechatronic systems. During the bibliometric analysis, no publications were identified that would offer a systematic methodology for creating different types of digital twins of electrohydraulic mechatronic systems at all stages of their life cycles. Thus, the creation of such a systematic methodology is an important scientific and practical task.

References

[1] Malik, Ali Ahmad, and Alexander Brem. “Digital Twins for Collaborative Robots: A Case Study in Human-Robot Interaction.” *Robotics and Computer-Integrated Manufacturing* 68 (April 2021): 102092. https://doi.org/10.1016/j.rcim.2020.102092.

[2] Preut, Anna, Jan-Philip Kopka, and Uwe Clausen. “Digital Twins for the Circular Economy.” *Sustainability* 13, no. 18 (September 2021): 10467. https://doi.org/10.3390/su131810467.

[3] Liu, Jianmin, Yi Dong, Yanbin Liu, Pu Li, Sheng Liu, and Tianqi Wang. “Prediction Study of the Heavy Vehicle Driving State Based on Digital Twin Model.” Paper presented at the 2021 IEEE International Conference on Power Electronics, Computer Applications (ICPECA), Shenyang, China, January 22-24, 2021. https://doi.org/10.1109/icpeca51329.2021.9362618.

[4] Secades Rodríguez, Alejandro, Jasper Volmer, and Davide Bagnara. “Simulation of Heavy-Duty Vehicles for the Use in Digital Twins”, pp. 127–38. In: Matt, D.T., R. Vidoni, E. Rauch, and P. Dallasega (eds). *Managing and Implementing the Digital Transformation. ISIEA 2022. Lecture Notes in Networks and Systems* 525, Springer, Cham, 2022. https://doi.org/10.1007/978-3-031-14317-5_11.

[5] Khan, Asmat Ullah, Lizhen Huang, Erling Onstein, and Yongping Liu. “Overview of Emerging Technologies for Improving the Performance of Heavy-Duty Construction Machines.” *IEEE Access* 10 (2022): 103315–36. https://doi.org/10.1109/access.2022.3209818.

[6] Baidya, Sabur, Sumit Kumar Das, Mohammad Helal Uddin, Chase Kosek, and C. J. Summers. “Digital Twin in Safety-Critical Robotics Applications: Opportunities and Challenges.” Paper presented at the 2022 IEEE International Performance, Computing, and Communications Conference (IPCCC), Austin, TX, USA, November 11-13, 2022. https://doi.org/10.1109/ipccc55026.2022.9894313.

[7] Zhang, Tao, Yongping Shi, Yongsheng Cheng, Yiming Zeng, Xin Zhang, and Liang Shen. “The Design and Implementation of Distributed Architecture in the CMOR Motion Control System.” *Fusion Engineering and Design* 186 (January 2023): 113357. https://doi.org/10.1016/j.fusengdes.2022.113357.

[8] Volontsevich, Dmitriy, Ievgenii Veretennikov, Vadym Karpov, and Kamil Židek. “Using Mathematical Modelling for Experimental Obtaining of Initial Data When Creating Digital Twins of Complex Technical Products”, pp. 263–71. In: Balog, M., A. Iakovets, and S. Hrehova (eds). *EAI International Conference on Automation and Control in Theory and Practice. EAI ARTEP 2023. EAI/Springer Innovations in Communication and Computing*. Springer, Cham. https://doi.org/10.1007/978-3-031-31967-9_20.

[9] Taheri, Abdolreza, Robert Pettersson, Pelle Gustafsson, Joni Pajarinen, and Reza Ghabcheloo. “Towards Energy Efficient Control for Commercial Heavy-Duty Mobile Cranes: Modeling Hydraulic Pressures Using Machine Learning.” Paper presented at the 18th Scandinavian International Conference on Fluid Power, SICFP'23, Tampere, Finland, May 30- June 1, 2023. https://doi.org/10.48550/arxiv.2307.16681.

[10] Skvorchevsky, Alexander. “Electronic Load Sensing for Integrating Electro-Hydraulic Mechatronic Actuators with Industry 4.0 and 5.0 Components”, pp. 440–55. In: Cioboată, D.D. (eds). *International Conference on Reliable Systems Engineering (ICoRSE) - 2023. ICoRSE 2023. Lecture Notes in Networks and Systems* 762. Springer, Cham. https://doi.org/10.1007/978-3-031-40628-7_37.

[11] Berri, P. C., and M. D. L. Dalla Vedova. “A Review of Simplified Servovalve Models for Digital Twins of Electrohydraulic Actuators.” *Journal of Physics: Conference Series* 1603 (September 2020): 012016. https://doi.org/10.1088/1742-6596/1603/1/012016.

[12] Dalla, Lorenzo, and Pier Carlo Berri. “A New Simplified Fluid Dynamic Model for Digital Twins of Electrohydraulic Servovalves.” *Aircraft Engineering and Aerospace Technology* 94, no. 1 (July 2021): 79–88. https://doi.org/10.1108/aeat-12-2020-0321.

[13] Berri, Pier Carlo, Lorenzo Dalla, and Simone Santaera. “Digital Twins for Prognostics of Electro-Hydraulic Actuators: Novel Simplified Fluid Dynamic Models for Aerospace Valves.” *IOP Conference Series: Materials Science and Engineering* 1226 (February 2022): 012106. https://doi.org/10.1088/1757-899x/1226/1/012106.

[14] Rituraj, Rituraj, and Rudolf Scheidl. “Towards Digital Twin Development of Counterbalance Valves: Modelling and Experimental Investigation.” *Mechanical Systems and Signal Processing* 188 (April 2023): 110049. https://doi.org/10.1016/j.ymssp.2022.110049.

[15] Peng, Guopeng, and S Liu. “Construction Technology of the Digital Twinning Model for the Erect-Fold Electromechanical-Hydraulic System of Radar Based on Co-Simulation.” Paper presented at the Third International Conference on Mechanical Design and Simulation (MDS 2023), Xi'an, China, March 3-5, 2023. https://doi.org/10.1117/12.2682024.

[16] Vrabič, Rok, John Ahmet Erkoyuncu, Peter Butala, and Rajkumar Roy. “Digital Twins: Understanding the Added Value of Integrated Models for Through-Life Engineering Services.” *Procedia Manufacturing* 16 (2018): 139–46. https://doi.org/10.1016/j.promfg.2018.10.167.

[17] Volontsevich, Dmitriy, and Alexander Skvorchevsky. “Restoration and Transformation of High-Tech Machine Building Industry by Implementing the Principles of the CALS-Concept in the Context of Industry 4.0 Development.” *Eastern-European Journal of Enterprise Technologies* 3, no. 1 (117) (June 2022): 15–24. https://doi.org/10.15587/1729-4061.2022.260045.

[18] Skvorchevsky, Alexander. “Increasing the Robustness of Computer Networks by Using Hybrid Centralized-Distributed Topology.” Paper presented at the 2022 IEEE 17th International Conference on Computer Sciences and Information Technologies (CSIT), Lviv, Ukraine, November 10-12, 2022. https://doi.org/10.1109/csit56902.2022.10000466.

[19] Skvorchevsky, Alexander. “Modern Requirements for Electrohydraulic Drives of Combat and Civilian Vehicles. ” In: *Hydro-Aeromechanics in Engineering Practice*, pp. 131–34. Kyiv: National Technical University of Ukraine “Kyiv Polytechnic Institute”, 2016. https://repository.kpi.kharkov.ua/handle/KhPI-Press/28264.

ISSN 1454 - 8003
Proceedings of 2023 International Conference on Hydraulics and Pneumatics - HERVEX
November 8-10, Băile Govora, Romania

IMPACT VELOCITY CONTROL OF HOPKINSON BAR MECHATRONICS SYSTEM USING DRIVING ROBUST PRESSURE, NUMERICAL CALIBRATION, STRAIN WAVE MEASUREMENT AND INVERSE ANALYSIS

Adinel GAVRUS[1]

[1]INSA Rennes, LGCGM-EA3913, University of Rennes, Rennes, France, adinel.gavrus@insa-rennes.fr

Abstract: *This scientific research proposes an improved experimental design together with a hybrid analytical-numerical analysis concerning high-speed pneumatic compression Split Hopkinson Pressure Bars (SHPB) mechatronics system developed at INSA Rennes (France). The main objectives are to describe the entire mechatronic pneumatic propulsion and to analyses the data acquisition. Impact velocity prediction, function of pressure driving and specific set point, elastic deformation shock waves and the proposed new numerical calibration method will be detailed. Experimental measurements and estimation of velocity-pressure curve uses a Hermite cubic splines interpolation method presented together with a numerical analysis of elastic deformation signals from strain gages or Bragg optical fibers. The proposed hybrid techniques use a parametric identification of an analytical model describing the striker propulsion and linear movement taking into account friction effects and a numerical calibration based on a complete finite element (FE) simulation of the entire SHPB device. This takes into account the propagation of elastic shock waves and all dynamic mechanical interactions at the contact interfaces between the launched impact bar at an imposed speed, the incident bar and the sending bar, an elastic-dynamic mechanical equilibrium model is used. Based on previous and current researches at INSA Rennes, as a real application of the proposed full SHPB analytical and FE models, can be shown the material constitutive laws identification using a two-step inverse analysis technique. The identified constitutive equations concern description of thermomechanical materials behaviour subjected to high deformation rates, large plastic deformations and high temperatures, especially when high gradients of all these variables occur during material loadings.*

Keywords: *Pneumatic SHPB Device, Hopkinson Bars (SHPB), Estimated Impact Speed, Hybrid Analytical-Numerical Calibration, Finite Elements Modelling, Numerical Calibration, Inverse Analysis*

1. Introduction

Various manufacturing processes and industrial applications developed in the last decade use metallic or non-metallic structures undergoing high rates of loadings, severe elasto-plastic strains, strain rates and temperatures. Furthermore, localized gradients of strain and stress or complex deformation paths occur during rapid, impact, choc or crash loadings. Modelling the corresponding real material thermos-mechanical behavior becomes a real scientific key. This purpose requires design of specific materials characterizing techniques as dynamic or rapid experimental tests using rigorous experimental calibration of used measurement sensors and reliable data analysis via improved analytical, numerical or hybrid analytical-numerical models. Because very high strain rates occur during these dynamic tests, elastic deformations waves travel along the experimental system bench compounds and specimen material, at very high velocities named celerity, of several kilometers per second. Therefore, it is difficult to have an intuitive understanding of the observed physical phenomena in part caused by strong coupling between different boundaries conditions. To perform the quality measurements and their reliability, during the dynamic deformations obtained from rapid loadings, it is nevertheless necessary to take account the quantitative description of elastic wave propagation. First rapid mechanical tests were conducted around 1870 by John Hopkinson who developed a specific mechanism to impact a cylindrical bar. Bertram Hopkinson [1] introduced in 1914 a pressure bar to can study and reproduce very short dynamic events such as the explosive detonation or the impact of different types of projectiles. The named Hopkinson pressure bar is based on the application of theory concerning elastic strain wave's propagation, to predict strains and stress magnitudes developed in the studied material sample. Hopkinson discovered that the small local displacements in the bar depend directly to the period of the elastic wave obtained during the very short times of the impact caused by the material sound celerity. In the case of materials undergoing an impact through a projectile, Davies [2] shows in 1948 that it is possible to measure the temporal form of the generated elastic wave using strain gauges instrumented bar. The first Split Hopkinson Pressure Bars system (SHPB) was designed in 1949 by Kolsky [3] which has used a gas propulsion device to obtain high speed of a projectile bar. He added two other metallic bars named incident and sending bars to realize a dynamic compression. Generally, the SHPB device can develop impact velocities up to 30-40 m/s and corresponding strain rates in the range of 10^2 to 10^4 s^{-1}. Further, other dynamic experimental set-up has been developed as the Taylor test (gas or explosive propulsion around of 100 m/s), Crossbow system (speed up to 10-30 m/s), traction or torsion Hopkinson Bars, Weight Falling and form last three decades specific hydraulic press using particular actuators and devices to can control the impact velocity (compression or traction speed up to 10 m/s). The main purpose of this scientific work is to describe a mechatronic SHPB compression test designed on GCGM Laboratory of INSA Rennes (France) using a pneumatic propulsion with a robust control of air pressure, a laser optic camera to measure projectile bar speed and automatic electronic data acquisition of bars elastic deformations. Results are presented concerning the use of a specific calibration method developed from a hybrid analytical and numerical finite element system modelling.

2. Pneumatic SHPB Mechatronics System

Kolsky found that the Cauchy stress and the elastic-plastic deformation of an impacted specimen can be directly related to the displacements fields of the incident and sending bars. Contrary of the classical Hopkinson pressure bar, the SHPB device use a projectile does no impact directly the material specimen. It is first an incident bar that receive the impact of the projectile (striker bar), subjected then to a lot of dynamic elastic deformation pulse. The propagation of elastic wave in the incident bars, in the specimen and finally in the sending bar it is more intense as the speed of striker is high and is lasts time longer as the projectile is long. This elastic wave is reflected partially by the material sample on the incident bar, the other part passes through it and is subsequently transmitted to a second bar named transmitter or sending bar [4-7].

2.1 Framework and SHPB design characteristics

The general scheme of mechatronic SHPB system designed and used at INSA Rennes (France) is presented in the Figure 1.

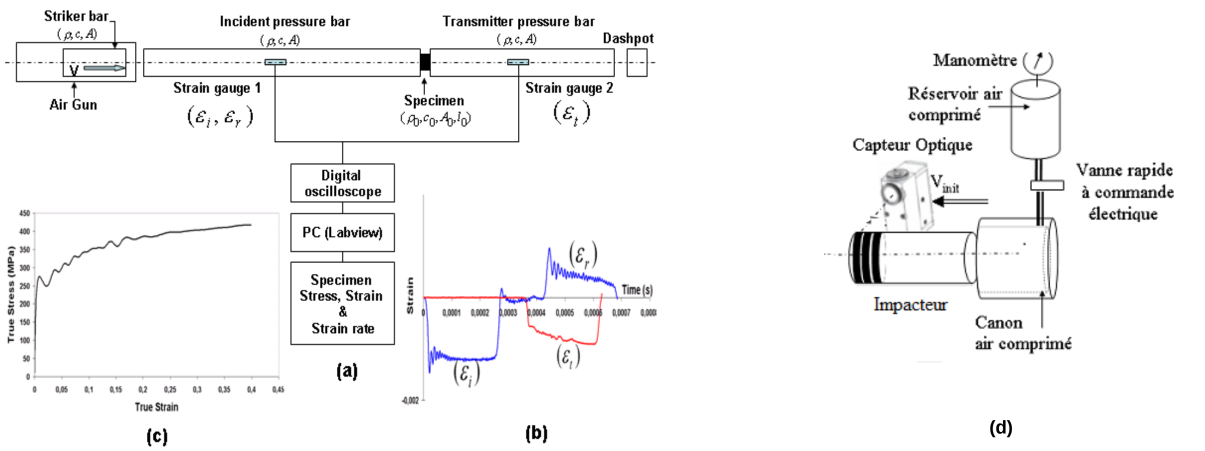

Fig. 1. General schema of the compression Split Hopkinson Pressure Bars (SHPB) bench: pneumatic propulsion bars design with automatic acquisition of laser camera and strain gauges A/B signals (incident $\varepsilon_i(t)$, reflected $\varepsilon_r(t)$ and transmitted $\varepsilon_t(t)$ elastic deformations) performed with a Labwiew program, true stress - true strain curves of material specimen obtained from David code [8].

According to the general theory of elastic wave propagation [4-8], to the type of specimen's materials and to the desired obtained strain and strain rate, the choice of the material and bars geometric size requires to take into account some physical conditions. In a first time it is necessary to have similar elastic impedances of the bars as those of tested material specimens. In particular, to can test steels, aluminium or titan alloys, the hardened high strength steel MARVAL18 is used for bars material (Table 1).

To avoid superposition of measured elastic strain gauges by incident and sending bars [7-8] it is necessary to take into account the minimum measurement time using the following relationships:

$$\Delta t_{measure} = t_i = 2\mathrm{l}_{\mathrm{bimp}} / c_b \le l_{bi} / c_b \text{ and } \mathrm{l}_{bt} / c_b \ge 0.5\mathrm{l}_{bi} / c_b \qquad (1)$$

It is then required to have $l_{bi} \ge 2\mathrm{l}_{\mathrm{bimp}}$ and $\mathrm{l}_{bt} \ge 0.5 l_{bi}$. The maximal average plastic strain of material specimen can be estimate from large displacements compression theory by $\bar{\varepsilon}_{\max} \approx \ln\left[1-(2v_{imp}l_{b_{mp}i} / l_0 c_b)\right]^{-1}$. Considering a cylindrical specimen with a length l_0 = 10 *mm* and an initial impact velocity v_{imp} = 10 *m/s* a value of $\bar{\varepsilon}_{\max}$ around of 25%-50% can be obtained for $\mathrm{l}_{\mathrm{bimp}} \in [0.5m, 1m] \Rightarrow l_{bi} \ge 1m \div 2m$ and $l_{bt} \ge 0.5m \div 1m$. More great plastic deformations of specimen, especially for smallest impact velocities, can be obtain for shorter specimens or specimens with special or unconventional local shape as dumbbell sample or hat one. To minimize effect of the radial dispersion elastic waves and to have bars elastic deformations conditions close to the infinite wave propagation theory [7], the bars diameters d_b must to be very small as compared to the twist of striker bar lengths i.e. $d_b \,/\, c_b t_i \;=\; d_b \,/\, 2l_{bimp} \ll 1$. The Table 1 and Table 2 synthetize the chosen material and geometric characteristics of INSA Rennes Hopkinson bars in order to perform compression impact tests with large plastic deformations of material specimen at high strain rates (more than 500s^{-1} – 1000s^{-1} corresponding to $v_{\mathrm{imp}} \in [10m/s, 30m/s]$.

Table 1: Material and geometric characteristics of SHPB bars (total length of bench support ≈ 5.5 m)

Bars	Air Gun	Striker Bar	Receiving Bar	Sending Bar
Material	MARVAL 18	MARVAL 18	MARVAL 18	MARVAL 18
Diameter [mm]	ϕ_{in} 30.0 and ϕ_{out} 40.0	ϕ 16.0	ϕ 16.0	ϕ 16.0
Length [m]	2.0	0.602 (0.5÷1)	2.0	1.3

Table 2: Elastic mechanical properties of MARVAL 18 steel bars

Temperature 20°C	E_b [GPa]	υ	$R_{0,2}$ [MPa]	ρ_b [Kg /m^3]	$c_b = \sqrt{E_b / \rho_b}$ [m/s]	$\mathrm{Z_b} = \rho_\mathrm{b}\mathrm{c_b} = \sqrt{\rho_b E_b}$ [Kg/m^{2}s]
MARVAL 18	186	0.33	1840	8000	4821.82	$38.57 \cdot 10^6$

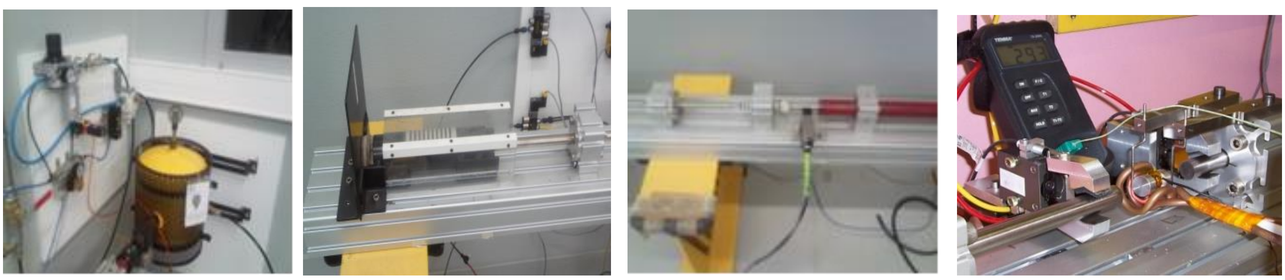

Fig. 2. View of experimental pneumatic SHPB bench with presentation of principal pneumatic propulsion system, control, measurement devices and inductive heating

As one can see in the Figure 2, the striker bar is driven by a pneumatic device using a tank with a volume V_0 of *20* l coupled on a pressurized air with maximum 10 bars via a circuit of rapid control, regulate and secure valves. Using a lot of plastic cylindrical PFTE collars mounted on the striker bar, this one is moved in axial translation by the air pressure propulsion on a distance of *1 m* inside the gun with 2 m length undergoing a small friction effect. The axial impact velocity is measured by a laser optic camera reading a barcode of *50 mm* large with a length of $\lambda_v = 5mm$ for each uniform distributed white/black slots via a paper barcode glued on the end of striker bar surface. The initial impact speed value is obtained by division of the slot length λ_v with the corresponding measured period times T_v recorded from a specific Labview program coupled on a high speed NI PCI 6110 acquisition card of 5 *MHz*. The Labview interface coupled to a digital VISHAY conditioner is also performed to record in Volts the experimental signals corresponding to two full strain bridges mounted on the half part of the incident bar and half part of the sending bar using a digital conditioner VISHAY (Figure 1). So the incident $\varepsilon_i(t)$, reflected $\varepsilon_r(t)$ and transmitted $\varepsilon_t(t)$ elastic strain waves of the bars can be estimated either through from a direct conversion using strain bridge formula or directly from a numerical calibration techniques. Computation of bars/specimen interfaces velocities and loads can be performed from analytical relationships based on the general dynamic elastic deformations propagation inside the bars [7] using David software [8]. A conventional thermocouple or an infrared camera coupled to an inductive heating coil together is used together with a thermal control device. The inductive heat system is then able to keep the initial metallurgical structure of metal specimen and to can estimate experimentally the material self-heating. It is then possible to perform impact compression tests for different initial temperature of material specimen. The identification of the thermo-mechanical material specimen behaviour in terms of true stress - true elasto-plastic strain for different strain rates and initial temperatures can be make using plasticity theory, hybrid numerical-analytical methods and inverse analysis strategy [9-14].

2.2 Pneumatic control circuit and experimental data acquisition

The propulsion control system of designed SHPB bench is fully pneumatic and in open loop as shown in the Figure 3. When the set pressure of tank air is reach, the operator triggers manually the air gun to trip the axial propulsion of the striker bar.

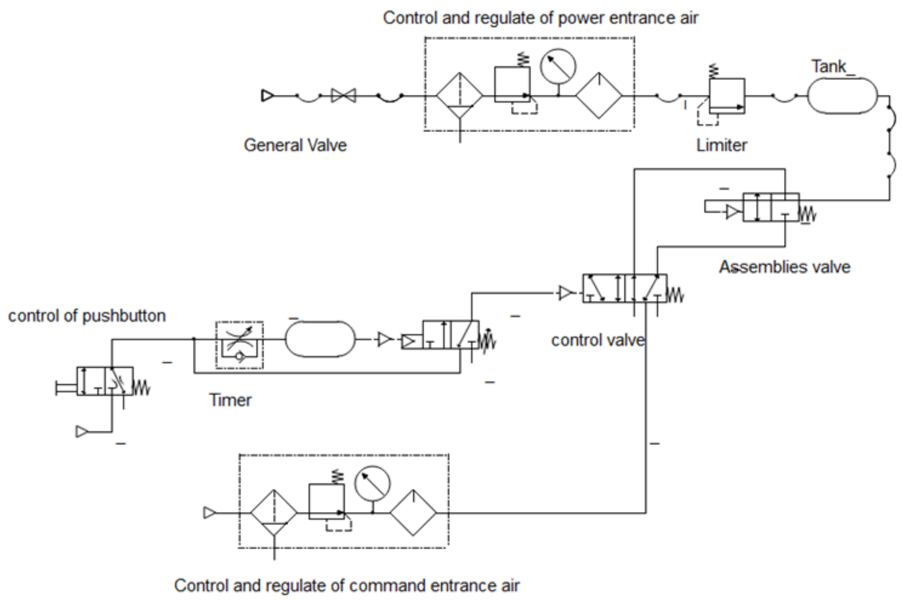

Fig. 3. Pneumatic control circuit used for propulsion of experimental mechatronic SHPB bench [16]

However, the implementation of a digital control system with feedback of different states of the system will improve its control allow precise and constant pressures when start the move of the striker bar inside the air gun. To resume, with an automatic control system, the pressure keeps constant value on the time gap between value pressure regulation and the launch of the test, the repeatability and robustness of the experiments guaranteed and more rigorous studies will be possible. After starting and triggering of the rapid control valve, the air gun projects the striker against the receiving bar. Before the shock, the laser sensor captures on the front of the incident bar the variation of a signal from an uniform succession of black and white slots with a length of λ_v. Thus is generate a square-shaped signal of period T_v, where the first rising edge acts as a trigger for optical sensor acquisition. The impact speed is deduced there from the ratio λ_v / T_v. The Labview language program developed for a real time acquisition of the optic sensor and gauge full bridges raw signals allows adjustment of the acquisition frequency f_a and of the scanning number b_s. The product $f_a \cdot b_s$ determines the total acquisition duration. In a first time to can calibrate the experimental bench, an experimental impact test without any specimen between the bars it realized. The Figure 4 plot the recorded experimental tensions obtained from the used laser camera reading the striker barcode with $\lambda_v = 5\,mm$ and from two full gauge bridges glued on incident and sender bars in order to measure the corresponding elastic wave strains for an air tank pressure around of 1.9-2 bars and an acquisition frequency f_a = 1 *MHz*.

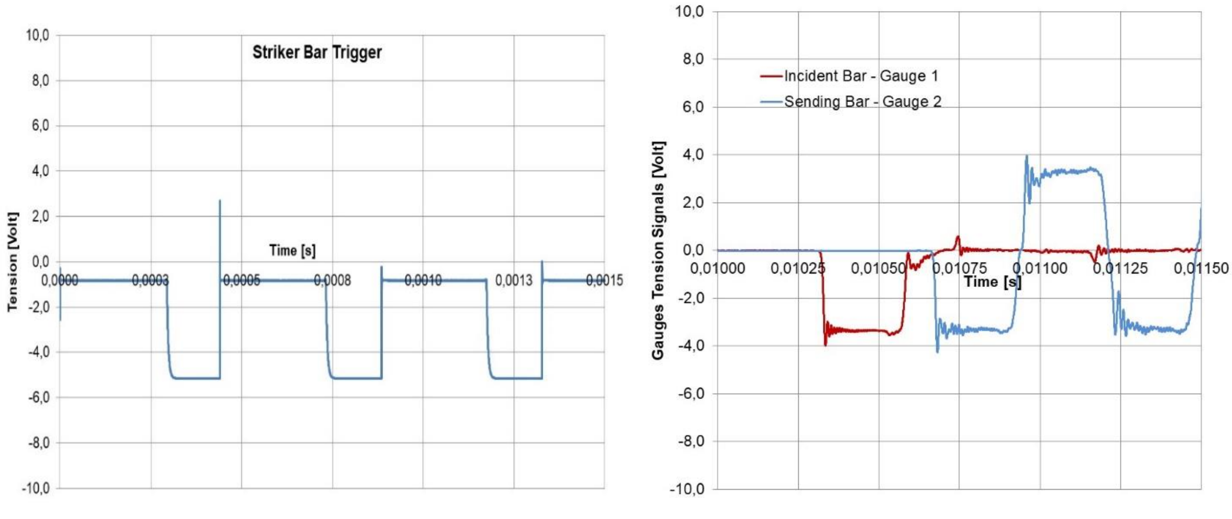

a) b)

Fig. 4. a) Square-Shaped Dirac tension signal of laser optical camera recorded by triggering option using Labview program, b) Gauges tension signal variation corresponding to the elastic wave deformation of the incident bar ($\varepsilon_i(t)$, $\varepsilon_r(t)$ for red curve) and sending bar ($\varepsilon_t(t)$ for blue curve) corresponding to a set tank air pressure of 1.9 bars - 2 bars [16]

As can be shown in Figure 4 a) the initial impact velocity can be estimate from the square-shape signal corresponding to the succession of black and white slots with a constant length of λ_v = 5 mm in the time period T_v estimate to be equal to 0.5138 *ms* by $v = \lambda_v / T_v \approx 10\,m/s$. Concerning the Figure 4b), in a classical way the full bridge gauge tension *U* (μV) is expressed in function of the corresponding elastic deformation value ε (μdef) starting from the formula:

$$U = U_0 F_g \varepsilon (1+\upsilon) / \left[2 + f_g \varepsilon (1-\upsilon) 10^{-6} \right] \quad (2)$$

where U_0 is the bridge supply voltage (expressed in Volt) and f_g the gauge factor given by the strain gauge. Starting from an acquisition frequency of 1 *MHz* and from the very short time of the impact period around of 1 *ms* it is required to set the VISHAY conditioner to record 1μ*V*/μ*def*. To obtain a reliable sensitive recorded tension, the dynamic conditioner amplifier uses a gain factor *G* i.e. $\hat{U} = GU$ and the equation (6) gives:

$$\varepsilon = 2\hat{U}\cdot 10^6 / \left[U_0 G F_g (1+\upsilon) - \hat{U} F_g (1-\upsilon)\right] \approx 2\hat{U}\cdot 10^6 / U_0 G F_g (1+\upsilon) \tag{3}$$

assuming $U_0 G \gg \hat{U}$ i.e. $U_0 \gg U$ where $\hat{U}$ (expressed in Volt) represents the tension values recorded by the output of Labview program.
According to the elastic strain gauge principle the variation of gauge deformation with the recorded tension is quasi-linear, consequently a calibration factor K_{exp} can be defined starting from the ratio between the corresponding gauge deformation value and the recorded tension i.e.:

$$K_{exp} = \varepsilon / \hat{U} \quad (\mu def / Volt) \tag{4}$$

For the used strain full bridge, the gauge factor f_g is equal to 2.09, the gain *G* is set around of 250 and the supply voltage of the bridge is chosen to be 7.5 *V*. Consequently, it is obtained a calibration factor K_{exp} = 1000/2.6 = 384.62 μ*def /Volt*.

2.3 Experimental estimation of initial impact velocity using Hermite interpolation method

The cubic Hermite spline method is an interpolation method by parts based on cubic Hermite polynomials. This method derives a third order polynomial of Hermitian form for each defined interval and only guarantees continuity for the first derivatives of polynomials interpolation. The cubic Hermite method has more local property than the classical cubic spline method. That is, if you change a data point xj, the effect on the interpolation result it is in the range defined by [x_{j-1}, x_j] and [x_j, x_{j+1}].

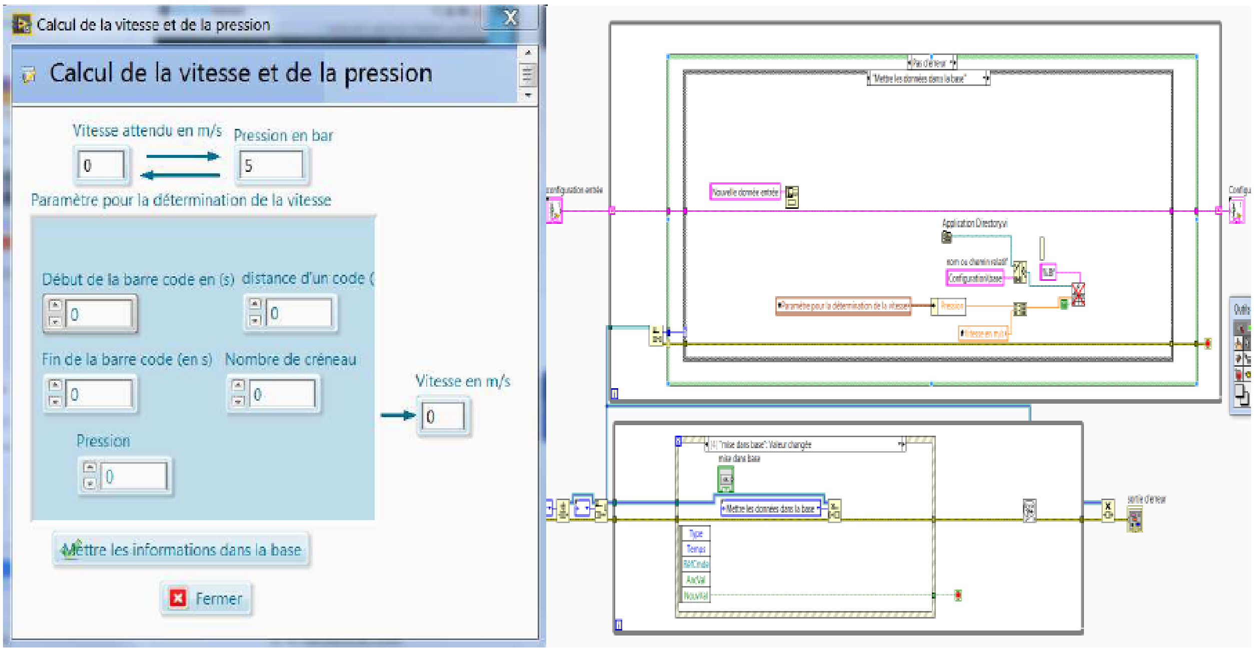

Fig. 5. Labview User Interface to set air pressure function of a predefined initial impact velocity

If known n experimental points, the Hermite polynomials P(x) of degree 2n+1 defining the function f variation is defined by

$$P_i(x) = f(x_i) + (x - x_i)\left[f'(x_i) - q'_i(x_i) f(x_i)\right],\ P(x) = \sum_{i=0}^{n} q_i(x) P_i(x) \text{ and } q_i(x) = \prod_{j=0, j\neq i}^{j=n} \left(\frac{x - x_j}{x_i - x_j}\right)^2 \tag{5}$$

Here *f* represents here the velocity variable and *x* the pressure value. *f'* is computed by a finite difference method starting from previous measured values. If coupling between Matlab and Labview it is more reliable to use the predefined function of cubic Hermite interpolation „*Pchip*" of Matlab. Concerning the use of SHPB system, the main purpose is to determine the tank air pressure according to the desired striker speed starting form a lot of previous experimental values and using interpolation based on the above Hermite functions *P(x).* On the basis of SHPB tests which have already been carried out, the user can choose to add each new measured velocity to the built base in order to improve interpolation quality and to obtain an auto-learning strategy. Using Labview program the Figure 5 show the obtained auto-learning user interface. Based on a lot of 15 experimental measurements of striker impact speed using the laser optic camera for a set of air pressure in the range of 1.6 bars – 2.9 bars, the Hermite interpolation and Labview interface find the velocity-pressure curve diagram pictured in Figure 6.

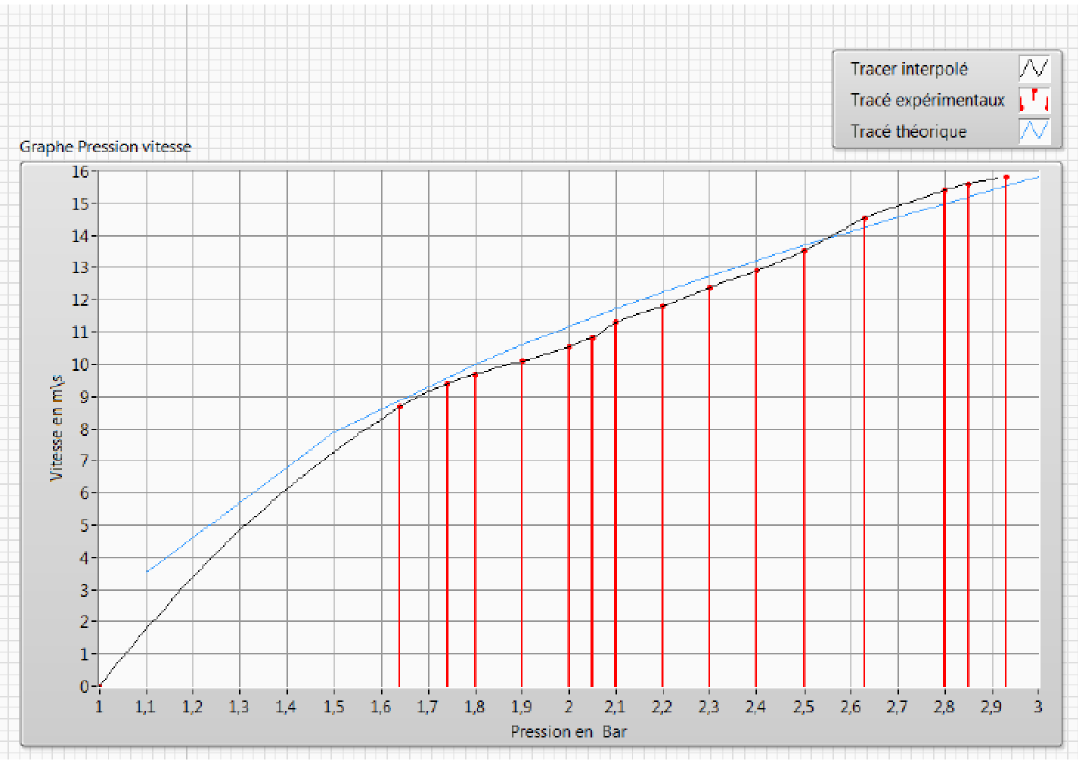

Fig. 6. Hermite interpolation of striker impact velocity – air pressure curve

Using this method, the user can estimate the air pressure choice corresponding to a specific initial impact velocity chosen in the range of 9 m/s – 15 m/s. This method can be use if experimental SHPB test not need precise initial impact speed. Therefore, regarding that the extrapolation outside the diagram range is too approximate and very imprecise a more robust control of striker impact velocity is need based on validation of a proposed reliable numerical calibration method.

2.4 Theoretical estimation of initial impact velocity

To be able to obtain a purely axial translation of the striker this one have a number of 5 glued cylindrical PTFE collars with a total length of $L = 80 \times 10^{-6}\ m$. Using theorem of mechanical energy balance the sum of kinetic energy variation of the striker ΔE_c and friction energy $E_f = \int_0^l \Delta E_f dx$ is equal to the work *W* of the bar surface force generated by air pressure i.e.:

$$\Delta E_c + E_f = \frac{1}{2}mv^2 + E_f = W = \int_0^l \left(\iint p(x) dS \right) dx \text{ with } m = \rho g l_{imp} \pi d_b^2 / 4 \tag{6}$$

where m is the mass of the striker bar, v the impact velocity obtained after the move on a distance equal to l, $p(x)$ represents the air pressure value of each axial bar position x *varying between 0 and* l and ΔE_f is the specific friction energy computed from an infinitesimal cylindrical slice with diameter D and length dx' corresponding to the collars contact.

Or if p_c is the initial absolute pressure inside the tank of volume V_0, taking into account the atmospheric pressure p_0 and the isothermal perfect gas law, the axial pressure variation is obtained from:

$$p(x)\left(V_0+Sx\right)=p_rV_0 \text{ with } p_r = p_c - p_0 \tag{7}$$

Assuming a uniform pressure distribution on the plastic collar glued on the striker bar along its section S, the corresponding mechanical work of pressure can be computed by:

$$W=\int_0^l p(x)Sdx=\int_0^l\left(\frac{p_rV_0S}{V_0+Sx}\right)dx=p_rV_0\ln\left(1+\frac{lS}{V_0}\right) \tag{8}$$

Concerning the contact between the collars of striker bar and inner surface gun, if supposed to have only smallest elastic deformation, a Coulomb friction law can be used and the corresponding friction energy can be computed by:

$$\Delta E_f=\int_0^L F_f dx' \text{ with } F_f=\mu\pi Dn_f \tag{9}$$

Here D is the collars diameter equal to the inner gun circular section diameter, n_f represents the specific normal force applied to the slice collars with dx' length and μ represent the Coulomb friction coefficient. Using axial mechanical equilibrium of collar infinitesimal slice with a length dx', supposing elastic incompressible cylindrical compression of collars and striker under the action of the axial pressure p(x), it can be written:

$$\sigma_{rr}(x')=n_f(x'),\sigma_{zz}(x') \text{ with } x'\in\left[x,x+dx'\right] \text{and } \sigma_{zz}(x)=p(x) \tag{10}$$

$$\left[\sigma_{zz}(x+dx')-\sigma_{zz}(x)\right]\pi D^2/4=\left[dn_f/dx'\right]dx'\pi D^2/4=\mu n_f dx'\pi D \tag{11}$$

where σ_{rr},σ_{zz} are respectively the radial and axial stresses.
Consequently, it can be expressed the specific normal force by:

$$n_f=p(x)\exp\left(-4\mu x'/D\right) \tag{12}$$

Finally using equation (9) the friction energy is given using following expression:

$$\Delta E_f=\left(\pi D^2/4\right)p(x)\left[1-\exp\left(-4\mu L/D\right)\right] \text{ and } E_f=W\left[1-\exp\left(-4\mu L/D\right)\right] \tag{13}$$

Starting from Eq. 6 the obtained impact velocity can be obtain from the following relationship:

$$v=\sqrt{\frac{2V_0}{m}\ln\left(1+\frac{lS}{V_0}\right)\exp\left(-4\mu L/D\right)}\cdot\sqrt{(p_c-p_0)} \text{ or } v=\left(\alpha'/\sqrt{l_{imp}}\right)\sqrt{(p_c-p_0)} \tag{14}$$

Here α' is a variable depending of tank capacity volume V_0, gun inner diameter D and section $S=\pi D^2/4$, friction coefficient μ, total collars length L and sticker material density ρ. Starting from the SHPB material properties and geometric characteristics given on Table 1 and 2 the tank volume is $V_0=20\,l=2\cdot10^{-2}m^3$, the displacement is l=*1m* and the collar surface glued on the front of the striker bar has a surface $S=\pi D^2/4=\pi\cdot30^2\times10^{-6}/4\,m^2=706{,}86\times10^{-6}m^2$ which approximate $\ln\left[1+(lS/V_0)\right]=0{,}035$ and $\alpha'=\alpha\approx0.029$ if neglecting friction phenomena i.e. μ = *0* as can be considered in a previous research work [16,17].

Using a numerical calibration strategy starting from experimental striker velocities measured by optic camera, a value of μ = 0.0162 is obtained solving a parameter identification problem based on $\underset{\mu}{Min}\left[\left(\sum_{i=1}^{N\exp}\left(v-v^{\exp}\right)^2\right)/\sum_{i=1}^{N\exp}v^{\exp^2}\right]$ and using a non-linear least squares Levenberg-Marquard algorithm of Matlab software. The identification error of friction coefficient is around of 3%. Regarding the experimental values of a Coulomb PTFE/Steel friction contact, the scientific literature shows a friction coefficient value around 0.02 close to the obtained identified value. Regarding the relationship (14), if friction term is taking into account it is obtain a factor $\alpha' \approx 0.027$. Then, it can be concluded that the estimation error of initial impact velocity is around of 7%- 8% between the case neglecting friction phenomenon and the case taking into account a Coulomb contact friction. Impact velocities estimations for different striker bar lengths l_{imp} from 0.5 *m* to 1 *m* are plot in Figure 7.

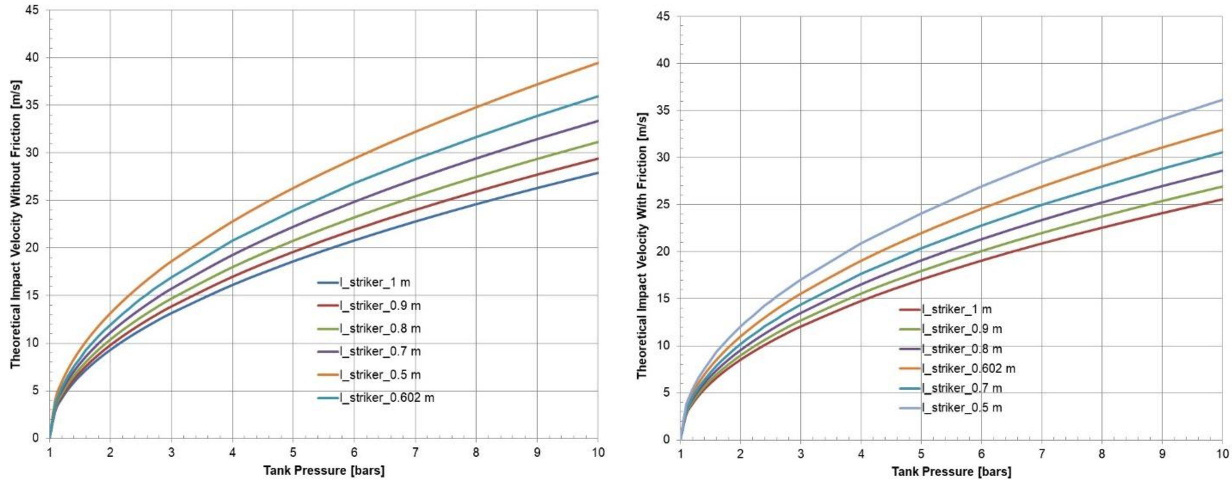

a) b)

Fig. 7. a) Curves variation of Theoretical Impact Velocities – Tank Pressure for different striker bar length without friction phenomena (0.5 m to 1 m), b) Curves variation of Theoretical Impact Velocities – Tank Pressure for different striker bar length using friction phenomena with μ = *0.0162* (0.5 m to 1 m)

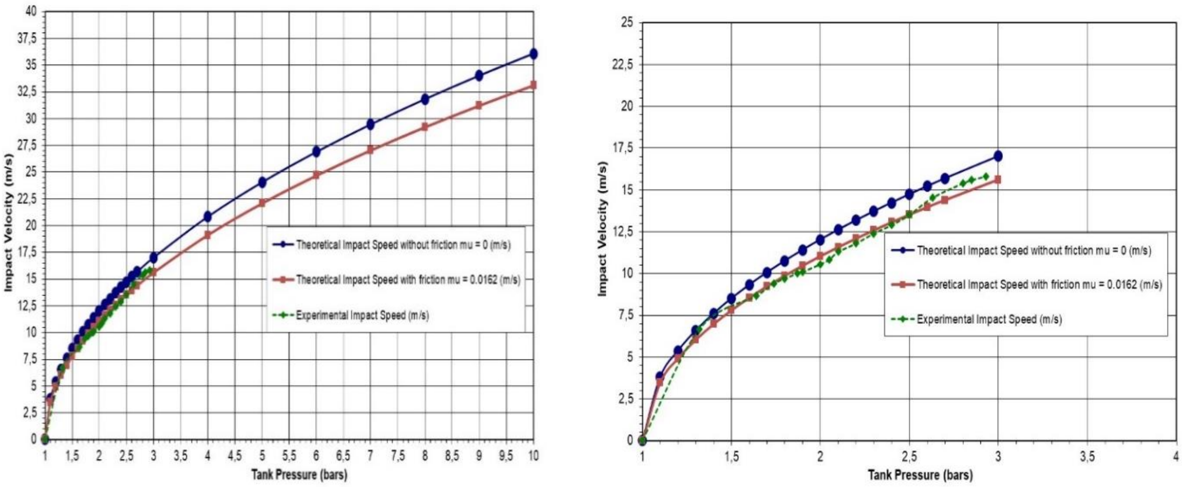

a) b)

Fig. 8. Comparison between experimental and theoretical impact speed values obtained for the striker with a length of 0.602 m a) without friction (μ = *0*) and b) taking into account the friction (μ = *0.0162)*

One can observe that using a maximal tank pressure of 8 bars for striker bars with short length (0.5 m to 0.6 m) the impact velocity varied from 5 *m/s* to 30-35 *m/s* as compared to an impactor with a length of 1 *m* where the maximum impact speed is limited to 25 *m/s*. The use of a striker with the length of 0.602 *m* (mass $m \approx 0,96\,Kg$), if the tank pressure is expressed in bars an estimation of impact velocity can be obtained by $v \approx 11,82\sqrt{(p_c - p_0)}$ if friction is neglected and by $v \approx 10,84\sqrt{(p_c - p_0)}$ if a friction coefficient μ = *0.0162* is used. Figure 8 shows the comparison between the experimental and theoretical impact velocities.

Table 3: Theoretical and experimental impact speed obtained from different values of tank pressure for the striker with a length of 0.602 m

Tank Pressure (bars)	Theoretical Impact Speed Estimation Without Friction (m/s)	Theoretical Impact Speed Estimation Using Friction (m/s)	Tank Pressure (bars)	Exp. Impact Speed (m/s)
1	0	0	1	0
1.1	3.80	3.49	-	-
1.2	5.38	4.93	-	-
1.3	6.59	6.04	1.32	6.68
1.4	7.61	6.98	1.55	6.86
1.5	8.51	7.80	1.64	8.67
1.6	9.32	8.55	1.74	9.41
1.7	10.06	9.23	1.8	9.7
1.8	10.76	9.87	1.87	10
1.9	11.41	10.47	1.9	10.1
2	12.03	11.03	2	10.56
2.1	12.62	11.57	2.05	10.84
2.2	13.18	12.09	2.1	11.3
2.3	13.72	12.58	2.2	11.8
2.4	14.23	13.06	2.3	12.4
2.5	14.73	13.51	2.4	12.9
2.6	15.22	13.96	2.5	13.52
2.7	15.68	14.39	2.63	14.54
3	17.01	15.60	2.8	15.4
4	20.84	19.11	2.85	15.6
5	24.06	22.07	2.93	15.82
6	26.90	24.67	-	-
7	29.47	27.03	-	-
8	31.83	29.19	-	-
9	34.03	31.21	-	-
10	36.09	33.10	-	-

The experimental values of initial impact velocities measured by laser camera for a lot of tank pressures show very good correlation with the curve of theoretical variation plotted in Figure 8b and values detailed in Table 3. An average estimation error of 8 % is obtained due essentially to the friction phenomena caused by the local contact of the guidance glued collars of striker bar with the inside surface of the gun.

3. Numerical Analysis

To make the SHPB mechatronic system analysis in both experimental and numerical point of view the Figure 9 pictures the flowchart of proposed integrated design strategy, robust control and identification of tested material specimen undergoing a thermo-mechanical compression impact.

Fig. 9. Flowchart of proposed hybrid analytical-numerical analysis of SHPB system using numerical calibration, entire SHPB Finite Element Modeling and Inverse Analysis

3.1 Numerical Calibration and Finite Element Modelling of SHPB System

To improve the experimental calibration procedure in order to avoid approximations of given gauge factor, gain choice and measurements errors, a robust and more general numerical method it is proposed. This numerical calibration method is based on a lot of empty SHPB experimental tests without specimen performed for different air tank pressure and consequently different initial impact velocities, using a Finite Element Modelling of the entire bar's system following the below steps:

I. Empty experimental compression SHPB test (without any specimen) with direct contact of incident and sending bar and at a set of initial impact velocity *v* chosen with respect to the above impact velocity-pressure diagrams. It can be proven theoretically that $\varepsilon_i < 0, \varepsilon_r = 0, \varepsilon_t = \varepsilon_i < 0$ [14];

II. Recorded of tensions time variation $\widehat{U}_i(t)$, $\widehat{U}_r(t)$ and $\widehat{U}_t(t)$ (corresponding to the experimental gauge elastic deformations $\varepsilon_i(t)$, $\varepsilon_r(t)$ and respectively $\varepsilon_t(t)$ found using Labview program);

III. Estimation of the real initial impact speed $\hat{v}$ from the time period T_v of the first square-shaped time Dirac signal of the recorded laser optic camera measurements using the formulas $\hat{v} = \lambda_v / T_v$;

IV. Estimation of the experimental celerity c_{exp} from the time period $t_{i_{\exp}}$ corresponding to the first slot of recorded incident signal $\widehat{U}_i(t)$ using the formulas $c_{\exp} = 2 l_{imp} / t_{i_{\exp}}$;

V. Finite Element Simulation of the entire SHPB system using same initial and boundaries conditions as the experimental one (same celerity speed value and same initial impact velocities) with extraction of elastic strains time variation $\varepsilon_{i_{num}}(t)$, $\varepsilon_{r_{num}}(t)$ and $\varepsilon_{t_{num}}(t)$ corresponding to the geometric points positions of the two gauge bridges (one on the half part of the incident bar and other on the half part of the sending bar).

VI. Computation of the numerical calibration factor $K_{num} = \mathrm{Max}\left|\varepsilon_{i_{num}}(t)\right| / \mathrm{Max}\left|\widehat{U}_i(t)\right| = \hat{\varepsilon}_{i_{num}} / \widehat{U}_i$

VII. Experimental – Numerical Comparisons of the time variation concerning incident, reflected and transmitted elastic strains.

An axisymmetric dynamic Finite Element Modelling of SHPB test choosing an initial impact velocity of 10 *m/s* and an incremental time of 10^{-6}s is performed using Cast3M [18], ABAQUS and LS-Dyna code [9-13, 14-15] based on tridimensional elastic properties of the bars, inertial effect and QUAD4 mesh (Figure 10).

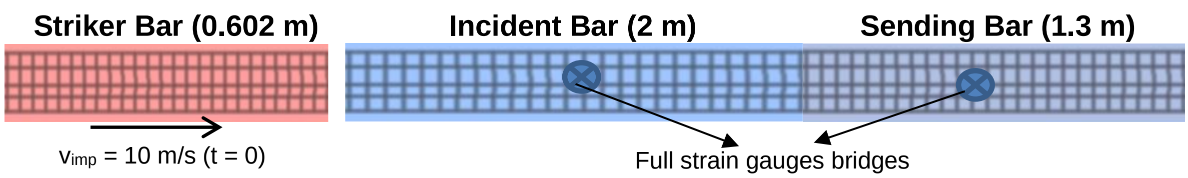

Fig. 10. Mesh of the striker, incident and sending bars used for a Dynamic Finite Element Simulation of the SHPB device using Cast3M, Abaqus and LS-Dyna code

Results concerning the elastic deformations and axial stress obtained from gauge bridges positions are illustrate in Figure 11.

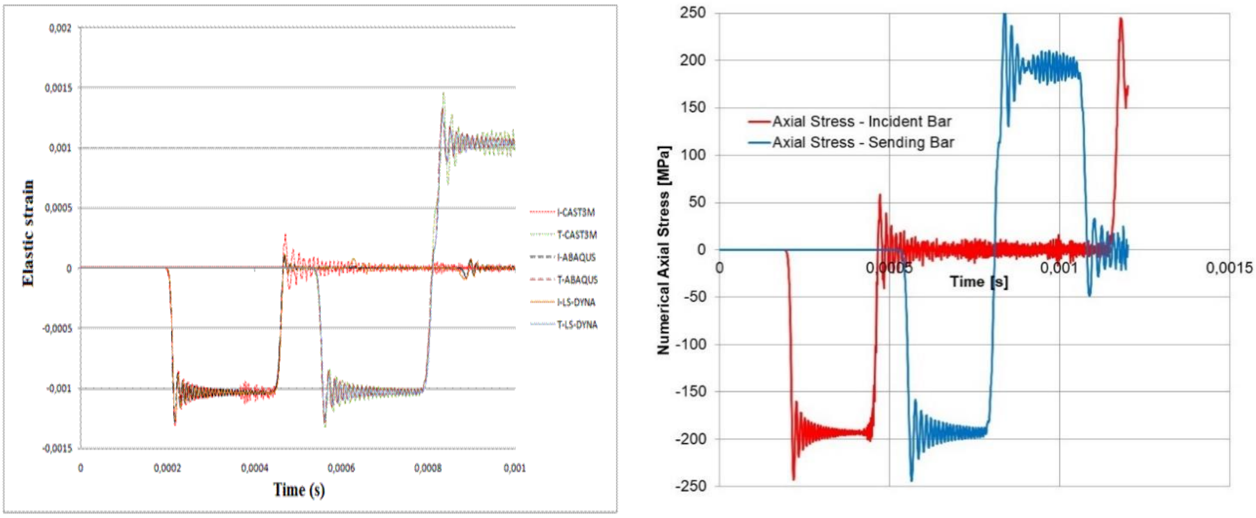

a) b)

Fig. 11. Numerical results corresponding to the strain gauge bridges position obtained from the Dynamic Finite Element Simulation using Cast3M, ABAQUS and Ls-DYNA code a) Elastic Strains, b) Axial Stress

An analytical estimation of calibration factor K_{an} can be obtained from the ratio of values corresponding to numerical incident elastic deformation $\hat{\varepsilon}_i$ and measured tension $\widehat{U}_i$:

$$K_{an} = \hat{\varepsilon}_i / \widehat{U}_i \ (\mu def / Volt) \tag{15}$$

Or the general theory of bar's elastic wave propagation shown that for an impact velocity *v* $\hat{\sigma}_i = 0.5 \rho c_b v \cong E_b \hat{\varepsilon}_i$ and $\hat{\varepsilon}_i = \rho c_b v / 2E_b = v / 2c_b$. So:

$$K_{an} = v \cdot 10^6 / 2c_{\exp} \hat{U}_i \ (\mu def / Volt) \tag{16}$$

Here the bar's celerity c_{exp} can be estimated using the expression (1) from the time period $t_{i_{\exp}}$ of the first slot of the recorded incident signal $\widehat{U}_i(t)$ by $c_{\exp} = 2 l_{imp} / t_{i_{\exp}}$. The signal of incident deformation measured in Volts has a value close to $\hat{U}_i = 3{,}33V$ with a time broadness $t_i = 0{,}254\,ms$ and the experimental celerity can be evaluated as $c_{\exp} = 2 l_{imp} / t_{i_{\exp}} = 2 \cdot 10^3 \cdot 0{,}602 / 0{,}254 \approx 4740\ m/s$. As compared to a previous estimation about of 4821 *m/s* [11] the error of the sound celerity is smallest that 2.5%. Using the equation (10), the analytical calibration factor becomes K_{an} = 317 *μdef /Volt* i.e. 17% differences as compared to the previous experimental or classical strain gauge's calibration factor i.e. K_{exp} = 384.62 *μdef /Volt*. From Fig. 8 it can be observed that $\mathrm{Max}\left|\varepsilon_{i_{num}}(t)\right|$ = 1034.7 *μdef* and $\mathrm{Max}\left|\sigma_{i_{num}}(t)\right|$ = 191 *MPa* values close to the analytical estimations given by $\hat{\varepsilon}_{i_{an}} = v / 2c_b \cong$ 1054.9 *μdef* and $\hat{\sigma}_{i_{an}} = 0{,}5 \rho c_b v \cong$ 189.6 *MPa*. Taking into account the experimental tension value obtained in Volts from the incident deformation signal, the numerical calibration factor can be estimated by $K_{num} = \widehat{\varepsilon}_{i\_num} / \widehat{U}_i = 310{,}7 \mu def\ / Volt$. As compared to the analytical value, the error is around of 2%. Despite the validation of the proposed calibration method it is possible to conclude that the numerical calibration strategy is more robust and can be performed for more complex conditions as for example in the case of viscoelastic or non-metallic materials bars, or for optic fibbers measurements of elastic deformations where analytical computation models are too approximate or no more valid.

3.2 Numerical Inverse Analysis of SHPB System

The entire Finite Element Model has been performed to simulate SHPB compression tests using different shape of specimens (dumbbell or hat cylindrical samples) undergoing complex strain path especially used to identify by a Two-Step Inverse Analysis strategy the non-linear thermo-mechanical material constitutive equations and the corresponding material coefficients. Details can be show in previous works of Gavrus et al. [9-17]. The proposed Two-Step Inverse Analysis consists in a first step to compute the specimen interfaces velocities and loads starting from the solution of an Analytical Inverse Problems based on equations of elastic wave propagation and on the measured strain gauges measurements followed by a second Inverse Analysis at the specimen scale using Finite Element Modelling of sample elasto-plastic deformations. Finally, the experimental strain gauges signals are compared to the computed ones using Finite Element Simulations of entire SHPB System to valid the used material constitutive law identification method pictured in Figure 12.

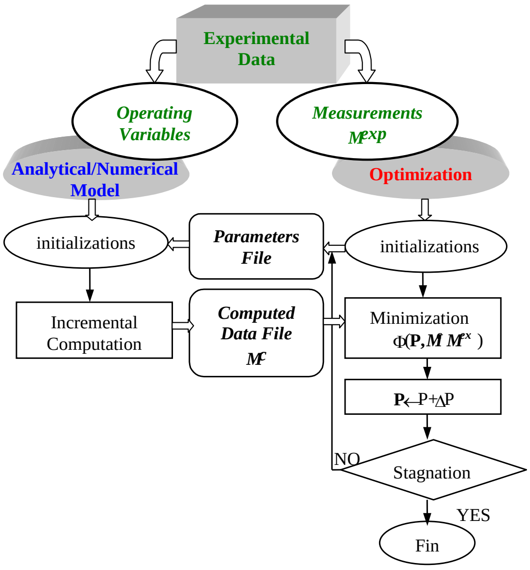

$$\Phi(P)=\frac{\sum_{k=1}^{N\exp}\left[M^{c}(P)-M^{ex}\right]^{2}}{\sum_{k=1}^{N\exp}\left[M^{\exp}\right]^{2}}$$

or

$$\Phi(P)=\sum_{k=1}^{N\exp}\left[\frac{\left(M^{c}(P)-M^{ex}\right)}{M^{ex}}\right]^{2}$$

GAUSS-NEWTON OR LEVENBERG-MARQUARD MINIMISATION ALGORITHM

$$[\Delta P]=-\left[\frac{d^{2}\Phi}{dP^{2}}\right]^{-1}\left[\frac{d\Phi}{dP}\right]$$

Identified Parameters P

Fig. 12. Inverse Analysis Principle applied to solve Non-Linear Identification or Inverse Problems

4. Conclusions

The above experimental design and quantitative description of the pneumatic compression mechatronic SHPB bench confirms the robustness of impact speeds control together with strong validations of their theoretical dependency on tank air pressure set. A new hybrid analytical-numerical calibration method was detailed in order to can estimate the elastic wave strains which travels with a specific celerity the incident and sending bars. A complete dynamic Finite Element Modelling and Simulation of the SHPB system without specimen has been performed to establish a more rigorous estimation of the conversion factor between the measured gauge full bridge tension and real elastic strain value. Comparisons with analytical formula based on elastic wave propagation theory of infinite bars have shown the high precision of the Finite Element Modelling results, which permit to valid the entire calibration strategy. It is also possible to confirm again the rightness of the proposed two-step Inverse Analysis technique developed from 1998 during previous research works at INSA Rennes to identify specific constitutive equations of metallic materials under severe loadings and complex deformation paths: large plastic strains, high strain rates, temperature influence and important local gradients of thermo-mechanical variables. Regarding the generality of the proposed numerical calibration method, this one will be apply in a future research work to improve the SHPB acquisition system by use of local Bragg optic fibers sensors and specific optical interrogators developed by Dimione Systems of France and Redondo Optics Company of USA to measure in a more accuracy manner the elastic deformations of the bars.

References

[1] Hopkinson, B. “A method of measuring the pressure produced in the detonation of high explosives or by the impact of bullets.” *Philosophical Trans. of the Royal Society of London* A213 (1914): 437-452.

[2] Davies, R.M. “A critical study of Hopkinson pressure bar.” *Philosophical Transactions of the Royal Society of London* A240, no. 821 (1948): 375-457.

[3] Kolsky, H. “An investigation of the mechanical properties of materials at a very high rate of loading.” *Proceedings of the Physical Society of London* B62 (1949): 676-701.

[4] Kolsky, H. *Stress Waves in Solids*. Oxford, Clarendon Press, 1953.

[5] Parry, D.J., P.R. Dixon, S. Hodson, and N. Al-Maliky. “Stress equilibrium effects within Hopkinson bar specimens.” *Journal de Physique IV Proceedings* 04 (C8) (September 1994): C8-107-C8-112.

[6] Gary, G., and H. Zhao. “Dépouillement de l'essai aux barres de Hopkinson par une technique de calcul inverse.” *Journal de Physique IV Proceedings* 04 (C8) (September 1994): C8-89-C8-94.

[7] Zhao, H. *Analysis of the Hopkinson bar test: Application to measuring the dynamic behavior of materials / Analyse de l’essai aux barres d’Hopkinson: Aplication a la mesure du comportement dynamique des materiaux*. PhD Thesis, Ecole Polytehnique, Paris, France, 1992.

[8] DAVID software, Ecole Polytehnique, LMS, Paris, France.

[9] Gavrus, A., J.–P. Le Baron, P. Caestecker, and E. Ragneau. “Investigation of High Speed Behaviour of Ductile Materials by Computer Simulation and Hopkinson Experimental Test.” Paper presented at International Conference on Advances in Mechanical Behaviour, Plasticity and Damage, EUROMAT 2000, Tours, France, November 7-9, 2000.

[10] Gavrus, A., P. Caestecker, E. Ragneau, and B. Davoodi. “Analysis of the dynamic SHPB test using the finite element simulation.” *Journal de Physique IV* 110 (September 2003): 353-358.

[11] Davoodi, B., A Gavrus, and E. Ragneau. “An experimental and numerical analysis of heat transfer problem in SHPB at elevated temperatures.” *Measurement Science and Technology* 16, no. 10 (2005): 2101-2108.

[12] Gavrus, A., B. Davoodi, and E. Ragneau. “A study of material constitutive behaviour at elevated temperature from compressive SHPB test using an inverse analysis method.” *Journal de Physique IV* 134, (August 2006): 661-666. EURODYMAT 2006 - 8th International Conference on Mechanical and Physical Behaviour of Materials under Dynamic Loading.

[13] Rotariu, A. *Contributions regarding the experimental determination of the mechanical properties of some materials in a dynamic regime / Contributii privind determinarea experimentală a proprietăților mecanice ale unor materiale în regim dynamic*. PhD Thesis, Military Technical Academy, Bucharest, 2007.

[14] Diot, S., D. Guines, A. Gavrus, and E. Ragneau. “Two step procedure for identification of metal behaviour from dynamic compression tests.” *International Journal of Impact Engineering* 34 (2007): 1163-1184.

[15] Gavrus, A., F. Bucur, A. Rotariu, and S. Cananau. “Mechanical Behavior Analysis of Metallic Materials using a Finite Element Modeling of the SHPB Test, a Numerical Calibration of the Bar’s Elastic Strains and an Inverse Analysis Method.“ *International Journal of Material Forming* 8, no. 4 (2015): 567-579.

[16] Gavrus, Adinel, Fabien Marco, and Sylvain Guegan. “Experimental Design, Modelling and Numerical Calibration of a High Speed SHPB Mechatronic System Using a Pneumatic Propulsion Device.” Paper presented at the 23rd International Conference on Hydraulics and Pneumatics HERVEX 2017, Baile Govora, Romania, November 8-10, 2017.

[17] Gavrus, Adinel, Sylvain Guegan, and Fabien Marco. “Impact Velocity Control of a Mechatronic Hopkinson Bar System with Robust Pressure Control, Digital Calibration of Strain Wave Measurement and Inverse Analysis.” / “Contrôle des Vitesses d’Impact d’un Système Mécatronique de Barres Hopkinson avec Commande Robuste de la Pression, Calibration Numérique de la Mesure des Ondes de Déformation et Analyse Inverse.” Paper presented at the 24th Congrès Français de Mécanique (CFM 2019), Brest, France, August 26 – 30, 2019.

[18] CAST3M – Finite Element Code, developed by Center of Atomic Energy CEA – France.

ISSN 1454 - 8003
Proceedings of 2023 International Conference on Hydraulics and Pneumatics - HERVEX
November 8-10, Băile Govora, Romania

CAD TOOLS, REVERSE ENGINEERING, 3D MEASURING AND ARTIFICIAL NEURAL NETWORKS IN AXIAL PISTON PUMPS STUDY

Nicușor BAROIU[1], Viorel PĂUNOIU[1], Virgil Gabriel TEODOR[1], Georgiana-Alexandra MOROȘANU[2], Marius GERU[2]

[1] Department of Manufacturing Engineering, "Dunărea de Jos" University of Galaţi, Romania
Nicusor.Baroiu@ugal.ro, Viorel.Paunoiu@ugal.ro, Virgil.Teodor@ugal.ro

[2] Open Hub Association, Galati, Romania
georgianamorosanu@thecon.ro, marius@openhub.ro

Abstract: *The correct definition of technical parameters in the construction of volumetric pumps, especially those with axial pistons, must take into account both their mode of operation, characteristic load curves, and their operating duration. Since hydraulic pumps in general, and axial piston pumps in particular, are equipment capable of utilizing the energy transmitted by the fluid at high powers and moments of operation, great attention is paid to them from the design phase to maintenance. This paper aims to address essential principles in the CAD modeling of an axial piston pump, a study on the inspection of the piston block using a specific reverse engineering measurement technique, which involves 3D scanning of these components and their measurement using specialized software (GOM Inspect), as well as the comparison, through overlay, of CAD models created using CATIA software with scanned models, highlighting the advantages of reverse engineering techniques compared to traditional CAD design. By using coordinate measuring machines, the free-form, internal, and external surfaces of the piston block were measured and inspected to generate coordinates of measured three-dimensional points on the surfaces, with the aim of defining the maximum distances between the real profile and the adjacent circle of the axis channels (deviations from circularity), through parameter specifications such as eccentricity, concentricity, and radial runout. Additionally, a neural network model is proposed for predicting the theoretical fluid flow rate of axial piston pumps based on their technical parameters, such as pump speed, number of pistons, effective piston diameter, or stroke, which aims to optimize the synchronization process between the drive shaft rotation and the piston block rotation and ensure efficient power transfer to the overall hydraulic system.*

Keywords: *Hydraulic pump, axial piston, CATIA, reverse engineering, GOM Scan, GOM Inspect, 3D measurement, artificial neural network (ANN)*

1. Introduction

Pumps are considered primary elements in the structure of hydraulic systems, which have the role of transforming mechanical energy into hydraulic energy and are designed to generate a power flow necessary to overcome the pressures developed against their own load [1,2,3]. Among them, hydraulic pumps with axial pistons, transform mechanical energy into hydraulic energy using pistons that move axially-alternatively in a pistons block, during the rotation of the central shaft, being among the most widespread in industrial and mobile hydraulic drives [4]. Due to the small moment of inertia and the axial balancing, they can operate at high speeds, frequently at *1500÷2000 rpm* and, in special cases, at *4000÷20000 rpm*, ensuring both the efficient transmission of the hydraulic fluid from the tank, as well as pumping it into hydrostatic systems at nominal working pressures and flows. They circulate flows between *Q=3÷800 l/min* at high and very high pressures p=200÷700 bar. These machines can reach powers up to *3500 kW* [5,6,7]. Axial piston pumps consist of a specially designed piston block within which the pistons move axially where, during operation, the central shaft of the pump is set into movement by an electric motor, which causes the piston to move. This process consists of two distinct and complementary stages: suction, when the piston moves in the axial direction, thus creating a suction space into the pump cylinder, and discharge, when the piston returns to its original position, reducing the volume of the cylinder.

This causes the pressure inside the cylinder to increase, which causes the fluid aspirated in the previous stage to be pushed into the hydraulic system. Thus, a constant flow of fluid is obtained at the pressure required to supply and control various hydraulic applications [3,8,9]. According to the location of the piston block in relation to the driving disk, three main categories of axial piston pumps are distinguished: with inclined block, with inclined disk, with rotating swashplate [1,7]. Multiple studies of axial piston pumps have been considered component analysis to understand and highlight a series of wear mechanisms under rapid maintenance conditions in order to reduce hydrostatic drive flow shutdown times involving such pumps [10,11,12]. This can be done both by 3D measurements of the surfaces of the pump components, especially of the pistons and their bores, whose non-uniformity can lead to not ensuring optimal loading and lubrication conditions [13,14], but also by optimizing the shape of the piston couple surface/cylinder, of technical operating parameters [15] through genetic algorithms [16] or neural networks [17,18], or graphical modeling or reverse engineering techniques [19,20,21].
Reverse engineering has gained momentum as an investigative method and starts from a real model or an existing construction of a functional technical component, identifiable by measurement, and retrieves appearance, shape and structure data, data used later to build digital 3D models [22]. Such a working technique, which starts from existing physical characteristics, but for which there is no specific technical documentation, is extremely useful in the reconditioning processes of various components within axial piston pumps.
Thus, if the constructive form of these components can be obtained much more easily by actually measuring them, by scanning and making 3D models of the components and is doubled by an analysis with neural networks, as universal approximators that work best if the systems that models have a high error tolerance, then some of the advantages of the reverse engineering technique over traditional CAD design can be highlighted. Among them could be exemplified: speed in processing the results, reduced time in transposing the models in digital form, precise determination of deviations by comparison with CAD model etc.
The paper presents a three-dimensional measurement technique specific to reverse engineering, which involves the 3D scanning of the piston block of an axial piston pump, followed by the dimensional measurement of the functional components with the help of a specific software (*GOM Inspect*) and comparison, by overlap, with the CAD model made with *CATIA* software. At the same time, an analysis based on an artificial neural network (*ANN*) of modeling and optimization was developed to determine the specific process variables corresponding to the theoretical fluid flow of axial piston pumps.

2. The scanning process

The scanning of the piston block from the axial piston pump structure was performed using the *Atos Core* [23] equipment, which relies on advanced and innovative technology to accurately and fully automate the inspection and measurement of the parts. The processing of the images obtained from the scanning process was performed with the help of the *GOM Scan* program, a specialized software solution designed to satisfy the requirements in the fields of reverse engineering and rapid protyping. Calibration procedures, automatic configuration of scan parameters such as resolution and exposure times and performing polygonalization were performed. The *GOM Scan* program provides data from the scanned surface in a three-dimensional representation, the measurement process being performed with or without the use of reference markers, which are adhesive elements that are applied both to the scanned object and to the table of the equipment before starting the actual process scanning. The software identifies and captures visible reference points in camera images.
These points are later recognized and used to transform all subsequent scans. In each subsequent scan, it is necessary to capture at least three known reference points to ensure the correctness of the transformations in the three-dimensional views. Thus, before starting the scanning procedure, reference markers are applied to the piston block, Figure 1.

Fig. 1. Applying reference markers to the piston block

In order to ensure a high level of accuracy in the scanning process, it is essential to use an anti-reflective spray that is applied to the part. After the reference markers have been carefully applied and after the surface of the part has been covered with the anti-reflective spray, the actual process scanning of the piston block is initiated, Figure 2.

Fig. 2. Applying the anti-reflective spray and starting the scanning process of the piston block

The piston block scanning process included a total number of 54 scans, of which 17 scans were performed for the top view, 7 scans for the side view, and 30 scans for the bottom view. This detailed approach to scanning from multiple angles and perspectives contributes to obtaining a comprehensive and accurate image of the analyzed object.
After the piston block scanning process is completed, the polygonalization step follows. This involves correlating and merging all scans performed on the object to obtain a complete and detailed numerical model. The polygonization process is initiated by accessing the *GOM Scan* menu and selecting the appropriate options: *Acquisition -> Measurement series -> Polygonize and Recalculate*.
Thus, the necessary calculations are performed to create the network of points that will represent the surface of the scanned part. To ensure the quality of the model and to remove any imperfections or unwanted edges on the surface of the scanned part, the *Select/Deselect Through Surface* command is used. This function allows the operator to precisely identify and remove unwanted details, thus ensuring that the final model obtained is as accurate as possible and precisely represents the scanned part.
Figure 3 shows the final result of the piston block scan made with the Atos Core equipment.

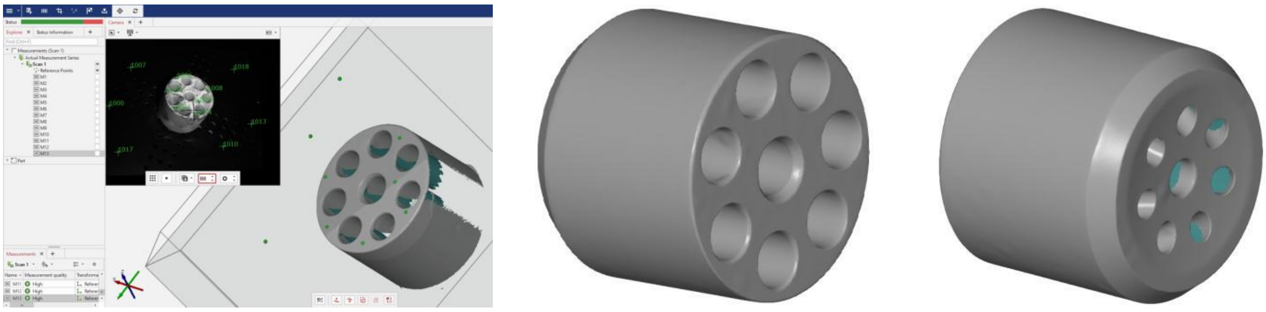

a. b.

Fig. 3. Sequences during the piston block scanning process (a) and scanned model of the piston block (b)

The scanned part will be saved as a file with **.stl* extension, which later allows it to be opened in a variety of design software such as *CATIA*, *AutoCAD*, *Autodesk Inventor*, *SolidWorks* etc. This file format (**.stl*) is a widely accepted standard in the CAD industry and enables the compatibility and efficient transfer of 3D models between different platforms and design applications.

3. The inspection process

The inspection process of the piston block is performed with the help of the *GOM Inspect* program, in order to determine the dimensional characteristics of the part and to create a model of it in a specialized software, in order to compare it with the CAD model. In a first stage, in order to determine the dimensions of the piston block, the construction of a reference system for the part is initiated. This process begins by creating a cylinder in the area inside it using the *Fitting Cylinder* function. The cylinder is built to approximate the shape and dimensions of that area. In the next step, a point is constructed, using the *Point from Line* function, with the direction defined by the axis of the cylinder. This point is an essential element in establishing the reference system. At the same time, the plane perpendicular to the axis of the cylinder is created using the *Point-Normal Plane* command. This plane has as reference point the previously created point, point *1*, and the direction of the normal will be given by the axis of the cylinder, Figure 4a.

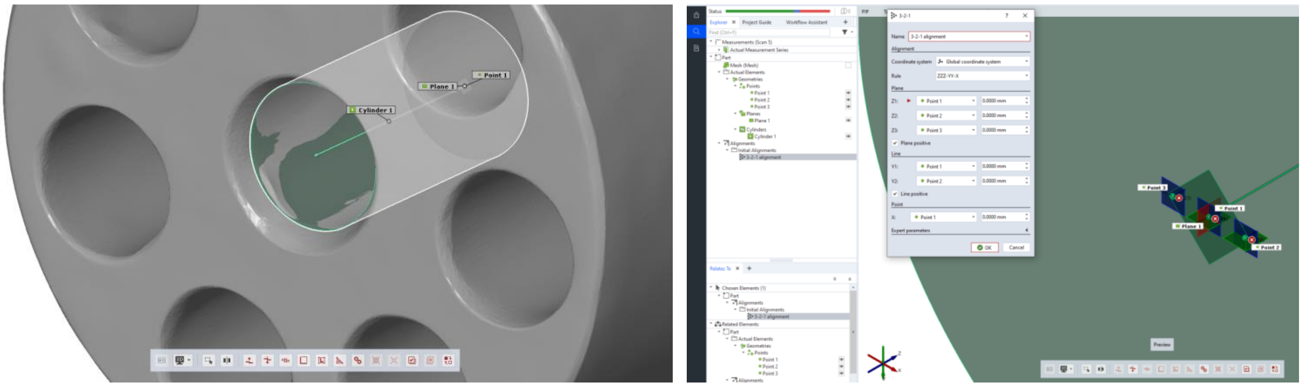

a. b.

Fig. 4. Generating the reference elements in order to establish the coordinate system of the part (a) and *3-2-1 Alignment* function in order to establish the coordinate system of the part (b)

In the final step of the process, an alignment operation is performed in order to establish the reference system, using the *3-2-1 Alignment* function, which is usually used as an initial system alignment. With the help of the *3-2-1 Alignment* command, the nominal reference system position is established. In this alignment process, six 3D points are used to define the reference system.
Thus, in addition to the initial point (*Point 1*), two additional points are created on plane *1*, this being done using the *Point* command. Thus, having all the elements built, the alignment process

that defines the reference system is performed, Figure 4b. To obtain the dimensions of the piston block, essential for building later the 3D model, the contour of the part is created using the *Single Section* function. Thus, to determine the cross sections, a reference plane is chosen that is parallel to the axis of the cylinder (*Z* plane), located at a specific distance of *17 mm*, respectively *-25 mm*, in relation to the initial reference plane, Figure 5.

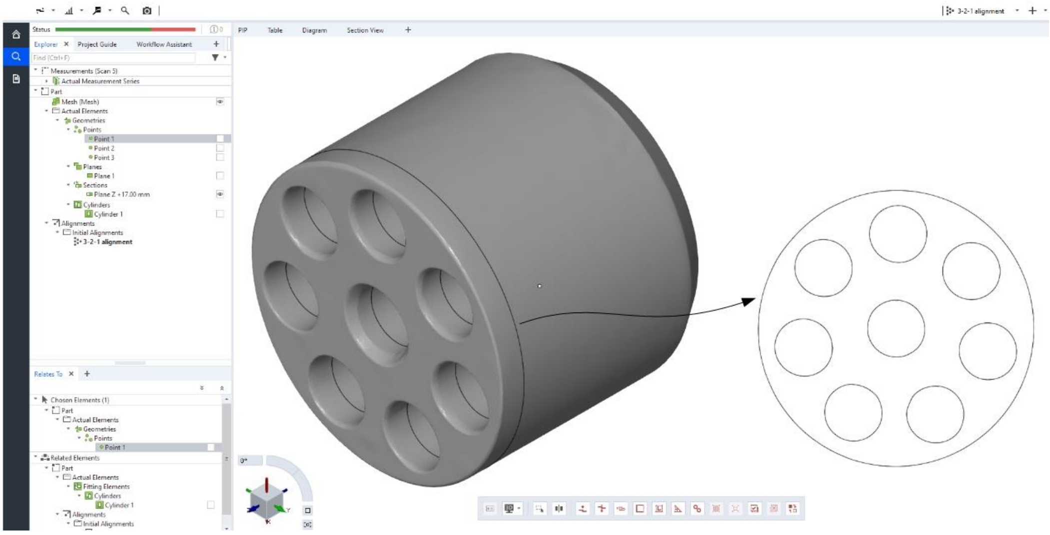

Fig. 5. The transversal cross-section of the piston block

Thus, using these sections, the dimensions of the piston block can be identified, which are necessary to create the 3D model in a dedicated software program. The dimensions of the cross sections are shown in Figure 6. These were determined by constructing circles on the surface of the contours, using the *Fitting Circle* command.

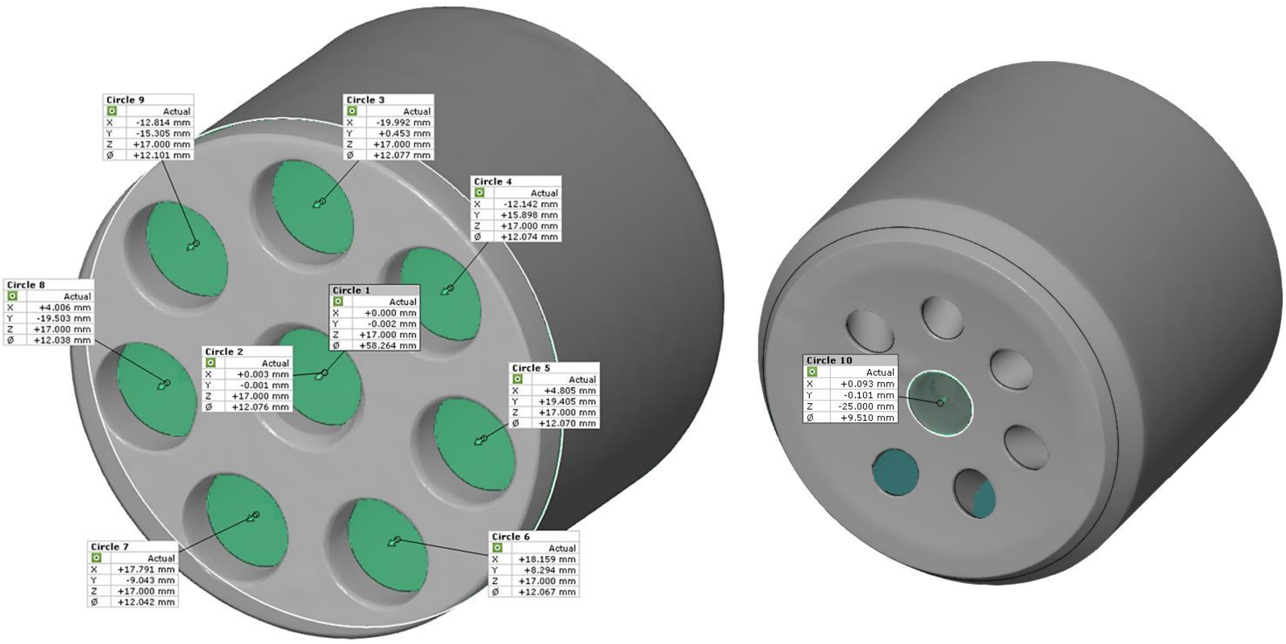

Fig. 6. The cross-section dimensions of the piston block

4. Graphical modeling of the piston block and comparison between models

The graphical modeling of the piston block was performed using the *CATIA V5R21* program in the *Part Design* module. *CATIA* is a computer-aided design software product developed by *Dassault Systèmes* [24]. This program is widely used in the engineering and design industry, allowing users to create complex 3D models and perform advanced analysis on them. Through *CATIA*, engineers and designers can perform detailed modeling of components and assemblies and apply various design functionalities such as simulations, tests and analyzes to verify their performance and quality. At the same time, it represents an essential tool in product development and in their design in a virtual environment before physical production. Therefore, the three-dimensional model of the piston block and the axial piston pump are shown in Figure 7. In its construction, 2D and 3D drawing commands were used, as well as editing commands (*Line*, *Point*, *Circle*, *Quick Trim*, *Pad*, *Shaft*, *Pocket*, *EdgeFillet* etc.).

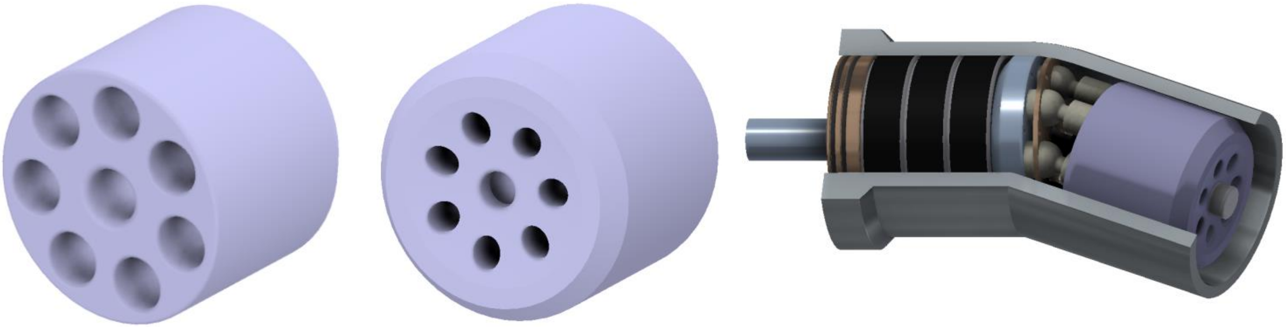

Fig. 7. 3D model of the piston block and the axial piston pump

The comparison between the two models of the piston block (CAD and scanned) was realized in the *GOM Inspect* software. The scanned model in **.stl* format and the CAD model in **.stp* format are imported into the GOM Inspect software. In the inspection process, an essential step is to align the actual model of the part, obtained by scanning, with the nominal model obtained by CAD modeling, since the two models are oriented differently from the coordinate system prescribed in the *GOM Inspect* program. There are several alignment methods available, but the most convenient and default method is prealignment. This prealignment process automatically performs a correlation of the two models, independent of the position in which the scan of the physical model was taken. By using these options of the prealignment function, a proper alignment can be ensured between the actual model and the nominal one, thus facilitating the process of inspecting and analyzing the part.

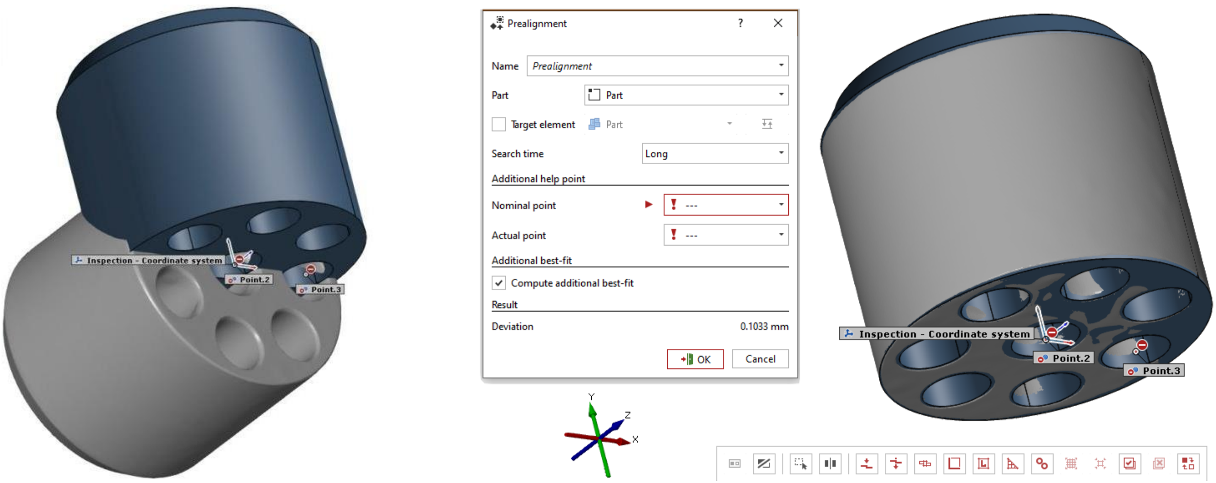

a. b.

Fig. 8. Orientation of the piston block models (a) and the overlap process (b)

Thus, Figure 8a shows the two models imported into the *GOM Inspect* program. In order to overlap the model scanned with the *Atos Core* equipment with the model made in the *CATIA* program, the *Prealignment* command, option *Long* is used, Figure 8.b. This step is essential to properly overlay the two models in the same reference system, thus facilitating the analysis and the inspection process. After the alignment between nominal and actual data has been achieved, the inspection process can be initiated, thus allowing the determination of dimensional deviations between the two sets of data. This process is done using the *Surface Comparison on CAD* command.
The result is presented in the form of a map of deviations, where they are visually represented by means of colors. In this context, the blue color indicates a negative deviation, the green color signifies a zero deviation, while the red color represents a positive deviation. In areas where dimensional deviations could not be calculated, they are highlighted on the deviation map with a gray color. After the map has been generated, the program presents a legend explaining the meaning of the values corresponding to each individual color. This legend is useful to better understand and interpret the information presented on the map, making the analysis process more accessible and comprehensible, Figure 9.

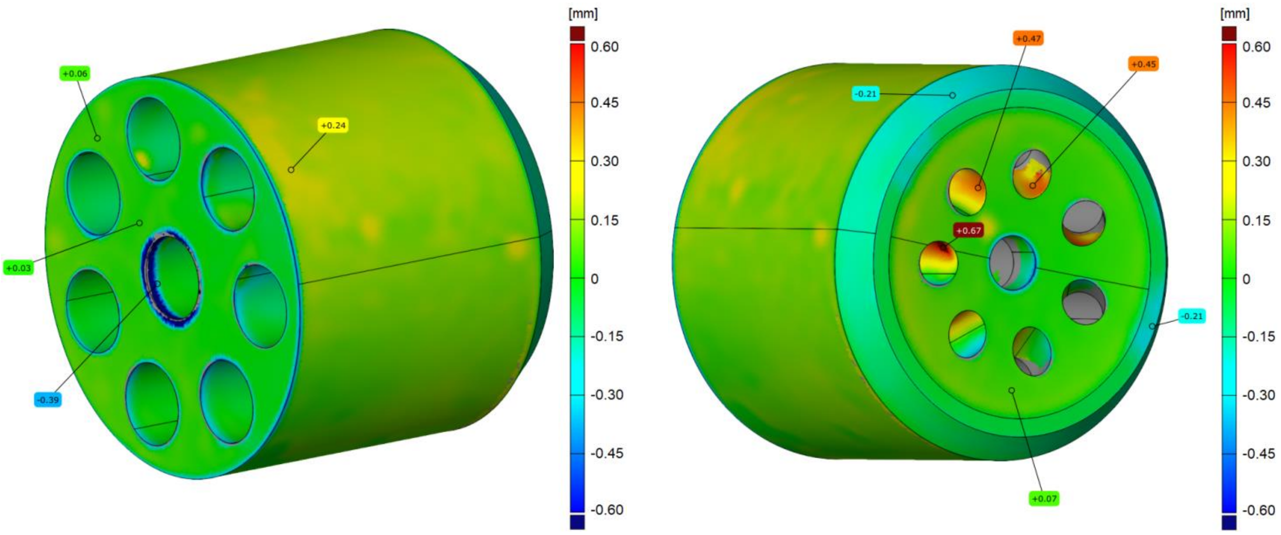

Fig. 9. The deviations map of the block piston

5. The precision of the geometric shape of the piston cylinders

Following the operation of axial piston pumps, a technical cycle of wear occurs due to the translational movement of the pistons in the block cylinders, the deviations from the precision of the geometric shape of the pistons cylinders, the most frequently encountered being the deviation from circularity and the deviation from cylindricity. The deviation from circularity or non-circularity is defined as the maximum distance between the real profile and the adjacent circle, Figure 10a, and the deviation from cylindricity is defined as the maximum distance between the real surface and the adjacent cylinder, considered within the limits of the reference length, Figure 10b. This deviation consists of the deviation from circularity, considered in the cross section of the part and the deviation of the longitudinal (axial) profile. The diameter and circularity errors were determined with the *Tesa Micro-Hite 3D* coordinate measuring machine [25], Figure 10c. The deviations from circularity in the piston cylinder sections were determined by measuring the diameters of the section in different directions. For each of the piston cylinders, marked with numbers from 1 to 7, the values of the diameters measured at several points, in an interval of 1÷5 mm below the frontal plane of the piston block, were determined.

a. b. c.

Fig. 10. Deviation from circularity (a) and cylindricity (b). Tesa Micro-Hite measuring machine (c) [25]

Table 1 shows the average values recorded for the piston cylinder diameters measured with the help of the *GOM Inspect* program, see Figure 6, respectively those recorded by measuring with the *Tesa Micro-Hite 3D* coordinate measuring machine.

Table 1: Values of piston cylinder diameters and tolerances

Cylinder No.	Cylinder diameter [mm] *GOM Inspect*	Tolerance [mm] *GOM Inspect*	Cylinder diameter [mm] *Tesa Micro-Hite 3D*	Tolerance [mm] *Tesa Micro-Hite 3D*
1	12.077	0.077	12.026	0.026
2	12.074	0.074	12.030	0.030
3	12.070	0.070	12.018	0.018
4	12.067	0.067	12.012	0.012
5	12.042	0.042	12.002	0.002
6	12.038	0.038	11.993	-0,007
7	12.101	0.101	12.044	0.044

Figure 11 shows the graphical representation of the tolerances obtained from *GOM Inspect* and *Tesa Micro-Hite 3D*.

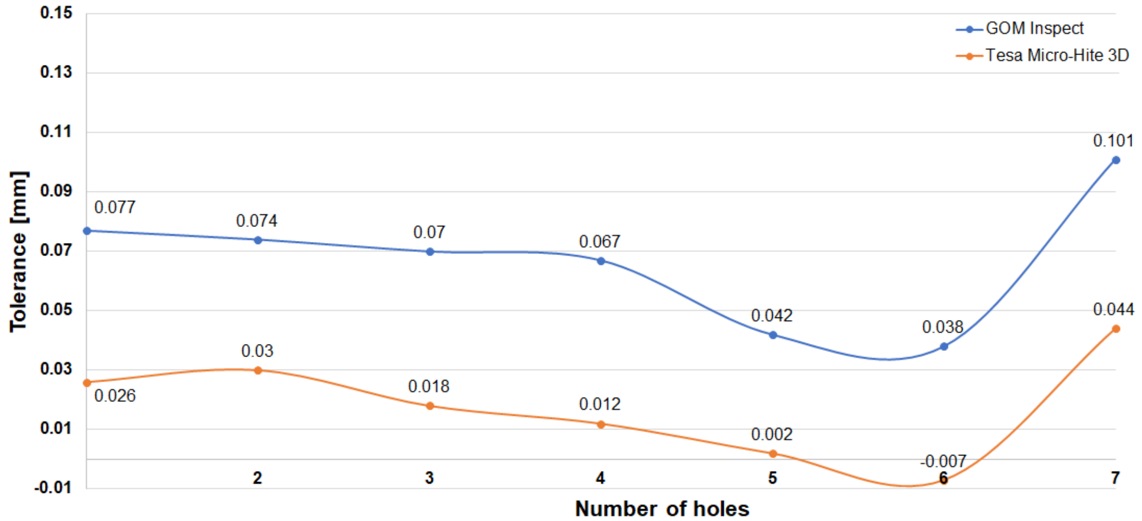

Fig. 11. Graphical representation of the tolerances obtained from *GOM Inspect* and *Tesa Micro-Hite 3D*

6. Artificial neural network (ANN) and piston stroke prediction in axial piston pump

In order to define the theoretical flow rate of the axial piston pump, the basic relationship is used:

$$Q = V \cdot n \left[\mathrm{m^3/s} \right], \tag{1}$$

where:
- V is the oil volume discharged at one rotation;
- n - pump speed, in rpm.

The oil volume discharged at one rotation of the piston block is:

$$V = \frac{\pi \cdot d^2}{4} \cdot h \cdot z \, \left[\mathrm{mm^3} \right], \tag{2}$$

where:
- d is the effective diameter of a piston, in mm;
- z - the number of pistons;
- h - piston stroke, in mm.

For n speed, the flow rate of the axial piston pump is given by the expression:

$$Q = 10^{-6} \cdot \frac{\pi \cdot d^2}{4} \cdot h \cdot z \cdot n \left[\mathrm{l/min} \right]. \tag{3}$$

To highlight the importance order of the parameters that influence the functionality of an axial piston pump, a piston stroke prediction method based on an artificial neural network (ANN) model is used. It starts from known values of flow (Q) and speed (n) of some types of Rotary Power pumps [26]. To train the neural network, the fact that the number of pistons is generally odd is taken into account and two such situations are considered - with 7 and 9 pistons, Table 2.

Table 2: Technical parameters of axial piston pumps [26] in ANN training

No.	n [rpm]	d [mm]	z	Q [l/min]
1	2500	20	7/9	312.50
2	3000	18	7/9	276.00
3	3000	16	7/9	186.00
4	3500	14	7/9	115.50
5	4000	12	7/9	46.00

A standard neural model consists of an input layer with 4 neurons corresponding to the input variables, a hidden layer containing 4 hidden neurons and an output layer containing one neuron corresponding to the piston stroke (h). For the multi-layer neural networks used as input parameters were: speed (n), piston diameter (d), number of pistons (z) and fluid flow rate (Q). In this way, 9 possible combinations are obtained. When training the networks, 8 of the combinations were used, the ninth one being used to check the training result, the stroke of the pistons, Figure 12a. After querying the networks, 16107 cycles, piston stroke values were obtained for various combinations, Figure 12b.

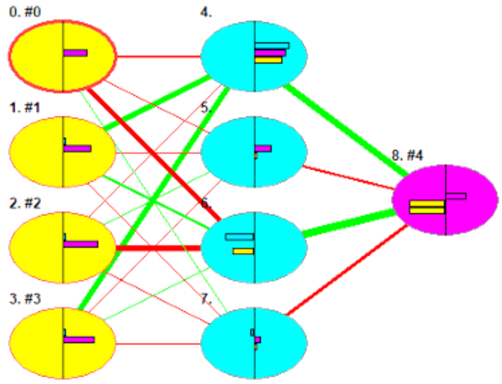

a.

	#0	#1	#2	#3	#4
Query	3600.0000	19.0000	9.0000	300.0000	40.9170
#0	2500.0000	20.0000	7.0000	312.5000	56.8700
#1	3000.0000	18.0000	7.0000	276.0000	51.6700
#2	3000.0000	16.0000	7.0000	186.0000	44.0700
#3	3500.0000	14.0000	7.0000	115.5000	30.6400
#4	4000.0000	12.0000	7.0000	46.0000	14.5300
#5	2500.0000	20.0000	9.0000	312.5000	44.2300
#6	3000.0000	18.0000	9.0000	276.0000	40.1900
#7	3000.0000	16.0000	9.0000	186.0000	34.2800
#8	3500.0000	14.0000	9.0000	115.5000	23.8300
#9	4000.0000	12.0000	9.0000	46.0000	11.3000

b.

Fig. 12. Neural model for piston stroke prediction (a); neural network training data (b)

Conclusions

The main defining characteristic of axial piston pumps is their ability to deliver a continuous fluid flow under pressure, making them essential components in the field of hydraulics, being recognized for their exceptional level of efficiency and their ability to deliver both pressure, as well as constant flow, essential features for a variety of industrial and mobile applications. The paper highlights how modern rapid analysis tools can give extremely valuable indications for a specific reaction to non-conformities in the functionality of such pumps. So:

- an automatic scanning and analysis system was used, with the help of which a quick and precise inspection of the piston cylinders was realized, reducing the effort and time required for manual measurement by traditional methods;
- the CAD model could be created both based on the dimensions in the data sheet, but also based on the scanned model. The accuracy of the models (CAD and scanned), by comparison, was proven by the upper and lower limit values of ±0.6 mm. Even if there are small deviations, they are due to the imperfections appearing in the piston block due to multiple operating cycles, as well as the measurement and scanning difficulties caused by the depth of the piston cylinders;
- powerful 3D measuring instruments were used to control dimensional deviations from circularity and cylindricity in the piston block, highlighting the superior accuracy of the coordinate measuring machine, but also the net superior working speed of the scanning system, which had the role to quickly create a 3D model, consisting of a ”cloud of points” obtained after scanning the inner surfaces of the piston cylinders, with the possibility of exporting them in various formats for digital design and analysis applications;
- following the analysis of the training results of the neural network, in defining the average value of the pistons stroke (h), the importance of the parameters, in descending order, are: fluid flow rate (Q), diameter of the pistons (d), speed (n), number of pistons (z). It can be concluded that the ANN approach is an appropriate tool for such an application, being able to lead to the design of some algorithms that assume the possibility of increasing the value of the fluid flow, but also of the diameter of the pistons, for a functionality with a higher technical yield.

Acknowledgments

This work is supported by the OpenInnoHub project - Creation of an open innovation hub in the Southeast Region (OpenInnoHub) *(Crearea unui Hub de Inovare Deschisă în Regiunea Sud-Est (OpenInnoHub))* in the framework of Competitiveness Operational Programme, financed from the European Regional Development Fund under the contract number 7/111/B Section/25.10.2022, SMIS Code: 153386.

References

[1] Baroiu, N., and G.A. Moroșanu. *Hydraulic Drive Systems / Sisteme de acționare hidraulică*. Galati, Academica Publishing House, 2022.

[2] Baroiu, N., D. Vișan, and O.D. Ciocan. *Technological hydrostatics and pneumatics - laboratory guide / Hidrostatică și pneumatică tehnologică - îndrumar pentru laborator*. Galati, Academica Publishing House, 2018.
[3] Khalil, M.K.B. *Hydraulic Systems, Volume 1 - Introduction to hydraulics for industry professionals.* Franksville, CompuDraulic LLC, 2016.
[4] Yang, H., B. Zhang, and B. Xu. “Development of Axial Piston Pump/motor Technology.” *Chinese Journal of Mechanical Engineering* 44, no. 10 (October 2008): 1-8.
[5] Skinner, Steve. Eaton Hydraulics. “Piston pumps.” *SlideToDoc*, Accessed September 19, 2023. https://slidetodoc.com/piston-pumps-steve-skinner-eaton-hydraulics-havant-uk/.
[6] HYDAC Group. “Axial piston pumps.” Accessed September 19, 2023. https://www.hydac.com/shop/en/pumps/axial-piston-pumps.
[7] Hydratrans Pty Ltd. “Pumps.” Accessed September 19, 2023. https://www.hydratrans.com/product/pumps/.
[8] Feng, Y., Z. Jian, J. Li, Z. Tao, Y. Wang, and J. Xue. “Advanced Control Systems for Axial Piston Pumps Enhancing Variable Mechanisms and Robust Piston Positioning.” *Applied Sciences* 13, no. 17 (2023): 9658.
[9] Yan, K., T. Liu, and H. Han. “Disassembling process and technology of axial piston pump for remanufacturing.” *International Journal of Mechatronics and Applied Mechanics* 11 (2022): 275-285.
[10] Schuhler, G., A. Jourani, S. Bouvier, and J.M. Perrochat. “Multi technical analysis of wear mechanisms in axial piston pumps.” *IOP Conf. Series: Journal of Physics* 843 (2017): 012077.
[11] Ernst, M., and A. Vacca. “Hydrostatic vs. Hydrodynamic Components of Fluid Pressure in the Tribological Interfaces of Axial Piston Machines.” *Tribology International* 32, no. 11 (2021): 456-457.
[12] Arinaga, S., K. Yoshida, S. Takada, M. Noda, and K. Inoue. “The Latest Trends in Oil Pump Rotors for Automobiles.” *SEI Technical Review* 82 (2016): 59–65.
[13] Zhang, J., L. Fei, B. Xu, W. Huang, W. Wu, Z. Guo, H. Xu, and X. Huang. “Simulation and Experimental Investigation on Low Wear Rate Surface Contour of Piston/Cylinder Pair in an Axial Piston Pump.” *Tribology International* 32, no. 1 (2021): 45-47.
[14] Bayer, C., and O. Enge-Rosenblatt. “Modeling of hydraulic axial piston pumps including specific signs of wear and tear.” Papers presented at the 8th International Modelica Conference, Dresden, Germany, March 20-22, 2011.
[15] Baroiu, N., and G.A. Moroșanu. “Graphical modelling and studies on hydraulic pump parameters.” *Journal of Industrial Design and Engineering Graphics.* 15, no. 2 (2020): 7-12.
[16] Tao, R., R.F. Xiao, and W. Yang. “Optimization design for axial flow pump based on genetic algorithm.” *Journal of Irrigation and Drainage Engineering* 36 (2018): 573–579.
[17] Liu, Z.M., X.G. Gao, Y. Pan, and B. Jiang. “Multi-Objective Parameter Optimization of Submersible Well Pumps Based on RBF Neural Network and Particle Swarm Optimization.” *Applied Sciences* 13, no. 15 (2023): 8772.
[18] Ye, J., L.D. Ge, and Y.X. Wu. “An Application of Improved RBF Neural Network in Modulation Recognition.” *Acta Automatica Sinica* 33, no. 6 (June 2007): 652–654.
[19] Baroiu, N., V.G. Teodor, V. Păunoiu, G.A. Moroşanu, and I.C. Dumitrescu. “Reverse Engineering Used to Profile a Gerotor Pump Rotor.” *Applied Sciences* 13, no. 19 (2023): 11069.
[20] Baroiu, N., G.A. Moroșanu, V.G. Teodor, R.S. Crăciun, and V. Păunoiu. “Use of reverse engineering techniques for inspecting screws surfaces of a helical hydraulic pump.” *International Journal of Modern Manufacturing Technologies* XIV (2022): 20-29.
[21] Berbinschi, S., V.G. Teodor, N. Baroiu, and N. Oancea. “Profiling methodology for side mill tools for generation of helical compressor rotor using reverse engineering.” *Annals of ”Dunarea de Jos” University of Galati* V: (2011): 111-116.
[22] Akerdad, M., A. Aboutajeddine, and M. Elmajdoubi. “Reverse Engineering Canvas (REC): A Visual Tool for Supporting Reverse Engineering Activities.” *International Journal on Interactive Design and Manufacturing* 15, no. 2-3: (2021): 249-257.
[23] ***. “ATOS Core in use with GOM Scan software.” Accessed September 25, 2023. https://www.youtube.com/watch?v=751kz4SF7ME.
[24] Dassault Systèmes. “Discover CATIA.” Accessed October 21, 2023. https://www.3ds.com/products-services/catia/.
[25] TESA Technology. Accessed October 21, 2023. https://www.tesatechnology.com/.
[26] Rotary Power. Accessed October 23, 2023. https://rotarypower.com/.

ISSN 1454 - 8003
Proceedings of 2023 International Conference on Hydraulics and Pneumatics - HERVEX
November 8-10, Băile Govora, Romania

EXPERIMENTAL ANALYSIS OF AN OPEN/CLOSED HYDRAULIC SYSTEM

Ionela BACIU[1], Mihai AVRAM[1], Bogdan GRĂMESCU[1], Victor CONSTANTIN[1]

[1] National University for Science and Technology Politehnica Bucharest, Department of Mechatronics and Precision Mechanics

ionela.baciu@upb.ro, mavram02@yahoo.com, bogdan.gramescu@upb.ro, victor.f.constantin@gmail.com

Abstract: *The paper presents the conception and design of a hydraulic system that can work both in closed circuit and in open circuit - which can be used in the laboratory for teaching purposes. The system contains both classical and proportional equipment, sensors for different fluidic (flow, pressure, temperature) and mechanical (speed) quantities and will be managed using a dedicated controller. From a functional point of view, the system will have several operating modes, which can be set by the user. The data provided by the sensors will be acquired and they will be analysed and in real time the controller will decide certain corrections so that the system evolves according to an imposed algorithm.*

Keywords: *Hydraulic System, Open circuit, Closed circuit*

1. Introduction

Today, hydraulics represents an increasingly important technology. Its qualities are highlighted whenever large and very large forces need to be developed under conditions of superior efficiency. The scope of application of hydraulic drive systems is extremely broad, ranging from the operation of robots, machine tools, automated lines, presses, lifting machines, chemical, metallurgical, and mining equipment to military and aerospace technology.
As a result, these systems find a wide field of application wherever automatic control of work phases is required, along with the programming of forces/moments, displacements, and speeds. They ensure various functions, facilitating the transition from one speed level to another, which is necessary for achieving high-precision positioning, ease, and flexibility in programming. A careful evaluation of this field allows the identification of the main trends and perspectives. Among these, a strong development in this field in the future must be noted; for this, fundamental and sustained applied research is necessary. At the same time, the significant role of equipment manufacturers in innovating and adapting to Industry 4.0 is evident.
The aspects presented above justify the importance given to this field in the curriculum of the Mechatronics study program, where a series of courses are planned to enable students to acquire competencies in the field of hydraulic drive systems. These courses include Pneumatic and Hydraulic Automations, Hydronics and Pneutronics, Intelligent Fluid-powered Drive Systems, Theoretical and Experimental Analysis of Hydronic and Pneutronic Systems. The theoretical aspects presented in these courses need to be accompanied by laboratory work to assist students in understanding the principles and methods presented in class. For this purpose, an appropriate material base is needed to align with the intended goals.
This is also the direction in which the subject of this applied work falls. The designed and currently under construction stand aims to help students understand the following aspects:

- The functional role of the automation equipment used; both classical and proportional equipment are considered.
- Highlighting the difference between a hydraulic drive system operating in a closed circuit and one operating in an open circuit.
- Presentation of methods for flow control through the resistive method and the volumetric method.

- Emphasizing pressure losses that occur due to fluid flow through various equipment (especially at the throttle level) and their effect on the working fluid's temperature.
- How to adjust the pressure in the system.
- How information is acquired, processed, and interpreted from the system.
- How the controller is programmed and a series of control algorithms are designed and implemented.

2. Material and Method

The system studied in this article is composed of an adjustable flow hydraulic pump P, hydraulic directional control valves with classical operation DH2 (used to operate the system) and DH1 (used to supply the pump), pressure transducers PAM and PAV, flow transducer TD, as well as pressure gauges M1 and M2 mounted upstream and downstream of a proportional throttle valve DROSEL_PROP. The system is also equipped with an accumulator, serving as a flow compensator ACC, along with the filter F, pressure relief valve Ssig and reservoir T. The hydraulic circuit is depicted in Fig. 1, along with the main characteristics of some of its constituent equipment. It is configured to allow a switch between the open circuit mode, which includes a reservoir, and the closed-circuit mode by decoupling the reservoir.

The operational steps for transitioning from open circuit mode to closed circuit mode are as follows:
Step 1: System startup – the DH1 directional control valve establishes the left distribution field, allowing circuit supply through the hydraulic pump (P). The DH2 directional control valve can be in either of its two positions – for hydraulic circuit operation or return. In both cases, the pressure relief valve (Ssig) is included in the loop.
Step 2: If a transition to closed circuit mode is desired, the DH2 directional control valve is actuated through the ALIM_ON electromagnet, enabling pressurized oil supply to the operated circuit. Once the desired pressure is reached, the DH1 directional control valve can be switched to the CI position.

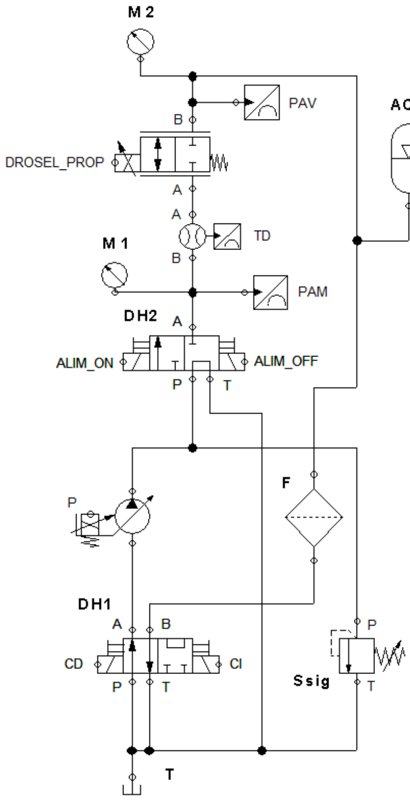

Fig. 1. Simulation network

Table 1: Components parameters

Component description	Characteristics
T – Hydraulic reservoir	Capacity: 80 liters
DH1 – Hydraulic distributor 4/2 with dual control (electric and manual)	Max. pressure: 350 bar Max. flow rate: 60 l/min Control voltage: 24V
P – Variable capacity hydraulic pump	Max. pressure: 350 bar Max. flow rate: 59 l/min Max. speed: 3300 Control voltage: 24V
DH2 – Proportional distributor 4/2	Nominal pressure: 280 bar Max. pressure: 350 bar Max. flow rate: 60 l/min Control voltage: 24V
M1 – Glycerin-filled pressure gauge	Measuring range: 0-310 bar
PAM – Analog pressure sensor, upstream	Measurement range: 0-250 bar Supply voltage: 18-30V
TD – Turbine flow meter	Accuracy: ± 0.5%, ± 1% Power supply: +24VDC
DROSEL_PROP – Proportional throttle valve	Max. pressure: 420 bar Nominal flow rate: 320 l/min Number of connections: 2 Switching positions: 2 Supply voltage: 24 VDC
PAV – Analog pressure sensor, downstream	Measurement range: 0-250 bar Supply voltage: 18-30V
M2 – Glycerin-filled pressure gauge	Measuring range: 0-310 bar
ACC – Hydraulic Accumulator	Max. flow rate 360 l/min Gas valve type: 7/8' 14 UNF high pressure Max. operating pressure: 690 bar Nominal volume: 1 l
F – Particle Filter	Height: 170mm Outer diameter: 64mm Inner diameter: 34mm
Ssig – Safety valve with direct-acting	Pressure range: up to 350 bar Flow rate: 26 l/min

In fig. 2, the logic control module is presented, where the connections between the logic stage and the control stage can be observed. On the left side of the figure, the inputs and outputs of the programmable controller are highlighted. The inputs of the programmable controller are denoted as I1 to I8, and the outputs as Q1 to Q8; its power supply is provided from a 24V source.
On the right side of the figure, the logical scheme behind the system's operation can be observed. By supplying I1, the system's working cycle is initiated. To ensure the system's stoppage, a button and a reset block have been installed simultaneously.

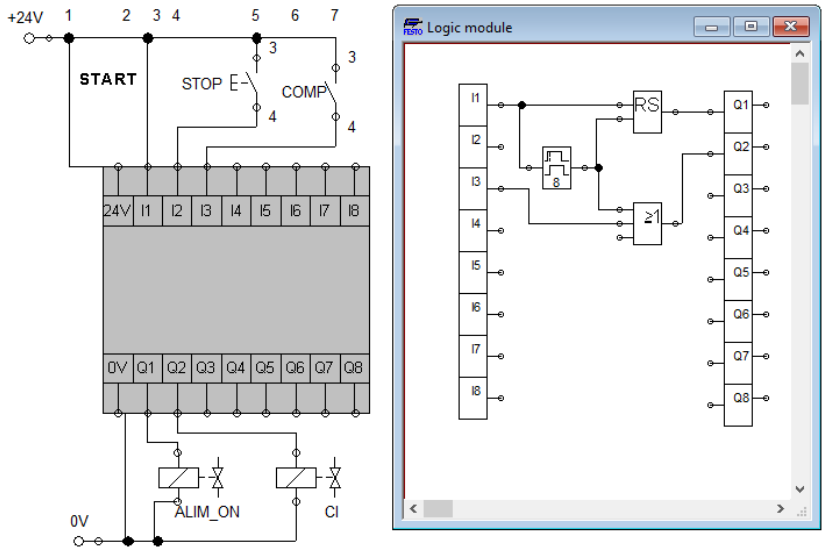

Fig. 2. Logic module connections

At the output port, Q1, the proportional electromagnet is connected, receiving the control signal for moving the hydraulic directional control valve drawer from the P-T position to the P-A position. When the pump starts, the fluid is not sent into the system but is directed back to the reservoir. The return to the preferential P-T position is achieved through the command of the second electromagnet, ALIM_OFF. The transition from an open hydraulic circuit to a closed one is done using a 4/2 directional control valve with proportional control. The preferred position of the directional control valve drawer is P-A, B-T, which means that the fluid enters the system through port A and returns to the tank through port B. The transition from an open circuit to a closed one is achieved by commanding the proportional electromagnet, CI, which once it receives the command signal, it moves the drawer to the P,T position - blocked and A-B - connected. The proportional throttle has the role of regulating the speed of the working fluid, respectively the speed of the actuation elements that could be connected in the system. The flow section through the throttle changes proportionally with the command signal sent through the Q2 port of the programmable controller. The flow section can be changed in several situations: when the pump has a low flow rate, and a too large passage section would lead to pressure losses in the system; another situation in which it is necessary to adjust the flow section is when the system does not require a large flow of fluid, and reducing the flow section leads to an increase in the pressure in the system, which can lead to the opening of the pressure relief valve and sending the fluid to the tank. The purpose of the hydraulic accumulator is to compensate the flow losses in the system, but also to store the hydraulic fluid when adjusting the flow section of the proportional throttle. The pressure relief valve ensures constant pressure in the system and does not allow exceeding the maximum pressure allowed in the system. When the set maximum threshold is reached, it opens and allows a quantity of fluid to exit the circuit.

Fig. 3 shows the control scheme for the hydraulic pump and regulation of the flow section for the proportional throttle. The pump flow rate variation law is given by means of a function generator, whose signal is amplified and transmitted to the actuation element. The movement of the mobile element, which changes the geometric volume, is proportional to the command signal. The control law of the proportional throttle is obtained based on the variations of the geometric volume of the pump. With the modification of the pump capacity, the throttle receives a command signal proportional to the displacement it must achieve. In order to determine the pressure drop on the throttle, it was decided to mount two analog pressure sensors upstream and downstream, the pressure difference between the two values is determined by a comparator. The comparator is provided with two analog inputs, one for each sensor. It allows real-time visualization of the upstream-downstream pressure difference on a display, as well as in the program. An analogue flow sensor, TD, has also been installed in the system, which allows monitoring the speed variations of the hydraulic fluid, provides an additional safety factor in the system and better control over possible flow losses, which could occur as a result of the operation defective components as well as anomalies in the operation of the pump.

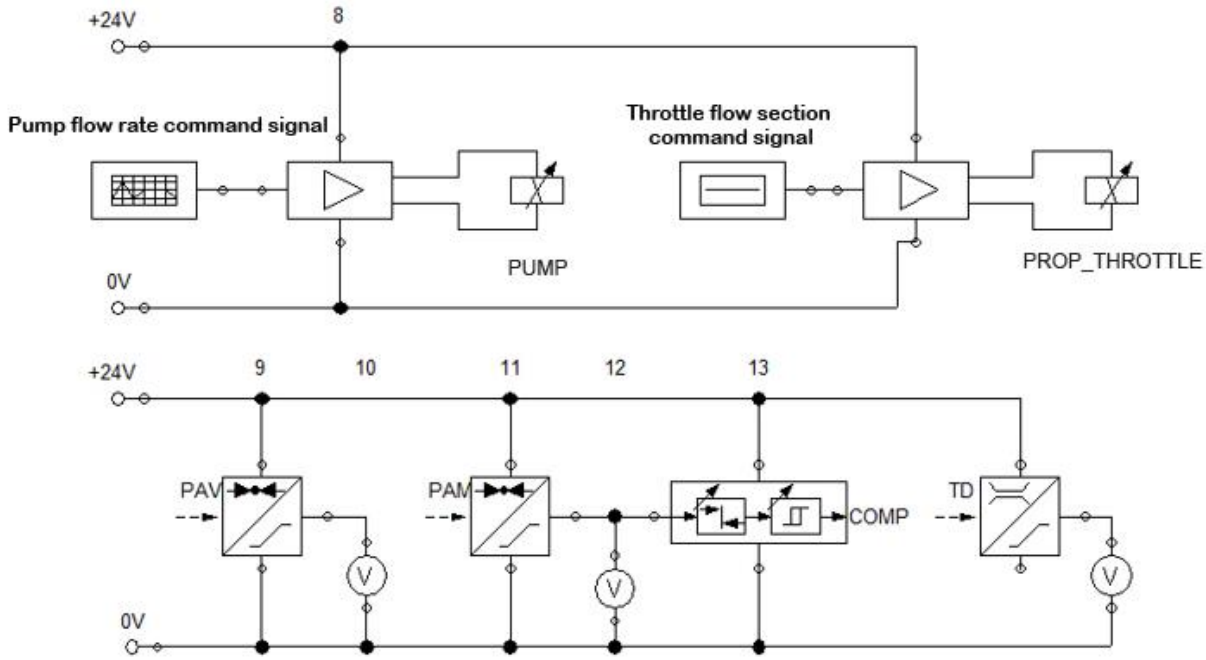

Fig. 3. Control scheme

3. Conclusions

In conclusion, the hydraulic system described in the article is a complex configuration involving various components such as an adjustable flow hydraulic pump, hydraulic directional valves, pressure and flow transducers, pressure gauges, a proportional throttle valve, an accumulator, a filter, pressure relief valve, and a reservoir. The system is designed to operate in both open circuit and closed-circuit modes, with the ability to transition between the two. The operational steps for transitioning from open circuit mode to closed circuit mode involve system startup, where the DH1 directional control valve establishes the left distribution field, allowing circuit supply through the hydraulic pump. If a transition to closed circuit mode is desired, the DH2 directional control valve is actuated to enable pressurized oil supply to the operated circuit, and the DH1 directional control valve can then be switched to the closed-circuit position. The logic control module, depicted in Fig. 2, highlights the connections between the programmable controller's inputs and outputs, which play a crucial role in initiating and stopping the system's working cycle. The proportional electromagnet, controlled by the programmable controller, is responsible for moving the hydraulic directional control valve drawer, facilitating the transition between open and closed-circuit modes. Fig. 3 provides a detailed control scheme for the hydraulic pump and regulation of the flow section for the proportional throttle. The pump's flow rate variation is governed by a function generator, and the control law for the proportional throttle is based on variations in the geometric volume of the pump. Analog pressure sensors upstream and downstream of the throttle, along with an analogue flow sensor, contribute to real-time monitoring and control of pressure and flow variations in the system. Overall, the system is designed with precision to regulate fluid flow, ensure safety through pressure control mechanisms, and allow for efficient operation in both open and closed-circuit modes. The integration of logic control and sensors enhances the system's adaptability and responsiveness to varying operational conditions.

References

[1] Rydberg, Karl-Erik. "Hydrostatic Drives in Heavy Mobile Machinery–New Concepts and Development Trends." SAE Technical Paper (1998): 981989. Paper presented at International Off-Highway and Powerplant Congress and Exposition, Milwaukee, Wisconsin, USA, September 14-16, 1998.
[2] Bury, Paweł, Michał Stosiak, Kamil Urbanowicz, Apoloniusz Kodura, Michał Kubrak, and Agnieszka Malesińska. "A Case Study of Open- and Closed-Loop Control of Hydrostatic Transmission with Proportional Valve Start-Up Process." *Energies* 15, no. 5 (2022): 1860.
[3] Mistry, Kayzad A., Bhaumikkumar A. Patel, Dhruvin J. Patel, Parth M. Parsana, and Jitendra P. Patel. "Design and Analysis of Hydrostatic Transmission System." *IOP Conference Series: Materials Science and Engineering* 310 (2018): 012048. Paper presented at the International Conference on Advances in Materials and Manufacturing Applications (IConAMMA-2017), Bengaluru, India, August 17–19, 2017.
[4] Zhu, Zhen, Gao Xiang, Dao Yuan Pan, and Yu Zhu. "Simulation Analysis on Hydrostatic Transmission Based on the MATLAB/SIMULINK." *Advanced Materials Research* 1037 (October 2014): 212-215.
[5] Li, Dong, Sujun Dong, Jun Wang, and Yunhua Li. "State-of-the-art and Some Considerations on Thermal Load Analysis and Thermal Management for Hydraulic System in MEA." *The Journal of Engineering*, no. 13 (January 2018): 399–405. Paper presented at The 4th International Symposium on More Electric Aircraft Technology (MEA 2017), Beijing, China, November 8–9, 2017.
[6] Kwon, Hyukjoon, Nathan Keller and Monika Ivantysynova. "Thermal Management of Open and Closed Circuit Hydraulic Hybrids – A Comparison Study." Paper presented at the 11th International Fluid Power Conference, 11. IFK, Aachen, Germany, March 19-21, 2018.
[7] Qu, Shaoyang, David Fassbender, Andrea Vacca, Enrique Busquets, and Uwe Neumann. "A Closed Circuit Electro-Hydraulic Actuator with Energy Recuperation Capability." Paper presented at the 12th International Fluid Power Conference, 12. IFK, Dresden, Germany, March 9-11, 2020.
[8] Emelyanov, R. T., A. S. Klimov, K. S. Kravtsov, I. B. Olenev, and E. S. Turysheva. "Improving the Efficiency of a Hydraulic Drive with a Closed-Loop Hydraulic Circuit." *Journal of Physics: Conference Series* 1515 (2020): 042078.
[9] Qu, Shaoyang, Federico Zappaterra, Andrea Vacca, Zifan Liu, and Enrique Busquets. "Design and Verification of An Open-Circuit Electro-Hydraulic Actuator System with An Integrated Electro-Hydraulic Unit." Paper presented at The 13th International Fluid Power Conference, 13. IFK, Aachen, Germany, March 21-23, 2022.
[10] Britannica, The Editors of Encyclopaedia. "hydraulic transmission." *Encyclopedia Britannica*, July 20, 1998. Accessed October 20, 2023. https://www.britannica.com/technology/hydraulic-transmission.
[11] Jani, D.B., Shah Ashish, Singh Aditya, Singh Yash, Singh Bishambhar, Singh Nikhil, and Singh Manmohan. "An Overview on Aircraft Hydraulic System." *International Journal of Innovative Research in Technology* 6, no. 5 (October 2019): 6-10.
[12] Brusov, V., A. Menshikov, and Y. Merzlikin. "Development of hydraulic transmission for implementing an active drive of the landing gear wheels of modern transport aircraft." *IOP Conference Series: Materials Science and Engineering* 779 (2020): 012020.
[13] Chen, Linlin. "Hydraulic Lifting and Rotating System Lifting Machinery Transmission Control Design." *Mobile Information Systems* (June 2022): 4617971.
[14] Qu, Shaoyang, David Fassbender, Andrea Vacca, and Enrique Busquets. "A Cost-Effective Electro-Hydraulic Actuator Solution with Open Circuit Architecture." *International Journal of Fluid Power* 22, no. 2 (May 2021): 233–258.
[15] Ho, Triet Hung, and Kyoung Kwan Ahn. "Design and control of a closed-loop hydraulic energy-regenerative system." *Automation in Construction* 22 (March 2012): 444-458.

ISSN 1454 - 8003
Proceedings of 2023 International Conference on Hydraulics and Pneumatics - HERVEX
November 8-10, Băile Govora, Romania

OPTIMAL DESIGN AND CFD VERIFICATION OF AXIAL FLOW FAN

Chan LEE[1], Hyun Seok KO[1], Sang Yeol LEE[2], Sang Ho YANG[2]

[1] The University of Suwon, clee@suwon.ac.kr

[2] Samwon E&B Co., turboh5@hanafos.com

Abstract: *The present paper provides a design optimization scheme of axial flow fan, which combines 3D fan blade geometry design program, performance prediction method and optimization algorithm to optimize the design variables of spanwise camber, stagger angles and chord lengths for maximizing fan efficiency. Through the design optimization process of fan rotor blade, optimal fan rotor is designed and then coupled with outlet guide vane. Computational fluid dynamics analysis is conducted to verify the performance and efficiency of the present fan with optimal fan rotor and outlet guide vane. The designed performance and efficiency of the present optimal fan agree well with the CFD results and the present optimal fan design gives the efficiency improvement of 6.7% compared to the initial design. The CFD verification results show that the present design optimization method is very suitable in actual design practice for developing high efficiency axial flow fan.*

Keywords: *Axial flow fan, Blade design, Efficiency, Design optimization*

1. Introduction

Axial flow fans are crucial flow components in various HVAC (Heating, Ventilation, and Air Conditioning) systems used in industrial, commercial, and residential sectors. However, due to the recent global concerns about climate change and carbon neutrality, the axial flow fan industry is compelled to develop fans capable of operating efficiently across a wide range. Achieving high fan efficiency relies significantly on the three-dimensional design of fan blade geometry, leading to extensive research on the design and analysis of axial flow fans for achieving high efficiency [1]. Wallis proposed a method for designing variable-pitch fans by utilizing correlations between flow angles and section lift coefficients [2]. According to the Howden fan development study [3], determining the spanwise blade angle distribution is a critical design challenge for variable-pitch fans and should be optimized through the application of various design methods, along with validation through measurement and CFD modeling. Spuy and Backstrom [4] also employed an optimization procedure to minimize the exit kinetic energy of variable-pitch rotor-only axial fans, resulting in the design of an optimal spanwise fan blade angle distribution.
Thus, the present paper proposes a new fan design method which can determine blade angle distribution and predict the performance and efficiency of designed fan. The present design method is coupled with optimization algorithm to maximize fan efficiency and construct a optimal fan blade design. The present optimal fan design results are verified by using CFD techniques. Furthermore, the present optimal design results are compared with initial design (conventional design) to examine efficiency and performance improvements of the optimal fan design.

2. Fan design and performance prediction methods of the FANDAS code

The authors developed a computer program, the FANDAS code, which can design 3-D fan blade geometry, conduct through-flow analysis on the designed fan, make fan performance and noise predictions by using the through-flow analysis results. Fig.1 shows the structure and computational procedure of the FANDAS code. The reliability and prediction accuracy of the FANDAS code have been verified by the comparisons with measurement and test results in previous research papers [5]. Therefore, in the present study, the FANDAS code is used as design tool and simulation engine to construct fan blade geometry and optimize fan blade design for maximum efficiency.

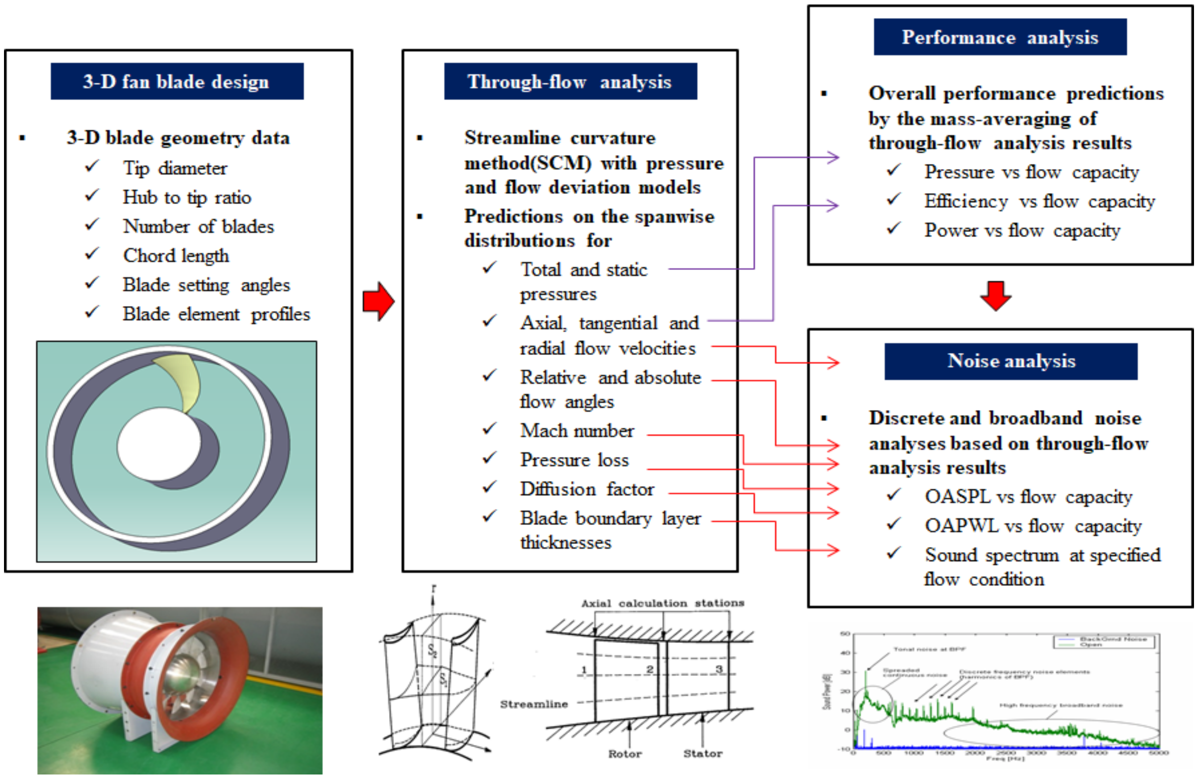

Fig. 1. Structure and computational procedure of the FANDAS code

2.1 Fan blade design

In this study, the 3D blade geometry design of the axial flow fan considers blade camber, stagger angles, and chord length distribution as the key design variables. Subsequently, blade section elements derived from these design variables are stacked along the blade span height from the hub to the tip for constructing the 3D fan blade shape. In this process, the camber line of the blade section is determined using a given camber angle and a single circular arc curve, with the addition of the NACA 65 airfoil thickness distribution on the camber line. These designed section elements are then stacked along the axis of the center of gravity, as depicted in Figure 2. This fan blade design process is conducted using the FANDAS code.

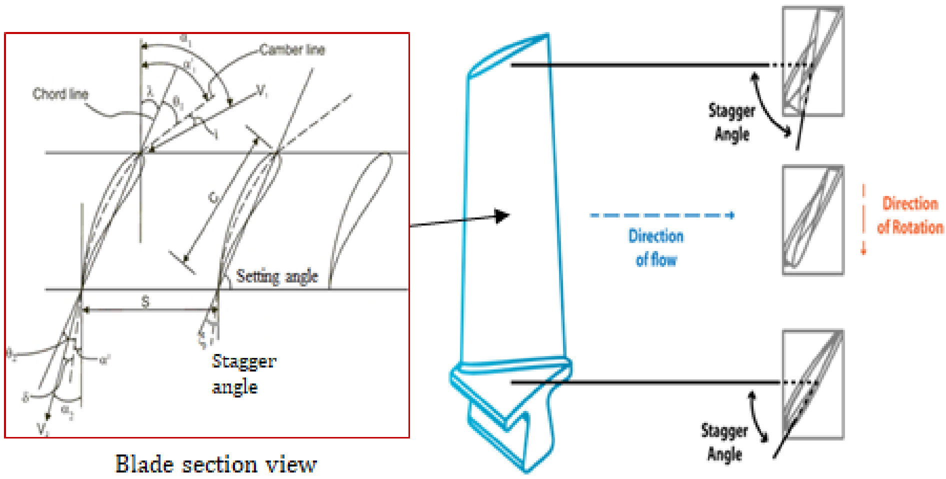

Fig. 2. Design and spanwise stacking of fan blade sections

2.2 Fan performance and noise predictions

Once the fan blade geometry is designed according to the aforementioned FANDAS code design process, the internal flow and performance predictions of the designed fan are conducted using the through-flow analysis method, which employs a streamline curvature computing scheme with total pressure loss models. The overall fan performance and efficiency are computed by mass-averaging the through-flow analysis results of total pressure and temperature on the fan outlet surface. Detailed explanations of the modeling and calculation procedures of the current through-flow analysis method are referred to Novak [6] and Lee [7]. Additionally, the noise generated by the designed fan is predicted, taking into account discrete frequency noise and broadband frequency noise components, applying Gutin's theory and Carlos's correlation models to the through-flow analysis results obtained earlier. The total noise level is also calculated by summing the noise components over entire frequency range. For a more in-depth description of the noise model is referred to Lee [8].
The flow distribution results calculated by the FANDAS code have been compared with measurements of the NASA 23B compressor rotor blade (please refer to the detailed design specifications in NASA TP-1523 [9]). As shown in Figs. 3-4, the predicted distributions of relative flow angle, relative, and axial flow velocities closely match the measurements along the blade span height. These excellent comparison results indicate that the current through-flow analysis method of the FANDAS code is highly suitable for predicting the fan flow field with a high level of prediction accuracy.

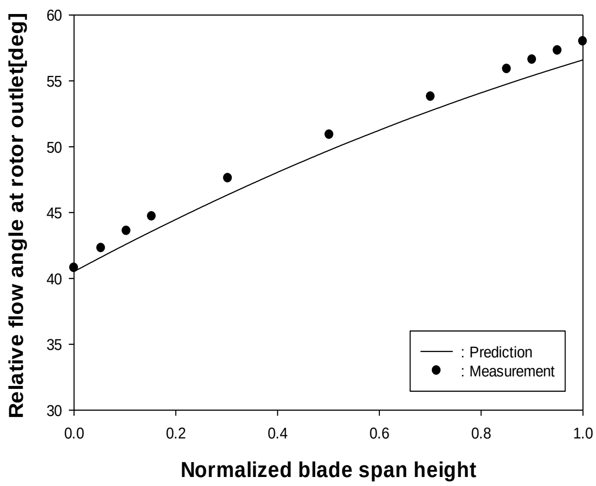

Fig. 3. Relative flow angle distribution of NASA compressor rotor blade

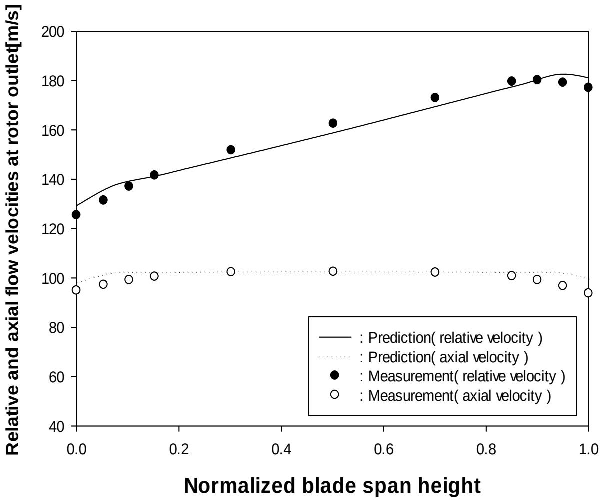

Fig. 4. Relative and axial flow velocity distributions of NASA compressor rotor blade

Furthermore, the FANDAS code has been applied to three different fan models designed by free vortex (FV), combined vortex (CV) or controlled blading (CB) design methods. The present study also conducts CFD calculations on these three fan models using the ANSYS CFX code. The CFD simulations in this study employs frozen rotor scheme and the SST k-ω turbulence model. Performance tests for the three fan models are carried out in a chamber-type test facility constructed and operated according to AMCA standards. Figs. 5 and 6 illustrates blade angle distributions of these three fan models and the comparisons between the current predictions (FANDAS), CFD results, and test results [10], showing very good agreements across the entire range of flow capacities. From these comparative results, it is evident that the present through-flow method of the FANDAS code is suitable for predicting changes in the performance curve due to different fan blading designs.
The predicted fan noise spectra by the FANDAS code have been compared with the measurement results of three fan models with forward-swept, straight, or backward-swept blades, as shown in Fig. 7. Noise spectrum measurements for the three fan models are conducted in an anechoic chamber-

type fan test facility using an FFT analyzer with a narrow-bandwidth of Δf =1 Hz. The results in Fig. 7 demonstrate that the present through-flow method coupled with a noise model can accurately predict the impact of blade sweep on the fan noise spectrum. As evident in Fig. 7, applying forward or backward blade sweep to the fan blade stacking design results in a phase shift cancellation of the Blade Pass Frequency (BPF) noise components produced in fan blade elements along the span height, significantly reducing the magnitudes of BPF harmonics when compared to the fan model with straight blades ("straight blade"). Based on the previous comparative results, it can be concluded that the FANDAS code is also suitable for fan noise prediction.

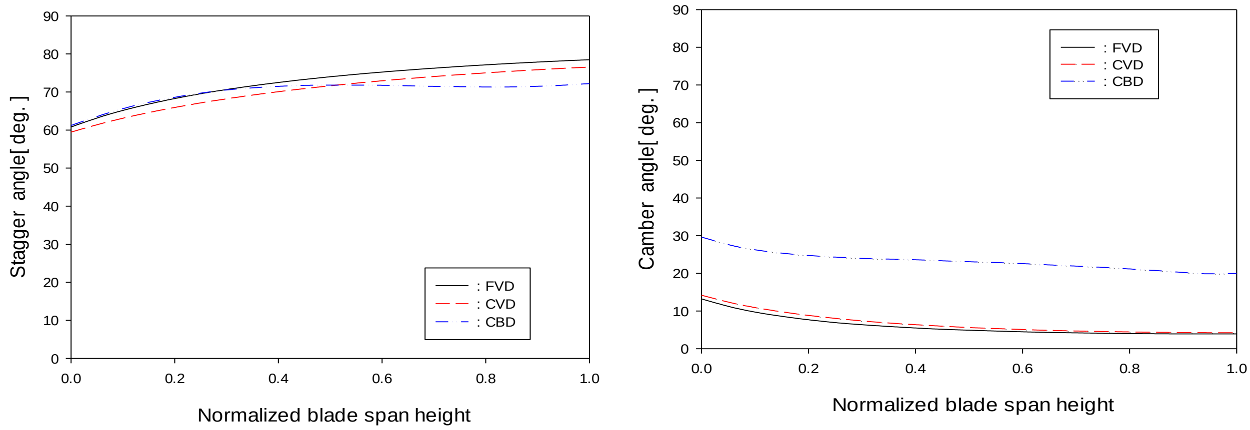

Fig. 5. Stagger and camber angle distributions of FVD, CVD and CBD axial flow fans

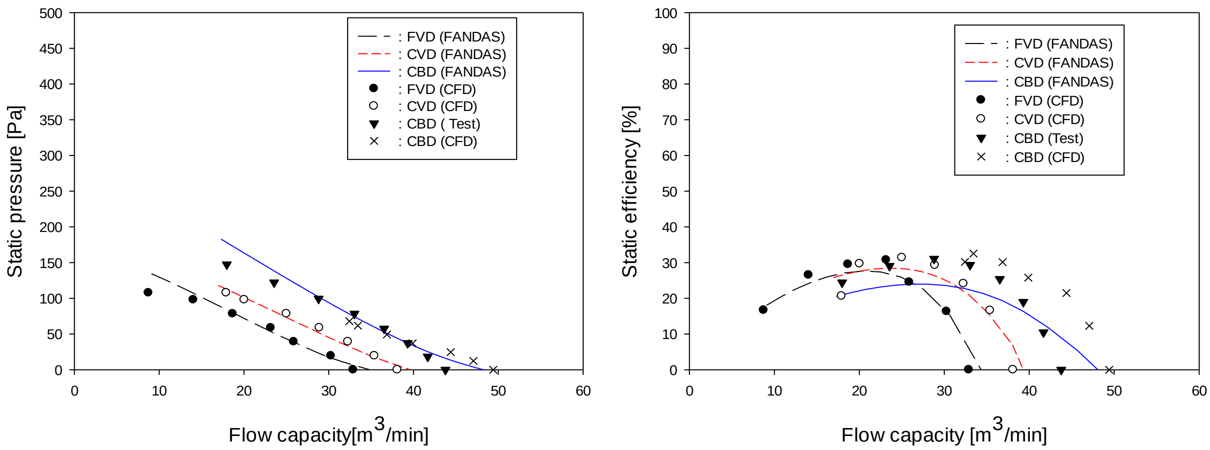

Fig. 6. Pressure and efficiency curves of FVD, CVD and CBD axial flow fans

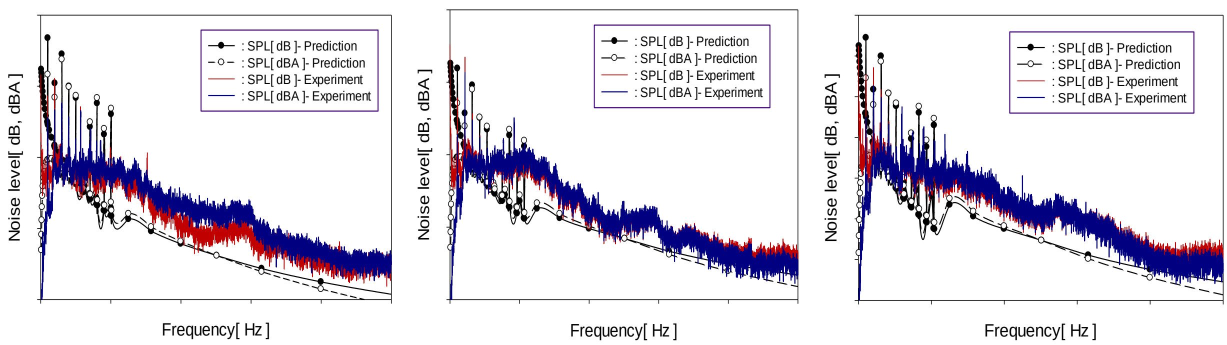

(a) Straight blade (b) Blade with backward-sweep (c) Blade with forward-sweep

Fig. 7. Noise spectra of three fan models with straight, backward and forward swept blades

3. Design optimization of an axial flow fan by using the FANDAS code

The present study formulates the design optimization problem for maximizing the total pressure efficiency (η) of an axial flow fan using the FANDAS code as the simulation engine. As depicted in Fig. 8, the FANDAS code is integrated with the Hybrid Metaheuristic Algorithm (HMA) from the PIAnO code [11] as the optimization technique. Additionally, mathematical formulations are developed utilizing camber angles and stagger angles as design variables. The HMA combines two different metaheuristic algorithms, namely, differential evolution (DE) and cuckoo search (CS), employing a bi-population concept. In this design optimization study, the objective function is defined as the total pressure efficiency of the fan, which is predicted by the FANDAS code. The design variables include the radial distributions of camber angle (θ_c), stagger angle (ξ), and chord length (c) of the fan rotor blade. Therefore, the optimization problem is defined as follows:

$$\text{Find } \theta_c(r),\ \xi(r) \text{ and } c(r) \text{ to maximize } \eta$$

with the constraints as Q = 3300 m^3/min, 650 < P_t < 850 Pa, Power < 55 kW,

$$0 < \theta_c,\ \xi < 90 \text{ deg. and } 0.5 < c/s < 2.5$$

where Q, P_t and s are fan flow capacity, total pressure and blade spacing.

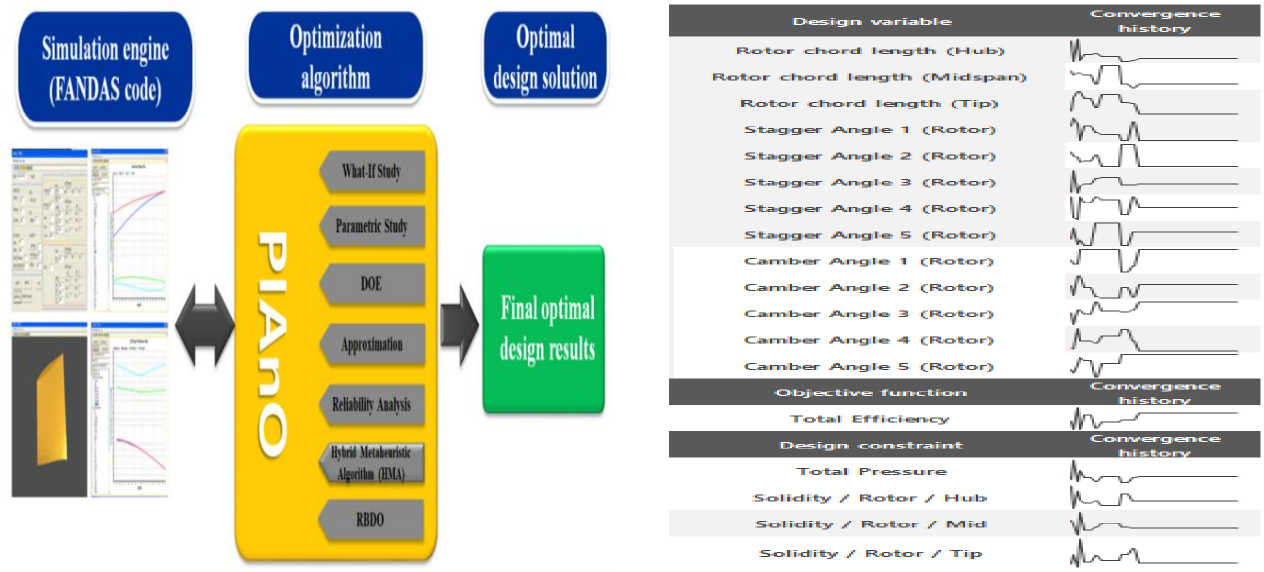

Fig. 8. Optimization scheme and convergence histories for an axial flow fan design

The present optimization technique is applied to the efficiency maximization problem of a variable-pitch axial flow fan. Multiple iterative calculations are performed to search for the optimal design solution, during which design variables and design constraints converge. After several iterations, the optimal design variables are determined as shown in Fig. 8 and the objective function is eventually calculated as presented. As shown in Fig. 9.the optimal camber angle is higher than the initial design across the entire blade span, while the optimal stagger angle at the hub is lower than the initial design, which was based on the free vortex concept [12]. The optimal chord length is smaller than the initial design, and its magnitude decreases from the tip to the hub. The optimal fan rotor blade geometry is generated using the FANDAS code with the optimal design variables (refer to Fig. 10), and the efficiency of the optimal fan is 85.8% which is improved by 6.7% when compared to the initial design.

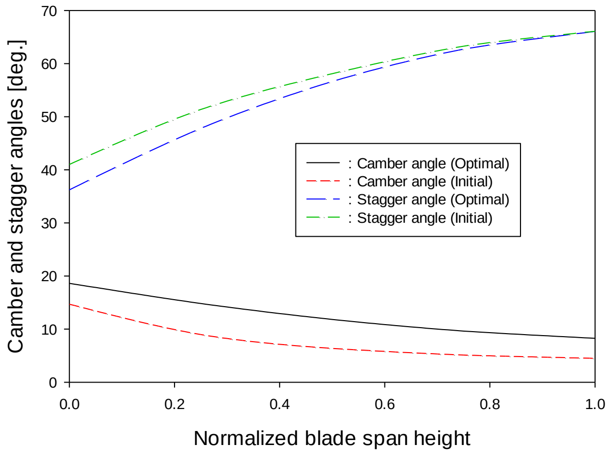

Fig. 9. Camber and stagger angle distributions of initial and optimal fan rotor blades

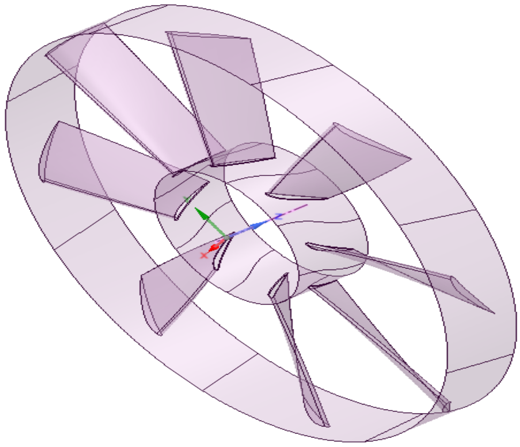

Fig. 10. 3-D geometry of optimal fan rotors

To validate the optimal fan design, Computational Fluid Dynamics (CFD) modeling is conducted in the flow domain of the optimal fan stage (optimal fan rotor with outlet guide vane), using a structured mesh system. Numerical calculations are carried out using the ANSYS CFX code [13] with the frozen rotor scheme and k-ω SST turbulence model. Fig. 11 presents the overall total pressure and efficiency curves of the optimal fan, with the FANDAS predictions closely matching the CFD results. In Fig. 11, the optimal fan model exhibits lower total pressure at the design point compared to the design constraint (P_T < 850 Pa) and has a wide operating range from 2700 to 3700 m^3/min. Fig. 11re 10 also shows that the efficiency of the optimal fan model is 85.8%, which is notably higher than the CFD result of 82.8% and significantly surpasses the initial design efficiency of 79.1% (as referenced in Table 2). The total efficiency of the optimal fan model is also maintained above 80% over a broad flow capacity range from 2700 to 4000 m^3/min. By adjusting the pitch angle of the optimal fan rotor blade relative to the design setting angle within the range of -5 to +5 degrees, the operating range, performance, and efficiency curves are shifted to lower or higher flow domains. Consequently, the optimal fan can operate with high efficiency above 80% over a wider flow capacity range from 2000 to 5000 m^3/min.

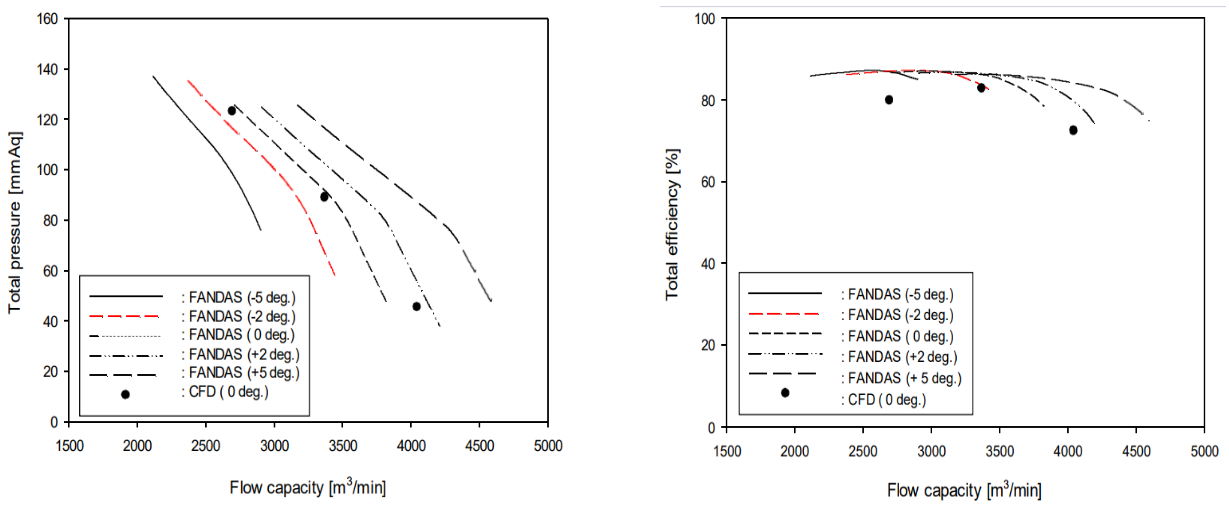

Fig. 11. Total pressure and efficiency curves of the optima fan design

4. Conclusions

This study presents a design program for axial flow fans and the design optimization study, which combines the utilization of the FANDAS code for fan blade design and the PIAnO code for optimization. As a result of this optimization process, the fan with optimal rotor blades shows 6.7% improvement in fan efficiency compared to the initial design. With this enhanced design, the optimal fan can operate efficiently over a wide range of flow capacities. Furthermore, when the fan is operated with variable-pitch adjustments, the optimal fan design maintains high efficiency over an even broader range of flow capacities.

Acknowledgments

This work was supported by the Korea Institute of Energy Technology Evaluation and Planning (KETEP) grant funded by the Korea government Ministry of Trade, Industry & Energy(MOTIE), Republic of Korea. (No. 2021202080026).

References

[1] Wright, T., and P. M. Gerhart. *Fluid Machinery: Application, Selection and Design*, 2nd edition. Boca Raton, CRC Press, 2009.
[2] Wallis, R. A. *Axial Flow Fans and Ducts*, 2nd edition. John Wiley & Sons, 1983.
[3] van der Spuy, S.J. "The Design of a Low-Noise Rotor-Only Axial Flow Fan Series." Master of Engineering Thesis, Department of Mechanical Engineering, University of Stellenbosch, 1997.
[4] van der Spuy, S. J., and T.W. von Backstrom. "Performance of rotor-only axial fans designed for minimum exit kinetic energy." *R & D Journal* 18, no. 3 (2002): 63-69.
[5] ***. FANDAS code user manual, Kyungwon Tech., 2017.
[6] Lee, C. "A performance prediction method of the axial flow fans with blade sweep." *KSFM Journal of Fluid Machinery* 24 (2021): 24-29.
[7] Novak, R.A. "Streamline curvature computing procedure for fluid flow problems." *ASME J. of Eng. for Power* 89 (1967): 487-490.
[8] Lee, C., and H.G. Kil. "A Through-flow Analysis Method of Axial Fan with BPF and Broadband Noise Models." *Int'l Journal of Fluid Machinery and Systems* 13, no. 4 (2020): 221-229.
[9] Britsch, Werner R., Walter M. Osborn, and Mark R. Laessig. "Effects of Diffusion Factor, Aspect Ratio, and Solidity on Overall Performance of 14 Compressor Middle Stages." NASA Technical Paper 1523, September 1979.
[10] Lee, C. "Development of an integrated computer program for the design, the performance and noise analyses of automotive cooling axial flow fan." Technical report. Hanon systems, 2016.
[11] ***. PIAnO code user manual, PIDOTEC, 2022.
[12] Dixon, S. L. *Fluid Mechanics and Thermodynamics of Turbomachinery*, 7th edition. Oxford, Butterworth-Heinemann, 2014.
[13] ***. ANSYS CFX code user manual, ANSYS, 2022.

ISSN 1454 - 8003
Proceedings of 2023 International Conference on Hydraulics and Pneumatics - HERVEX
November 8-10, Băile Govora, Romania

APPRECIATION OF WEAR ON ACTIVE SURFACES OF THE AUTOMATIC HYDRAULIC SYSTEMS IN TERMS OF CONTAMINATING PARTICLES

Aristia-Ioana POPOVICI[1], Mihail Ioan SAVANIU[1]

[1] Technical University of Civil Engineering Bucharest (UTCB) – Faculty of Mechanical Engineering and Robotics in Constructions

ioana.popovici@utcb.ro; mihai.savaniu@utcb.ro

Abstract: *Automatic Hydraulic Systems (AHS) are made of hydraulic or electrohydraulic elements. Electro-hydraulic servo valves (SV) are used in automatic systems to ensure high performance. Due to the requirements imposed by the systems, the SV must have a design and manufactured specifications that should ensure a minimum of wear overtime. Wear particles resulting from other components of the AHS are driven by the hydraulic oil and cause erosive wear of the SV. This paper presents the study of the abrasive erosion of SV by simulating the impact of the particles on their active surface and quantifying the erosion by using the classical models of erosive wear.*

Keywords: *Erosive wear, servo valves, modeling-simulation, analytical wear model, solid particle*

1. Introduction

The electro-hydraulic servo valves (SV) are the most complex components of AHS that provide information transfer from electronic area to hydraulic area of hydraulic systems.
In essence, the SVs are a key component for the control systems; servo valves convert electrical control signal (current, voltage) into output value (flow, pressure) of the system. Between input-output there are mechanical, hydraulic and electrical connections. The most common SVs are those with flow control with two amplification stages (preamplifier and hydraulic amplifier).
The spool-sleeve join (the main coupling of hydraulic amplifier) is made with very precise tolerance of form, dimensional and position, and with very low roughness for a proper operation and high performance of SV's.
Theoretical and experimental research has aimed to analyze the cause that generate SV components degradation (wear), especially those produces by friction and characteristic wear, among which progressive contamination of the hydraulic oil is the most important [1].
Spool and sleeve surfaces are subject to erosion in two cases:

1. Direct erosion on spool surface occurs when the spool is moving and particles from infested fluid are hitting spool's surfaces from SV's inlet to outlet (figure 1);

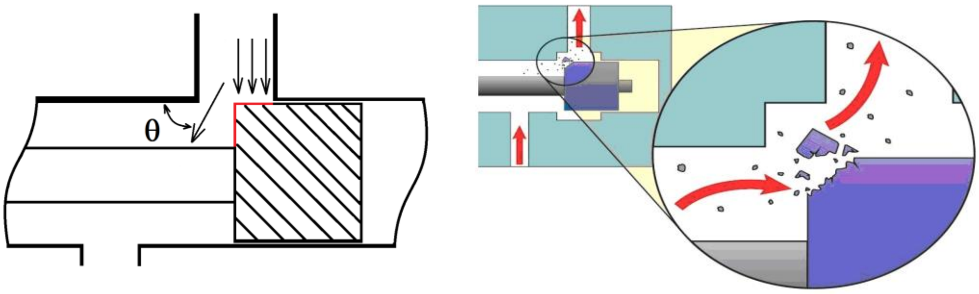

Fig. 1. Direct erosion on spool surface [2]

2. Erosion in annular clearance between spool and sleeve – the particles carried by fluid are entering the gap and causes surface erosion (figure 2).

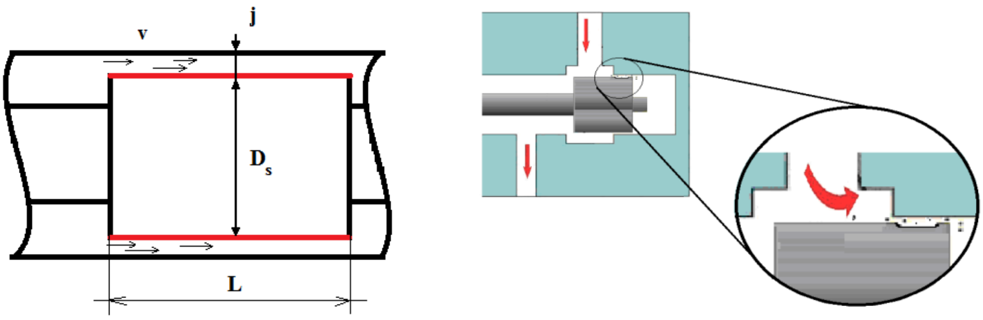

Fig. 2. Erosion in spool-sleeve clearance [2]

Hard particles that are entering the gap between the spool and sleeve can be found in three cases: moving freely through the gap, set on one of the friction surfaces, or making a “bridge” between the two surfaces.

Abrasive erosion is determined by speed, mass, shape, concentration, mechanical and metallurgical characteristics of contaminating particles. This is the most active form of wear for AHS, the most important source of involved surface damage. Small particles of micron size can be “crowded” in areas where the flow is achieved with lower speeds, in which they can plastically “weld” due to contact stress exceeding allowable pressures. Thus, overcrowding particles formed have more intense erosive effects than those of the separate particles.

Superficial mechanical fatigue is favored by cracks occurrence in the superficial surface layer, caused mainly by the formation and sheer of microjoints created at the asperity's peaks contact which is characteristic for adhesion wear. Fatigue wear particles is generated after following specific fatigue cycle: initiation, propagation and achieve critical crack length.

Effects caused by abrasive particles impact on target areas are determined by hydraulic oil characteristics of AHS and by mass contaminants characteristics. For high pressure and oil flow speeds abrasive-erosion effects are considerable.

Contaminating particles are described by size, number, concentration, nature, mechanical and metallographic characteristics of the material. It turned out that the most dangerous in terms of erosion and abrasion, are particles with sizes up to 5µm which enter in the gap between spool and sleeve [3]. Hard contaminating particles with sizes smaller than the radial clearance between spool and sleeve, usually in the range 1÷4 µm, are capable of temporary sticking to the sleeve [4].

The accumulation of contaminating particles in the small gaps, as that between the spool and sleeve, produces the uneven distribution of the radial load and the increase of the axial load necessary for the spool movement.

In this paper studies were carried out on the erosion wear of the SV coupling under different opening degrees, contaminated particle concentrations and considering the inlet and outlet pressures. This article focuses on the theoretical and simulation studies of the erosion and wear of SV spools and sleeves. Figure 3 shows the workflow chart of these studies.

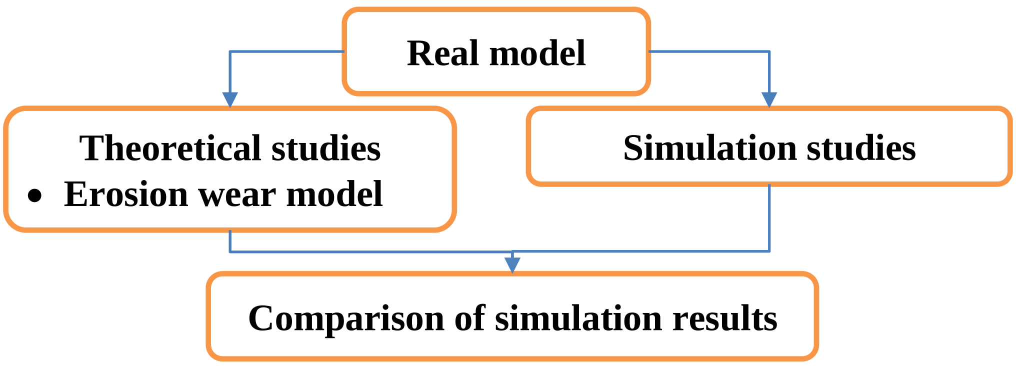

Fig. 3. Workflow chart

2. Tension state at hydraulic contact between spool and sleeve

Using SolidWorks Flow Simulation software fluid flow in spool-sleeve coupling was simulated. The software allows the definition of the working fluid (density, viscosity variation model, etc.). In this paper there was considered a contaminated hydraulic oil HLP 46. The flow of oil having solid contaminated particles inside the valve is a liquid-solid two-phase flow, in which the oil is the continuous phase, and the contaminated particles are the discrete phase.
For flow analyze, there were established boundary conditions and the flow space which was limited by inserting lids on the input and output areas of the fluid, as shown in figure 4 and as follows:

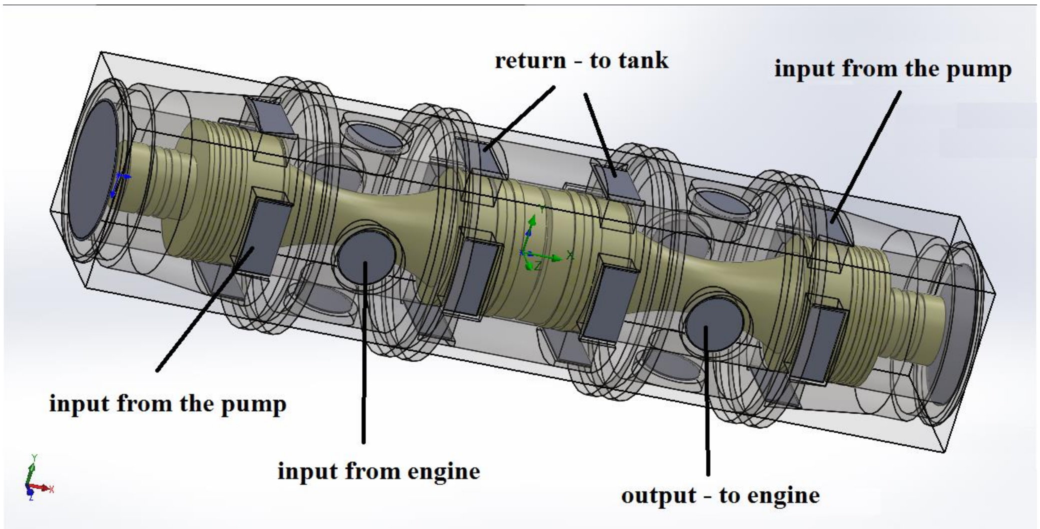

Fig. 4. Boundary condition for spool-sleeve coupling

1. Input from the pump – it was considered the input flow;
2. Output to engine – outlet pressure was imposed;
3. Input from the engine – it was imposed engine pressure;
4. Return (to tank) – atmospheric pressure;
5. Fluid-solid interface conditions – clearance in spool-sleeve coupling.

Simulations have been performed considering the spool opening of 0.5 mm and 0.1 mm.
After running the computing finite element applied for considered fluid flow were obtained results on flow path and velocity distribution (or pressure) inside the spool-sleeve coupling geometry. These results are shown in figures 5 a and b (both for contaminated oil at 1200 operation hours).

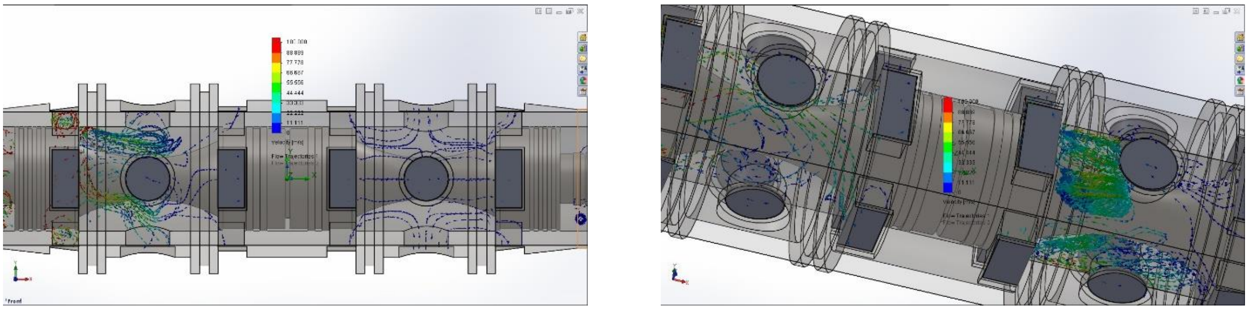

a) b)

Fig. 5. Flow path and speed flow variation for contaminated oil: a) spool movement of 0.1 mm; b) spool movement of 0.5 mm

3. Erosion analysis in terms of hydraulic oil contamination

3.1 Erosion wear rate obtained from fluid flow simulation

In the flow of liquid-solid fluids, the erosion of wall material by solid particles is a usual form of wear. The trajectory of contaminated particles in the flow field influences the flow field and the prediction of wear on the boundary surface.
During SV's operation, solid contaminating particles follow the fluid, and constantly hit the spool or sleeve, that causes the wear of the spool sleeve coupling.
The SolidWorks [5] program allows visualization of contaminating particle trajectories, and it can calculate erosion wear rate with the following equation:

$$R_{erosion} = \sum_{P=1}^{N_p} K \frac{m_p C(d_p) f(\theta) V^{b(V)}}{dS} \quad (1)$$

where: $\mathbf{R_{erosion}}$ – the erosion wear rate of the SV's coupling, [kg/m²s]; $\mathbf{N_p}$ – the number of solid contaminating particles; $\mathbf{m_p}$ – mass of particles carried by fluid in a certain time [kg/s]; **V** – difference between the particle's velocity and the wall speed, [m/s]; **dS** – a finite element surface of solid contamination particles impacting the wall of the coupling, [m²]; **K** – erosion coefficient; **C**(d_p) – coefficient that defines erosion dependence of the particle size; **b(V)** – coefficient that defines erosion dependency of the particles relative speed; **f(θ)** – coefficient that defines erosion dependency of the impact angle; **θ** – the impact angle between the contaminating particles and the wall of the SV's coupling.

Erosion dependency coefficients can be tabularly defined by angle, speed, etc.
Equation (1) defines the physical significance of the wear quality of the spool sleeve in relation to the erosion rate in erosion wear.
Regarding the contamination particles, their trajectories were highlighted for the input area (figure 6.a) and output area (return to tank) (figure 6.b) to and from the SV. There were considered 200 particles of 2 μm size and the particle concentration of 3.33·10-5 kg/s.

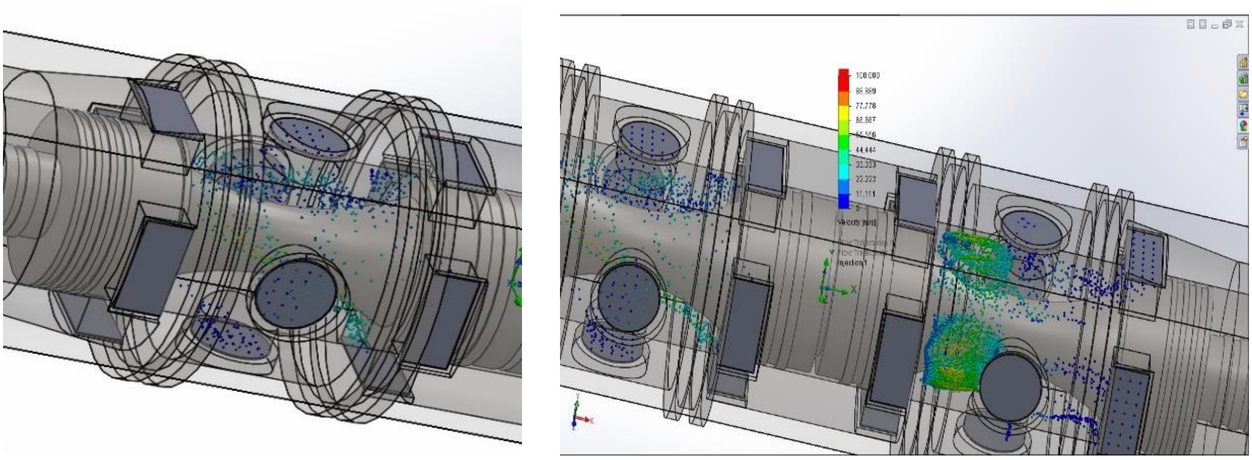

a) **b)**

Fig. 6. The trajectory for the imput area: a) spool displacement of 0.1 mm; b) spool dispalacement of 0.5 mm

In table 1 are presented the values of wear rate for different areas of the servovalve spool, for two different spool opening (0.1 mm and 0.5 mm).

Table 1: Wear rate values obtained from fluid flow simulation

The area subject to erosion	**Ware rate values** [kg/m^{2}s]	
	Spool opening of 0.1 mm	**Spool opening of 0.5 mm**
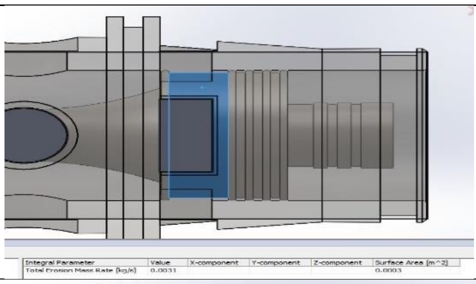	**0.0017**	**0.0031**
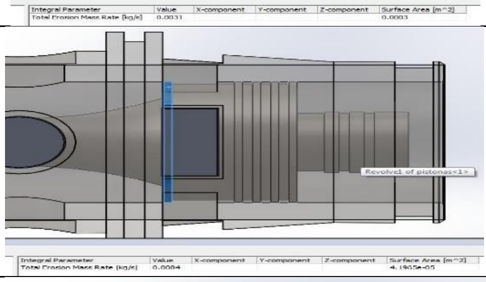	**0.0025**	**0.0084**
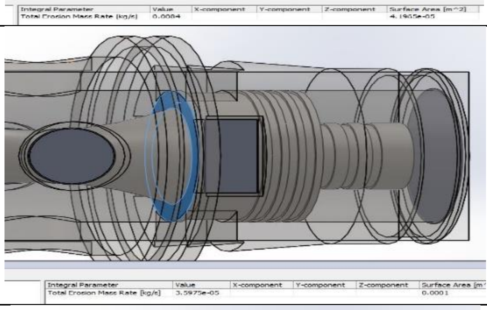	**7.3713·10^{-6}**	**3.5975·10^{-5}**
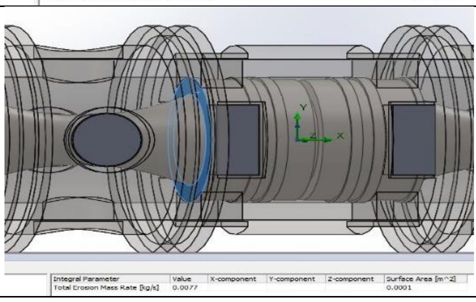	**0.00622**	**0.0077**

3.2 Wear rate obtained with the classical models for erosive wear

3.2.1 Classical models for erosive wear

The main form of failure of SV coupling elements is erosion failure. Finnie [6] has conducted theoretical and experimental studies on the erosion and wear mechanism of plastic impact of the contaminating particles and proposed a micro-cutting theory of erosion and wear, from which an empirical formula for its erosion was derived, and the micro-cutting theory was verified through experiments. The disadvantage of his theory is that when particles are eroded at large angles, there is a large error between the equation of wear and the experimental results. Bitter [7] proposed a deformation wear theory based on micro-cutting wear and deformation wear mechanisms. According to this theory, that material wear is the result of a combination of micro-cutting and plastic deformation wear, with cutting wear dominating when solid particles hit the surface of an object at a small angle, and deformation wear dominating when particles hit the surface of an object at a large angle.

1) Finnie's models
First Finnie's model
For the calculation of the wear rate (defined as the ratio between the mass of the worn material and the mass of the eroded material), Finnie [6] considers sharp abrasive particles, their recoil effects and micro-cutting effects and that the material is plastically deformed following the impact of the abrasive particle.
The calculation relationships proposed by Finnie have the following structure:

$$R_u = \frac{p_a \cdot \rho_m \cdot v^2 \cdot (1-c_r^2)}{0.9272 \cdot H_S \cdot \psi \cdot K_F}\left(sin\,2\,\alpha - \frac{6}{K_F} sin^2\,\alpha\right), \quad \text{for} \quad tg\alpha \leq \frac{K_F}{6} \tag{1}$$

$$R_u = \frac{p_a \cdot \rho_m \cdot v^2 \cdot (1-c_r^2)}{0.9272 \cdot H_S \cdot \psi \cdot K_F}\left(\frac{K_F}{6} cos^2\,\alpha\right), \quad \text{for} \quad tg\alpha \geq \frac{K_F}{6} \tag{2}$$

where: $\boldsymbol{R_u}$ – dimensionless wear rate; $\boldsymbol{p_a}$ – the percentage of abrasive particles with micro-cutting effects [kg/m³]; $\boldsymbol{\rho_m}$ – target material density [kg/m³]; $\boldsymbol{v}$ – particle impact speed [m/s]; $\boldsymbol{\alpha}$ – the angle of incidence [degrees]; $\boldsymbol{c_r}$ – restitution coefficient; $\boldsymbol{H_s}$ – static hardness [N/m²]; $\boldsymbol{\Psi}$ – the ratio of the contact length ($\boldsymbol{L}$ [μm]) and cutting depth ($\boldsymbol{\delta}$ [μm]) of impact area; $\boldsymbol{K_F}$ – the ratio of the horizontal component ($\boldsymbol{F_o}$ [N]) and the vertical component ($\boldsymbol{F_o}$ [N]) of the characteristic impact force.

Second Finnie's model
For the second model, Finnie reconsider the percentage of the abrasive particles with micro-cutting effects by reducing the pa factor from 50% to 10%. Thus, the calculation relations become:

$$R_u = \left(\frac{p_a}{2K}\right)\frac{\rho_m \cdot v^2 \cdot (1-c_r^2)}{0.9272 \cdot H_S}\left(sin\,2\,\alpha - \frac{8}{K_F} sin^2\,\alpha\right), \text{ for } tg\alpha \leq \frac{K_F}{8} \tag{3}$$

$$R_u = \left(\frac{p_a}{16}\right)\frac{\rho_m \cdot v^2 \cdot (1-c_r^2)}{0.9272 \cdot H_S}\left(cos^2\,\alpha\right), \text{ for } tg\alpha \geq \frac{K_F}{8} \tag{4}$$

2) Bitter's model
Bitter considered that the abrasive erosion mechanism has two components that occur simultaneously: the micro-cutting component, which occurs at small incidence angles, and the repeated deformation component of the target surface. In the case of micro-cutting, Bitter considers two cases related to the moment when micro-cutting ceases, the tangential component of the velocity has a certain value when the particle leaves the surface and the case when this speed becomes zero during the micro-cutting process [7].
The total erosive wear rate is the sum of the two component and is differentiated by the value of the impact angle at which the particle leaves the surface:

$$R_u = R_{u,DW} + R_{u,C_1}, \quad \text{for} \quad \alpha \leq \alpha_0 \tag{5}$$

$$R_u = R_{u,DW} + R_{u,C_2}, \quad \text{for} \quad \alpha > \alpha_0 \tag{6}$$

where α_0 - corresponds to the angle of impact at which the tangential component of speed is zero, which occurs when the particle leaves the incident surface.

For repeated surface deformation component, Bitter suggest the following relation for calculating the rate of wear:

$$R_{u,DW} = \frac{\rho_m (U_i\,sin\,\alpha - U_{el})^2}{2\varepsilon_D} \tag{7}$$

When the tangential component of the particle speed is not zero, the wear rate is defined with the following equation:

$$R_{u,C_1} = \frac{2\rho_m C_1 (U_i \sin\alpha - U_{el})^2}{(U_i \sin\alpha)^{0.5}} \cdot \left(U_i \cos\alpha - \frac{\varepsilon_C C_1 (U_i \sin\alpha - U_{el})^2}{(U_i \sin\alpha)^{0.5}} \right) \qquad (8)$$

and for the second case, when the speed is zero, the following relation is used:

$$R_{u,C2} = \frac{\rho_m \left(U_i^2 \cos\alpha - C_2 (U_i \sin\alpha - U_{el})^{1.5} \right)}{2\varepsilon_C} \qquad (9)$$

For the previous equation, the terms have the following meaning: $\boldsymbol{R_{MC_1}}$, $\boldsymbol{R_{MC_2}}$ and $\boldsymbol{R_{M,DW}}$ – dimensionless erosion wear rate; ***v – impact speed components:*** $\boldsymbol{U_i}$ - impact speed of the particle [m/s] and $\boldsymbol{U_{el}}$ - the impact speed that is reached at the elastic limit of the material [m/s]; $\boldsymbol{\varepsilon_D}$ - the specific energy of deformation [J/m]; $\boldsymbol{\rho_a}$- density of the erosive particle material [kg/m^3]; $\boldsymbol{\rho_m}$ – density of the target material [kg/m^3]; $\boldsymbol{E_e}$ - modulus of elasticity on impact [N/m^2]; $\boldsymbol{\varepsilon_c}$ - the specific wear energy for microcutting [J/m]; $\boldsymbol{C_1}$ and $\boldsymbol{C_2}$ - constants with specific relations; $\boldsymbol{H_s}$ – static hardness [N/m^2]; $\boldsymbol{\alpha}$ – the angle of incidence [degrees].

3.2.2 Classical models for erosive wear

For the studied erosion wear models is considered the material 38 MoCrAl 9 with the properties specified in table 2. It is also considered the influence of the material of the abrasive particle through the density parameters (ρ_{ab}), considering the concentration of contaminating particles.
For Finnie models, the influence of the particle characteristics is considered by the pa factor (percentage of abrasive particles) calculated according to the particle concentration.
In table 4 are listed the values of the parameters involved in the calculation equations of the analyzed models.

Table 2: The parameters of the calculating equations

Model	Parameters	
	Specific to the model	**Common to the models**
Finnie	$\boldsymbol{p_a}$ **-** the percentage of abrasive particles with micro-cutting effects • 50% for the first model: $\boldsymbol{p_a}$=10^{-2} kg/m^3; • 10% for the second model $\boldsymbol{p_a}$=2·10^{-3} kg/m^3; $\boldsymbol{\Psi}$ – the ration of the contact length and the cutting depth of the impact area: 10 for SV's material;	$\boldsymbol{\rho_m}$ - density of the target material: 7800 kg/m^3; $\boldsymbol{\rho_{ab}}$ - density of the target material: 4000 kg/m^3; HB - surface hardness: 570·10^6 [N/m^2] ***E*** - Young's modulus: 2.1·10^{11} [N/m^2] $\boldsymbol{\alpha}$ - incidence angle: 69° and 79° ***v*** - particle impact speed: 0.1÷10 m/s; μ - friction coefficient between the particle and the material: 0.1. $\boldsymbol{c_r}$ - restitution coefficient: 0.5;
Bitter	$\boldsymbol{\alpha_0}$ - the angle at which the speed is zero: 0^o; $\boldsymbol{\varepsilon_D}$ - the specific energy for wear: $\boldsymbol{\varepsilon_D}$ – elastic deformation: 4.7·10^{10} J/m^3; $\boldsymbol{\varepsilon_C}$ - micro-cutting: 2.2·10^{10} J/m^3	

Considering the equations and the specific parameters, the variation of the erosive wear rate was analyzed for each model presented, depending on the impact speed that is a common parameter for both models. The results obtained are listed in figures 7 and 8.

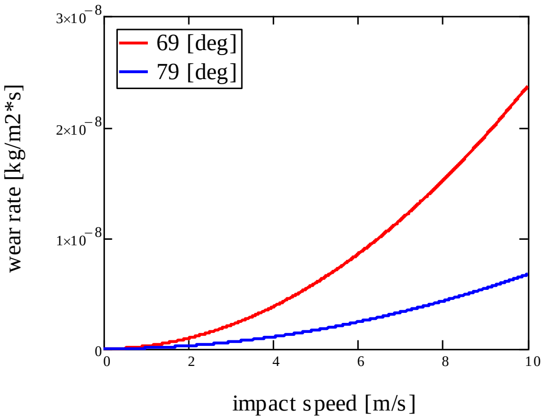

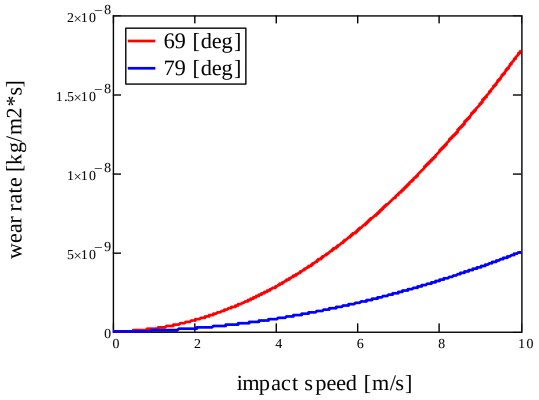

a) **b)**

Fig. 5. Variation of wear rate depending on the impact speed:

a) Finnie's first model; b) Finnie's second model

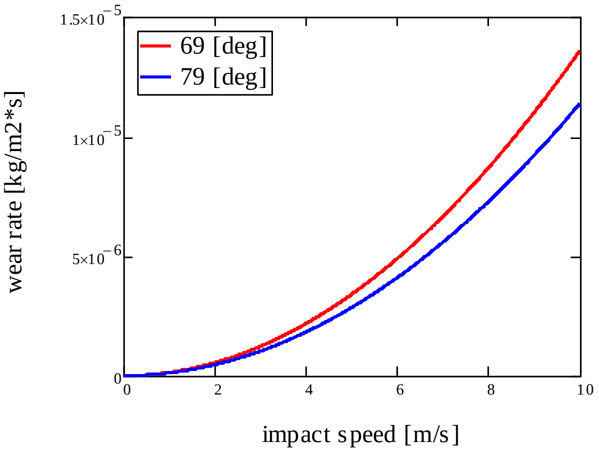

Fig. 6. Variation of wear rate depending on the impact speed for Bitter's model

Table 3 includes the values of the erosive wear intensity measured for two considered values of the impact speed. The impact angles are 69° and 79° and are specific to the spool opening considered in the earlier flow analysis.

Table 3: The values of the erosion wear rate for two impact angles

Model		**Wear rate depending on two considered values of the impact speed [kg/m²·s]**	
		v_1 = 2	**v_2 = 10**
Finnie 1	**69°**	$9.57 \cdot 10^{-10}$	$2.37 \cdot 10^{-8}$
	79°	$2.66 \cdot 10^{-10}$	$6.69 \cdot 10^{-9}$
Finnie 2	**69°**	$7.11 \cdot 10^{-10}$	$1.77 \cdot 10^{-8}$
	79°	$1.99 \cdot 10^{-10}$	$5.04 \cdot 10^{-9}$
Bitter	**69°**	$4.54 \cdot 10^{-7}$	$1.36 \cdot 10^{-5}$
	79°	$5.48 \cdot 10^{-7}$	$1.14 \cdot 10^{-5}$

4. Conclusion

Due to the extremely high pressure which develops in the flow space, SV elements are elastically deformed until the lubricant film is broken and there is direct contact between the spool and the sleeve. Finite element analysis of flow and strain generated by the contaminated hydraulic oil in the clearance between spool and sleeve, highlighted the areas most exposed to erosive wear.
The study highlights the occurrence of high strains, randomly located (according to the relative position of the pattern elements - 0.5 respectively 0.1 mm) on the contact area with the pressure fluid, but not as a direct result of the fact that their areas are hardened (by heat treatment) so it can be considered that the maximum strain does not lead to plastic deformation but to an elastic deformation of superficial layer, which may lead in time to fatigue. If it is considered the particles impact, this process is accelerated.
The results confirmed the prediction of erosion models, which the intensity of erosive wear is greatly reduced in the coupling clearance. The maximum erosion rate increases with the opening degree and reaches a maximum value when the opening degree is 0.5 mm.
There is a certain amount of sleeve erosion near the corners (table 1); for the spool, the erosion wear rate of the sharp edge of the control surface of the slide valve sink groove is significantly greater than that of the sharp edge of the control surface of the convex shoulder.
The erosion rate is influenced by the contaminated solid particles of the oil, with the increase in the contaminated solid particles parameter, the erosion rate changes more obviously. The erosion rate is less affected by the change in opening degree and increases with the increase in opening degree.
By comparing the values of the two mathematical models from table 3 it was found that the minimum value of the wear intensity results for Finnie's models and the maximum value is in Bitter case. These differences are due to the different parameters the models consider and as Bitter specifies two components of the erosive wear.
The presented studies must be confirmed through experimental research to show which model has the most exact calculation equation.
In the presented analysis were considered the two of the most influential parameters: opening degree (corresponding to the flow rate of the valve) and oil contamination with solid particles.
It is necessary for further study on the erosion wear of SV's coupling considering more parameters, like temperature and operating pressure. These studies can establish a mathematical model that predicts with great accuracy the wear phenomenon of the SV coupling parts.
This experimental study will be used to analyze the SV's performances by simulating their motion to specified parameters.

References

[1] Arnell, R.D., P.B. Davies, J. Halling, and T.L. Whomes. *Tribology – Principles and design application*. London, MacMillan Education Ltd., 1991.
[2] Popovici, A.I. *Contribution to study of wear effects on the performance of automatically controlled hydraulic systems / Contribuții la studiul efectelor uzării asupra performanțelor sistemelor hidraulice de reglare automată*. Bucharest, PhD Thessis, 2012.
[3] Rădulescu, Gheorghe, and Mary Ilea. *Physico-chemistry and technology of lubricating oils / Fizico-chimia si tehnologia uleiurilor lubrifiante*. Bucharest. Technical Publishing House, 1982.
[4] Pătruţ, Petre, and Nicolae Ionel. *Hydraulic Drives and Automation – Theory, devices, automatic systems and industrial applications / Acţionări hidraulice şi automatizări – Teorie, aparate, sisteme automate şi aplicaţii industriale*. Bucharest, “Naussica” Publishing House, 1998.
[5] https://www.solidworks.com. Accessed September 16, 2023.
[6] Finnie, I. “Some observations on the erosion of ductile metals.” *Wear* 19, no. 1 (January 1972): 81-90.
[7] Bitter, J.G.A. “A study of erosion phenomena part I.” *Wear* 6, no. 1 (January–February 1963): 5–21.

ISSN 1454 - 8003
Proceedings of 2023 International Conference on Hydraulics and Pneumatics - HERVEX
November 8-10, Băile Govora, Romania

EXPERIMENTAL RESEARCH ON A CLAMPING DEVICE

Adrian Constantin HANGANU[1]

[1] "Gh. Asachi" Technical University of Iași, Faculty of Machine Manufacturing and Industrial Management

Abstract: *In the catalogs of the manufacturers of hydraulic devices, we do not find the operating characteristics that, in industrial practice, the application of too high forces caused deviations in the shape of the parts processed on NC machining centers.*
In this paper we report our experience in the experimental research of a hydraulically actuated modular technological device. The special test stand, with three operating positions (calibration, radial stroke measurement, radial force measurement), with 2 digital measuring chains with multiparametric output signal, the proposed virtual instrumentation and established research methodology determine the innovative character of the work.

Keywords: *Hydraulic, test stand, experimental research, clamping device*

1. Introduction

In an extensive monographic study [1] I highlighted, at length, almost all aspects regarding the current state of knowledge related to technological devices in general, and hydraulically actuated ones in particular. From this study, the current trends in the use of hydraulic drives in different branches of activity resulted, considering their indisputable advantages, demonstrated theoretically and validated by the practice of applications; they refer, in particular, to: high power density, ensuring an optimal regulation of work processes, increasingly faster response speeds to commands, good dynamic performance, their compatibility with electronics, informatics and mechatronics through specific elements interface etc. For these reasons, the use of hydraulic systems has experienced a spectacular trend highlighted by the increase in equipment production, with increasingly higher performances, between 20÷35%, in the last 25 years.
It should be noted that, due to the increase in the performance of current equipment, the usual working pressures have increased from 10÷25 MPa to 35, 50, 70 or even 100 MPa with notable applications also in the hydraulic actuation of processing devices in the automotive industry. Devices operated in this way achieve an extremely high clamping capacity, unthinkable in the past, at small dimensions and dimensions, with major consequences regarding their architecture. Associated with original orientation solutions, for example with purely technological ("non-functional") orientation surfaces and modularization, Fig. 1, such devices allowed the development of intensive processing technologies with significant economic effects.

Fig. 1. Modularized hydraulic device

Fig. 2. Clamping a complex blank on a 5-axis CNC machining center

The previous own research [2] was developed with new research methods for the design and optimization of the construction and operation of these types of devices, in the category of those hydraulically operated from medium and high-pressure units, with wide application in the processing technologies specific to the automotive industry from Romania (Fig. 2).
Starting from some observations and findings based on Ishikawa diagrams, with effect on the precision of machining parts on CNC machining centers, we experimentally researched the influence of clamping forces and strokes because in the catalogs of the manufacturers of hydraulic devices we do not find the operating characteristics.
The research was carried out on a modularized device, hydraulically actuated, Fig. 3 and Fig. 4, with the characteristics:
- maximum force: 26 kN;
- maximum axial stroke: 9 mm;
- minimum fixing diameter: 16+0.1 mm;
- maximum radial stroke of the jaws: max. 1 mm;
- maximum working pressure: 35 MPa;
- - the jaws of the device perform a radial extension movement, self-centering, as a result of the movement on an inclined plane of a plunger, multiple wedge type, integral with the piston of the hydraulic cylinder.

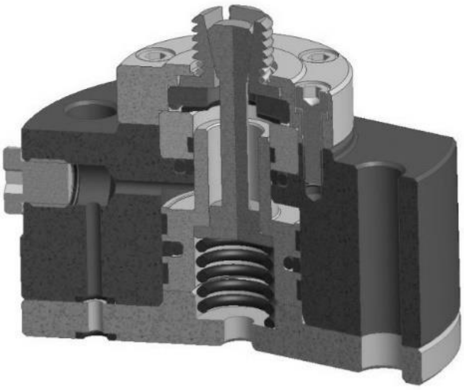

Fig. 3. The pull-down clamping device

Fig. 4. Assembly scene of the hydraulic clamping device

2. Innovative stand for testing the hydraulic clamping device to be optimized

We designed, using Autodesk Inventor, a special stand (Fig. 5÷9) to testing the hydraulic device.

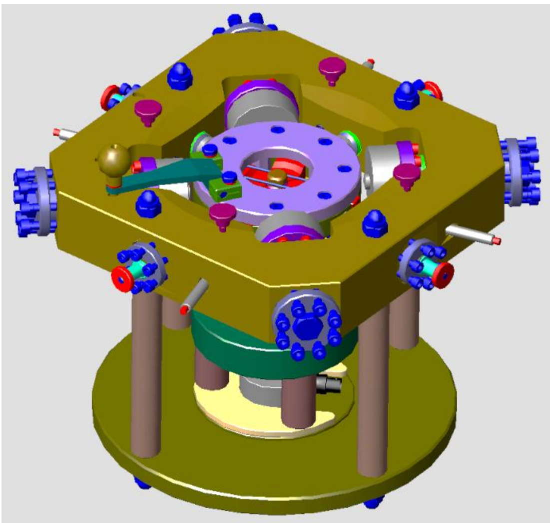

Fig. 5. 3D design: the test-stand equipped to evaluate the stroke and the force operation

Fig. 6. Test-stand with the plate with the plunger indexed middle/ in calibration position

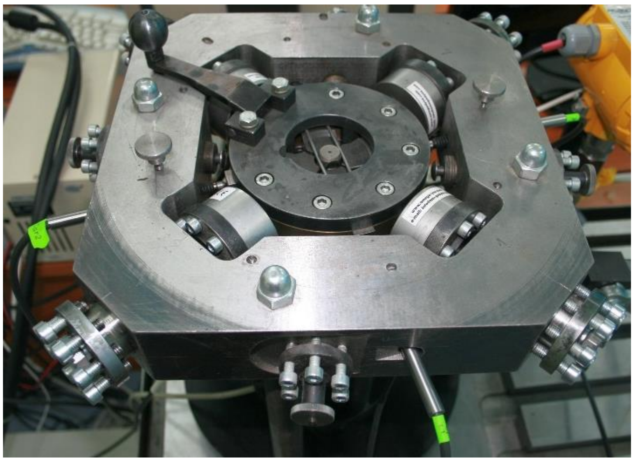

a) left indexing - the plunger takes the tightening stroke of each bar and transmits it to the displacement transducer

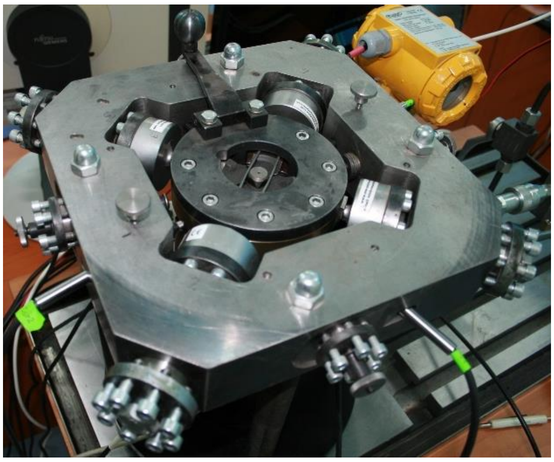

b) right indexing - the plunger takes the clamping force of each bar and transmits it to the force transducer

Fig. 7. Details of the other two indexing positions of the plunger plate

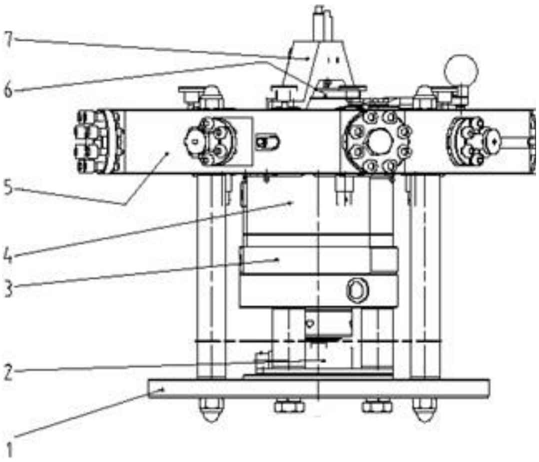

a) lateral view

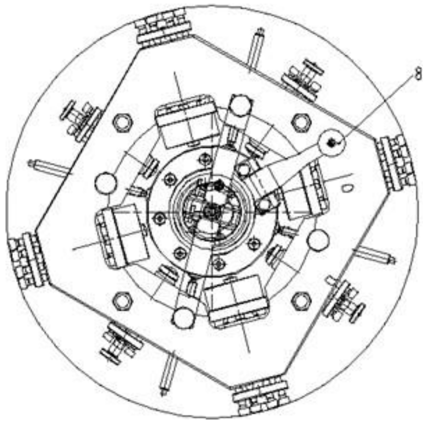

b) upper view

Fig. 8. 2D design: the test-stand for pull-down clamping device

1 – Main body; 2 – Force transducer (for axial force, action or/and clamping force); 3 – Support alimentation – pressure circuit; 4 – Testing device; 5 – Motion transducers assembly (4 pieces, for radial/clamping strokeevaluation) 6 – Force transducer (preliminary force evaluation); 7 – Displacement transducers assembly (1 piece for action stroke evaluation, 1 piece for preliminary and clamping stroke evaluation); 8 – Adapters with radial plungers.

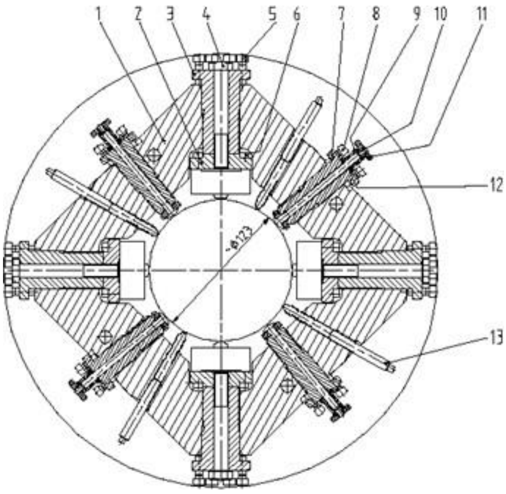

Fig. 9. 2D section/ test-stand for pull-down clamping device

1 – Transducer support for displacement and force; 2 – Force transducer (for radial/clamping force evaluation); 3 – Force transducer support; 4 – Clamping screw for force transducer assembly; 5 – Screw for force transducer pre- charging; 6 – Clamping screw for force transducer; 7 – Position system for displacement transducer; 8 – Special nut; 9 – collar bush; 10 – Plunger with spherical head; 11 – Bush; 12 – Elastic washer; 13 – Displacement transducer.

The stand allows for additional equipment, Fig. 10, with a displacement and force translation yoke for evaluating the force and axial travel of the blank clamping.

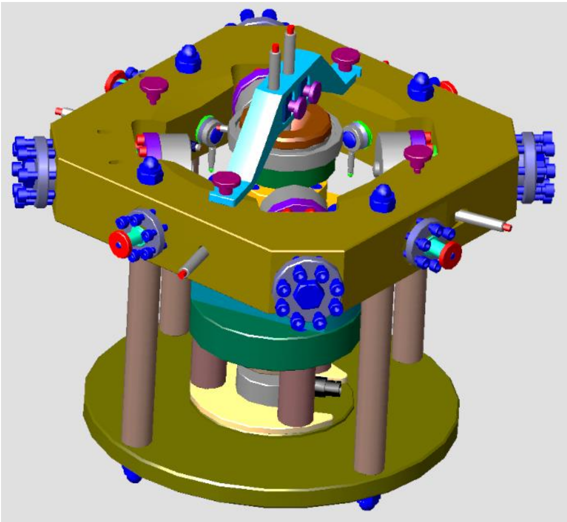

a) 3D design

b) Photo

Fig. 10. The test-stand with the additional equipped to evaluate the axial stroke and force

3. Research apparatus for experimenting with the hydraulic clamping device to be optimized

The hardware and software components used for the displacement parameters measurement chain are shown in Fig. 11, Fig. 12 and Tab. 1.

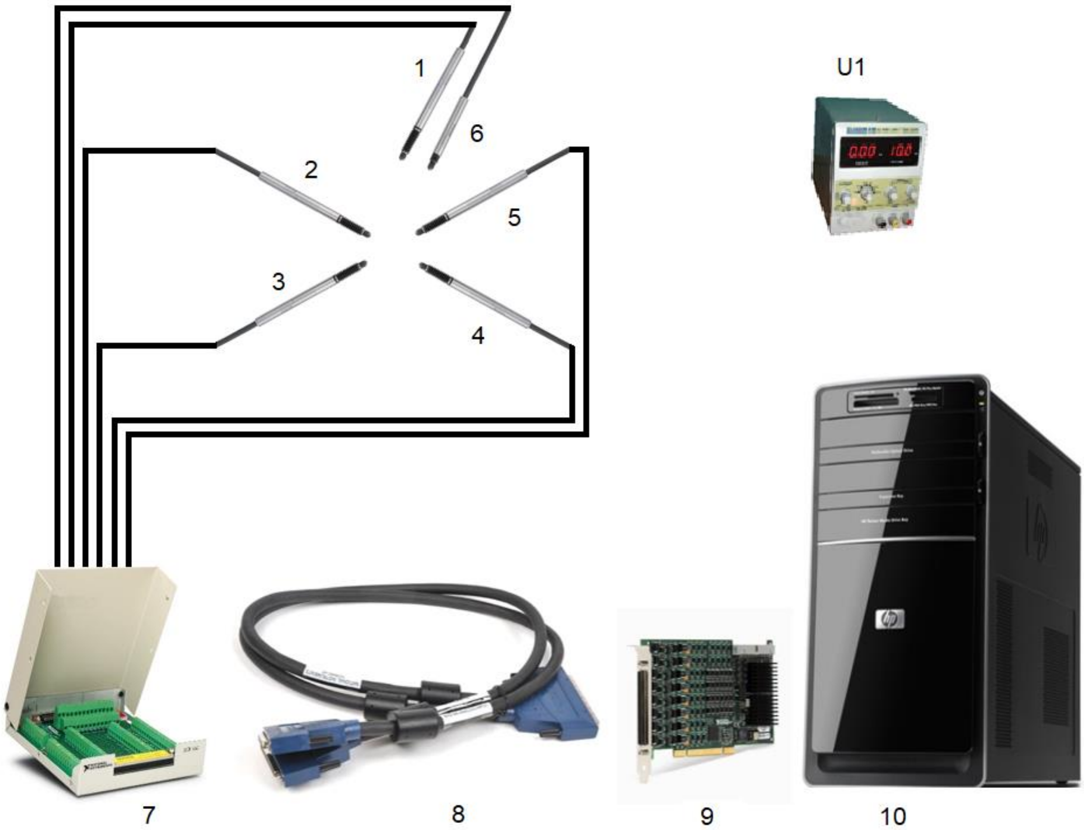

Fig. 11. Sketch of the displacement parameter measurement chain

Table 1: The hardware and software components used for the displacement parameters measurement chain

Pos	The measured parameter		Transducer type	Code/ licence	Characteristic sizes	
	Symbol	Race of			specific	common
1	c_a	actuation/ displace-ment of the piston	digital, displace-ment, with three-phase A/ B/ Z output signal of voltage-differential, rectangular shape	DK812R5 / Sony	- measurement range: 0-12 mm; - resolution: 0.5µm; - accuracy: 1.5 µmp-p; - maximum response speed: 100 m/min.	- with output signal with three phases A/B/Z of voltage-differential, rectangle-round shape (according to the EIA-422 norm); - fixing diameter: ø8-0.009 mm; - fixing length: 18 mm; - the maximum tightening torque of the notched bush screw: 0.6 Nm; - signal period/step: 40µm; - vibration resistance (10-2000 Hz): 100 m/s2; - impact resistance (11ms): 1000 m/s2; - supply voltage: +5 VDC; - consumed power: 1.8 W; - protection class: IP66; - temperature range: 0-50°C; - signal cable length: 2.5 m.
2	c_{sr1}	radial clamping / jaws 1, 2, 3 an4		DK812R5 / Sony		
3	c_{sr2}					
4	c_{sr3}					
5	c_{sr4}					
6	c_{sa}	axial clamping of the blank		DK802R / Sony	- measurement range: 0-2 mm; - resolution: 0.1µm; - accuracy: 1 µmp-p; - maximum response speed: 42 m/min.	

Pos	Name	Code/ licence	Characteristic sizes
7	Multi-function DAQ I/O connection box	SCB-100 / National Instruments	- SCSI socket with 100 pins; - 6 microswitches for multi-functional I/O settings; - 101 screws for fixing signal cables; - separate temperature sensor connection option.
8	Data cable	SH100-100-F / National Instruments	- male SCSI plug with 100 pins/ connection to SCB-100; - length 2 m; - male plug with 100 pins/ connection to NI 6624..
9	PCI acquisition card	6624 / National Instruments	- number of input channels: 26 (3 for each transducer and 2 extra PFIs); - maximum input frequency: 400 kHz; - minimum input pulse width: 1 µs; - recommended power: 0.75 A at +5 VDC; - number of output channels: 8; - maximum current: 100 mA/ channel; - output supply voltage: 8-48 Vdc; - I/O resolution: 32 bits; - female plug with 100 pins/ connection SH100-100-F; - PCI socket/ desktop computer connection.
10	Desktop computer	ACH67/ Dell	- minimum Intel Core 2 Duo, 1 GHz, 2 GB RAM, minimum 100 GB HDD, minimum 2 PCI ports, minimum power supply 400 W, video card with 2 VGI/DVI/DisplayPort outputs; - minimum Windows 7 Pro license; - minimum NI-DAQ 7.1 license; - peripherals: 2 LCD monitors, keyboard, mouse.
U1	Stabilized power supply	TXN-1502D / Hiaoxin	- supply voltage/ mains frequency: 220 VAC/50 Hz; - protective fuse: 0.5 A; - stabilized output voltage: 0-15 Vdc adjustable; - output current: 0-0.2 A adjustable.

The equipment and software used for the force, pressure, temperature parameter measurement chain are shown in Fig. 13, Fig. 14, Fig. 15 and Tab. 2.

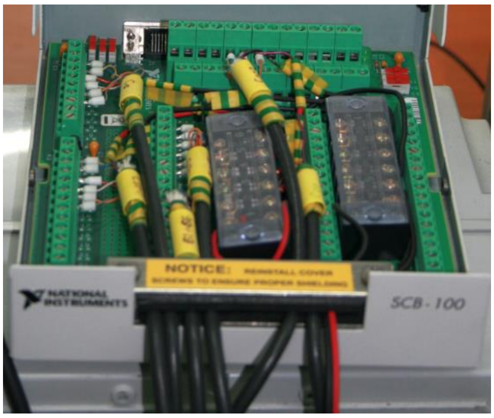

Fig. 12. Detail of the connections made in the DAQ connection box multifunctional I/O SCB-100

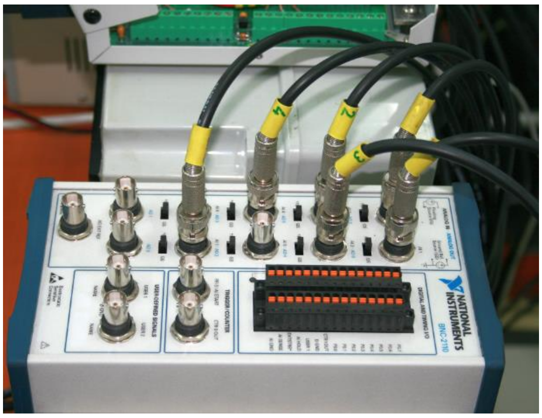

Fig. 13. Detail of the connections made in the BNC-2110 multifunctional DAQ I/O connection box

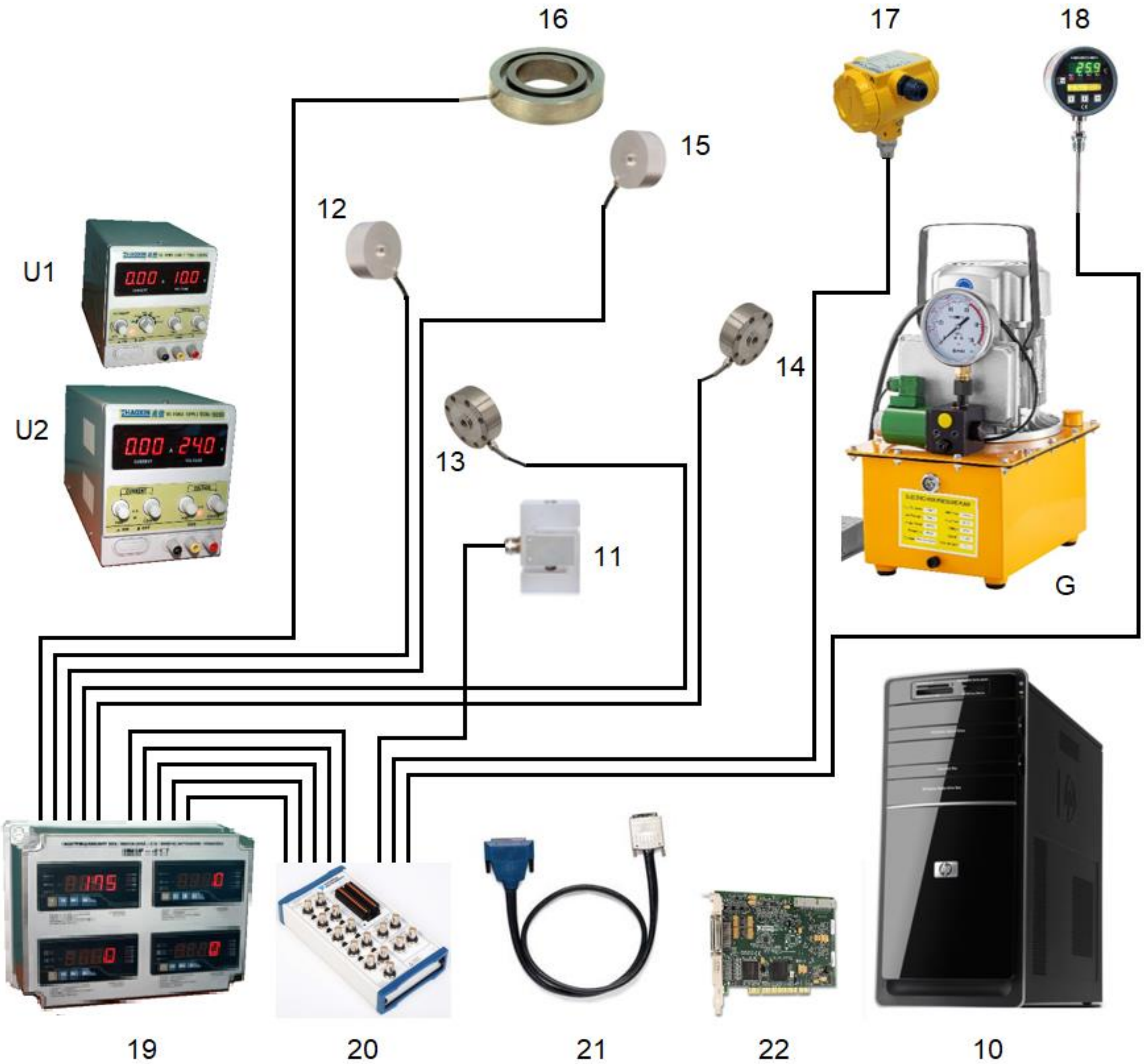

Fig. 14. Sketch of the of the force, pressure, temperature parameter measurement chain

Table 2: The hardware and software components used for the force, pressure, temperature parameter measurement chain

Pos	The measured parameter: Symbol	The measured parameter: Force of	Transducer type	Code/ licence	Characteristic sizes
11	Q	hydraulic cylinder actuation	Load cell, compression - traction, with tensometric marks	K-25 / Lorenz	- measurement range 2-50 kN; - sensitivity: 2 mV/V; - compression precision class: 0.1%; - maximum dynamic force (DIN 50100): 35 kN; - supply voltage: 2-12 VDC; - repeatability: 0.08%; - signal converter for strain gauge cells, input signal 2 mV/V, output signal 12±8 mA, accuracy class 0.1, protection class IP60.
12	S_{r1}	radial clamping / jaw 1, 2, 3, 4	Load cell, compression with tensometric marks	LC305-20K lbs / Omega	- measurement range 0-8.9 kN; - excitation: 10 Vdc (maximum 15 VDC); - output signal: 2 mV/V (±0.25%); - 5 calibration points: 0, 50, 100, 50, 0 %; - linearity: ±0.15% FSO; - hysteresis: ±0.1% FSO; - repeatability: ±0.05% FSO - zero balance: ±2% FSO.
13	S_{r2}				
14	S_{r3}				
15	S_{r4}				
16	S_a	axial clamping of the blank		LC8400-213-10K lbs / Omega	- measurement range 0-4.45 kN; - excitation: 10 Vdc (maximum 15 Vdc); - output signal: 2 mV/V; - linearity, hysteresis, - repeatability: ±0.5% FSO< - zero balance: ±2% FSO.
17	p	pressure generated by the hydraulic power unit	with tensometric mark	APCE 2000-AL / Applisens	- measurement range: 0-50 MPa; - accuracy class: 0.075%; - output signal: 4-20 mA; - supply voltage 13.5-36 VDC.
18	T	hydraulic oil temperature		DTMF580P B1A40S / Henschen	- measurement range: 0-80°C; - accuracy class: 0.5; - output signal: 4-20 mA; - supply voltage 15-30 VDC.

Pos	Name	Code/ licence	Characteristic sizes
19	Display panel with 4 digital indicators and signal conversion (Fig. 15)	IMIP-417/ ACH innovation	- 4 x Asahi Keiki A5212-17 modules; - input: tensometric mark 2 mV/V; - output: analog and 0-10 V; - accuracy ±0.1%; - supply voltage 24 Vdc.
20	Multi-function DAQ I/O connection box	BNC-2110 / National Instruments	- 8x Analog In, 2x Analog Out, 1x Analog Ext Ref, 2x digital and timing I/O, 2x Trigger/Counter, 2x User-defined signals; - 68-pin SCSI socket.

Table 2: (continuation)

Pos	Name	Code/ licence	Characteristic sizes
21	Data cable	SHC68-68-EPM / National Instruments	- male SCSI plug with 68 pins/ connection to BNC-2110; - male plug with 68 pins/ connection to NI 6229.
22	PCI acquisition card	6229 PCI/ National Instruments or 6036E PCMCIA/ National Instruments	- number of input channels: 16 differential; - ADC resolution: 16 bits; - simple rate: 250 kS/s; - signal bandwidth (-3 dB): 700 kHz; - input voltages: ±0.2 / ±1 / ±5 / ±10 Vdc; - number of output channels: 4; - maximum current: ±5 mA; - output supply voltage: ±10 Vdc; - female socket with 68 pins/ connection SHC68-68-EPM; - PCI socket/ connection to desktop computer or PCMCIA-PCI adapter or laptop PCMCIA socket.
10	Desktop computer	ACH67/ Dell	- minimum Intel Core 2 Duo, 1 GHz, 2 GB RAM, minimum 100 GB HDD, minimum 3 PCI ports, minimum power supply 400 W, video card with 2 GI/DVI/DisplayPort outputs; - minimum Windows 7 Pro license; - minimum NI-DAQ 7.1 license; - peripherals: 2 LCD monitors..
U1	Stabilized power supply	TXN-1502D / Hiaoxin	- supply voltage/ mains frequency: 220 ±10% Vac/ 50 Hz; - protective fuse: 0.5 A; - stabilized output voltage: 0-15 Vdc adjustable; - output current: 0-0.2 A adjustable.
U2	Stabilized power supply	RXN-305D / Hiaoxin	- supply voltage/ mains frequency: 220 ±10% VAC/ 50 Hz; - protection fuse: 1.5 A; - stabilized output voltage: 0-30 Vdc adjustable; - output current: 0-0.5 A adjustable.
G	70 MPa hydraulic power unit with multiplier or high pressure pump	UAH.700 or UH.700 / Hydramold	- maximum pressure: 70 MPa; - maximum flow: 0.2 l/min; - installed power: 2.2 kW; - supply voltage/ frequency:220 VAC/50 Hz - 500 bar throttle for flow limitation.

The innovative display panel with 4 digital indicators and signal conversion is shown in Fig.15. The characteristic sizes are indicated in table 2, at position 19. The panel was needed for:
- conversion of the strain gauge signal into a 0-10 Vdc output signal for 5 load cells, compression with strain gauges;
- stand calibration without National Instruments acquisition system; the Asahi Keiki A5212-17 modules were set to display the compression force value.

a) view from the digital displays b) the In and Out connections

Fig. 15. Display panel with 4 digital indicators and signal conversion from 2 mV/V to 0-10 V

The signal is received from 5 compression load cells, maximum 4 simultaneously (5xIn 2 mV/V 2+2 Out 0-10VDC, 14-36 VDC), which imposed the condition of introducing some electrical couplers on the data cable of the LC8400-213-10K load cell as well as on the data cable of a single load cell load LC305-20K.

4. Conception in LabView of the virtual instrument and the block diagram for the analysis of the dependence between the parameters measured at the hydraulic cylinder and the radial clamping force at the jaws of the device

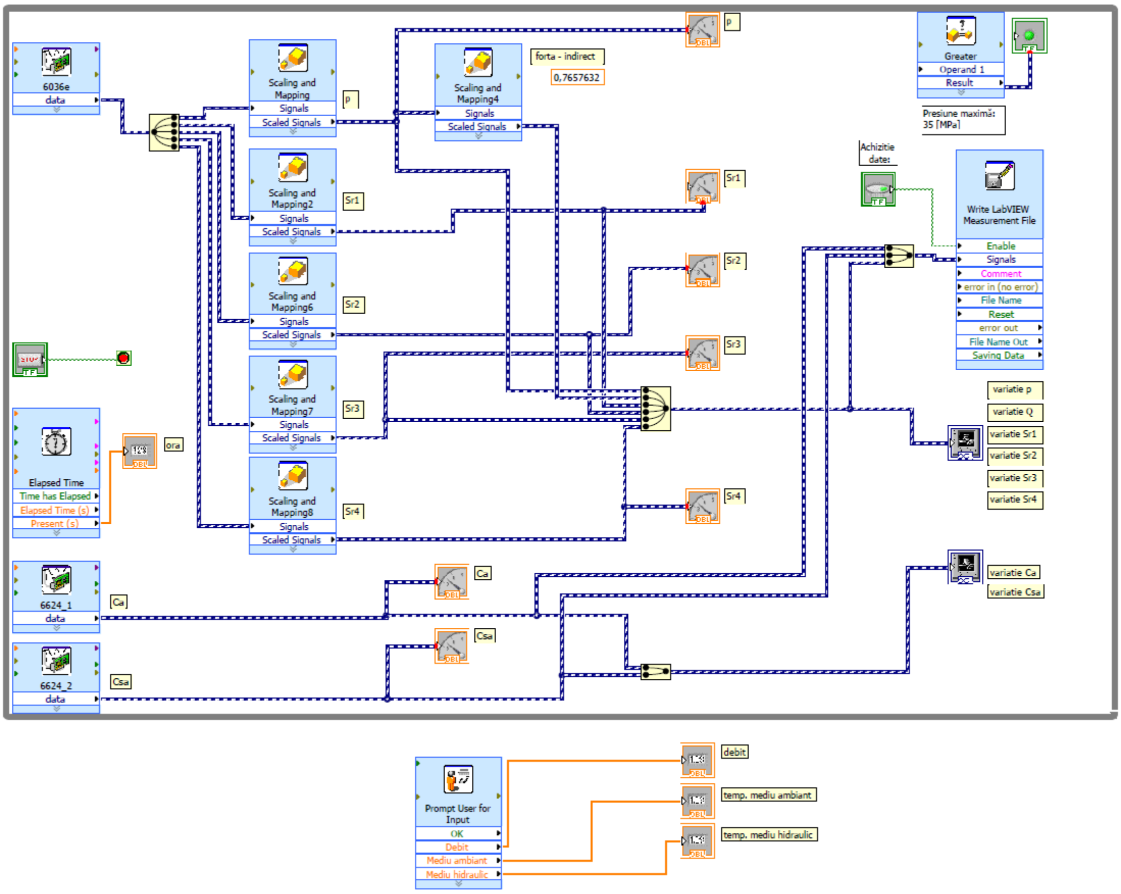

Fig. 16. Block diagram for the analysis of the dependence between the parameters measured at the hydraulic cylinder and the radial clamping force of the jaws of the clamping device

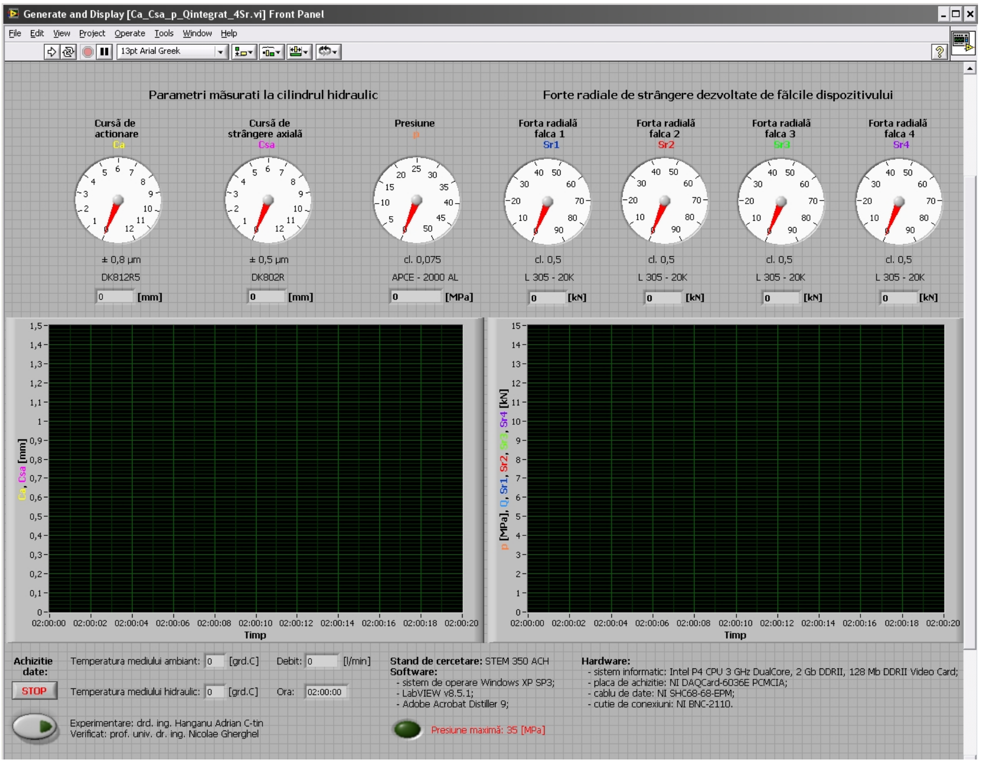

Fig. 17. Virtual LabView innovative tool for analyzing the dependence between parameters measured at the hydraulic cylinder and the radial clamping force of the clamping device jaws

5. Experimental research on the analysis of the dependence between the parameters measured at the hydraulic cylinder and the radial clamping force of the device jaws

I used the previously mentioned virtual tool and stand equipment 2; in Fig. 18 we presented photo captures during the experiment and in Fig. 19 and Fig. 20 are plots of the real-time plotting of the signals of the pressure transducer, two displacement transducers and 4 compression load cells with strain gauges / time evolution of the quantities c_a, c_{sa}, p, S_{r1}, S_{r2}, S_{sr3} and S_{r4}.

Fig. 18. Photo capture during the experiment

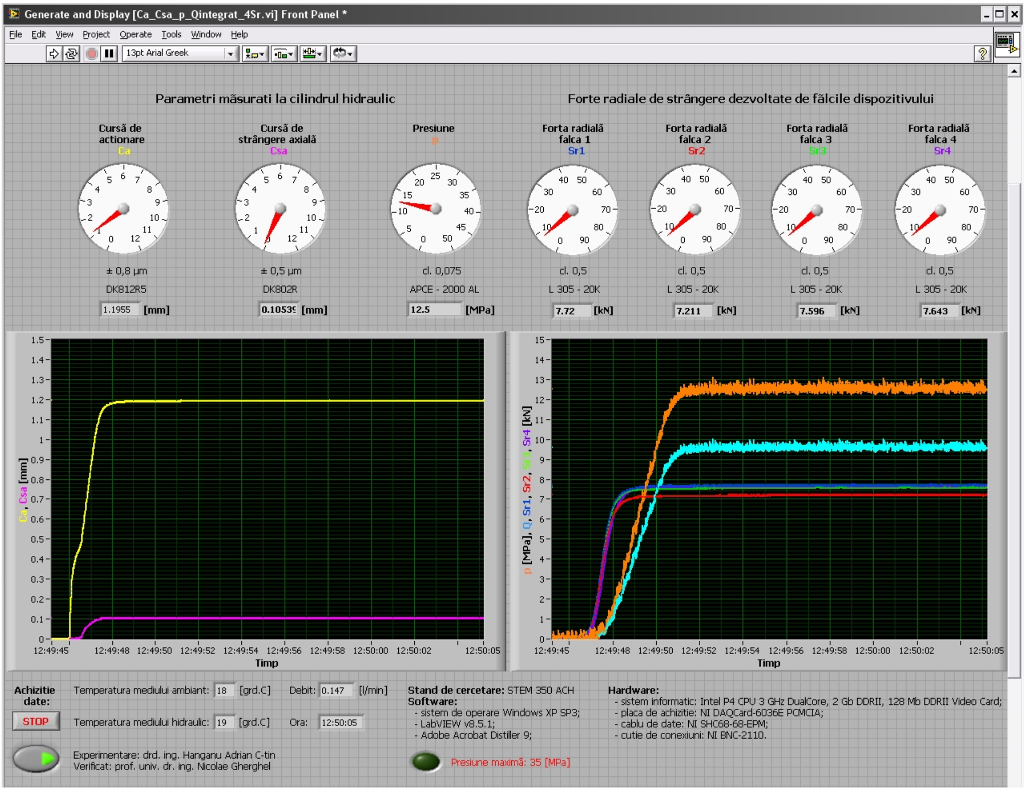

Fig. 19. Screenshot of the visual data acquisition interface with 7 measuring instruments and two graphs of real-time plotting of the quantity signals of c_a, c_{sa}, p, S_{r1}, S_{r2}, S_{sr3} and S_{r4} (adjusted pressure:12,5 MPa)

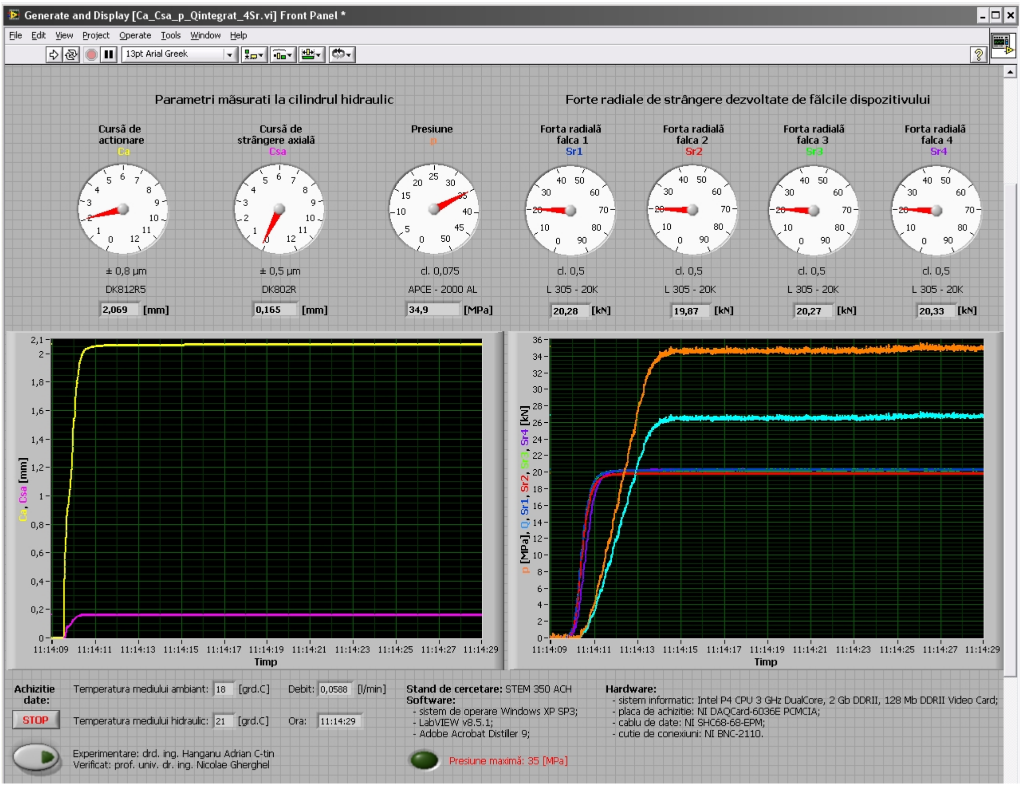

Fig. 20. Screenshot of the visual data acquisition interface with 7 measuring instruments and two graphs of real-time plotting of the quantity signals of c_a, c_{sa}, p, S_{r1}, S_{r2}, S_{sr3} and S_{r4} (adjusted pressure:35 MPa)

For the evaluation of the parameters measured at the hydraulic cylinder and the radial clamping force of the device jaws, semi-finished products of different brands of alloy steel were used, with improvement heat treatment at various hardness values, with a technological fixing hole of the same nominal size, then it was ordered the connection to the hydraulic group where the pressure has been adjusted to values between 12.5 and 35 MPa (Fig. 19 and Fig. 20), in steps of 2.5 MPa. According to the diagrams $c_a(t)$, $c_{sa}(t)$, p(t), Q(t) – obtained by integration as pressure filtering, respectively $S_{r1}(t)$, $S_{r2}(t)$, $S_{r3}(t)$ and $S_{r4}(t)$ an increase proportional to the value of the regulated pressure at the hydraulic group of the actuation stroke, the axial clamping stroke and the radial clamping forces of the jaws is observed.
The experimental determinations were carried out 10 times, using three blanks of different materials and with a technological hole of the same nominal size.
The displayed values are recorded by LabView and allow the data to be saved on the computer's hard disk in a text file with a dedicated name with the extension .lvm.

6. Analysis and interpretation of the results regarding the dependence between the parameters measured at the hydraulic cylinder and the radial clamping force of the device jaws

The inputs were the data of the experimental determinations presented in the previous paragraph, recorded by LabView on the hard disk of the computer; data files were imported into MsExcel to make characteristic plots for detailed data analysis/interpretation.
In Fig. 21 and Fig. 22 we superimposed the characteristic curves for the actuation stroke $c_a(t)$, the axial clamping stroke $c_{sa}(t)$, pressure p(t), and the radial clamping force specific to each jaw of the device: $S_{r1}(t)$, $S_{r2}(t)$, $S_{sr3}(t)$, $S_{r4}(t)$ – data acquisition specific to the visual data acquisition interfaces diagrams in Fig. 19 and Fig. 20.

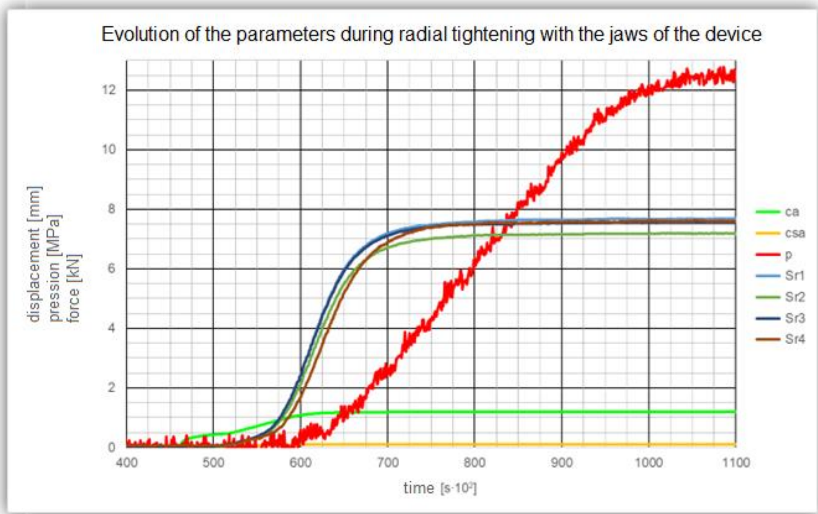

Fig. 21. Variation over time of parameters c_a, c_{sa}, p, S_{r1}, S_{r2}, S_{sr3} and S_{r4} for a pressure of 12.5 MPa regulated at the hydraulic group

By analyzing the characteristic curves in Fig. 21 and Fig. 22, for semi-finished products of different brands of alloy steel, with heat treatment for improvement at various values of hardness, but with technological fixing hole having the same nominal size, we observed all the curves of the parameters c_a, c_{sa}, p, S_{r1}, S_{r2}, S_{sr3} and S_{r4} have the same allure but all have steeper ramps and higher stall values as hydraulic group pressure increases.
The characteristic curves of $S_{r1}(p)$, $S_{r2}(p)$, $S_{sr3}(p)$ and $S_{r4}(p)$ in Fig. 23 and Fig. 24 were drawn for pressures adjusted to the hydraulic group of 12.5 MPa, respectively 35 MPa; it can be seen that they have similar grooves regardless of the pressure value, being of the 2nd degree curve type.

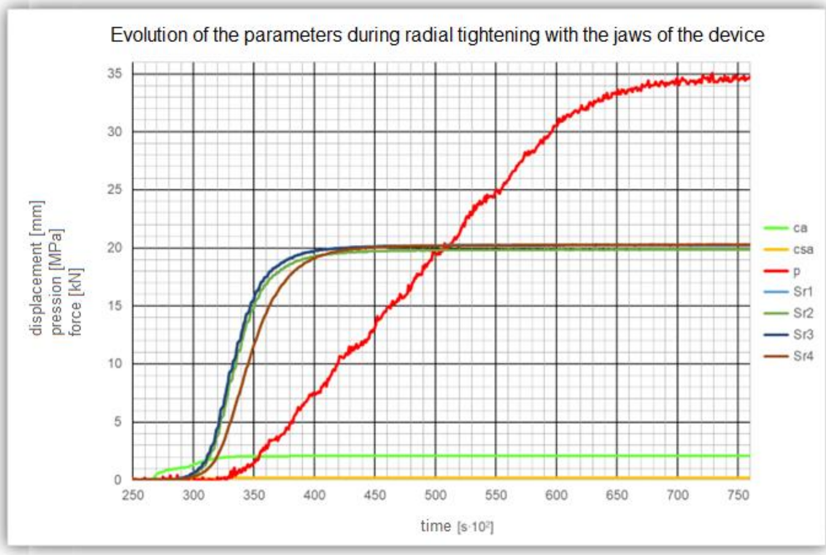

Fig. 22. Variation over time of parameters c_a, c_{sa}, p, S_{r1}, S_{r2}, S_{sr3} and S_{r4} for a pressure of 35 MPa regulated at the hydraulic group

For a pressure of 12.5 MPa set at the hydraulic group, it is observed that the maximum average value of the radial clamping force on a jaw, of 7.5 kN, corresponds to a pressure of 7.5 MPa, and when the pressure increases up to 12 .5 MPa, the maximum value of 7.5 kN is kept.
Similarly, for a pressure of 35 MPa set at the hydraulic group it is observed that the maximum average value of the radial clamping force on a jaw, of 20 kN, corresponds to a pressure of 20 MPa, and up to 35 MPa the maximum value is maintained and never mind the increase in pressure.
This means that the maximum values of 7.5 kN and 20 kN, respectively, correspond to the force developed by the cylinder piston, force demultiplied by the multiple wedge. In Fig. 21 and Fig. 22 it is observed that when the actuation stroke reaches the bearing value, the maximum value of the radial force is obtained. Thus, the safety factor for maintaining the maximum value of the radial tightening force is between 1.(6) and 1.75, for pressures between 12.5 MPa and 35 MPa.

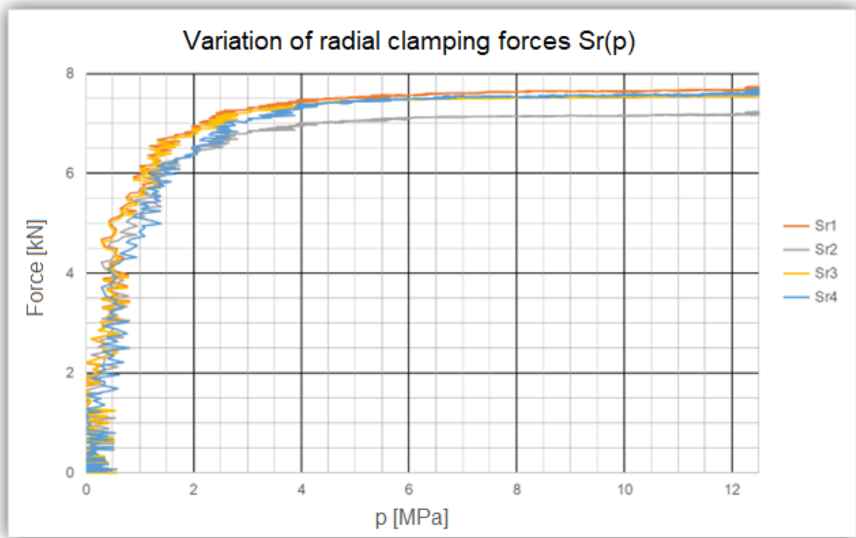

Fig. 23. $S_{r1}(p)$, $S_{r2}(p)$, $S_{sr3}(p)$ and $S_{r4}(p)$ characteristics for a pressure of 12.5 MPa regulated at the hydraulic power unit

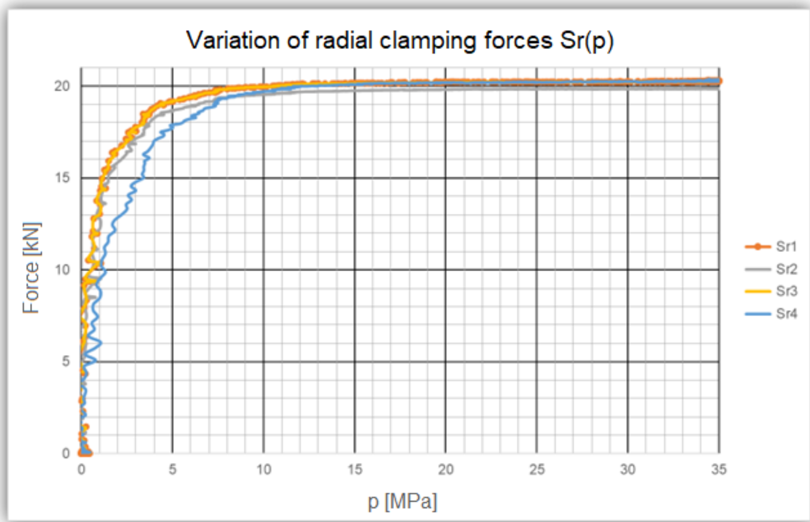

Fig. 24. S_{r1}(p), S_{r2}(p), S_{sr3}(p) and S_{r4}(p) characteristics for a pressure of 35 MPa regulated at the hydraulic power unit

7. Conclusions

The analysis of the results of the experimental research was carried out by importing the data files into Excel, from the Microsoft Office package, with data processing and creating graphs according to the proposed objective, as appropriate by superimposing the evolution over time of the values displayed on the visual acquisition interface or by making of characteristic curves depending on the working pressure.
The characteristic curves have a similar appearance to the one found in the specialized literature, with the difference that we used a measurement system that allowed the acquisition of signals with at least 250 kS/s, LabView and Excel instead of reading the values displayed by analog or digital instruments followed by editing graphics by interpolating the read values.
By using the digital instrumentation and the fourth virtual instrument in LabView we plotted the characteristic curves for the radial forces at different values of the regulated pressure at the hydraulic group, between 11.5 and 35 MPa. The characteristic curves S_{r1}(p), S_{r2}(p), S_{sr3}(p) and S_{r4}(p) have similar shapes regardless of the pressure value, being of the 2nd degree curve type, the maximum values being reached at pressures from 1.(6) times up to 1.75 times lower than the value set at the hydraulic group, these being precisely the safety coefficients for keeping the maximum radial force constant.
All acquired data can be further processed by making details in the desired intervals or in inflection areas, but other characteristic curves can also be made.

References

[1] Hanganu, Adrian Constantin. *Optimization of technological devices with hydraulic actuation*. / *Optimizarea dispozitivelor tehnologice cu acţionare hidraulică*. Iași, Politehnium Publishing House, 2007.
[2] Hanganu, Adrian Constantin, and Cătălin Gabriel Dumitraș. "Test stand for hydraulic clamping devices." *Bulletin of the Polytechnic Institute of Iași. Construction Machinery Section* 63 (67), no. 1 (November 2017): 75-88.

ISSN 1454 - 8003
Proceedings of 2023 International Conference on Hydraulics and Pneumatics - HERVEX
November 8-10, Băile Govora, Romania

METHOD AND MEANS OF MEASURING PULSATING FLOWRATES OF OSCILLATING HYDRAULIC PRESSURE INTENSIFIERS

Teodor Costinel POPESCU[1,*], Alexandru-Polifron CHIRIȚĂ[1], Krzysztof NIEŚPIAŁOWSKI[2], Ana-Maria Carla POPESCU[1]

[1] National Institute of Research & Development for Optoelectronics/INOE 2000, Subsidiary Hydraulics and Pneumatics Research Institute/IHP, Bucharest, Romania

[2] KOMAG Institute of Mining Technology, Gliwice, Poland

* popescu.ihp@fluidas.ro

Abstract: *Oscillating hydraulic pressure intensifiers (miniboosters), which consume low pressures at high flowrates to supply high pressures at low flowrates to hydraulic (linear and rotary) motors, have a pulsating mode of operation. The flowrate of the pumping units equipped with such intensifiers must be measured with a device compatible with this operating regime. The compatibility of the device assumes the absence of moving inertial masses and a rapid response to flowrate variations caused by pressure variations. The authors designed such a device, which comprises a differential pressure transducer, connected to two pressure intake ports, mounted upstream and downstream of a calibrated orifice. Dimensioning the calibrated orifices, designing the device and optimizing its performance were carried out with Simcenter Amesim numerical simulation software.*

Keywords: *Low pressure, minibooster, high pressure, pulsating mode of operation, calibrated orifice, differential pressure transducer*

1. Introduction

An oscillating hydraulic pressure intensifier [1,2,3] works like a small piston pump that has different active surfaces (Fig. 1). In a static hydraulic system, it will supply a smaller and smaller flowrate until the pressure at its outlet, required by the system load, is reached.

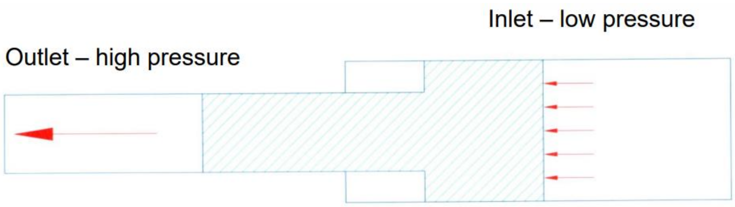

Fig. 1. Minibooster operation assimilated to piston pump operation

The pumping unit in Fig. 2, consisting of **low-pressure electric pump,** 4/2 **hydraulic directional control valve**, electrically-operated, and **minibooster**, supplies a single acting and spring-return hydraulic cylinder.

On the **extension stroke** of the cylinder rod, oil enters the piston chamber, which increases its volume. The piston of the minibooster, which works like a piston pump, is hydraulically actuated **S** with the **PCV** slide valve. It moves alternately left and right, generating the variable volume chambers **V1**, **V2**, and supplies the hydraulic cylinder with a pulsating flowrate, thus: in the **suction** phase, the hydraulic oil pushed by the **low-pressure** pump opens the **CV1** check valve and **fills** the **V2** volume chamber; in the **discharge** phase, the hydraulic oil at **high pressure** in the **V2** volume chamber opens the **CV2** check valve and supplies the hydraulic cylinder.

On the **retraction stroke** of the cylinder rod, the oil in the piston chamber, which decreases in volume, is drained to the tank, through the **PDV** unlockable check valve, controlled by the low-pressure pump.

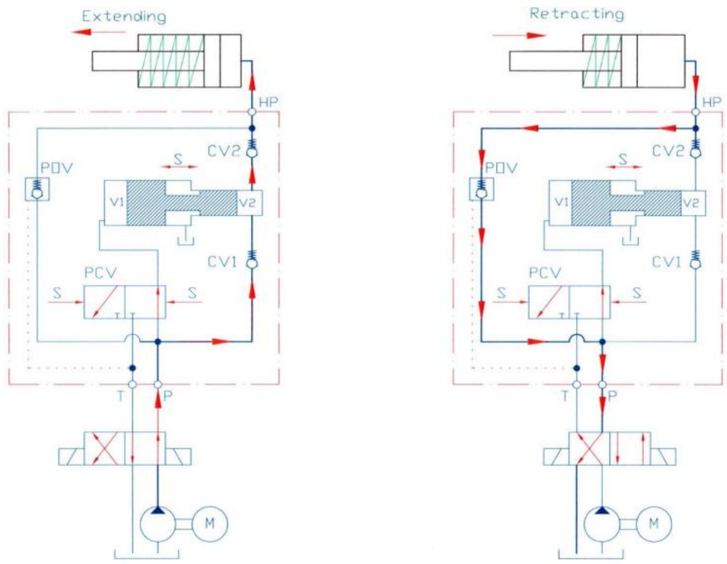

Fig. 2. Supplying a hydraulic cylinder with a pumping unit equipped with a minibooster

Static applications of pumping systems equipped with miniboosters (high pressure resistance tests for pipes and tanks, achieving high pressing or tightening forces) are not influenced by the pressure and flow pulsations (oscillations) at the output of the minibooster [4]. For **dynamic applications**, with hydraulic cylinders moving with high load, constant or variable, over the entire stroke, pressure and flow oscillations at the output of the minibooster can disrupt the uniformity of the displacement of the hydraulic cylinder connected to that minibooster [5].

The pulsating flowrate measuring device covers the range of three HC7 miniboosters, with intensification factors **5.0**, **6.6** and **7.6**, presented in Fig. 3 and Table 1 [6]. All these miniboosters are supplied at the inlet port with a flowrate of approx. **10.5 l/min**, supplied at **200 bar** by a low-pressure pump.

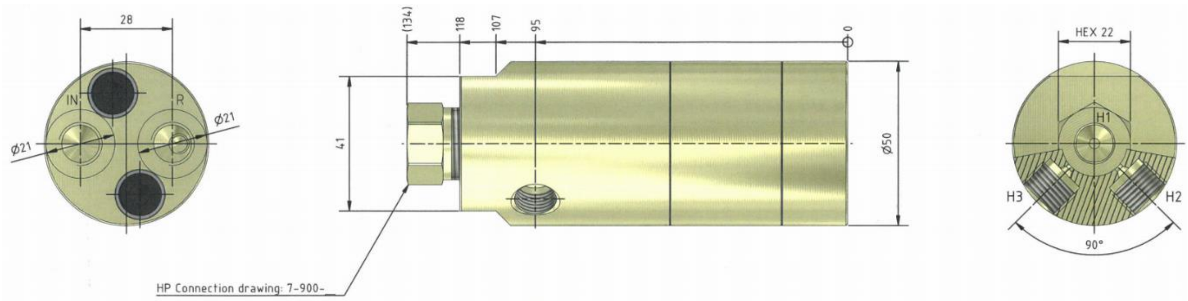

Fig. 3. Dimensions of the HC7 minibooster

Table 1: Technical features of the HC7 minibooster

Intensification factor i [-]	**Primary pressure / Secondary pressure [bar]**	**Maximum flowrate in the primary [l/min]**		**Maximum flowrate in the secondary [l/min]**		**Dimensions of the primary connections**		**Dimensions of the secondary connections**	
		Catalogue	**Used**	**Catalogue**	**Used**	**IN**	**R**	**H1**	**H2**
5.0	0...200 / 0...1000	14.0	10.5	1.6	1.2	¼” BSP	¼” BSP	M22x 1.5	9/16-18UNF
6.6	0...200 / 0...1320	13.0	10.5	1.3	1.05	¼” BSP	¼” BSP	M22x 1.5	9/16-18UNF
7.6	0...200 / 0...1520	13.0	10.5	1.1	0.88	¼” BSP	¼” BSP	M22x 1.5	9/16-18UNF

ISSN 1454 - 8003
Proceedings of 2023 International Conference on Hydraulics and Pneumatics - HERVEX
November 8-10, Băile Govora, Romania

The uniformity of the displacement of a cylinder under load, supplied with an oscillating flowrate provided by one of the miniboosters from table 1, can be assessed on the stand [7] in Fig. 4, having the hydraulic diagram shown in Fig. 5.

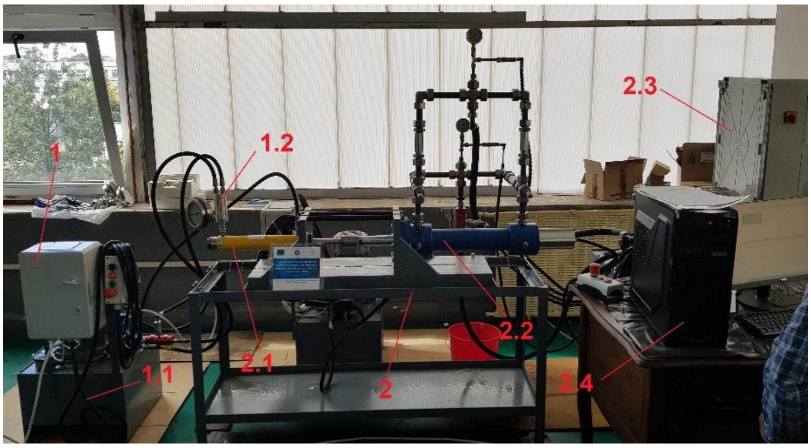

Fig. 4. Test stand for pumping units equipped with miniboosters:
1=high-pressure pumping system (HPPS); **1.1**=low-pressure pumping group; **1.2**=minibooster; **2**=test stand for HPPS; **2.1**=high pressure test cylinder (TC); **2.2**=load cylinder (LC); **S_{cs} / S_{cp}=4.4**; **2.3**=pumping unit for LC filling; **2.4**=system for stand control and experimental data acquisition.

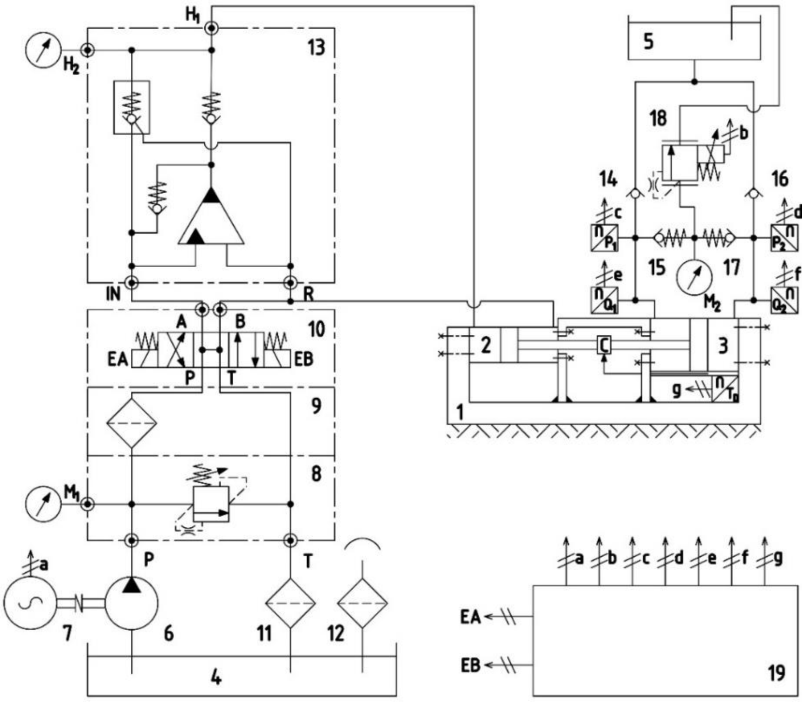

Fig. 5. Hydraulic diagram of the test stand for pumping units equipped with miniboosters:
1=hydraulic cylinder fixing frame; **2**=test cylinder TC; **3**=load cylinder LC; **C**=coupling; **4**=oil tank; **5**=oil tank; **6**=low-pressure pump; **7**=electric motor; **8**=pressure control valve; **9**=pressure filter; **10**=open-center 4/3 hydraulic directional control valve, electrically-operated; **P**,**T**=ports for pressure and directional control valve tank; **A**,**B**=ports for directional control valve consumers; **11**=return filter; **12**=fill / vent filter; **13**=minibooster; **IN**,**R**,**H**=inlet, return and minibooster high pressure ports; **14**,**15**,**16**,**17**=check valves; **18**=load pressure control proportional valve; **19**=electrical control and data acquisition panel; **EA**,**EB**,**a**,**b**=electrical control signals to directional control valve, pump drive motor and proportional valve; **c**,**d**,**e**,**f**,**g**=data acquired from pressure (**P1**,**P2**), flow (**Q1**,**Q2**) and displacement (**T_D**) transducers.

2. Numerical simulation of the operation of the flowrate measuring device

Measuring of the pulsating flowrate will be carried out successively, on two hydraulic circuits (the stand in figs. 4 and 5):
a) high-pressure ***circuit H1*** in the secondary of the pressure intensifier, which supplies the ***hydraulic test cylinder*** (2); on this circuit, the flowrate varies between the value of approx. ***10 l/min***, that is the maximum flowrate of the low-pressure pump, which supplies the primary of the pressure intensifier and bypasses the intensifier, and approx. ***1 l/min***, that is the maximum flowrate on the output of the intensifier, at the amplified pressure;
b) output circuit from the hydraulic load cylinder (3), namely on the circuit of the proportional pressure valve (18); on this circuit the flowrate varies from ***44 l/min***, value corresponding to the flowrate of **10 l/min** from the intensifier secondary, to ***4.4 l/min***, value corresponding to the flowrate of **1 l/min** from the intensifier secondary (the ratio of the active surfaces of the two cylinders coupled on the stand is $\mathbf{S_{cs} / S_{cp} = 80^2 / 38.1^2 = 4.4}$).
On the stand in figs. 4 and 5, the flow vs. pressure characteristic of the minibooster will be experimentally determined, Fig. 6, and flowrate will be measured indirectly, with a device consisting of a ***calibrated orifice*** and a ***differential pressure transducer***, type Protan PR3200, Fig. 7.

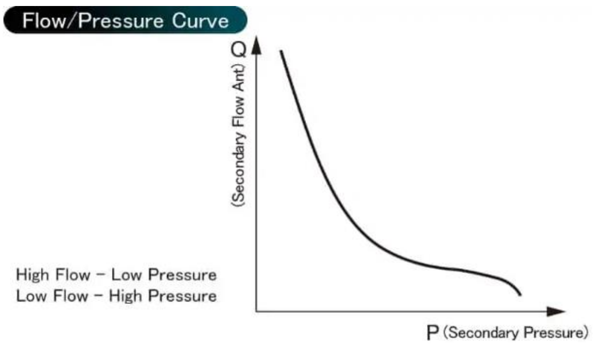

Fig. 6. Minibooster flow vs. pressure characteristic

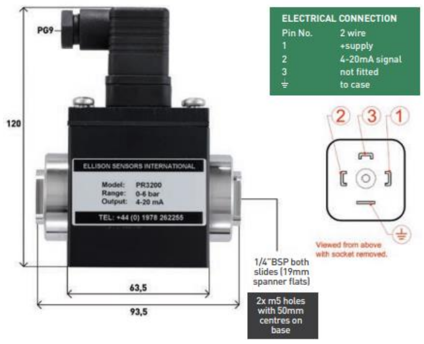

Fig. 7. PR3200 differential pressure transducer

The main technical features of the **PR3200-0100AR** differential pressure transducer are: *output signal = 4...20 mA (2 wires); supply voltage = 10...36 V d.c.; reference pressure = differential; measuring range = 0...100 bar; accuracy = ± 0.5% across the range; static pressure = 400 bar; connection to the installation = 1/4" BSP female thread.*
Knowing the **flow coefficient** of the calibrated orifice, C_Q , which is determined experimentally, **area** of the calibrated orifice, A, **differential pressure** Δp, measured with the differential pressure transducer and fluid **density**, ρ, from Bernoulli's equation, the flowrate calculation formula results:

$$Q = C_Q \cdot A \cdot \sqrt{\frac{2\Delta p}{\rho}} \tag{1}$$

For $[C_Q] = [-]$, $[A] = m^2$, $[\Delta p] = N/m^2$ and $[\rho] = kg/m^3$, it results $[Q] = m^3/s$.

2.1 Numerical simulation model

Fig. 8 shows the device simulation network [8] consisting of: an oil ***tank***; an adjustable capacity ***pump***, driven by a 1000 rpm ***motor***; ***nine flow sections***, supplied by the pump and denoted by letters from **A** to **E'**, which effectively represent the sections on the flow path inside the flowrate measuring device; ***two pressure transducers***; ***a comparator***; an adjustable normally closed ***pressure valve*** to simulate the load. Notations in fig. 8 have the following meanings: **p1:** pressure transducer mounted upstream of the calibrated orifice; **p2:** pressure transducer mounted downstream of the calibrated orifice; **(S2): Dn10** flow sections (**C**, **C`**, **D**, **E**, **E`**), with various lengths, determined constructively from the conditions of positioning of the two pressure intake ports of the transducer and the condition of compliance with the minimum length for flow stilling; **(S1):** sections

A and **B**, which correspond to the four convergent-divergent orifices, with the role of ensuring the pressure drop needed to calculate the four flowrates.

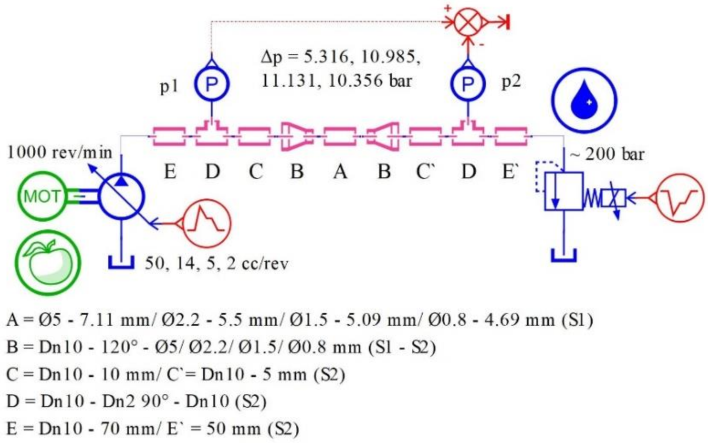

Fig. 8. Numerical simulation network in Simcenter Amesim of the flowrate measuring device

Apart from the geometric shape and lengths of the sections, the simulation also takes into account the relative roughness of the inner axial surfaces of the sections, as well as the properties of the hydraulic fluid, mentioned in Fig. 9.

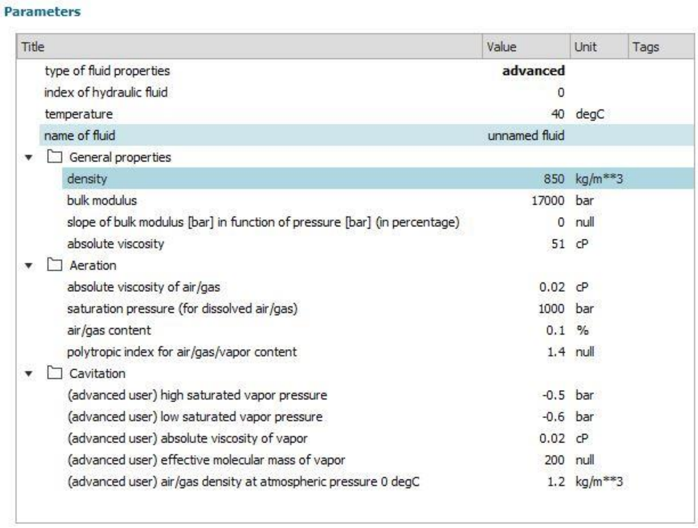

Parameters

Title	Value	Unit	Tags
type of fluid properties	advanced		
index of hydraulic fluid	0		
temperature	40	degC	
name of fluid	unnamed fluid		
General properties			
density	850	kg/m**3	
bulk modulus	17000	bar	
slope of bulk modulus [bar] in function of pressure [bar] (in percentage)	0	null	
absolute viscosity	51	cP	
Aeration			
absolute viscosity of air/gas	0.02	cP	
saturation pressure (for dissolved air/gas)	1000	bar	
air/gas content	0.1	%	
polytropic index for air/gas/vapor content	1.4	null	
Cavitation			
(advanced user) high saturated vapor pressure	-0.5	bar	
(advanced user) low saturated vapor pressure	-0.6	bar	
(advanced user) absolute viscosity of vapor	0.02	cP	
(advanced user) effective molecular mass of vapor	200	null	
(advanced user) air/gas density at atmospheric pressure 0 degC	1.2	kg/m**3	

Fig. 9. Hydraulic fluid properties

2.2 Results of numerical simulations

With the help of numerical simulations, four calibrated orifices were dimensioned, with convergent-divergent inlets/outlets, which will be successively mounted inside the flowrate measuring device, respectively one for each of the four representative flowrates of the miniboosters in Table 1; each of these orifices provides the optimum pressure drop for the flowrate for which it was designed.

Designing of the flowrate measuring device was carried out with simultaneous observance of **three conditions:** ***pressure drop as low as possible*** on the calibrated orifice, to reduce the flowrate measurement error; ***positioning of the pressure intake ports*****,** downstream and upstream of the calibrated orifice, observing the minimum flow stilling lengths; ***ensuring laminar flow through the calibrated orifice***, namely *Re < 2300*, where the *Re* number is given by the relation:

$$Re = \frac{V \cdot l}{\nu} \tag{2}$$

where *Re* = dimensionless Reynolds number *[-]*; *V* = fluid velocity in *[m/s]*; *l* = characteristic length in *[m]*; ν = fluid kinematic viscosity in *[m²/s]*.

The numerical simulation model in Fig. 8 **is run for four cases**, each case corresponding to a different value of the maximum flowrate of the adjustable capacity pump.

In case 1, shown in the graph of Fig. 10, a calibrated orifice is dimensioned corresponding to the measurement of a flowrate of ***10 l/min***, the maximum flowrate of the pump being set to *14 l/min*. **It results:** orifice diameter is ***2.2 mm***, pressure drop is ***10.985 bar***, and ***flow is laminar***, because ***Re = 1606***.

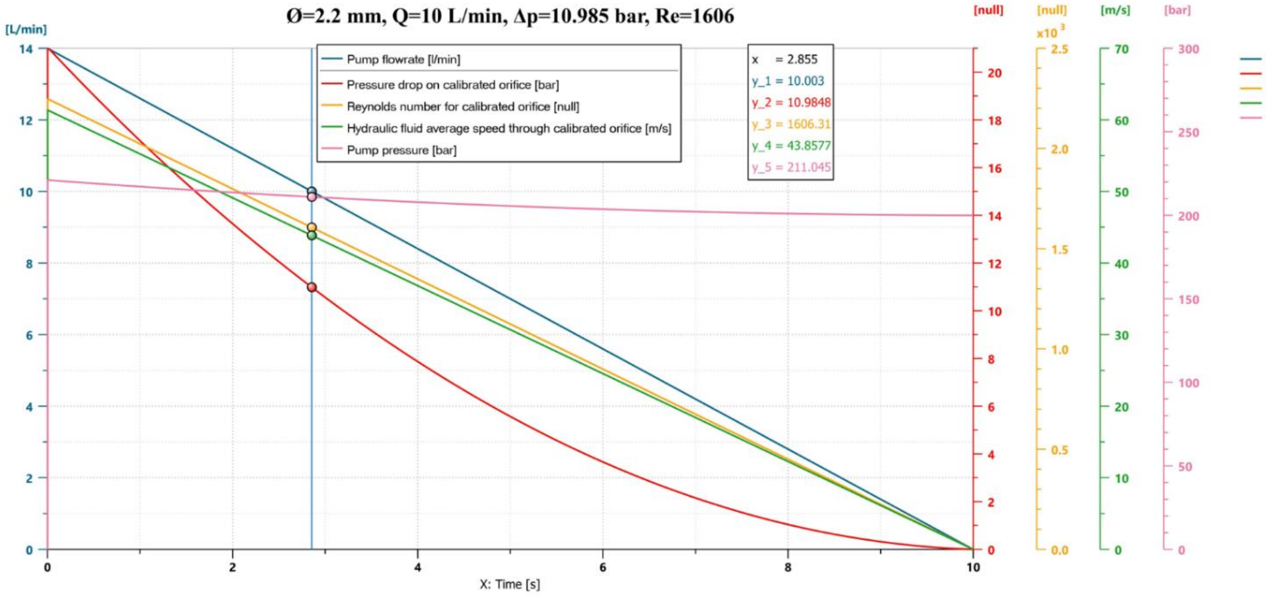

Fig. 10. Optimal dimensioning of the calibrated orifice for measuring a flowrate of 10 l/min

In case 2, shown in the graph of Fig. 11, a calibrated orifice is dimensioned corresponding to the measurement of a flowrate of ***1 l/min***, the maximum flowrate of the pump being set to *2 l/min.* **It results:** orifice diameter is ***0.8 mm,*** pressure drop is ***10.356 bar***, and ***flow is laminar***, because **Re = 442**.

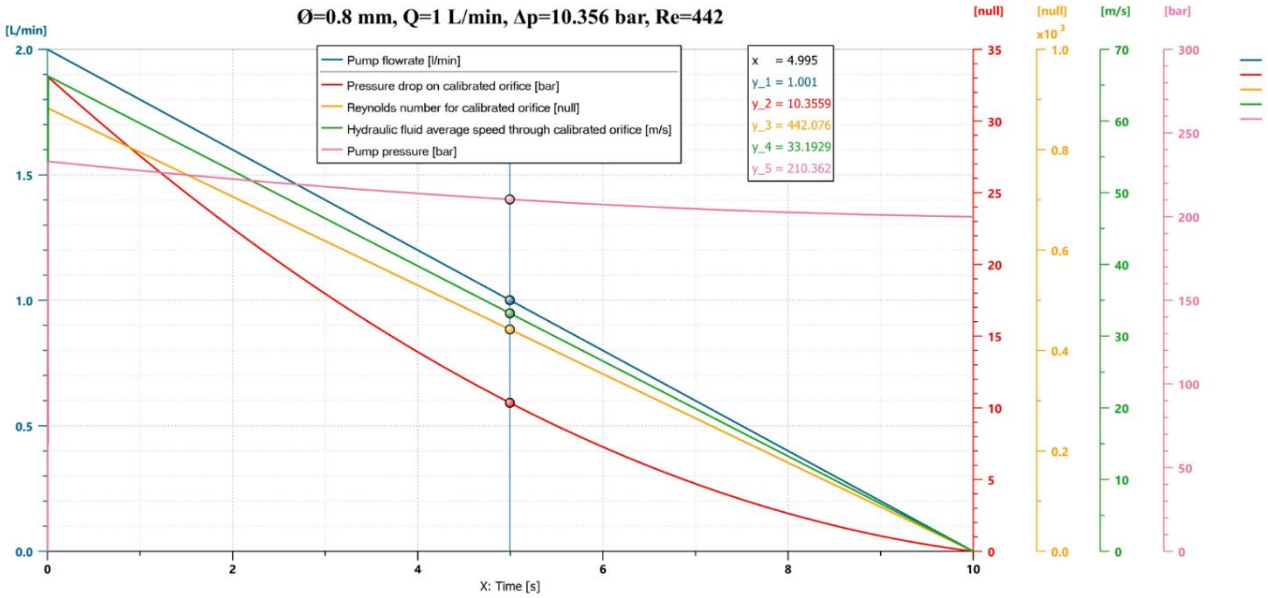

Fig. 11. Optimal dimensioning of the calibrated orifice for measuring a flowrate of 1 l/min

In case 3, shown in the graph of Fig. 12, a calibrated orifice is dimensioned corresponding to the measurement of a flowrate of ***44 l/min***, the maximum flowrate of the pump being set to *50 l/min*. **It results:** orifice diameter is ***5 mm***, pressure drop is ***5.3 bar***, and ***flow is no longer completely laminar***, because the value of the Reynolds number exceeds 2400, namely ***Re = 3110***, although measures have been taken to decrease the velocity of fluid through the orifice by increasing the diameter. However, a pressure drop of less than ***5 bar*** is not acceptable for the flowrate of ***44 l/min***, because with this orifice it is also desired to measure a minimum flowrate of ***10 l/min***, with a pressure drop of approximately ***1.4 bar***.

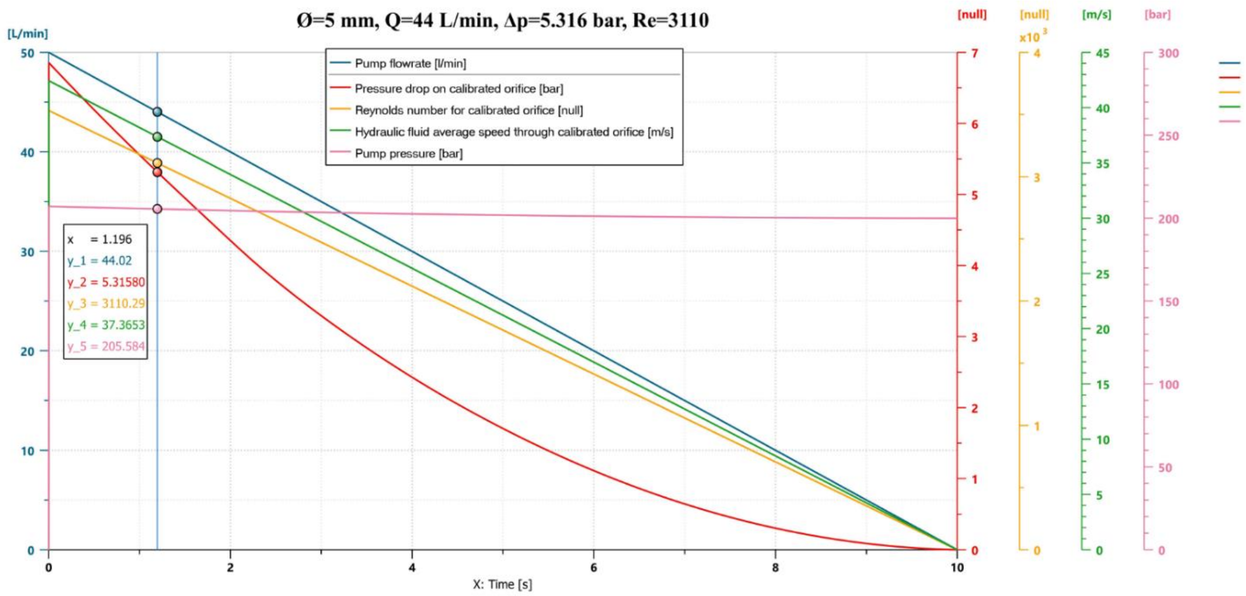

Fig. 12. Optimal dimensioning of the calibrated orifice for measuring a flowrate of 44 l/min

In case 4, shown in the graph of Fig. 13, a calibrated orifice is dimensioned corresponding to the measurement of a flowrate of ***4.4 l/min***, the maximum flowrate of the pump being set to *5 l/min*. **It results:** orifice diameter is ***1.5 mm***, pressure drop is ***11.13 bar***, and ***flow is laminar***, because ***Re = 1306***.

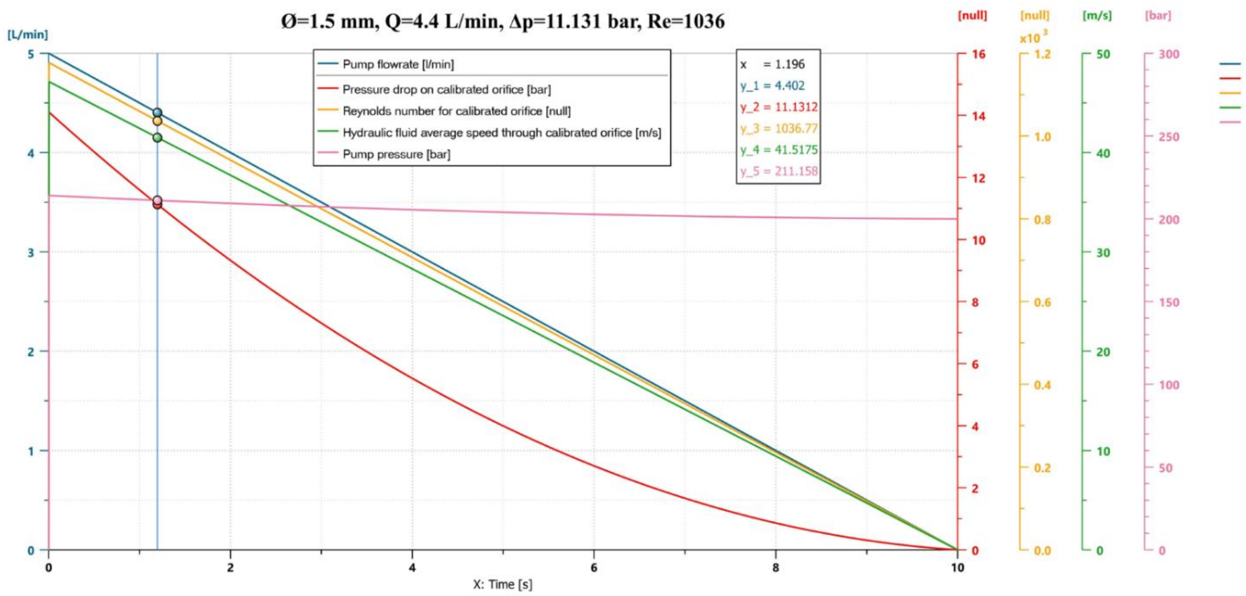

Fig. 13. Optimal dimensioning of the calibrated orifice for measuring a flowrate of 4.4 l/min

Fig. 14 shows the four calibrated orifices with diameters of ***5***, ***2.2***, ***1.5*** and ***0.8*** mm, necessary to measure flowrates in the vicinity of the values of ***44***, ***10***, ***4.4*** and ***1 l/min***. It can be noticed that all the orifices have: ***the same overall dimensions***, so that they can be mounted in the body of the flowrate measuring device; ***the same angle of 120º***, of convergence and divergence, for easy processing; ***different inner diameters***, with usual values.

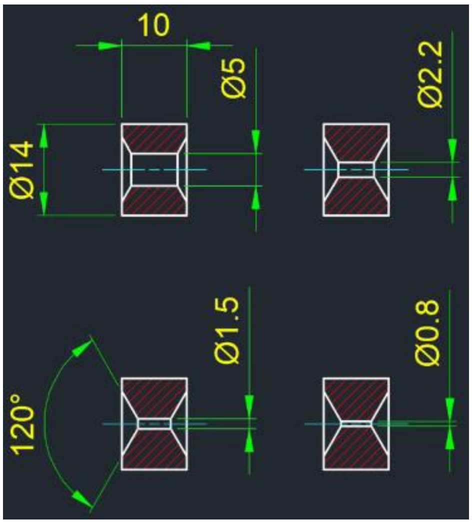

Fig. 14. The four calibrated orifices of the flowrate measuring device

2.3 Designing the flowrate measuring device

The component elements of the pulsating flowrate measuring device are shown in the assembly drawing in Fig. 15.

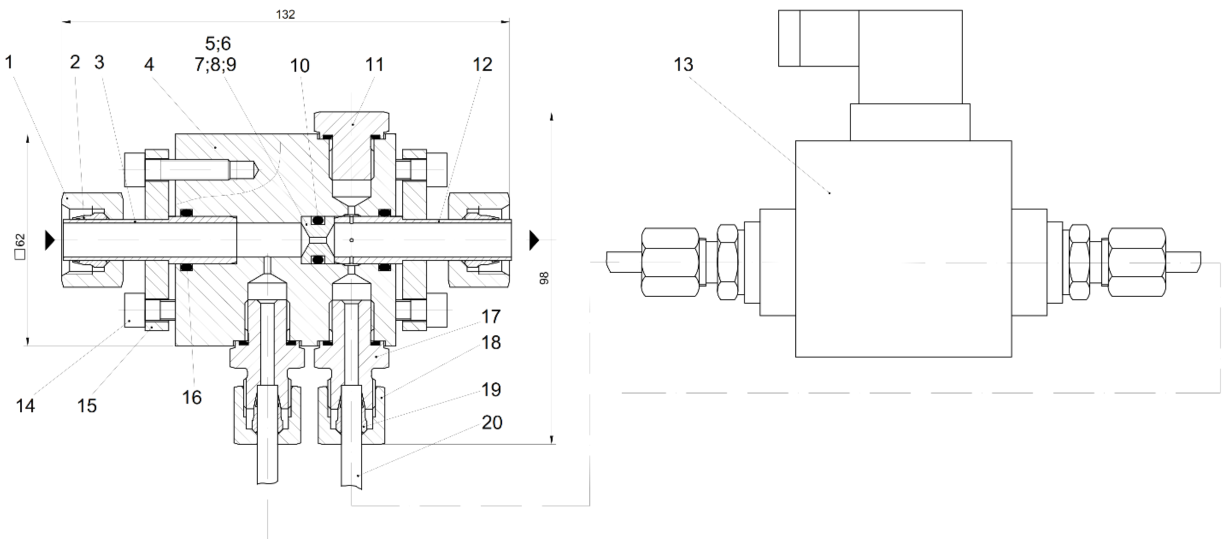

Fig. 15. Pulsating flowrate measuring device; assembly drawing

The pulsating flowrate measuring **device** contains a body, **item no. 4**, in which two pipes with a machined inner surface and an inner diameter of 10 mm are inserted into the central axial area, **item no. 3** and **item no. 12**, upstream and downstream of the calibrated orifice, respectively one of the items no. **5**,**6**,**7**,**8,** or **9**, which are sealed inside the body with one 2.5x9 O-ring each, **item no. 10**, each pipe being fixed to the body with a clamping plate, **item no. 15**, and four M6x25 screws, **item no. 14**.

The two pipes are sealed in the body with one 2.5x14 O-ring each, **item no. 16**, and on the outer end of the body, they have mounted one M20x1.5 union nut, **item no. 1**, and a cutting ring, **item no. 2**, both parts being necessary to connect the flowrate measuring device to one of the measuring circuits mentioned in section 2. The hydraulic fluid flows through the flowrate measuring device from left to right along a path with cylindrical internal geometry, nominal diameter Dn10, which is throttled in the area of the calibrated orifice.
The pressure intake ports connect to the differential pressure transducer, **item no. 13**, by means of four G1/4" threaded connections, **item no. 17**, four M14x1.5 union nuts, **item no. 18**, four cutting rings, **item no. 19** and three meters of 6x1 pipe, **item no. 20**.
Before use, the flowrate measuring device is vented, by loosening the G1/4" threaded plug, **item no. 11**, after which the tightening is done again.
The other calibrated orifices, Fig. 14, namely items no. **8**, **7**, **6,** and **5**, will be mounted in the device when it is intended to measure flowrates around the values of **44**, **10**, **4.4** and **1 l/min**.

2.4 Connecting the flowrate measuring device

The assembly drawing in Fig. 16 shows the way of connecting the pulsating flowrate measuring device to the differential pressure transducer in Fig. 7 and to the stand in Fig. 4.

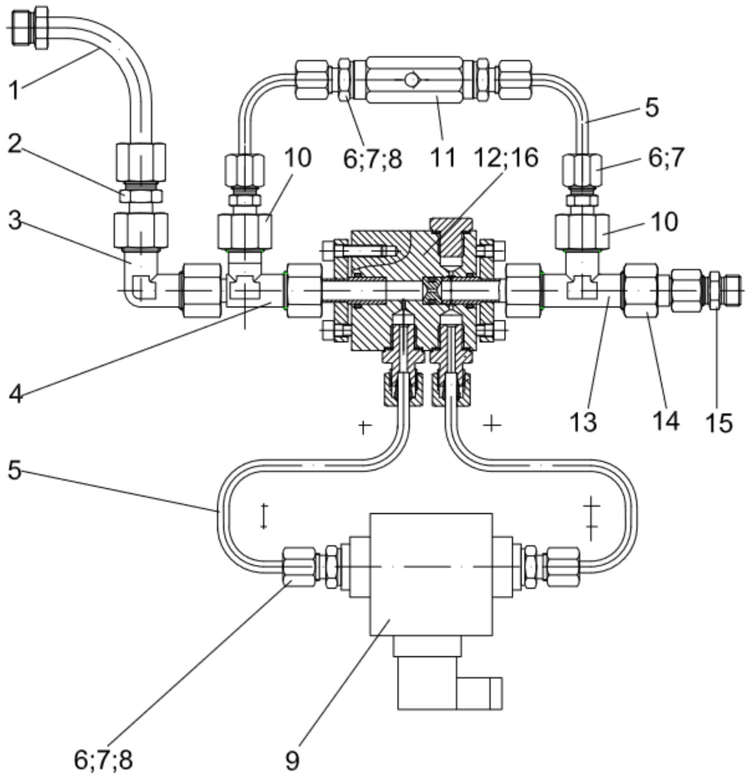

Fig. 16. Pulsating flowrate measuring device; assembly drawing for connection to the stand

The device, **item no. 12**, connects to the **differential pressure transducer**, **item no. 9**, with two 6x1 pipes, **item no. 5**, two union nuts, **item no. 6**, two cutting rings, **item no. 7**, and two G1/4-M14x1.5 threaded connections, **item no. 8**.
The device is connected to the stand in figs. 4 and 5 with a 90^o pipe connection - M18-external thread / M18-internal thread, **item no. 1**, an M16/M16 nipple, **item no. 15**, an L-M20 threaded joint, **item no. 4**, an M20 T-joint, **item no. 13**.
The check valve, **item no. 11**, is mounted with two union nuts, **item no. 6**, two cutting rings, **item no. 7** and two G1/4-M14x1.5 threaded connections, **item no. 8** on a circuit that bypasses the pulsating flowrate measuring device (the device measures a flowrate only if fluid flows through it from left to right).

3. Conclusions

- ***The device is important for measuring flowrates at the output of oscillating hydraulic pressure intensifiers*** (miniboosters), under conditions where the pumping frequency of the oscillating piston is variable, decreasing as the pressure in the hydraulic system increases (fig. 6), and the ***technical documentation*** of these products ***specifies only the maximum flowrate from the secondary of the miniboosters*** (fig. 3 and table 1).
- ***When calibrating the*** flowrate measuring ***device*** the pressure difference measured between the two pressure intake ports will be taken into account, when the nominal diameter ***Dn10*** cylindrical geometry is no longer narrowed down by the calibrated orifice. This measurement will be carried out with the calibrated orifice ***Ø10***, ***item no. 9***, mounted in the flowrate measuring device.
- ***For each of the four calibrated orifices*** in fig. 14, mounted in the pulsating flowrate measuring device, one flow coefficient C_Q will be determined experimentally, as the ***ratio between the flowrate measured with a standard measuring instrument*** *(for example, graduated cylinder + timer)* and ***the flowrate measured with the presented device***. This coefficient is introduced in relation (1), for the experimental, indirect determination of the value of the measured flowrate.
- ***After developing the device***, it will be mounted on the stand in figs. 4-5, and the results of flowrate measurements for the 3 minboosters in table 1, which successively feed the test cylinder, at various loads, will be presented in a future paper.

Acknowledgments

This work was carried out through the Core Program within the National Research Development and Innovation Plan 2022-2027, carried out with the support of the Romanian Ministry of Research, Innovation and Digitalization (MCID), project no. PN 23 05. The research was financially supported by a project funded by MCID through Programme 1 – Development of the national research & development system, Sub-programme 1.2–Institutional performance–Projects financing the R&D&I excellence, Financial Agreement no. 18PFE/30.12.2021.

References

[1] ScanWill Fluid Power ApS. “ScanWill Brochure 2022”. Accessed October 10, 2023. https://scanwill.com/wp-content/uploads/2023/09/ScanWill-Brochure-2022-LowRes.pdf.
[2] Espersen, Christen. “Pressure Boosters in Hydraulic Systems - A Solution Which Is Often Overlooked.” June 23, 2018. Accessed October 10, 2023. https://nanopdf.com/download/pressure-boosters-in-hydraulic-systems_pdf.
[3] The Pioneer Group. “Hydraulic Booster.” Accessed October 10, 2023. https://goptc.jp/minibooster/.
[4] Günaydın, A.C., M. Halkacı, F. Ateş, and H.S. Halkacı. “Experimental Research of the Usability on Double Acting Intensifiers in Hydroforming.” Paper presented at the 2nd International Conference on Mechanical, System and Control Engineering ICMSC 2018, Moscow, Russia, June 21 - 13, 2018. *MATEC Web of Conferences* 220 (2018): 04001. Accessed October 10, 2023. https://www.matec-conferences.org/articles/matecconf/pdf/2018/79/matecconf_icmsc2018_04006.pdf.
[5] Popescu, Teodor-Costinel, Alexandru-Polifron Chiriță, Ana-Maria Carla Popescu, and Alina-Iolanda Popescu. “Use of pumping units equipped with oscillating hydraulic pressure intensifiers for displacement of cylinders with heavy loads over the entire stroke.” *Mining Machines* 40, no. 4 (2022): 238-248.
[6] miniBOOSTER Hydraulics A/S. “HC7.” Accessed October 10, 2023. https://www.minibooster.com/hc7/.
[7] Popescu, Teodor Costinel, Alexandru-Polifron Chiriță, Andrei Vlad, and Constantin Teodoru. *Stand for testing high-pressure pumping systems equipped with miniboosters / Stand pentru testarea sistemelor de pompare la presiuni înalte echipate cu miniboostere*. Patent application No. 00252/ 18.05.2023.
[8] Siemens AG. “Simcenter Amesim software.” Accessed October 10, 2023. https://plm.sw.siemens.com/en-US/simcenter/systems-simulation/amesim/

ISSN 1454 - 8003
Proceedings of 2023 International Conference on Hydraulics and Pneumatics - HERVEX
November 8-10, Băile Govora, Romania

PERFORMANCE EVALUATION OF HYDROKINETIC ROTORS USING CUSTOM MADE ON-SITE TESTING SYSTEM

Rareș-Andrei CHIHAIA[1], Gabriela CÎRCIUMARU[1], Lucia-Andreea EL-LEATHEY[1], Alexandru-Ionel CONSTANTIN[1], Corina BĂBUȚANU[1], Constantin DUMITRU[1]

[1] National Institute for R&D in Electrical Engineering ICPE-CA Bucharest, rares.chihaia@icpe-ca.ro

Abstract: *The paper presents the performance evaluation of two hydrokinetic rotors with geometric similarity using a specially developed on-site testing system. The necessity of this system derives from the need to effectively measure the power output produced by a hydrokinetic turbine during design stage. For an adequate characterisation and performance evaluation, similar models on a progressive scale were used. The increased diameters that can supply significant power require larger models which cannot be tested on testing benches in laboratory conditions. Therefore, testing should be performed on-site in real operating conditions of the river or channel where potential problems might be encountered such as the variation of the water level, turbine anchoring and electrical insulation of the generator and power output cables. In this regard, there was developed a dedicated and portable testing stand able to test hydrokinetic rotors of up to 1 m diameter with a generated effective torque of up to 20 Nm. The testing system was designed so that the electronic and electric components are placed outside the water and requires low power supply that can be provided from batteries when used in remote areas. The system operation only requires a laptop, a DC current source for the electromagnetic brake and a battery assembly. The system can achieve measurement of characteristic parameters such as power, mechanical torque or power coefficient for hydrokinetic rotors. The first measuring campaign focused on the performance evaluation of two hydrokinetic rotors: a small one with a diameter of 200 mm surrounded by a diffuser and a larger one with a 700 mm diameter without shroud on. Two different sites with increased water velocity were assessed. The torque and rotational speed parameters were registered using a torque transducer linked to a compatible software application, which allows data acquisition, real time monitoring and further analysis of the results.*

Keywords: *Hydrokinetic turbine, on-site testing, power output, data acquisition and analysis.*

1. Introduction

Hydrokinetic turbines use the kinetic energy of the water for producing ecological electricity without impacting the surrounding environment, with minimal influence on the river natural flow conditions without using a dam or diversion head works. The kinetic energy is available on most rivers although the power density represents an important obstacle for large-scale development. In contrast to conventional water turbines which operate based on a certain head and flow, the hydrokinetic turbines operate with reduced efficiency based on the similar principle as wind turbines. Thus, the maximum power coefficient (C_p) is usually below 0.45 and the only way to increase the power extracted is to increase the water velocity or to provide a shroud or diffuser around the rotor. Thus, the flow is concentrated from a larger surface which locally increases the velocity. The design of the rotor blades is a very complex process due to the fact that the performance of these turbines depends on various parameters like number of blades, tip speed ratio, air foil type, blade pitch, chord length and twist angle along the blade. Specific design methods are required in order to address certain issues related to performance, operational optimization, feasibility and environmental impact [1]. Among the advantages of hydrokinetic turbines, there is worth mentioning that these are easy to install, their operation being simple, while the maintenance costs are affordable.
The most convenient method to study them is to use small scale models driven in closed circuit testing stand or using towing tanks. The limitation of this approach is that larger rotors cannot be tested due to their size limitation and the proximity to the testing channel walls which determines the so-called blockage effect.
If the blades rotate near the channel walls, then the turbine performance in a partially blocked flow needs correction in order to reflect the operation in unbounded free stream conditions [2, 3].

Therefore, on-site testing can represent a solution at hand for performing rotors evaluation while ensuring constant water depth and velocity during measurements. The research aimed the on-site evaluation of the hydrokinetic turbines performance by using an improved rotor design which has been previously tested [4, 5] in order to identify if the power output is according to the results of the reduced scale model tested in a closed channel circuit.

Several papers and studies addressed various aspects regarding the operation of hydrokinetic turbines suitable to tidal currents [6] or to high velocities rivers [7]. Although these studies have addressed the characteristic determination of the hydraulic parameters, providing some important knowledge on related fluid mechanics phenomena, the information is not sufficient for a quantitative characterization and power estimations for such water turbines.

The issue of adapting and using the characteristics of experimental rotor models on a different scale was also addressed [2]. According to some literature recommendations, it is possible to adapt the power coefficient vs. tip speed ratio (TSR) curve in order to achieve correct power estimations. In some cases, the scale difference exceeds 1:30. Thereby, it is clear that an assessment is difficult to achieve.

Computational design optimization tools such as the Rotor Optimization Algorithm tested by Sale et al. [8] may be used for hydrokinetic turbine designs. The algorithm includes 15 defined variables in 5 control points, namely the blade hub, blade tip, and even spaced points in between. Afterwards, a Genetic Algorithm (GA) uses constraints and dependencies in order to determine the optimal shape of the blades. Optimizing a rotor for maximum hydrodynamic efficiency does not necessarily result in a turbine generating the highest annual energy production, but is rather related to maximizing the turbine efficiency (increasing approach angle/velocity) [9]. A possible reason for a low power coefficient of several solutions is represented by massive flow separation on the hub surface due to high adverse pressure gradient inside the diffuser, resulting on low mass flow capture and, hence, poor performance [10]. Riglin et. al [11] tested a hydrokinetic turbine prototype for river applications that was built for experimental testing in the circulating water channel at the Naval Surface Warfare Center, US. The prototype was designed based on numerous blade characterization and optimization analyses conducted using computational fluid dynamics (CFD) simulations. Testing was conducted for channel flow speeds ranging from 1.0 m/s to 1.7 m/s. The shrouded turbine with a tip diameter of 0.68 m, 3 blades and diffuser area ratio of 1.31 tested at 1.5m/s had a peak power coefficient of 0.37 at a tip speed ratio of 2.50.

Many of the applications developed for improving the operation of hydrokinetic turbines [12,13] have represented short-term testing installations. Thus, the evaluation of long-term functioning of these units is difficult to predict, although these short-term applications do provide insights on attainable power outputs. The research aims to continuously improve a certain rotor design by collecting more specific data regarding its operation in order to draw a more accurate prediction curve. The experimental data can be used for the achievement of correlations between rotor size, water velocity and mechanical power output and can lead to the efficiency estimation of other rotor designs just by scale model laboratory testing. If a large rotor is envisaged to be tested, the on-site system is another useful tool suitable to characterize a rotor design from model to large scale. Moreover, by using the data obtained in real operating conditions, a specific electric generator with a certain torque and rotational speed can be developed given that these turbines require custom made electric generators for increased efficiency.

2. Development of the hydrokinetic rotors and on-site testing system

The design of the hydrokinetic rotors used for testing was developed in other previous projects regarding the optimization of hydrokinetic turbines [14]. The optimum chord length calculation was performed for each section along the rotor blade and the most appropriate airfoil type was chosen. Simulations performed with Qblade software revealed the effect of the chord length for each section. The software generates specific curves when one of the input parameters varies in the given range (attack angle, velocity, rotational speed). It has been shown that changes in chord length along the blades and variation of the twist angle have a significant impact regarding the power output. The blade design and airfoil type are presented in Figure 1.

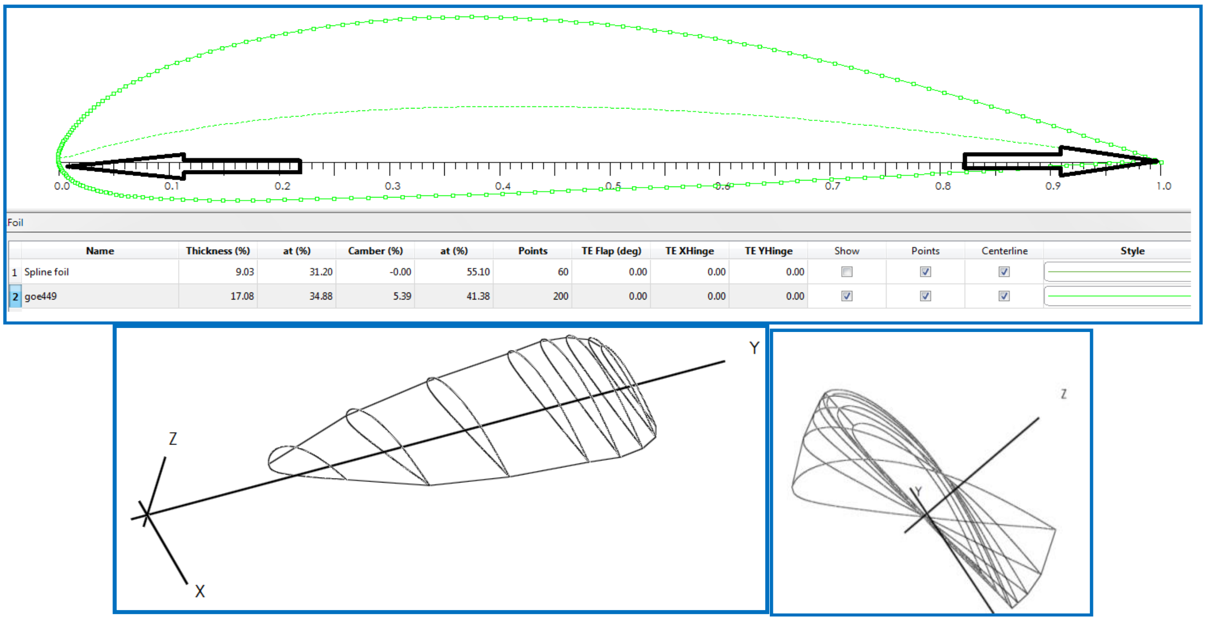

Fig. 1. Improvements of the rotor blades structure achieved for the determination of the optimal geometry [8]

Based on the calculation methods suggested in [15] as well as the results obtained by successive simulations, the optimum rotor geometry allowing the increase of the conversion efficiency was achieved. A first rotor model with a diameter of 200 mm was built using 3D printer and tested in a closed-circuit testing bench designed for axial hydraulic turbines [4]. The experimental testing of the model showed that the best results were obtained for a pitch angle of 40° when the supplied power reaches a maximum value of 4.2 W at a water velocity of 0.9 m/s. In the following stage, the design was improved by printing the rotor model in a single part with rounded hub and fixed blade position [16]. The rotor design presented in Figure 2 has four twisted blades with GOE 449 profile and variable chord length.

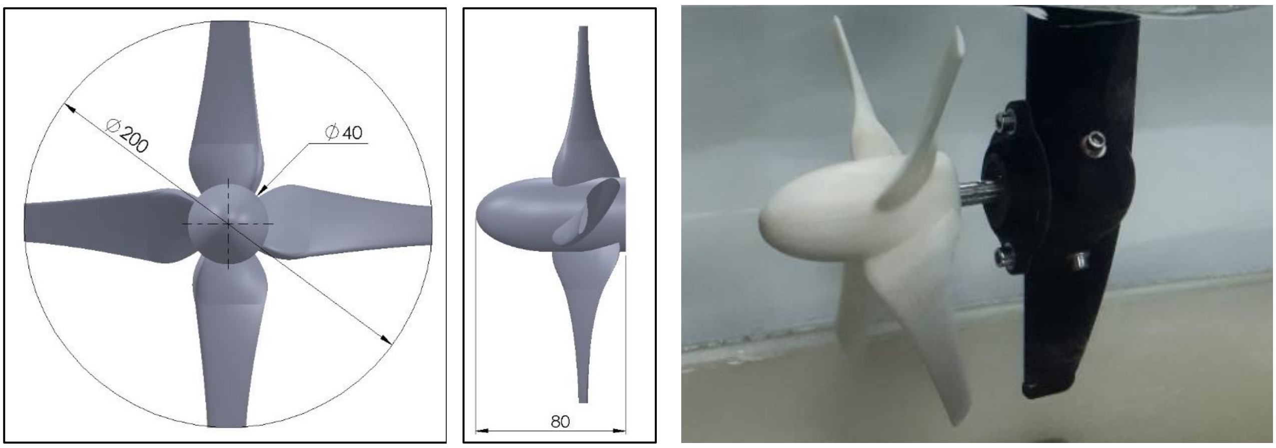

Fig. 2. 200 mm hydrokinetic rotor – 3D view and printed object prepared for testing [10]

The same design was also used for the second rotor which was manufactured at a larger scale respecting the geometric similarity. This was developed by several parts joined together by screws. The resulting diameter of the rotor was 700 mm. The rotor comprises four blades including their support and the central hub as presented in Figure 3. The geometric similarity will provide conditions for comparison between progressive scale rotors.

Fig. 3. 3D printed 700 mm rotor

For on-site testing of the rotors and better understanding of their behaviour in real operating conditions, a special system was developed. It is based on mechanical transmission with bevel gear and positioning system on boat, pontoon or bridge. The movement of the rotor is transmitted through an inner shaft at the top of the installation, where a torque and speed measuring system is placed within a specially constructed enclosure. The enclosure comprises an assembly of elastic couplings, torque transducer and electromagnetic brake, capable of performing torque measurements up to 20 Nm and speeds up to 4000 rpm. It has a simple and robust design in order to ensure a quick assembly and facilitate easy maintenance and further adjustments. The system shown schematically in Figure 4 is modular and allows the transducer or brake to be replaced or inspected without significant operations.

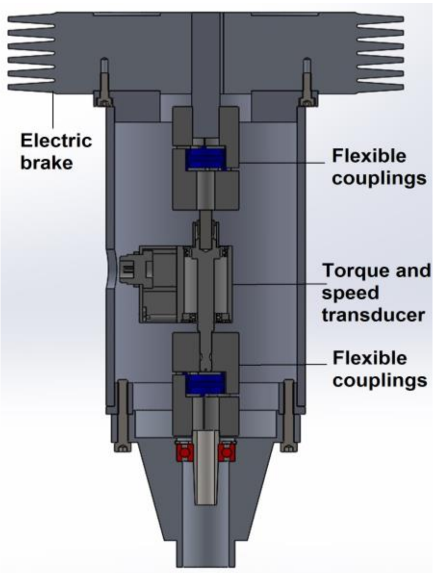

Fig. 4. Torque and speed measurement unit

Since field testing was considered, the components were chosen in order to be easily transported and installed, with low power consumption provided by batteries without grid connection. Therefore, a torque transducer was used with data transmission via USB port, powered at 5 V, with a required maximum current of 500 mA. A dedicated USB amplified extension cable with a length of 20 m provides the connection to a laptop running the data acquisition software for recording the measured values. The DR-3003 transducer model, manufactured by Lorenz Messtehnik Gmbh is characterized by an accuracy class of 0.1% of the full scale. The sensor is linked through VS3 interface ensuring that analog sensor signals will be digitized with up to 16-bit resolution. By the measuring rate of 5000 measurements/s per measuring channel, high-dynamic measurements can be achieved. Another critical component of the testing system is the electromagnetic brake which ensures the load of the turbine similar to an electric generator. The advantage over a conventional electric generator is that torque and speed values can vary significantly, the power adjustment being determined by the gradual loading of the brake until the rotor stops. An electromagnetic brake with a maximum torque of 35 Nm, FRAT 350 model, produced by Mobac Gmbh, was chosen. The final enclosure of torque and speed measurement unit is presented in Figure 5a. Figure 5b indicates the content of the enclosure which consists of torque transducer and related flexible couplings.

Fig. 5a. Enclosure of the torque and speed measurement unit

Fig. 5b. Torque transducer and flexible couplings

The torque and speed measurement unit was assembled with a mechanical transmission of the testing installation fitted with bevel gear at the end which transmits the movement from the immersed horizontal rotor to vertical plane, resulting the assembly in Figure 6. A fastening system is provided in the upper part of the assembly. It facilitates the fixed grip to the pontoon or bridge.

Fig. 6. On-site testing system with a 700 mm rotor ready for testing

The mechanical transmission connects the hydrokinetic turbine to the test system and has a length of 720 mm from the rotor axis to the torque and speed measuring system, allowing to test hydrokinetic turbines with diameters up to 1 m. The use of this system generates mechanical losses, which cannot be determined by using the torque transducer and have to be determined separately. Therefore, the torque loss due to friction caused by the bearings was previously rated at 0.24 Nm. This value will be subtracted from the result of the useful torque measurements at the turbine shaft because it cannot be determined directly with the torque transducer, placed behind the transmission chain. A stiffening rod is added to the assembly to avoid bending the drive shaft when large rotors are tested in high velocity water.

3. On-site hydrokinetic rotors testing

Testing was performed in two sites with water velocities above 1 m/s. The 700 mm rotor was tested in the tailrace channel of Mihăilești hydroelectric plant, Giurgiu County, Romania. In order to achieve the experiments, a pontoon was designed and built in the frame of a previous project related to low head hydrokinetic turbines suitable to natural or artificial water courses. The pontoon shown in Figure 7 was positioned in the middle of the channel, being anchored on both banks. At the upstream side of the pontoon, the testing system was deployed using a retractable support. The median water velocity can reach 1.6 m/s in the channel, when all the water turbines of the hydroelectric power plant operate at full potential. Testing was performed at 1.45 m/s at a depth measured from the tip of the upper blade of around 50 mm. Experimental testing imaging of the 700 mm rotor are presented in Figure 7.

Fig. 7. 700 mm rotor testing

Figure 7 shows the system in upright position aligned and prepared for testing. Also, there are indicated the downward position, when the rotor is submerged in water as well as the devices and equipment used for operating the system. Several trials were performed and the resulted data was stored for further analysis and interpretation. During the tests, the water turbines of the hydroelectric power plants were set to operate at maximum capacity in order to maximize the water flow rate in the tailrace channel so to obtain a velocity of 1.45 m/s in the immersion area of the rotor. The water velocity was measured by using SonTek 3D Doppler Velocimeter equipment - Micro ADV (Acoustic Doppler Velocimeter) which operates in the range of 0.001 to 4.5 m/s.
The 250 mm hydrokinetic turbine was tested on a channel through which the excess water from the Roșu Treatment Plant reaches Morii Lake located in Bucharest, Romania.

Through this channel, the water from Argeș river supplements the Morii Lake volume.
The location was chosen considering the channel has significant water velocity and is provided with a pedestrian bridge which allows the immersion of the testing rig. During experimenting, a water current meter was also immersed to measure the median water velocity. To increase the rotor speed as well as the output power, a hydrodynamic profiled diffuser was mounted. This shroud facilitates the power increase by creating a high pressure area inside. A divergent diffuser with an output diameter of 250 mm was used. Measurements images are shown in Figure 8.

Fig. 8. Experimental testing of the 250 mm shrouded rotor

During tests, shaft torque and rotational speed values were recorded by progressive loading of the electromagnetic brake powered by an adjustable DC source. The source was powered by a 1kVA inverter connected to a 12V battery able to supply at least 3 hours of continuous measurements. The data was saved by the torque transducer application in csv file format and exported subsequently for further processing.

4. Results and interpretations

Given the registered torque and rotational speed values *n*, other specific parameters were calculated, as follows: the mechanical power available at the turbine shaft - *P*, the power coefficient - C_p, tip speed ratio – *TSR* representing the ratio between the peripheral speed and the velocity of the considered fluid. These determined values lead to the characteristic curves $C_p = f(TSR)$ and $P=f(n)$ can be drawn. The power output *P* can be calculated by using the formula:

$$P = M\omega \tag{1}$$

where *M* – is the torque, and *ω* the angular speed, which can be determined as:

$$\omega = \pi n/30 \tag{2}$$

In order to determine the $C_p = f\ (TSR)$ curve, it is necessary to determine TSR by the formula:

$$TSR = v_{per.}/v \tag{3}$$

where $v_{per.}$ represents the rotational speed at the periphery of the rotor and *v* the upstream median water velocity, which can be determined as follows:

$$v_{per.} = \omega R \tag{4}$$

Where *R* is the radius of the tested rotor.

The power coefficient represents the ratio between the determined mechanical power P and the theoretical power $P_{th.}$ which is given by the following relation:

$$P_{th.} = 1/2 \cdot \rho A v^3 \tag{5}$$

where A is the equivalent area of the rotor and ρ the water density.

In the case of the 700 mm diameter rotor, the characteristic curves determined at 1.45 m/s velocity are shown below in Figure 9 – Power curve and Figure 10 – Power coefficient curve.

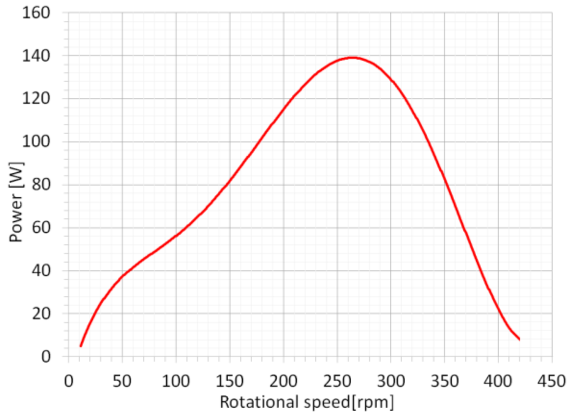

Fig. 9. Power curve for the 700 mm rotor

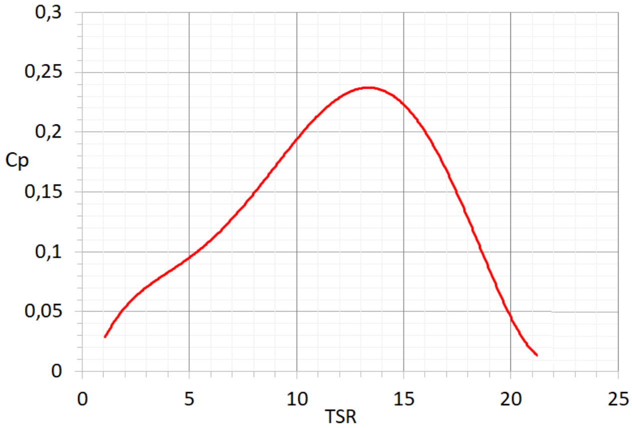

Fig. 10. Power coefficient curve for the 700 mm rotor

For the 200 mm rotor, the characteristic curves determined at 1.42 m/s velocity are shown in Figure 11 – Power curve and in Figure 12 – Power coefficient curve.

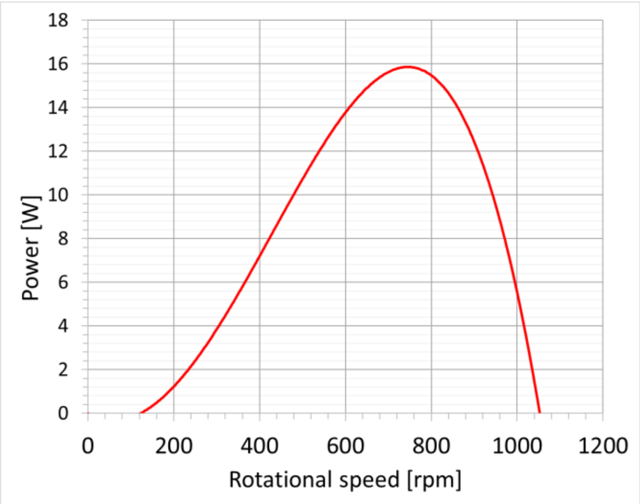

Fig. 11. Power curve for the 200 mm rotor with shroud

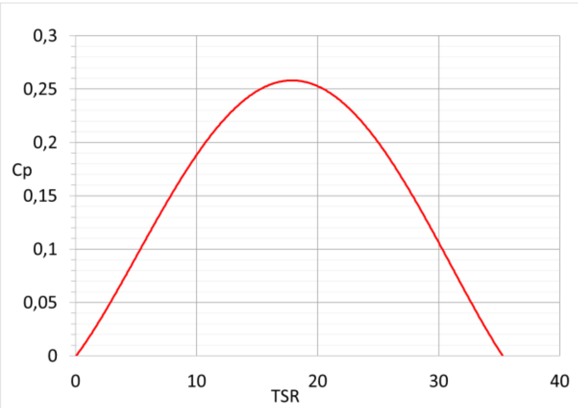

Fig. 12. Power coefficient curve for the 200 mm rotor with shroud

As depicted in Figure 12, the increased value of the power coefficient C_p is obtained in the case of a lower TSR value given the increased size of the rotor. Larger rotors determine reduced rotational speeds and according to relation (3) the TSR reduces accordingly. The power coefficient for the both rotors was approximately 0.25 while the shrouded rotor is characterized by slightly increased values. Prediction curve could not be drawn given that one of the rotors was tested with a diffuser which locally increased the rotational speed of the rotor.

The diffuser was used in the scope of increasing the starting torque of the 200 mm rotor which is difficult to drive due to reduced size and residual torque of the brake and the bevel gear. Thereby, it improves the power output of the rotor, but reduces the operating range with increased efficiency as can be seen in Figure 11. Thus, the diffuser influences the registered parameters compared to bare rotor. A comparison at different scale is possible only if the studied rotors are the same type, either with or without shroud. The registered parameters using the installation allow to further design an electrical generator suitable to be used in the determined range of rotational speed and torque. The evaluation of the rotor specific parameters allows the determination of the generator's efficiency and its related devices like controllers and inverters. Nevertheless, the on-site testing system proved useful for the evaluation of a considered rotor with or without diffuser in terms of rotational speed and generated power.

5. Conclusions

The paper presents a tool which is useful for the continuous development of hydrokinetic rotors by identifying the power produced at certain rotational speed values. The determined parameters are critical for designing an electric generator, another important component of the turbine. In this regard, a dedicated and portable testing stand was developed which was able to test two similar hydrokinetic rotors at different scale: a small one with 200 mm diameter surrounded by a diffuser and a larger one with 700 mm diameter without shroud. The two impellers were tested on two different sites with available increased water velocity. The developed system can achieve measurement of characteristic parameters such as power, mechanical torque or power coefficient for hydrokinetic rotors. The torque and rotational speed parameters were registered using a torque transducer linked to a compatible software application, which allows data acquisition, real time monitoring and further analysis of the results. Testing procedures showed that the on-site testing system can achieve the performance evaluation in terms of torque, power and rotational speed of rotors tested in channels with water velocity around 1.5 m/s. Future work considers testing different rotor designs and identification of other suitable rivers or channel where hydrokinetic turbines can be installed successfully.

Acknowledgments

This work was supported by the Romanian Ministry of Education, Research and Digitalization by Nucleu contract no. 42N/2023, project no. PN 23140101/2023 and project number 25PFE/30.12.2021 – Increasing R-D-I capacity for electrical engineering-specific materials and equipment with reference to electromobility and "green" technologies within PNCDI III, Programme 1.

References

[1] Cîrciumaru, Gabriela, and Rareș-Andrei Chihaia. *Improving the energy conversion of wind and hydrokinetic turbines by experimental analysis on scale models*. Rousse, Angel Kanchev University Publishing House, 2021, ISBN 978-619-7546-49-1.
[2] Bahaj, A.S., A.F. Molland, J.R. Chaplin, and W.M.J. Batten. "Power and thrust measurements of marine current turbines under various hydrodynamic flow conditions in a cavitation tunnel and a towing tank." *Renewable Energy* 32, no. 3 (2007): 407-426.
[3] Shahsavarifard, M., E.L. Bibeau, and V. Chatoorgoon. "Effect of shroud on the performance of horizontal axis hydrokinetic turbines." *Ocean Engineering* 96 (2015): 215-225.
[4] Chihaia, Rareș Andrei, Florentina Bunea, Gabriela Oprina, and Lucia-Andreea El-Leathey. "Power Prediction Method Applicable to Horizontal Axis Hydrokinetic Turbines." Paper presented at IEEE 2017 International Conference on Energy and Environment (CIEM), Bucharest, Romania, October 19-20, 2017.
[5] Chihaia, Rareș-Andrei, Lucia-Andreea El-Leathey, Gabriela Cîrciumaru, and Nicolae Tănase. "Increasing the Energy Conversion Efficiency for Shrouded Hydrokinetic Turbines Using Experimental Analysis on a Scale Model." Paper presented at EENVIRO 2018 Conference - Sustainable Solutions for Energy and Environment, Cluj-Napoca, Romania, October 9-13, 2018.

[6] van Elsa, Rudi Henri, and Antonio Cesar Pinho. “The Brazilian experience with hydrokinetic turbines.” Paper presented at the 7th International Conference on Applied Energy – ICAE2015 – Agriculture in an interconnected world, Milan, Italy, August 9-14, 2015.

[7] Trudeau, Matthew G. *Structural and hydrodynamic design optimization enhancements with application to marine hydrokinetic turbine blades*. Master's Thesis. The Pennsylvania State University, 2011.

[8] Sale, D., J. Jonkman, and W. Musial. “Hydrodynamic optimization method and design code for stall-regulated hydrokinetic turbine rotors.” Paper presented at the ASME 28th International Conference on Ocean, Offshore, and Arctic Engineering, Honolulu, Hawaii, May 31 – June 5, 2009.

[9] Niebuhr, C.M., M. van Dijk, V.S. Neary, and J.N. Bhagwan. “A review of hydrokinetic turbines and enhancement techniques for canal installations: Technology, applicability and potential.” *Renewable and Sustainable Energy Reviews* 113 (2019): 109240.

[10] Rezek, Thiago J., Ramiro G.R. Camacho, and Nelson Manzanares-Filho. “A novel methodology for the design of diffuser-augmented hydrokinetic rotors.” *Renewable Energy* 210 (2023): 524-539.

[11] Riglin, Jacob, Fred Carter, Nick Oblas, W. Chris Schleicher, Cosan Daskiran, and Alparslan Oztekin. “Experimental and numerical characterization of a full-scale portable hydrokinetic turbine prototype for river applications.” *Renewable Energy* 99 (2016): 772-783.

[12] Anyi, M. *Water current energy for remote community: design and testing of a clogfree horizontal axis hydrokinetic turbine system*. PhD Thesis. University of South Australia, 2013.

[13] Bachant, P., M. Wosnik, B. Gunawan, and V.S. Neary. “Experimental study of a reference model vertical-axis cross-flow turbine.” *PLoS ONE* 11, no. 9 (2016): e0163799.

[14] Chihaia, Rareș-Andrei, Gabriela Oprina, Sergiu Nicolaie, Andreea El-Leathey, Corina Băbuțanu, and Adrian Nedelcu. “Assessing the blade chord length influence on the efficiency of a horizontal axis hydrokinetic turbine.” Paper prestented at the 2016 International Conference on Hydraulics and Pneumatics HERVEX, Baile Govora, Romania, November 9-11, 2016.

[15] O’Doherty, T., A. Mason-Jones, D. Doherty, C. Byrne, I. Owen, and Y. Wang. “Experimental and computational analysis of a model horizontal axis tidal turbine.” Paper presented at the 8th European Wave and Tidal Energy Conference EWTEC, Uppsala, Sweden, September 7-10, 2009.

[16] Chihaia, R.-A., G. Cîrciumaru, T. Nicolae, A. Voina, L.-A. El-Leathey, and C. Dumitru. "Portable on-site testing system for hydrokinetic turbines." Paper presented at 2022 8th International Conference on Energy Efficiency and Agricultural Engineering (EE&AE), Ruse, Bulgaria, June 30 – July 2, 2022.

ISSN 1454 - 8003
Proceedings of 2023 International Conference on Hydraulics and Pneumatics - HERVEX
November 8-10, Băile Govora, Romania

THE IMPORTANCE OF MAINTENANCE IN HYDRAULIC DRIVE SYSTEMS FOR MICRO HYDROPOWER PLANTS: A COMPARATIVE ANALYSIS

Daniel-Vasile BANYAI[1]

[1] Technical University of Cluj-Napoca, Daniel.Banyai@termo.utcluj.ro

Abstract: *This comparative study aims to thoroughly explore the impact of maintenance on the energy efficiency of micro hydropower plants and to analyse maintenance techniques and practices that contribute to the optimal operation of hydraulic drive systems. To achieve this goal, three specific cases were examined. By collecting and analysing empirical data, this study provides a comprehensive overview of how proper maintenance can influence the performance and durability of micro hydropower plants.*

Keywords: *Small hydropower plant, maintenance, fluid power actuation*

1. Introduction

Micro hydropower plants are an integral part of the renewable energy landscape. They play a pivotal role in providing clean and sustainable electricity to communities, especially in regions with access to flowing water sources such as rivers, streams, or even small waterfalls. Unlike large-scale hydropower plants that require massive dams and reservoirs, micro hydropower plants are characterized by their compact size and minimal environmental impact. They offer an environmentally friendly solution for harnessing hydropower without causing significant disruption to local ecosystems.
For water diversion, the river water level has to be raised by a barrier, the weir (1). The water is diverted at the intake (2) and conveyed by the channel (3) along the landscape´s contour lines. The spillways (4) protect against damage from excessive water flow.

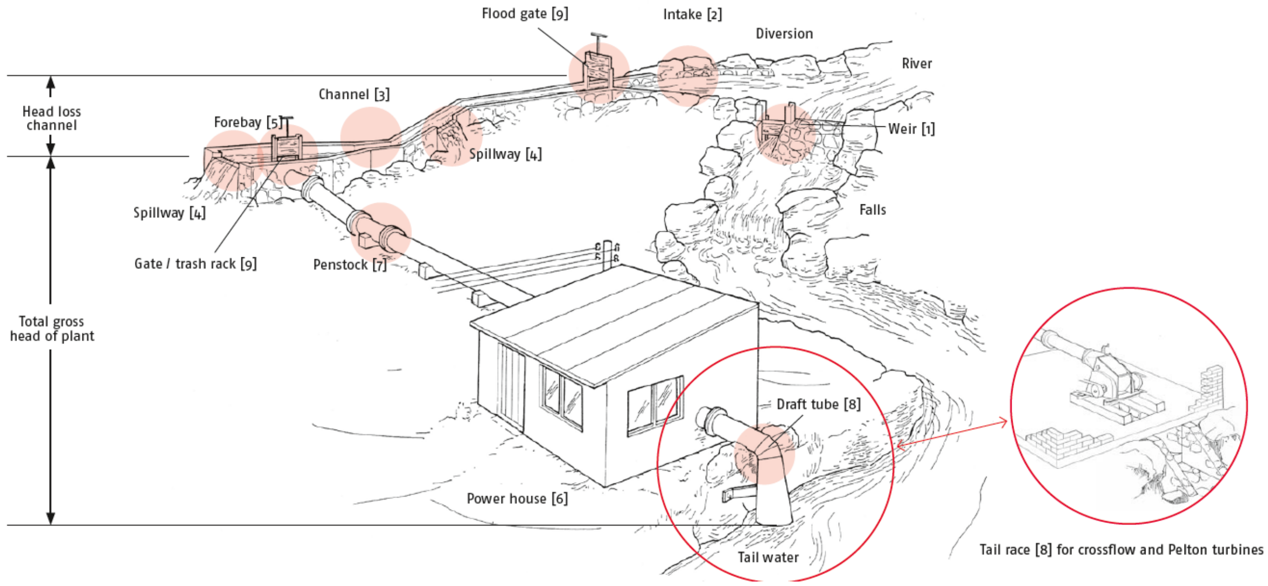

Fig. 1. Components of a small-scale hydropower plant [1]

Water is slowed down and collected in the forebay (5), from where it enters into the penstock (7), the pressure pipe conveys the water to the power house (6) where, the turbine, responsible for converting the energy of flowing water into mechanical energy, the generator that transforms the

mechanical energy into electrical energy and the control system, used to regulate the flow of water and adjust the turbine's speed, are installed. The water is discharged via the draft tube (8) or a tail race channel in case of crossflow or Pelton turbines. [1]
Typically, these systems employ hydraulic turbines, such as Pelton, Francis, or Banki turbines, to efficiently harness the energy of the flowing water. These turbines are equipped with control mechanisms and hydraulic actuators that adjust the flow of water based on the electricity demand or other external factors. Usually, a Pelton turbine with a power below 2 MW is equipped with four or six injectors, for speed regulation, a deflector mechanism, for breaking the turbine, and a butterfly valve for completely shutting off the turbine supply.

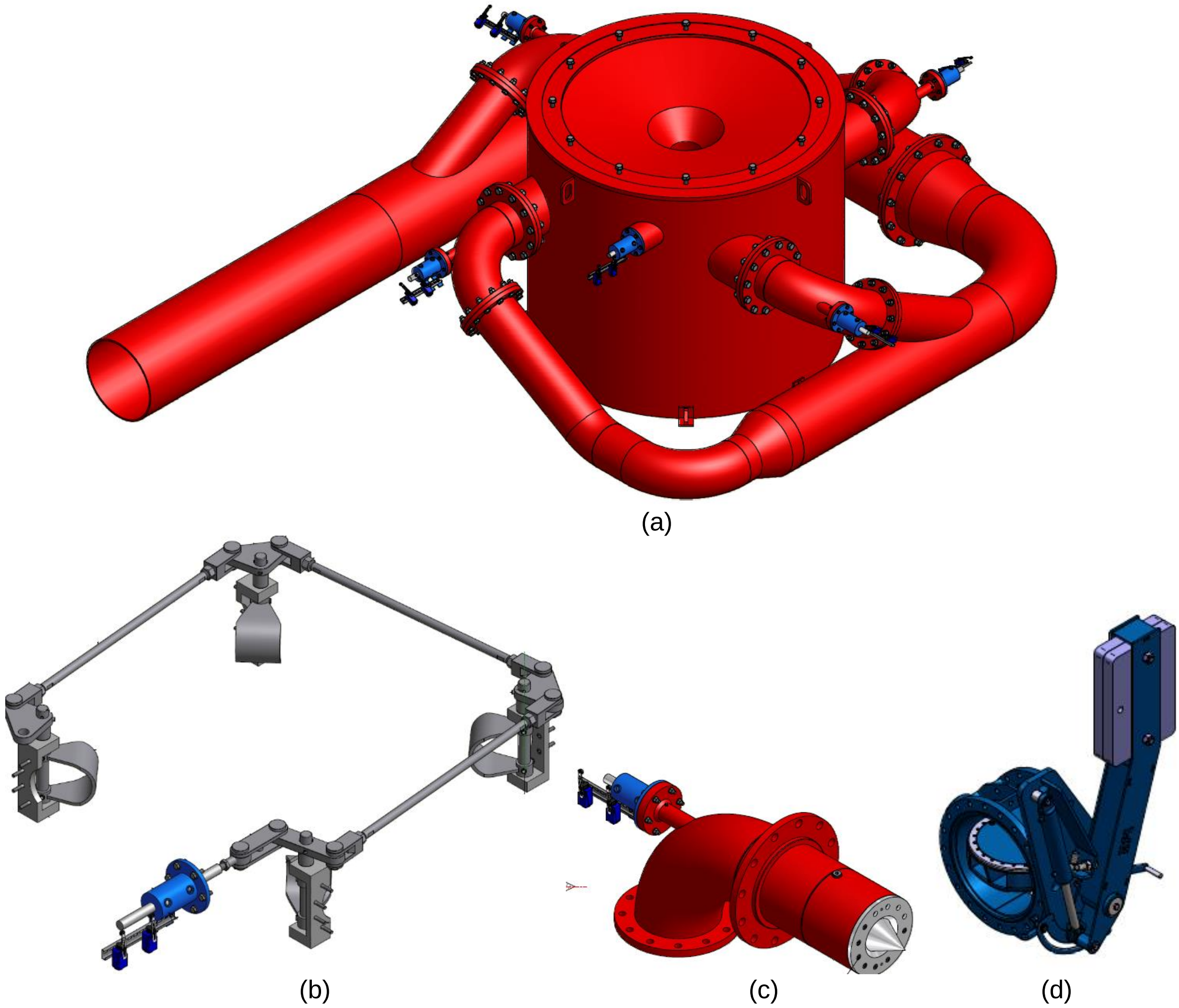

Fig. 2. Low power Pelton turbine < 2 MW
(a) the turbine casing connected to the supply pipe (in blue the hydraulic cylinders). (b) deflector mechanism with hydraulic cylinder. (c) injector for adjusting the turbine speed. (d) butterfly valve with hydraulic cylinder and counterweight.

The hydraulic drive system is a critical component of micro hydropower plants, as it ensures the efficient and precise regulation of turbine performance, which ideally should work without interruptions. In these systems, fluid power is used to control the flow of water to the turbine, thereby managing its rotational speed and, consequently, the electrical output.
The fluid power drive system comprises various key components, an accompanying schematic representation is show in figure 3.

Gear pumps are responsible for drawing in and pressurizing hydraulic fluid.
The pressure relief valve ensures that the hydraulic system maintains safe pressure levels by diverting excess fluid back into the reservoir.
The bladder accumulator, filled with nitrogen, acts as a storage and pressure maintenance device for the hydraulic fluid.
The manifold block with distributors is responsible for directing hydraulic fluid to various components.
Hoses serve as conduits for hydraulic fluid to flow between different parts of the system.
Non-Return Valves prevent backflow of hydraulic fluid, ensuring the system functions as intended.
Hydraulic cylinders are used to convert hydraulic energy into mechanical motion, used for control and actuation purposes of the butterfly valve, turbine injectors and deflector mechanism.
Filters are critical components that remove contaminants and particles from the hydraulic fluid, ensuring the system remains clean and free from debris that can cause damage or reduce efficiency.
The ability to finely tune the hydraulic drive system plays a crucial role in the overall efficiency and productivity of the microhydropower plant. By maintaining and optimizing this system through proper maintenance practices, operators can ensure a consistent and reliable energy supply, ultimately contributing to the sustainable generation of clean electricity. [2]
Understanding these components and their interactions, is crucial to grasp the intricate role that the hydraulic drive system plays in the overall efficiency and operation of microhydropower plants.

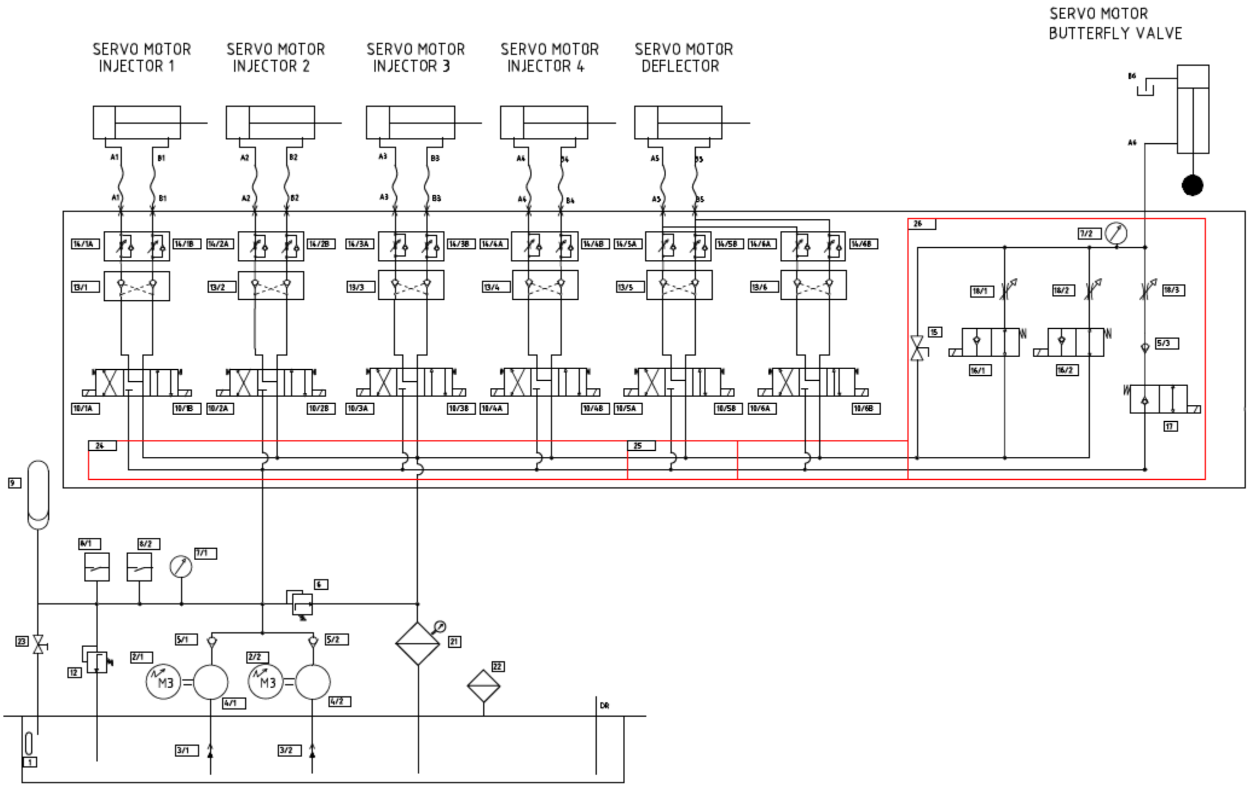

a)

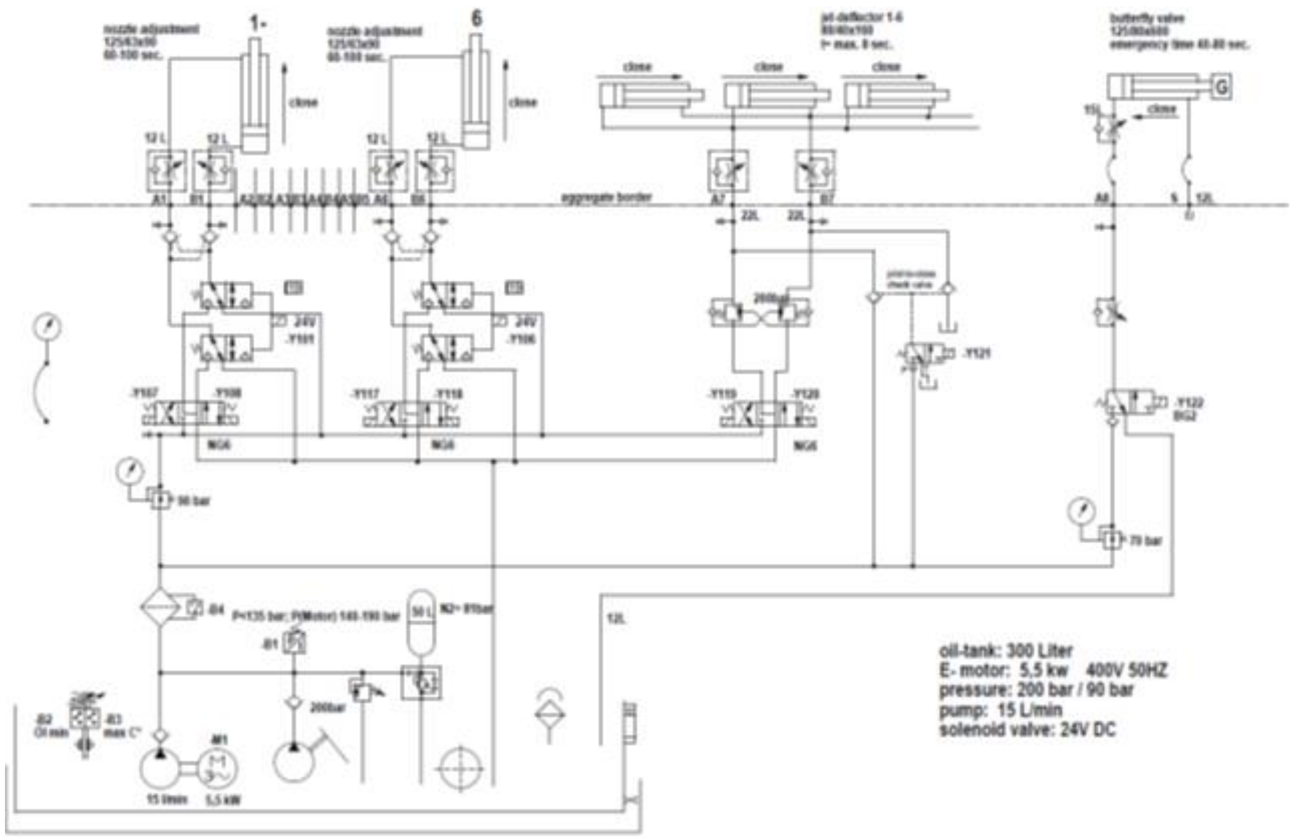

b)

Fig. 3. Fluid power system layout for Pelton turbine control
a) simple version (6 hydraulic cylinders); b) more complex version (13 hydraulic cylinders)

2. Basic information of the surveyed power plants

In this chapter, the essential information is provided, about the three surveyed micro hydropower plants, each equipped with Pelton turbines. This information serves as the foundation for the subsequent comparative analysis of maintenance impact on their performance.

Case A:

- Location: Cluj County
- Turbine Type: Pelton turbine with 6 injectors.
- Installed Capacity: 1,6 MW.
- Year of Commissioning: 2013.
- Fluid power system for turbine control: Figure 3 a).
- Water Intake Features: The water intake is equipped with hydraulically operated metal sluice gates, racks, and an automatic rack cleaner for the inclined grate at the water inlet into the conduit.
- Maintenance Information: The project designer provided general information on maintenance and a periodic maintenance plan.

Case B:

- Location: Alba County
- Turbine Type: Pelton turbine with 4 injectors.
- Installed Capacity: 0.729 MW.

- Year of Commissioning: 2012.
- Fluid power system for turbine control: Figure 3 b).
- Water Intake Features: The water intake lacks hydraulic actuators and relies on grates and an automatic cleaner for the grate.
- Maintenance Information: The project designer did not provide general maintenance information or a periodic maintenance plan.

Case C:

- Location: Bistrița-Năsăud County
- Turbine Type: Pelton turbine with 4 injectors.
- Installed Capacity: 0.402 MW.
- Year of Commissioning: 2014.
- Fluid power system for turbine control: Figure 3 b).
- Water Intake Features: The water intake lacks hydraulic actuators and relies on grates and an automatic cleaner for the grate.
- Maintenance Information: The project designer did not provide general maintenance information or a periodic maintenance plan.

This foundational information sets the stage for the comparative analysis, allowing us to understand the variations in equipment, maintenance practices, and their impact on the performance of these micro hydropower plants.

3. Comparative Analysis

In this section, a comparative analysis is conducted to assess the influence of maintenance practices on the technical condition and performance of the surveyed micro hydropower plants, specifically Case A, Case B, and Case C. Efficiency decline graphs are employed to depict the decrease of efficiency over time, with maintenance scores serving as the basis of categorization: 1 (comprehensive recommended practices), 2 (infrequent maintenance), and 3 (minimal intervention limited to component replacements essential for functionality).

Case A

Maintenance Score:

Years 1-5: 1 (Proactive Maintenance)
Subsequent Years: 2 (Reactive Maintenance)
Total in 10 years: 1,5

The graph below visualizes the decline in efficiency:

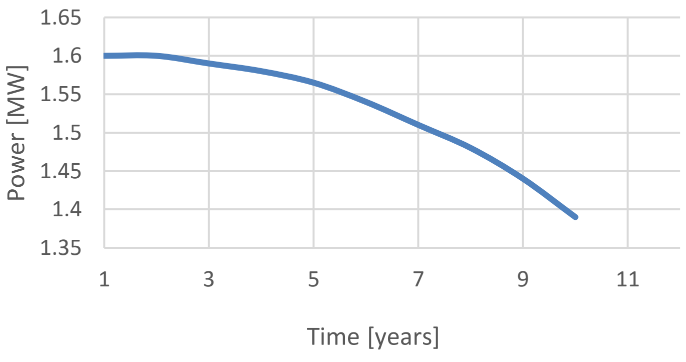

Fig. 4. Variation of global efficiency over time - Case A

Observations: The graph reveals a gradual but notable decline in efficiency. The reduction in power output, with 17%, is attributed to the transition from proactive to reactive maintenance practices.

Case B

Maintenance Score:

Regular Periodic Maintenance: 2 (Infrequent Maintenance)
Component Replacements: 3 (Minimal Reactive Maintenance)
Total in 11 years: 2,5

The graph below illustrates the efficiency decline:

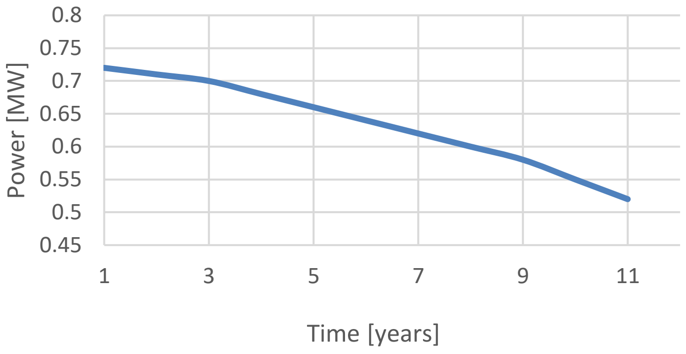

Fig. 5. Variation of global efficiency over time - Case B

Observations: The graph demonstrates a more substantial reduction in efficiency, with power output diminishing by 37%. The sporadic nature of maintenance activities contributes to this decline.

Case C

Maintenance Score: 3 (Minimal Reactive Maintenance with Limited Protective Measures), for whole period of 9 years.

The graph highlights the drastic efficiency decline:

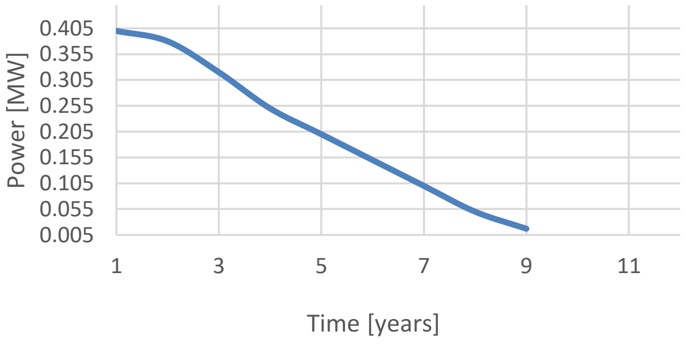

Fig. 6. Variation of global efficiency over time - Case C

Observations: The graph portrays a remarkable 96.6% reduction in efficiency, with power output almost negligible. The complete absence of proactive and periodic maintenance practices, alongside the lack of protective measures at the water intake area, is the primary driver of this severe efficiency drop.

All three cases were periodically technically inspected, the last check being in 2023, and the status was recorded as shown in the following table:

Table 1: Technical inspection report of the fluid power unit (August-September 2023)

No.	Designation	Inspection/Measurements	Case A	Case B	Case C
1	Oil	Fluid level	O	O	O
		Contaminants, Colour	R	R	X
		Temperature	R	R	R
2	Oil Tank	Air breather; Ball valve; Cleaning cover	O	R	R
		Oil level indicator	O	O	O
		Thermostat	O	-	-
		Oil level gauge	O	-	-
3	Pipes; Hoses; Fittings	Check leakages	R	R	R
		Tensions from fixation, bendings, strangulation	R	R	R
4	Gear pumps	Check alignment with drive mechanism	O	O	O
		Couplings	O	O	R
		Noise	O	O	O
		Increasing pressure	R	R	R
		Wear or damaged internal parts	R	R	R
5	Suction Filter	Warping	X	X	X
	Filter with indicator/	Indicator	X	X	X
6	Pressure valves	Temperature	O	O	O
		Noise	O	O	O
		Adjustments	O	O	R
7	Pressure sensor	Compared with gauge	O	R	R
8	Check valve (pumps)	Temperature, Noise, , Leaks	R	R	R
9	Hydraulic accumulator	Gas Pressure	R	R	R
		Temperature	O	O	R
10	Accumulator block	Temperature, Noise, Leaks	R	R	X
11	Solenoid valves	Voltage	O	O	O
		Temperature, Noise, Leaks	O	R	R
12	NC & NO valves	Temperature, Noise, Leaks	O	R	R
13	Pilot non-return valves	Temperature, Noise, Leaks	O	R	R
14	Check valve	Temperature, Noise, Leaks	O	R	R
15	Throttle valves	Temperature, Noise, Leaks	O	O	R
		Adjustments	O	O	R
16	Cylinders	Leaks	R	X	X

where:
O = Good operating parameters;
R = Operational but Needs in-depth Tests and Work;
X = Out of normal operating parameters;

3.1. Implications and Recommendations

The maintenance scores assigned to each case were determined based on a comprehensive evaluation of their maintenance practices:

- Maintenance Score 1 (Proactive Maintenance): This score was assigned to Case A for the initial five years, reflecting their proactive approach to maintenance by following recommended practices, including regular inspections, preventive maintenance, and adherence to maintenance schedules.
- Maintenance Score 2 (Infrequent Maintenance): This score was attributed to Case A beyond the initial five years. Case B received this score as they conducted periodic maintenance at intervals of 1-2 years, signifying a somewhat structured approach. However, their maintenance practices were infrequent and inconsistent, impacting efficiency.
- Maintenance Score 3 (Minimal Reactive Maintenance): Case B for rare maintenance interventions, and Case C for minimal reactive maintenance. It signifies minimal proactive or periodic maintenance, with a focus on component replacement only when essential for functionality.

These maintenance scores reflect the evolving nature of maintenance practices within each case, highlighting their varying degrees of proactive and reactive approaches.
The efficiency decline graphs provide vital insights into the profound impact of maintenance practices on micro hydropower plant performance. To address these findings:

- Proactive Maintenance (Case A): The graph showcases a discernible decline in efficiency when maintenance transitions from proactive to reactive. To mitigate this reduction, Case A should reinstate proactive maintenance measures and adhere to recommended practices.
- Periodic Maintenance (Case B): The graph exemplifies a more substantial reduction in efficiency due to intermittent maintenance practices. To maintain power output and efficiency, Case B should implement a more frequent and consistent maintenance schedule.
- Limited Maintenance (Case C): The graph underlines a severe decline in efficiency resulting from the absence of maintenance practices. Case C must prioritize comprehensive maintenance, including protective measures in the water intake area, to rectify this dramatic decline.

The graphical findings underscore the pivotal role of maintenance in sustaining efficiency and the longevity of micro hydropower plants. In the subsequent sections, best practices for hydraulic drive system maintenance will be explored, and recommendations provided to enhance the technical condition and performance of the equipment, ultimately contributing to the sustainable generation of clean electricity.

4. Best Practices for Hydraulic Drive System Maintenance

This section delves into the crucial aspects of maintaining hydraulic drive systems in microhydropower plants, focusing on key practices and recommendations that can enhance the technical condition and performance of these systems.

4.1. Proactive Maintenance

Proactive maintenance is a fundamental approach to ensure the reliability and efficiency of hydraulic drive systems. It involves a structured framework of activities that include:
Regular Inspections: Implementing periodic checks of all system components, including pumps, valves, filters, and hydraulic cylinders, to identify wear, leaks, or other issues. [3]

Preventive Maintenance: Adhering to a scheduled maintenance plan that includes tasks such as oil changes, lubrication, and cleaning of critical components. These tasks help prevent wear and ensure optimal operation. [3]
Maintenance Scheduling: Establishing a calendar of maintenance activities and adhering to it consistently. This includes regular maintenance intervals that ensure components are serviced before issues arise. [3]

4.2. Component Specific Maintenance

Maintenance is a combination of all the technical actions, administrative and managerial taken during the lifecycle of the equipment in order to maintain or restore the ability to perform the desired function (acc. To European Standard EN 13306). From this definition it shows that maintenance activities that include the identification, measurement, control operation, testing, detecting faults, repair, adjustment or replacement of parts items and service. [4]
Each component of a hydraulic drive system requires particular attention:
Pumps with Gear Wheels: Regularly inspecting gear pumps to ensure they operate efficiently and replacing worn-out gears promptly to maintain performance.
Valves and Relief Valves: Checking and calibrating pressure relief valves to avoid over-pressurization, which can cause damage to the system.
Filters: Replacing filters at recommended intervals to maintain oil cleanliness, preventing contamination and wear on system components.
Hydraulic Cylinders: Regularly monitoring the condition of hydraulic cylinders, including seals and rods, and promptly addressing any leaks or wear.
Check Valves: Ensuring that check valves are operational to prevent reverse flow in the system, which can lead to damage.

4.3. Protection and Monitoring

Water Intake Protection: Implementing protective measures at the water intake area to prevent debris, sediments, or foreign objects from entering the system. Grates, screens, and automatic cleaners can be used to maintain water quality.
Continuous Monitoring: Employing monitoring systems to track system parameters such as pressure, flow, and temperature. These systems can provide early warnings of potential issues. [5]

4.4. Training and Documentation

Staff Training: Ensuring that maintenance staff are adequately trained to perform maintenance tasks effectively and safely. Training programs can enhance their understanding of hydraulic systems and maintenance procedures.
Documentation: Creating and maintaining comprehensive maintenance records, including equipment manuals, maintenance schedules, and records of all maintenance activities performed.

5. Conclusion

This article has explored the comparative analysis of maintenance practices in micro hydropower plants, emphasizing the profound impact of maintenance on performance and efficiency. The implementation of proactive maintenance strategies, comprehensive component-specific maintenance, protection measures, monitoring systems, and well-documented practices are vital for maintaining optimal performance.
Micro hydropower plants play a significant role in sustainable energy generation. Through effective and proactive maintenance practices, they can continue to provide clean and reliable electricity for years to come. The knowledge and recommendations provided in this article serve as a foundation for enhancing maintenance practices in these critical energy systems.
By adhering to best practices and continuous improvement in maintenance, micro hydropower plants can fulfil their potential in contributing to a cleaner and more sustainable energy future.

References

[1] Schnitzer, Valentin. "Micro Hydro Power - Scout Guide." *Hydro Power, AMES — E / GTZ*, 2009. Accessed October, 2023. https://energypedia.info/images/3/3b/Hydro_scout_guide_ET_may10.pdf.
[2] Smith, John. "Hydraulic Drive Systems in Microhydropower Plants: Maintenance Challenges and Solutions." *Journal of Renewable Energy Engineering* 8, no. 2 (2021): 115-130.
[3] Brown, Lisa M. "Proactive Maintenance Practices for Sustainable Energy Generation: Case Studies in Microhydropower Plants." International Conference on Sustainable Energy Systems, Proceedings, 2020, pp. 45-59.
[4] Drumea, Petrin, Catalin Dumitrescu, Alexandru Hristea, and Constantin Chirita. "Methods of diagnosing malfunctions in hydraulic actuations." Paper presented at the 22nd International Conference on Hydraulics and Pneumatics HERVEX 2016, Baile Govora, Romania, November 9-11, 2016.
[5] Williams, David A. "Efficiency and Reliability in Microhydropower: A Comprehensive Analysis of Maintenance Strategies." *Renewable Energy Journal* 15, no. 3 (2019): 201-218.

ISSN 1454 - 8003
Proceedings of 2023 International Conference on Hydraulics and Pneumatics - HERVEX
November 8-10, Băile Govora, Romania

COMPARATIVE STUDY OF NON-INVASIVE METHODS USED FOR MEASURING THE HUMAN JOINT ANGLES AND JOINT'S RANGE OF MOTION IN STATIC AND DYNAMIC CONDITIONS

Cristian Radu BADEA[1], Paul-Nicolae ANCUȚA[1], Sorin Ionuț BADEA[1], Florentina BADEA[1]

[1] The National Institute of Research and Development in Mechatronics and Measurement Technique (INCDMTM)

adresacontact@gmail.com; paul.ancuta@incdmtm.ro; sorin_ib@yahoo.com; mihaiflori@yahoo.com

Abstract: *The analysis of the human body motions, as well as the postural analysis, are extremely important activities because they provide essential information about human biomechanics, depending on which systems and corrective exercises can be created to allow both an increase in the efficiency of individuals in the various fields in which they are involved (military, lucrative, domestic or sports), as well as an improvement in their quality of life. The actions undertaken in this regard are generally limited by the impossibility of performing non-invasive, ultra-precise measurements of the various body segments. Therefore, estimating the positions of human anatomical elements can be done in several ways, each of which has both advantages and disadvantages. Starting from this fact, in the action of choosing between the currently existing movement analysis systems, one will have to take into account both the qualitative and quantitative aspects of the provided results.*

Keywords: *Motion analysis, inertial, video analysis, body landmarks, biomechanics, neuromuscular, human joints angles, joint's range of motion (ROM)*

1. Introduction

Estimating human position by analysing video images can be used in software applications for measuring and validating physical exercises and controlling gestures of the whole body. MediaPipe Pose Landmarker allows you to detect human body landmarks in an image or video. In this mode, key body locations can be identified to analyse posture and classify movements. MediaPipe pose uses machine learning (ML) models and provides body landmarks in image coordinates and 3D world coordinates [1].
Inertial motion analysis systems are extremely useful for determining the correctness of human biomechanics. The main advantage of these inertial systems is the possibility of determining the biomechanical parameters without requiring prior constraints regarding the degrees of freedom of the various anatomical elements (which leads to certain limitations by comparison with the natural human movements) and also the possibility of capturing all body segments without the occurrence of obturation phenomenon as is the case with motion analysis video systems. On the other side, determining the various anthropometric parameters as precisely as possible is extremely useful when it comes to the calibration of inertial motion analysis systems, which decisively depends on the quality of this type of information.
These motion analyses can be both quantitative in nature (for example: number of repetitions, speed of a body segment, etc.) and qualitative (for example: correct postural attitude assessment, performing the movement over the entire joint range of motion, gait analysis [2] etc.). Thus, each system and/or tool used in the determination of human biomechanics addresses a certain type of analysis, due to both its facilities and limitations.

2. Previous and related works

The paper [3] presents an introduction to the field of inertial motion analysis, focusing its attention on the analysis that is carried out with the help of modern mechatronic inertial motion capture systems, highlighting both the advantages and disadvantages of using such a system and

highlighting the main constituent elements of these systems as well as the necessary steps that must be performed to be able to perform such an analysis.
The paper[4] presents the most important aspects related to the occurrence of positioning errors that appeared during the motion analysis sessions carried out with the help of the Xsens MVN system, before and after the post-processing of the information captured by to the MEMS sensors of the system, located on the human body, and related to the scenario in which the action takes place at the floor level (considered as having an incompressible surface), this representing the only element of contact between the human subject under analysis and the environment.

3. Material and method

The experiments were carried out using the following hardware equipment: an inertial motion analysis system, a stereo vision type camera, a laptop, a digital protractor, a angle gauge, a roulette, a ruler, an fixed bars assembly and elements of props used as physical benchmarks for carrying out calibrations and respectively for ensuring the necessary framework for carrying out experiments under repeatability conditions. The software programs used are MediaPipe and OpenCV for video analysis and MVN Analyze for inertial analysis.

3.1 Inertial motion analysis system

The tests carried out using the inertial motion analysis system Xsens MVN, were aimed on testing the facilities and limitations of such a system, as well as on the comparison between the this and a video analysis system. Xsens MVN is one of the best performing inertial motion analysis systems [5][6], based on a MEMS sensor network, each of which contains a combination of accelerometer, gyroscope and magnetic field sensors , whose signals are processed by a microcontroller, by means of advanced processing algorithms, in order to obtain information regarding the kinematics of the body segments of the individual under analysis and its global positioning, the data thus obtained being then transferred to a virtual biomechanical model, which reproduces, in real time, the movements of the person in question.
The hardware subassembly used in the study is called MVN Link and is a 3D kinematic analysis system, adapted to the human body, composed of a network of MEMS, interconnected by means of electrical cables, mounted/mountable, in predetermined positions, on a "Lycra" type of suit, the latter allowing the user to have maximum freedom of movement, but also having the role of reducing the time required for the positioning/repositioning of the MEMS. MVN Link can be used both indoors and outdoors, on rough terrain, in areas with low lighting. The results provided by MVN Link do not require post-processing, since the MEMS used do not suffer from the occlusion phenomenon, as in the case of optical markers. Also, the data provided by this system can easily be used by other software applications.
This system benefits from the presence of several extremely important elements, some of which are even innovations implemented for the first time by the manufacturer of this system, Xsens, namely:
- since the communication between the inertial system and the computer system, on which the motion analysis software is installed, is carried out wirelessly, the signal frequency is relatively low, around 100Hz, but this fact does not affect the quality of the analysis of movement due to the fact that the sampling frequency of the signal, by MEMS, is very high, of approx. 1000 Hz. In order to be able to maintain a high precision, the signal captured by the sensors that make up each MEMS is stored and transmitted incrementally, thus, in the event of a disruption in wireless communication, the data obtained by the MEMS are temporarily stored in a central sensory unit and then transmitted to computer, when communication is restored. Thus, the terminology used has undergone some changes regarding the sampling frequency (sampling rate), which has been replaced by "update/refresh rate";
- the signal transmitted by MENS is not influenced by distortions in the magnetic field, thanks to a function (named Magnetic Field Mapper), which allows the placement of MEMS on ferromagnetic surfaces, while maintaining the quality of the provided signal, as well as eliminating restrictions

regarding the working environment in that the system in question can be successfully used in motion analyses that are carried out inside the rooms with special metal reinforcement, in the car, plane, or train, or near the devices that use radio frequency;
- the high-resolution reprocessing engine, which allows offline reprocessing (or post-processing), of high-resolution information, which leads to an increase in the quality of the data provided by the system, by correcting the "slip" at the level of the foot, correcting the multi-point type contact, improving the consistency of the data, improving the accuracy of the data regarding joint angles and 3D kinematics and improving the accuracy of estimating the global 3D positioning;
- the possibility of including the analysed type of movement, in one scenario at a time, depending on the characteristics of the floor (incompressible, respectively compressible-elastic floor), on the performing the movement on different levels (as in the case of the analysis of the stairs climbing /descending, vertical walls climbing, etc.), or on the absence of a clear contact with the ground (as is the case with the analysis of skating and/or skiing);
- live detection of multiple contact points, which allows the analysis of walking in hands, of climbing and climbing stairs. In order to minimize positioning errors, the MVN Analyze software uses the contact points between the subject under analysis and the environment, which are usually anatomical protrusions considered to have the potential to physically interact with the environment, for example: the heel, elbow, knee [7]. Error minimization is achieved by combining the biomechanical model with advanced contact detection algorithms;
- the lack of orientation constraints, applied to the virtually modelled segments, as well as angular constraints applied to the joints, since the modelling of the joints of the virtual mannequin is based on the human anatomical structures that allow 6 degrees of freedom [8]. The information obtained is not manipulated by the system, to create the appearance of natural movements, but reflects exactly the values measured by the system's MEMS [9] [10].

3.2 Hardware and software used in the video analysis

The following components were used to perform the experiments:
Hardware components:
- Laptop DELL Vostro 15 3000 (two USB 2.0 ports, a USB 3.0 port, an Ethernet port, headphone/mic jack, DVD drive, VGA port, 15inch display 1366x768, core i5 8th Gen, 8 Mb RAM)
- Intel RealSense D435 Web Camera, which is equipped with a pair of depth sensors, an RGB sensor and an infrared projector and is connected via USB 3.0 Type-C.

Software components:
- UBUNTU operating system version 18.04.6 LTS;
- OpenCV software package version 4.7.0;
- The MediaPipe software package;
- Python version 3.10.5.

3.3 Types of biomechanical analyses performed and the imposed conditions

The biomechanical analyses carried out were structured in two sections, as follows:
- A static analysis section, necessary to perform a calibration of the two analysis systems used. In this section, the focus was on the capacity of the two motion analysis systems to determine in static conditions the joint angles at the level of the elbows and knees of the human subject;
- A dynamic analysis section. In this section, the focus was on the ability of the two motion analysis systems to determine, in dynamic conditions, the joint angles at the level of elbows and knees of the human subject, as well as the correct detection of joint's range of motion. Thus, this section was composed of:
  - a set of five sessions intended for the analysis of the flexion/extension movements of the right and left elbow joint respectively, consisting of ten movements (alternating biceps-triceps contractions, see Fig.1) having different amplitudes;
  - a set of sessions intended for the analysis of the flexion/extension movements of the right and respectively the left knee joint, consisting of ten movements (squats) with different amplitudes (see Fig.2).

In order to fulfil the proposed objective, certain conditions were imposed and respected, as follows:

- throughout the motion analysis sessions, the human subject was equipped with the sensory suit of the Xsens MVN inertial motion analysis system;
- during the analysis sessions, attention was focused on the knees and elbows joints;
- the analysis sessions carried out at the level of the elbow joint also included experiments in which the corresponding upper limb was wrapped in a red cloth, to increase the accuracy of the determinations by obtaining a colour contrast in relation to the sensory suit;
- the analysis sessions were carried out by reporting the positions of the human subject to fixed elements. Thus, a fixed bars assembly was used to ensure the necessary framework for performing motion analyses under repeatability conditions;
- both for the analyses intended for the elbow joint and for those intended for the knee joint, a set of five analysis sessions was created in which the entire body of the human subject was positioned angularly rotated in relation to the calibration landmark, by 0°, 15°, 30°, 45° and 60°;
- in order to be able to ensure obtaining and maintaining the joint angles as correctly as possible, necessary for the static analysis, a specially designed angle gauge was used so that it could be placed and maintained between the arm and forearm, respectively tibia and femur and having the angle of interest of 90°;
- in order to ensure a standardized measurement of the angles and the of joint's range of motion, an electronic protractor with a resolution of 0.1° was used, mounted at the level of the studied joint, distally, on its lateral face.

A software application was written in order to create twenty *.avi* files during the flexion-extension exercise of the right elbow and the right knee for each position of the human subject's body using the video camera. These films were analysed frame by frame in order to identify the coordinates of the three points of interest (shoulder, elbow and wrist for the upper limb, respectively hip, knee and ankle for the lower limb) necessary to calculate the joint angle. At the same time during the movement cycles, the sensors positioned on the special training suit sent the acquired data to the inertial motion analysis software, this software determining the joint angle in real time. Figures 1, 2, 3 and 4 below show the dynamic and static video analysis sessions of the elbow and knee joints of the human subject.

Fig. 1. Successive positions of the human subject for measuring the right elbow joint flexion angle

Fig. 2. Successive positions of the human subject for measuring the right knee joint flexion angle

Fig. 3. Successive positions of the human subject carried out for the static determination of the flexion angle of the right elbow joint

Fig. 4. Successive positions of the human subject carried out for the static determination of the flexion angle of the right knee joint

4. Results

The numerical results obtained were analysed and represented in the form of graphs of variation of the measured size, namely of the angles of the joints of the elbows and respectively the knees of the human subject under analysis.

4.1 Monitoring the right elbow flexion

The variation of the flexion/extension angles value of the right elbow as it is extracted from the processed frames is shown in the graphs in Fig.5.

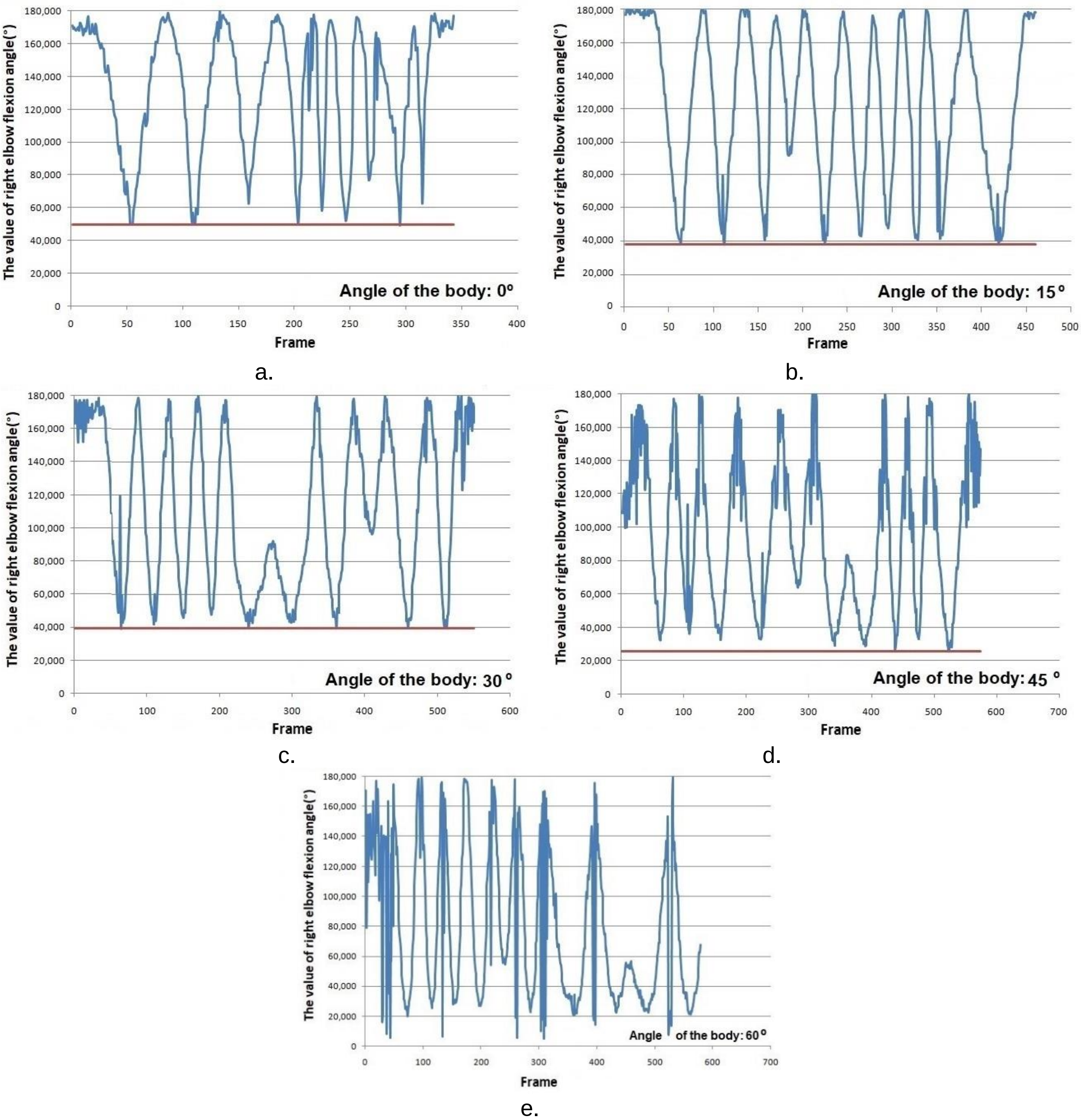

Fig. 5. The results obtained after processing the video frames of flexion/extension movements at the level of the right elbow joint

ISSN 1454 - 8003
Proceedings of 2023 International Conference on Hydraulics and Pneumatics - HERVEX
November 8-10, Băile Govora, Romania

There were image frames in which human body landmarks could be detected by software and therefore the flexion/extension angle was not represented on the graphs. This was the case of the set of frames associated with the rotation position of the human body at 60°, where the dispersion of the data did not allow the quick detection, using software successive comparisons, of the minimum value of the flexion/extension angle. Table 1 shows the data processing situation for the flexion movement of the right arm, as it was monitored by the video application.

Table 1: The data acquired and processed by the video application for the movement of the right elbow

The position of the body relative to the fixed reference on the floor	Total number of frames	Number of frames having detected Landmarks	Minimum flexion angle (°)
Rotation: 0°	672	342	49.83
Rotation: 15°	536	461	38.07
Rotation: 30°	601	551	39.36
Rotation: 45°	588	574	25.75
Rotation: 60°	615	614	Not detected

4.2 Monitoring the right knee flexion

The variation of the flexion/extension angles value of the right knee as it is extracted from the processed frames is shown in the graphs in Fig.6.

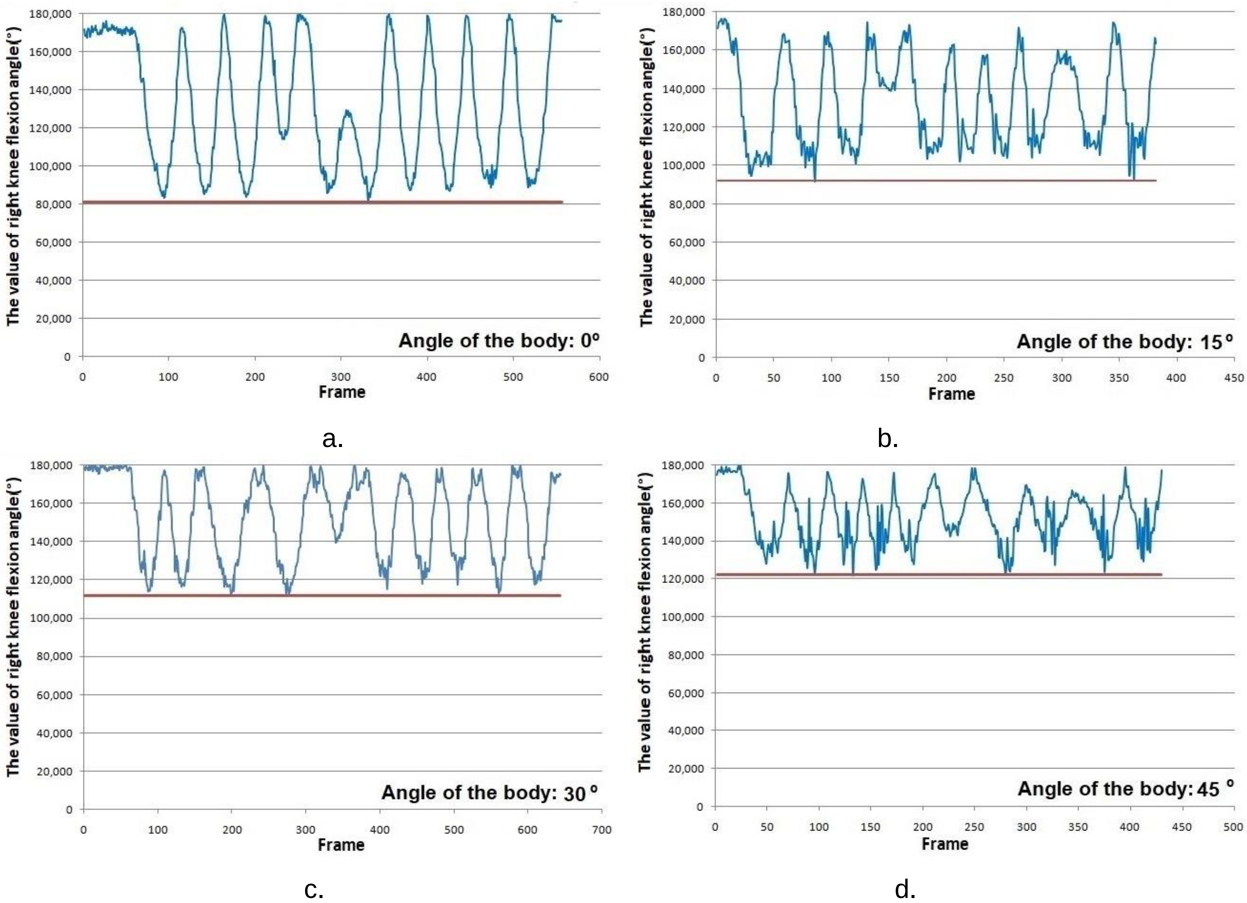

Fig. 6. The results obtained after processing the video frames of flexion/extension movements at the level of the right knee joint

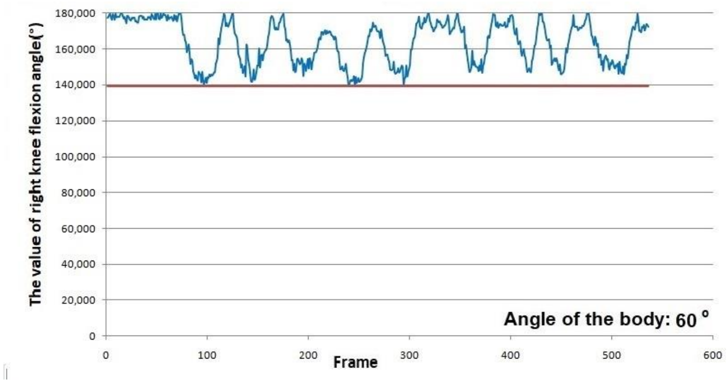

e.

Fig. 6. The results obtained after processing the video frames of flexion/extension movements at the level of the right knee joint

There were image frames in which human body landmarks could be detected by software and therefore the flexion/extension angle was not represented on the graphs. Table 2 shows the data processing situation for the flexion movement of the right knee, as it was monitored by the video application.

Table 2: The data acquired and processed by the video application for the movement of the right knee

The position of the body relative to the fixed reference on the floor	Number of frames	Number of frames having detected Landmarks	Minimum flexion angle (°)
Rotatie 0°	571	556	81.16
Rotation: 15°	532	382	91.87
Rotation: 30°	667	644	111.82
Rotation: 45°	569	430	122.10
Rotation: 60°	581	536	139.66

4.3 Monitoring the right arm fixed position

The measurement of the 90° flexion angle of the right elbow joint depending on the processed video frame is shown in the graphs in Fig.7.

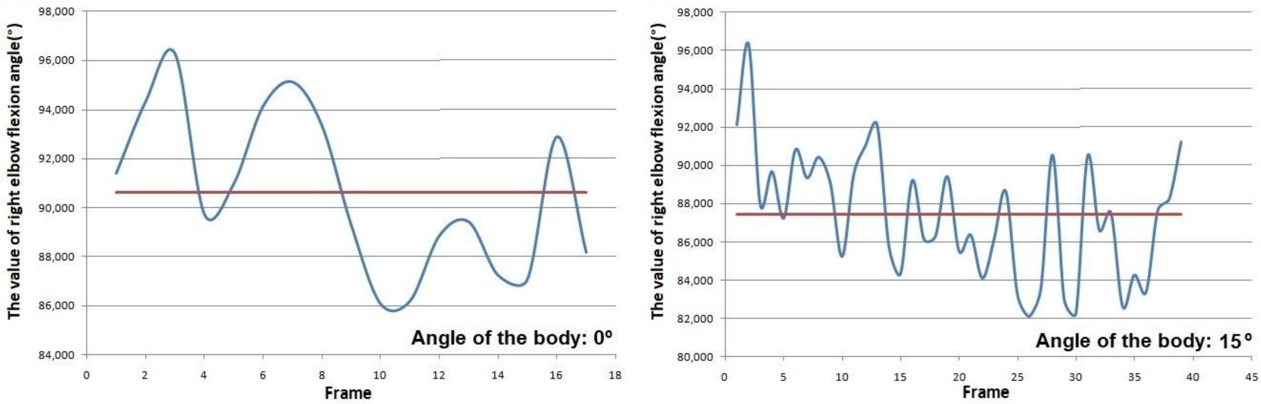

a. b.

Fig. 7. The comparative results obtained after processing the video frames for the angles of the right elbow joint, having the angle gauge mounted on its inner face

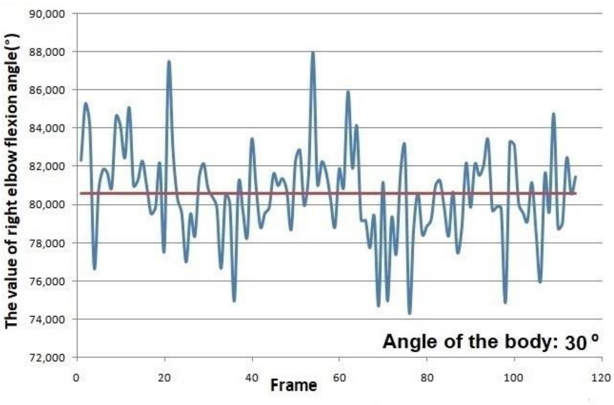

c.

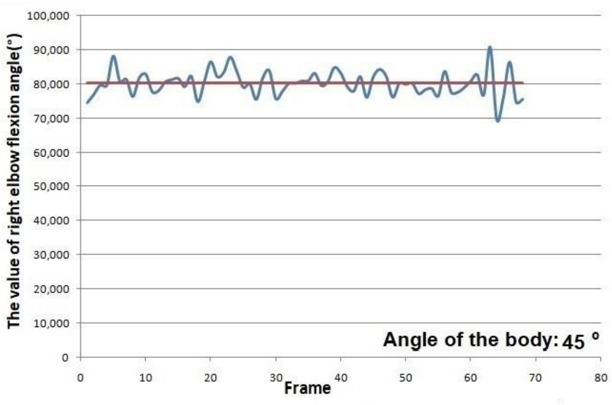

d.

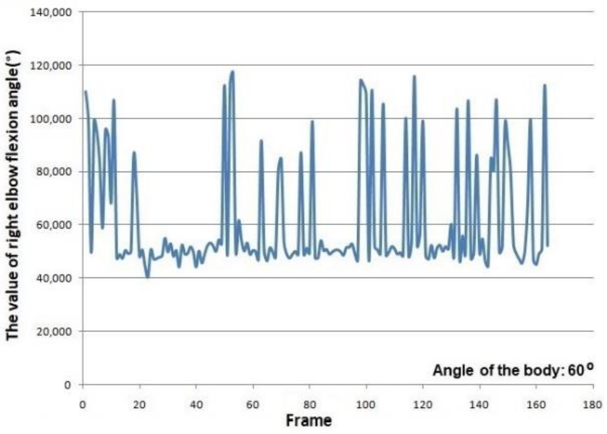

e.

Fig. 7. The comparative results obtained after processing the video frames for the angles of the right elbow joint, having the angle gauge mounted on its inner face

There were image frames in which human body landmarks could be detected by software and therefore the flexion angle was not represented on the graphs. Table 3 shows the data processing situation for the angular position in static conditions of the right elbow joint, as it was monitored by the video application.

Table 3: The data acquired and processed by the video application for the static flexion position of the right elbow joint

The position of the body relative to the fixed reference on the floor	Number of frames having detected Landmarks	Average value of flexion angle (°)
Rotation: 0°	17	90.61
Rotation: 15°	39	87.43
Rotation: 30°	114	80.56
Rotation: 45°	68	80.17
Rotation: 60°	164	N/A

4.4 Monitoring the right foot fixed position

The measurement of the 90° flexion angle of the right knee joint depending on the processed video frame is shown in the graphs in Fig.8.

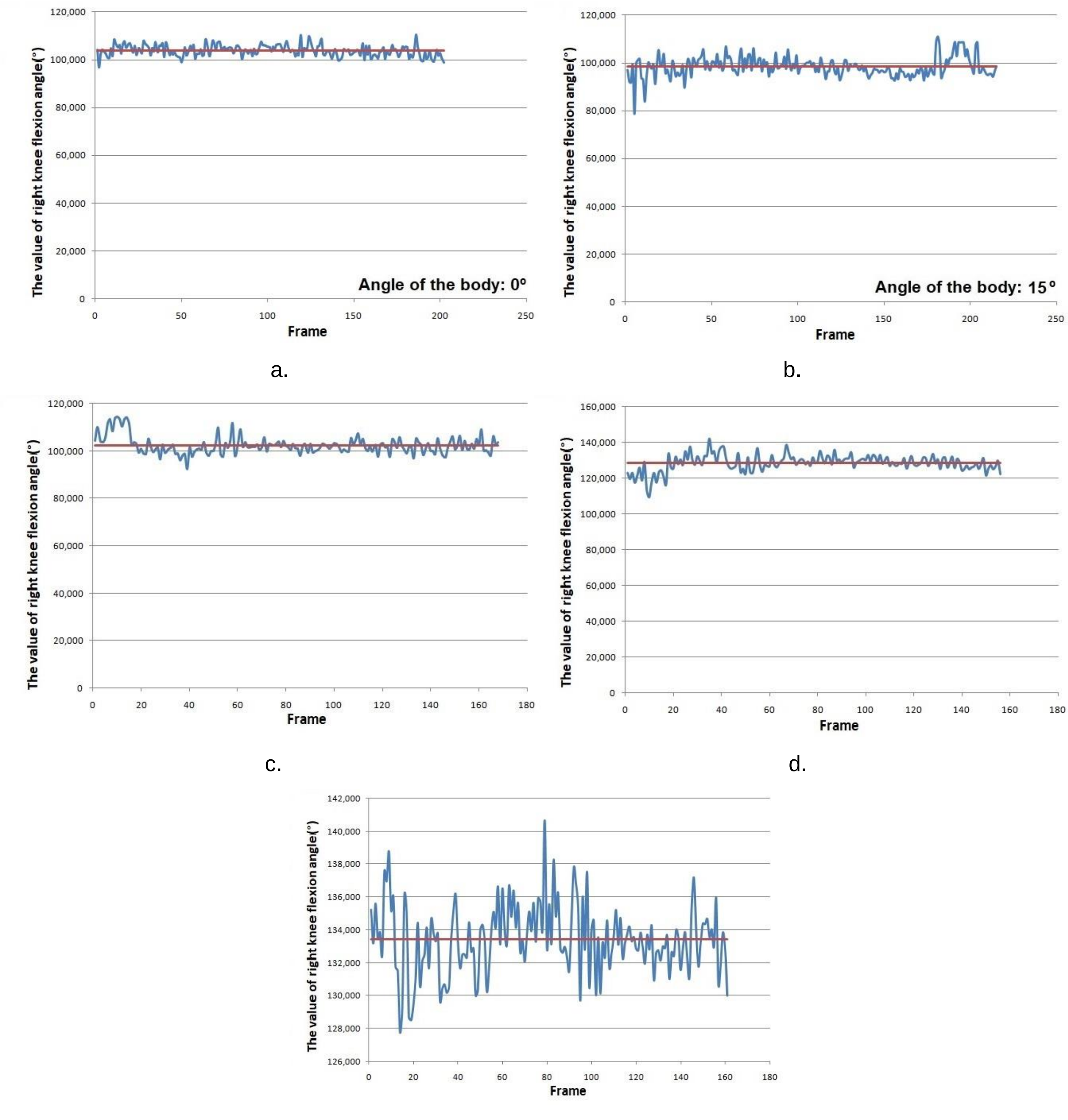

a. b. c. d. e.

Fig. 8. The comparative results obtained after processing the video frames for the angles of the right knee joint, having the angle gauge mounted on its inner face

Table 4 shows the data processing situation for the angular position in static conditions of the right knee joint, as it was monitored by the video application.

Table 4: The data acquired and processed by the video application for the static flexion position of the right knee joint

The position of the body relative to the fixed reference on the floor	Number of frames having detected Landmarks	Average value of flexion angle (°)
Rotation: 0°	202	103.77
Rotation: 15°	215	98.43
Rotation: 30°	168	102.40
Rotation: 45°	156	128.47
Rotation: 60°	161	133.42

4.5 Static analysis sessions using *Xsens MVN* inertial motion analysis system

a. Static analysis section - within these analyses the human subject had to maintain, with or without external help, certain positions corresponding to certain joint angles (at the level of the elbow and knee joints) determined with the help of the electronic protractor and/or the 90° angle gauge.
In order to be able to determine the correctness of the estimation of joint angles and of joint's range of motion, with the help of the Xsens MVN inertial motion analysis system, the values provided by the system in question were compared with those recorded on the digital protractor, as well as with the angle determined by positioning the angle gauge inside the joints in question. This digital protractor was chosen because it is commonly used in anthropometric measurements, being known as a goniometer.
Thus, the comparative analyses were focused both on the determination of a relationship of proportionality between the values indicated on the digital protractor and those provided by the Xsens MVN inertial system, as well as on the verification of the accuracy of the latter. Fig.10 shows the results obtained in the case of the previously mentioned analysis. For this analysis, the human subject had to keep his forearm in three consecutive different positions, corresponding to the following flexion/extension angles indicated on the digital protractor: -8.8°, 65.2° and 98° respectively.

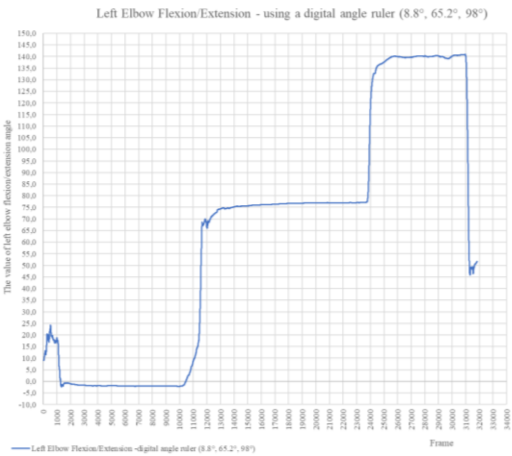

Fig. 9. The results obtained using Xsens MVN inertial analysis system, in the case of maintaining the flexion/extension angles at the level of the left elbow joint, for three different angular positions

Analysing the graph in Fig.9, one can see the three levels corresponding to the previously mentioned flexion/extension angles. Following an elementary calculation, it can be established that the angle of -8.8° indicated on the digital protractor corresponds to an extension angle of -1.98° in the inertial system. If there was a proportionality between these two measurements, it would mean that for the flexion angle of 65.2° indicated on the electronic protractor, the inertial system should indicate an angle of approximately 14.67°, respectively for the flexion angle of 98° indicated on the electronic protractor, the inertial system should indicate an angle of approximately 22.05°. However, the graph shows an angle of approximately 76.64° and 139.94°, respectively. The situation is repeated if the other two angles indicated by the digital protractor are taken as a reference. It thus emerges the fact that a proportionality between the two measurements cannot be determined, this fact could be due to one of the following phenomena: the occurrence of a gross error of the inertial system, or the change in the position of the digital protractor in relation to the initial position.

Due to the fact that the digital protractor was placed and fixed on the external face of the arm and the forearm respectively, the conducted experiments highlighted the following aspects:

- the maximum and minimum values of the joint's range of motion recorded with the help of the digital protractor differed not only from one session to another (each session presupposing a repositioning of the digital protractor on the arm of the human subject under analysis), but also from one movement to another. The differences were created, as expected, by the location of the joint of the digital protractor in relation to the studied joint, by the muscular reaction at the stroke ends of the movement, a phenomenon that produced the displacement of the measuring instrument used, in relation to his initial position. More precisely, this change in the position of the digital protractor during movement was due to the impossibility of fixing in place the measuring instrument in question, directly on the bone surfaces (which has the advantage of not changing its three-dimensional shape in relation to the joint angle) and the lack of fixed physical landmarks having a well-defined shape, which allows precise and repeatable successive repositioning;
- even if the forearm was kept in supination throughout the execution of the flexion/extension movements at the elbow joint, a displacement of the digital protractors position still occurred in relation to its initial position. As expected, another thing happened in this situation, namely the decrease of the maximum amplitude of the studied joint, by decrementing the value of the upper limit of the flexion angle, due to the biceps muscle contraction necessary to maintain the supination of the forearm.

This latter phenomenon was also observed in the case of the analyses performed with the angle gauge positioned on the inner face of the elbow joint. In the case of these analyses, the attention was focused on the ability of the inertial system to provide values that indicate that the movement at the level of the elbow joint it is blocked, due to the placement of the mentioned instrument inside the elbow joint and to its fastening on the arm and forearm.

Analysing the graph in Fig.10, it can be seen that the Xsens MVN inertial system correctly indicates the fact that the flexion angle at the level of the right elbow joint is properly maintained within certain limits.

Fig. 10. The amplitude of the variation of the flexion/extension angle at the level of the right elbow joint, blocked due to the positioning of the angle gauge inside it

The variation of the flexion angle, graphically indicated in Fig.10, it is relatively small (approximately 0.4°) and is most likely due to the attempt of the human subject under analysis to maintain the imposed angular position. Thus, it can be observed that, even in the case of physical blocking of the joint movement, there is still an angular variation due to the modification of the shape of the muscles with which the angle gauge is in contact, this amplitude being able to decrease once the biceps muscle gets in a relaxed state. It should be mentioned, in the case of this analysis, the fact that the digital protractor did not register changes in the angle value. This clearly denotes the fact that this last-mentioned instrument cannot be mounted so well as to be able to record even the smallest possible variations and also clearly highlights the involvement of the bicep’s contraction in the angular variations that occur, as well as a compression of the soft body segments in contact with the angle gauge. An extremely important element in this analysis is that the value of the flexion angle is different from the value of the angle gauge, due to the fact that the latter is in contact with the muscles and not with the bones, the joint angles being determined according to the specialized literature by reference to bone structures. It should be mentioned that the flexion/extension angle within the Xsens MVN it is represented by the angle between the forearm in the "0" position of the calibration of the system in question and the position of the forearm at a certain moment in time. More precisely, the flexion angle does not represent the angle between the arm and the forearm. Xsens MVN thus assigns positive angle values to the flexion movement and negative values to the extension movement, regardless of whether it is the upper or lower limb.

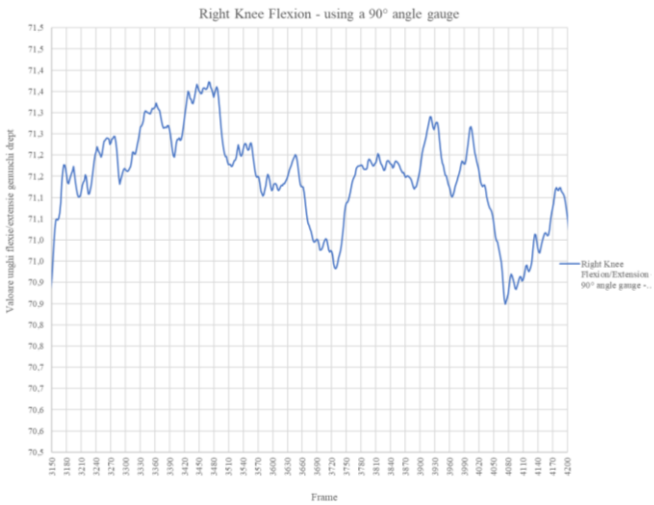

Fig. 11. The amplitude of the variation of the flexion/extension angle at the level of the right knee joint, blocked due to the positioning of the angle gauge inside it

The analysis performed with the angle gauge positioned at the level of the elbow joint was also applied at the level of the knee joint (see Fig.11). And in this situation, the phenomena observed in the previous case appear. Thus, analysing the graph in Fig.11, it can be seen that the Xsens MVN inertial system correctly indicates a relative blockage at the level of the knee joint. The variation of the flexion angle, found graphically, is, as in the case of the knee joint, relatively small (approximately 0.5°) and is most likely due to the attempt of the human subject under analysis to maintain the imposed angular position, as well as due to the compression of the soft body’s segments in contact with the angle gauge.

In order to confirm or deny this assumption, a new analysis was carried out, composed of five sessions, which assumed the repetition of the restriction of the elbow and knee joints movement, respectively. In this case, the human subject has had the task of maintaining the same muscle tension in the analysed joint, on the inner side of which the angle gauge was placed. Analysing the data provided by the Xsens MVN inertial system, it can be seen that it correctly indicates the blockage at the level of the elbow joint (see Fig.12) and respectively the knee (see Fig.13), in all five dedicated sessions.

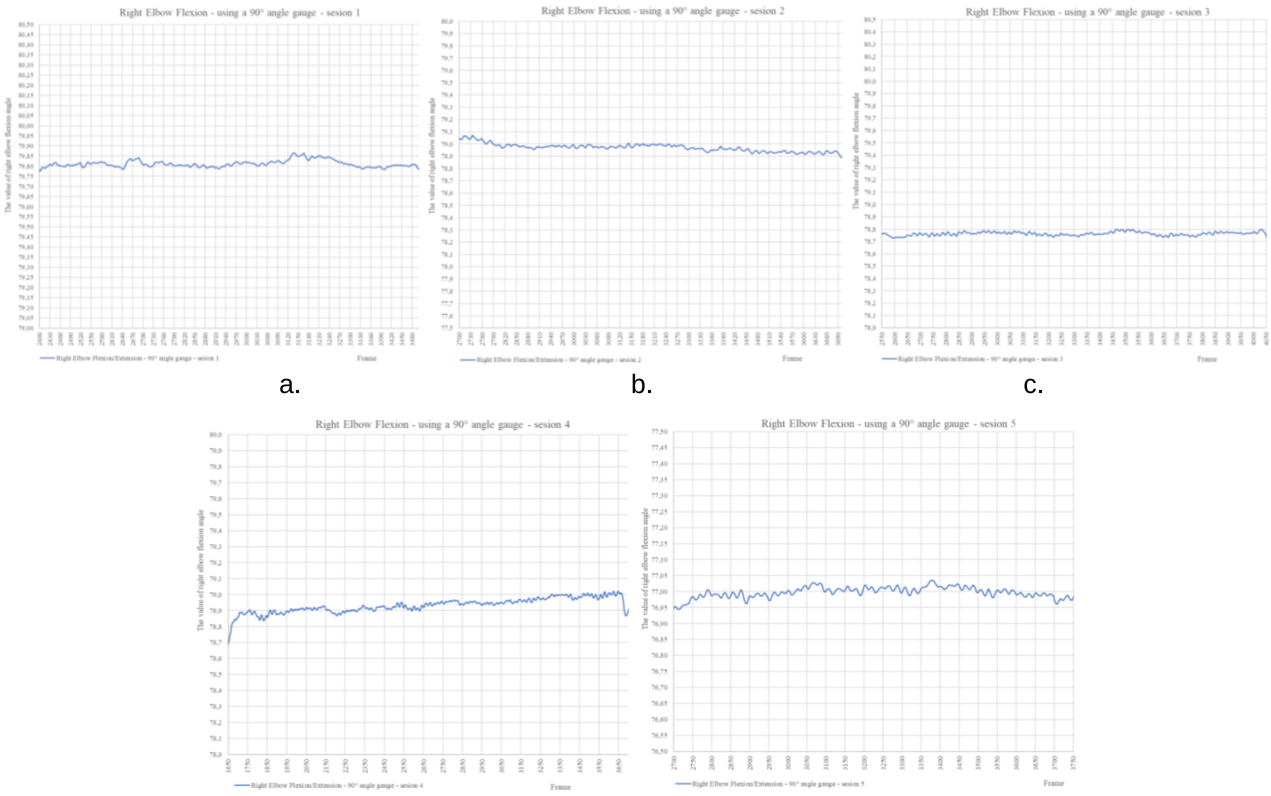

a. b. c.

d. e.

Fig. 12. The results obtained in the five motion analysis sessions carried out using Xsens MVN, regarding the amplitude of the variation of the flexion/extension angle at the level of the right elbow joint, blocked due to the positioning of the angle gauge inside it

In the case of the elbow joint, the amplitude of variation of the flexion angle is the same in all five sessions (approximately 0.4° - see Fig.12), differing only in the average value of the angle in question. This variation is clearly due to a combination of factors, namely: the different muscle tension from one session to another, the impossibility of identical placement of the angle gauge from one session to another and the compressibility of soft anatomical elements (skin and muscles).

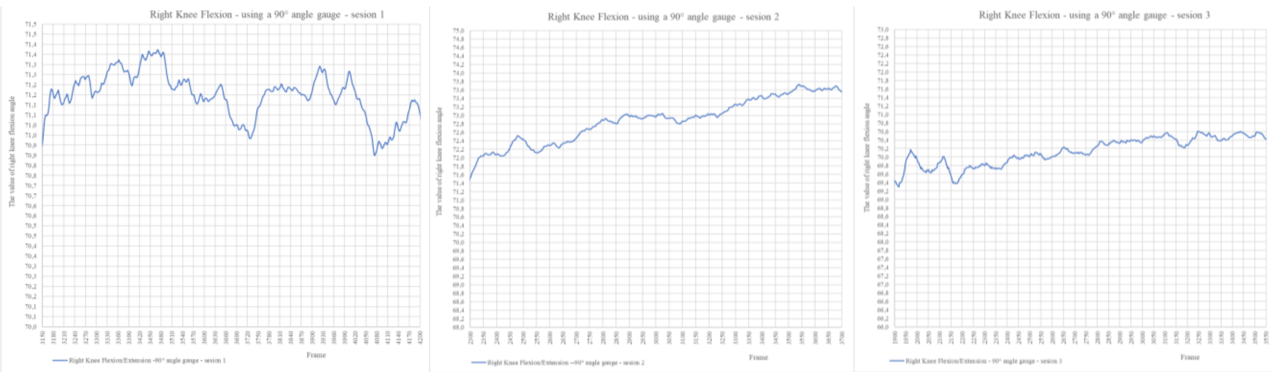

a. b. c.

Fig. 13. The results obtained in the five motion analysis sessions carried out using Xsens MVN, regarding the amplitude of the variation of the flexion/extension angle at the level of the right knee joint, blocked due to the positioning of the angle gauge inside it

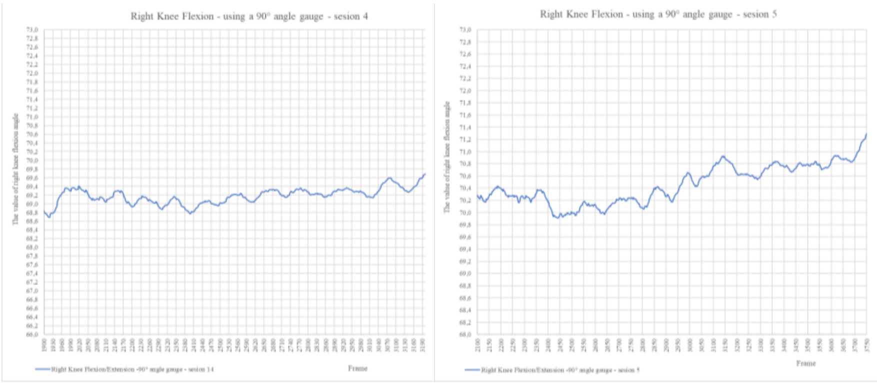

d. e.

Fig. 13. The results obtained in the five motion analysis sessions carried out using Xsens MVN, regarding the amplitude of the variation of the flexion/extension angle at the level of the right knee joint, blocked due to the positioning of the angle gauge inside it

Analysing the graph of the variation of the amplitude of the flexion angle at the level of the knee (see Fig.13), with the angle gauge mounted on its internal face, it can be considered that the phenomenon appeared in the case of the elbow joint and manifests in the same way in this case as well, the differences being given by : a different neuromuscular control between the lower and upper limbs (neuromuscular control at the level of the upper limbs being clearly higher due, mainly, to the fact that they are trained throughout life to perform precision movements) and the pressure exerted on the lower limbs due to the vertical position of the body during the sessions dedicated to knee analysis.
Therefore, it can be said that the hypothesis of the appearance of an angular variation due to the human subject's attempt to maintain the position even in the case of a physical blockage applied to the joint in question, in contact with the angle gauge, is confirmed.

4.6 Dynamic analysis sessions using *Xsens MVN* inertial motion analysis system

In these analyses, the human subject had to perform ten flexions/extensions at the level of the elbow and/or knee joints, the movements being limited or not in a certain direction with the help of props whose shape and position in space cannot be modified. The purpose of these analyses is to determine the ability of the Xsens MVN inertial system to properly determine the flexion/extension angle and respectively the joint’s range of motion. In this situation, the role of the prop was to ensure the necessary framework for the execution of joint movements with a predetermined range of motion, limited by the contact at the end of the stroke between the moving body segments and it.

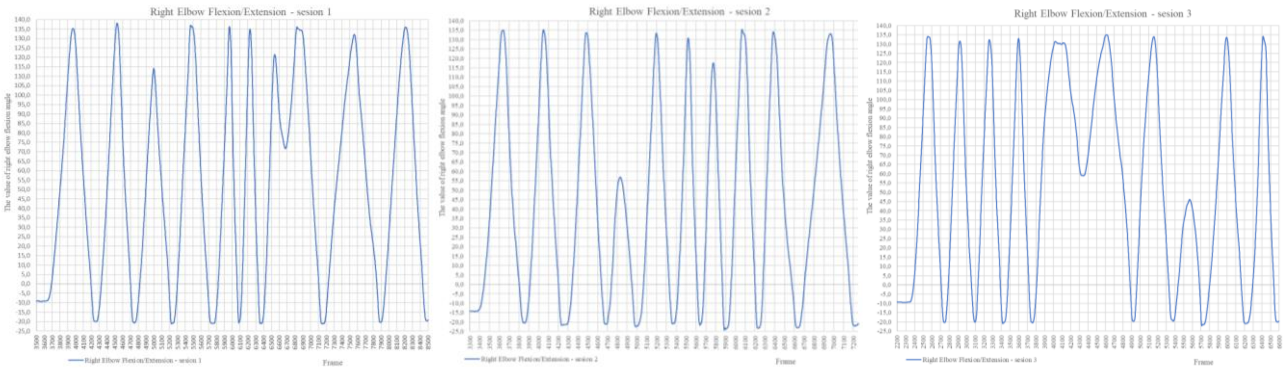

a. b. c.

Fig. 14. The results obtained in the five motion analysis sessions carried out with the help of Xsens MVN, regarding the range of motion at the level of the right elbow joint, during an exercise performed without additional loading

ISSN 1454 - 8003
Proceedings of 2023 International Conference on Hydraulics and Pneumatics - HERVEX
November 8-10, Băile Govora, Romania

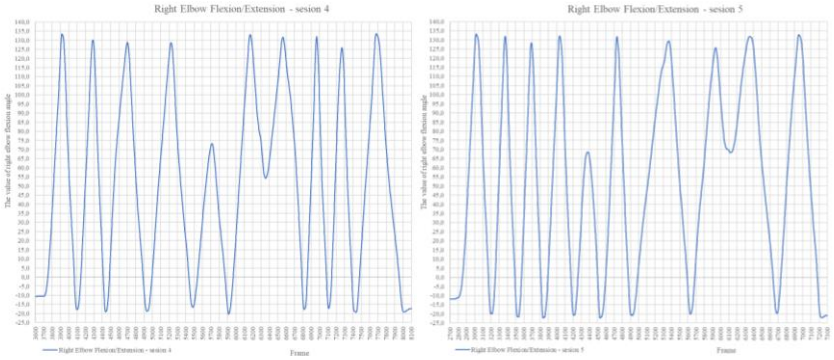

d. e.

Fig. 14. The results obtained in the five motion analysis sessions carried out with the help of Xsens MVN, regarding the range of motion at the level of the right elbow joint, during an exercise performed without additional loading

In the case of the elbow joint, the movements were mechanically limited by the contact with the outer face of the chin of the human subject undergoing analysis, with the head previously fixed in an immutable position for the entire duration of an analysis session. Intermediate flexion/extension movements were also performed, in order to clearly demonstrate the ability of the Xsens MVN inertial system to properly determine the flexion angle. As can be seen in Fig.14, the amplitude differences between the ten flexion/extension movements performed in each analysis session are clearly highlighted. It can also be observed that the average value of the range of motion is approximately the same in the five sessions, the small differences of tenths of a degree being most likely generated by the compression of the soft body segments, following the contact with the limiting elements.

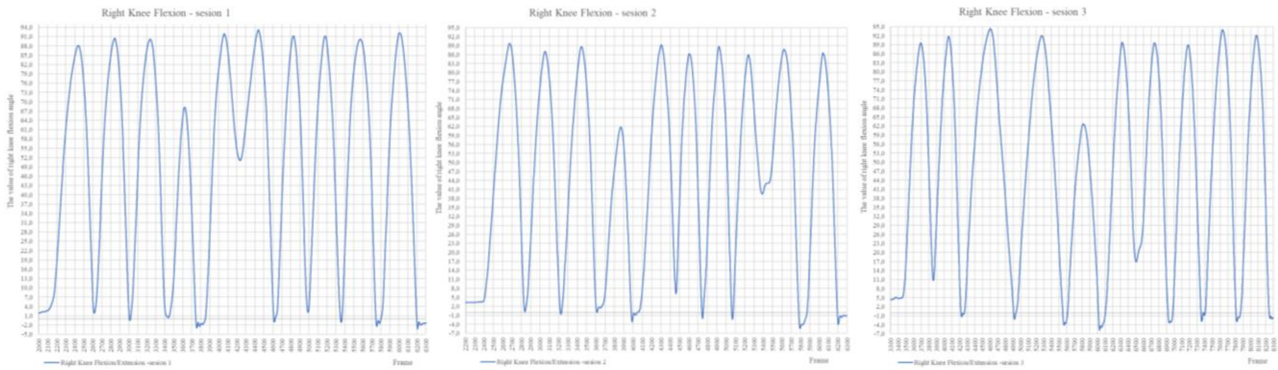

a. b. c.

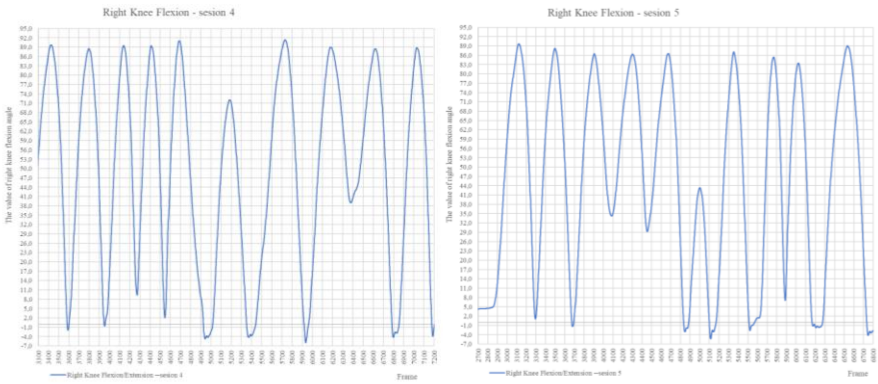

d. e.

Fig. 15. The results obtained in the five motion analysis sessions carried out with the help of Xsens MVN, regarding the range of motion at the level of the right knee joint, during an exercise performed without additional loading

Analysing the data from Fig.15, which shows the flexion/extension movements at the knee level limited lower by the contact with the fixed bars assembly having an unmodifiable spatial position, it can be clearly seen that the phenomena highlighted in the analysis of the flexion/extensions at the elbow level, manifests itself in the same way in the currently analysed joint. The difference compared to the situation of the elbow joint is given by the fact that the variation in aptitude between the movements performed are greater in this case (approximately 1° to 3°). This aspect is clearly due to the fact that the soft body elements that come into contact with the limiter in the case of flexion/extension at the level of the knee joint have a higher volume than those in the case of the elbow joint, thus allowing a higher level of compression.

4.7 Comparative analysis between the two systems: inertial system and video system

Data acquired by the inertial motion analysis system and data obtained by processing successive video frames were processed to obtain the flexion-extension angles. The graphs have local minima and maxima, which correspond to incomplete flexion-extension movements. The flexion-extension movements performed faster or slower are highlighted on the graph by the numerical value of the ascending and descending slopes associated with each movement. As expected, for all the graphs obtained with the help of the inertial system, the maximum and minimum values of the measured angles (for the full flexion movement) are not affected by the positioning of the human subject's body in relation to the video camera image plane. Instead, the minimum values of the angles measured with the help of the video application, corresponding to full flexion, are different, depending on the rotation angle of the human body compared to the fixed reference on the floor. In order to allow a comparative analysis of the quality of the graphic representations, the values of the angle supplements obtained through video analysis were represented in the graph in Fig.16.b.

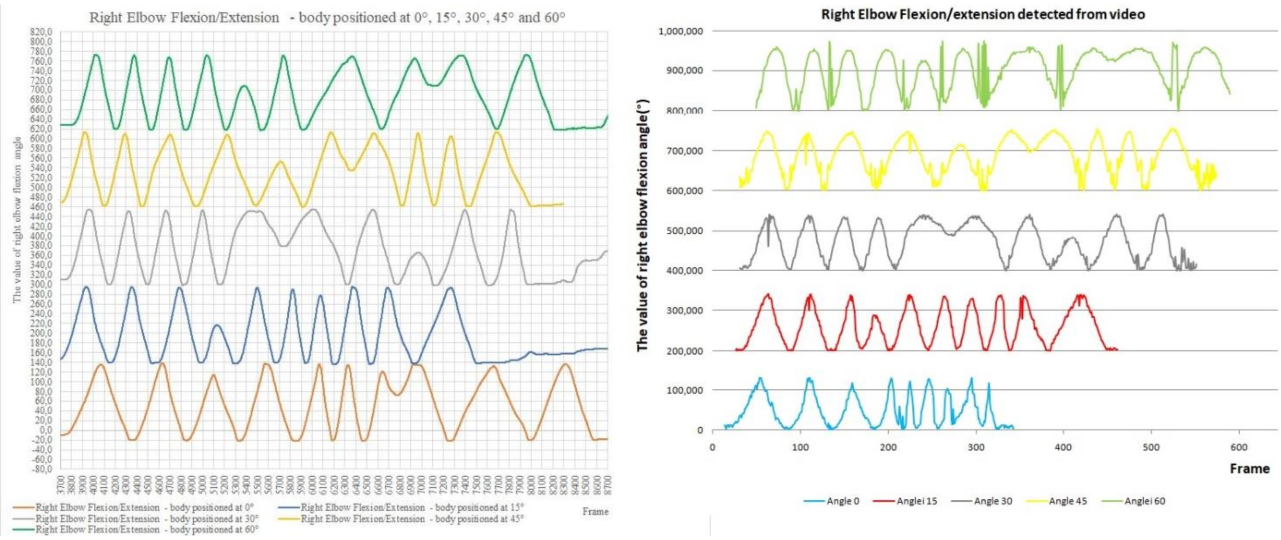

a. b.

Fig. 16. The comparative results of flexion/extension movements at the right elbow joint level, obtained with: a) Xsens MVN inertial system; b) video analysis

The graphs obtained by video analysis have a different number of points because body landmarks could not be extracted from some video frames. Also, in some successive video frames from the film associated with the positioning of the human body at 60° from the camera plane, incorrect positions for the shoulder, elbow and wrist were detected, for the shoulder the calculated angle values are not acceptable. The synoptic analysis of the two graphs indicates that the allure of these graphs is the very similar.

The comparative presentation of the results for the flexion/extension movement of the right knee joint level is depicted in Fig.17.

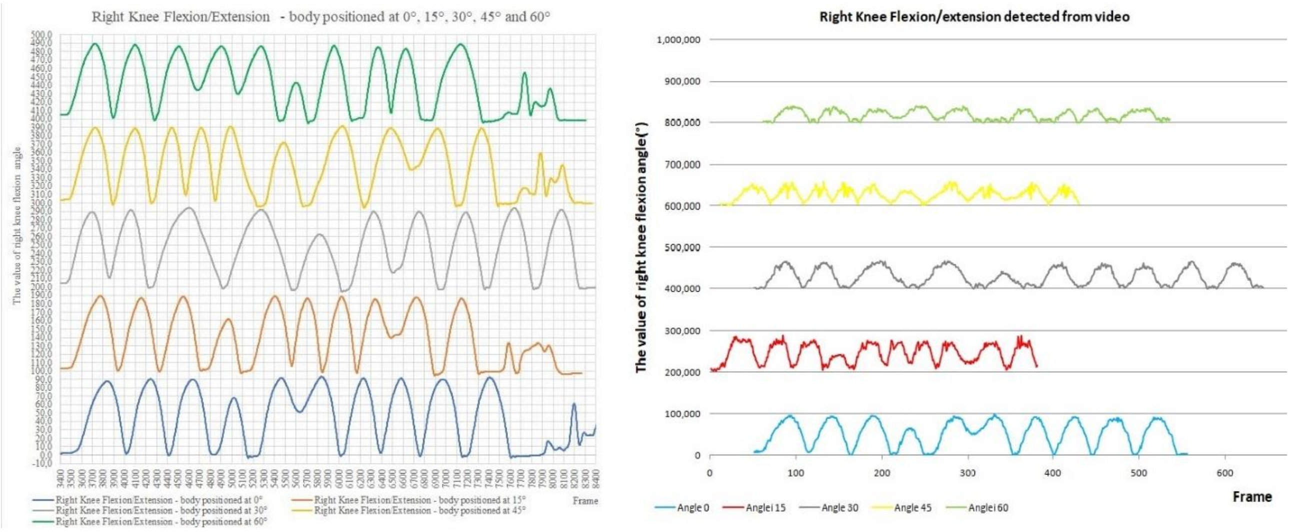

a. b.

Fig. 17. The comparative results of flexion/extension movements at the right knee joint level, obtained with the help of: a) Xsens MVN inertial system; b) video system

5. Conclusions

Video analysis of moving images of the human body using MediaPipe software is an affordable method of calculation and quantitative evaluation of the movements made by human subjects during sports training. The experiments carried out revealed the fact that the relative position of the human subject to the room plane influences the calculated value of the flexion-extension angle. Because both the T-shirt and the pants of the sports suit, used by the human subject, are black, some image frames could not be processed. The adopted solution was to create a colour contrast between the moving arm and the rest of the body. Taking into account the previously mentioned facts, we can assert that, if the video analysis includes an initial stage of adequate calibration, this method will also allow a qualitative evaluation of the movements of human subjects. Future research will address the following aspects: augmenting the video analysis method with data delivered by acceleration, rotation, magnetic sensors and measuring the distance of the human body from the video camera plane, as well as increasing the speed of real-time detection of body landmarks, by writing software applications in the C++ language.
The Xsens MVN inertial system provides a precise method of motion analysis when the quality of the information provided by it is evaluated from a biomechanical point of view. More precisely, for the cases presented in the present paper, this means that the precision of measuring the joints angles and the joint’s range of motion must be correlated with the phenomena that occur in the case of the human joint motion and not through the prism of a hinge-type mechanical joint, in which the joint elements are non-deformable. Thus, in a biomechanical analysis, the biological component can significantly modify the result of the analysis, mainly due to the high deformability of the anatomical elements involved both in making the movement and in limiting it, as well as due to the precision of making the movements, or more exactly the level of neuromuscular control of the human subject under analysis.
Although the digital protractor is used in the anthropometric measurements (goniometer), it was found during the tests described in this article, that it cannot represent a standard for the evaluation of the two analysis systems (inertial and video), mainly due to the impossibility of achieving a precise, stable and repeatable positioning of the measuring instrument, on the segments of the human body joints.

Acknowledgments

This work was carried out through the NUCLEU Program, conducted with the support of MCID (Ministry of Research, Innovation and Digitization), project number: PN 23 43 03 01 -17N/2023. This scientific paper provides the opportunities for the creating international collaborations through the project “Support Center for International RDI projects in the field of Mechatronics and Cyber-MixMechatronics”, Grant agreement no. 323/340002/23.09.2020, SMIS 108119.

References

[1] MediaPipe. “Pose landmark detection guide.” Accessed October 2, 2023 https://developers.google.com/mediapipe/solutions/vision/pose_landmarker/.
[2] Constantin, Anghel, and Gheorghe I. Gheorghe. “CMOS transducer with linear response using negative capacity that can be used in mechatronic systems for force measurement in human walking analysis and in the future in MEMS and NEMS applications.” Paper presented at the CONTROLO 2016 - 12th Portuguese Conference on Automatic Control, Guimarães, Portugal, September 14-16, 2016. *CONTROLO 2016. Lecture Notes in Electrical Engineering* 402 (2017): 483–494.
[3] Badea, Cristian Radu. “Researches on inertial mechatronic motion analysis systems, based on mems.” *The Scientific Bulletin of VALAHIA University, Section –MATERIALS and MECHANICS* 16, no. 15 (2018): 44-50.
[4] Badea, Cristian Radu, and Sorin Ionuț Badea. “The positioning errors generated by Xsens MVN inertial system during the analysis of Push-ups exercise, using the Single Level scenario, before and after the calling of REPROCESS function.” *International Journal of Mechatronics and Applied Mechanics*, no. 4 (2018): 120-133.
[5] Schepers, Martin, Matteo Giuberti, and Giovanni Bellusci. ‘’Xsens MVN: Consistent Tracking of Human Motion Using Inertial Sensing.’’ XSENS TECHNOLOGIES B.V., Technical Report, March 2018.
[6] Guo, Liangjie, and Shuping Xiong. ‘’Accuracy of Base of Support Using an Inertial Sensor Based Motion Capture System.’’ *Sensors* 17, no. 9 (September 2017): 2091.
[7] Badea, Cristian Radu. ‘’Study on the influence of contact points, scenarios and graphical reference elements on the motion analysis process, carried out using the inertial mechatronic system MVN Analyze.’’ *International Journal of Mechatronics and Applied Mechanics* 2, no. 6 (2019): 74-81.
[8] Roetenberg, Daniel, Henk Luinge, and Per Slycke. ‘’Xsens MVN: Full 6DOF human motion tracking using miniature inertial sensors.’’ XSENS TECHNOLOGIES B.V., April 2013.
[9] Zhang, Jun-Tian, Alison C. Novak, Brenda Brouwer, and Qingguo Li. ‘’Concurrent validation of Xsens MVN measurement of lower limb joint angular kinematics.’’ *Physiological Measurement* 34, no. 8 (August 2013): 63-69.
[10] Wouda, Frank J., Matteo Giuberti, Giovanni Bellusci, and Peter H. Veltink. ‘’Estimation of Full-Body Poses Using Only Five Inertial Sensors: An Eager or Lazy Learning Approach?’’ *Sensors* 16, no. 12 (December 2016): 2138.

ISSN 1454 - 8003
Proceedings of 2023 International Conference on Hydraulics and Pneumatics - HERVEX
November 8-10, Băile Govora, Romania

RESEARCH INTO FREON-FREE ECOLOGICAL COMPRESSED AIR COOLING AND CONDITIONING PROCESSES

Florin TEIȘANU[1,*], Constantin CHELAN[1], Marinela BUTOI[1], Daniela IOVAN[1], Daniel OCOLEANU[1], Cristian-Eugeniu SĂLCEANU[1], Ancuța Mihaela ACIU[1], Cristina Maria NIŢU[1], Claudiu NICOLA[1], Marcel NICOLA[1], Mihai TEIȘANU[2]

[1] National Institute for Research, Development and Testing in Electrical Engineering - ICMET Craiova

[2] Faculty of Automatic Control and Computer Science - Politehnica University of Bucharest

* tunuri@icmet.ro

Abstract: *Documents such as the Lisbon Protocol and the EU Green Pact call for the development of environmentally friendly processes and technologies to drastically reduce greenhouse gas emissions (carbon dioxide, freons, etc.) and limit the devastating consequences of climate change. Today, most industrial refrigeration, air conditioning and personal comfort processes are carried out using equipment that uses freons (chlorofluorocarbons) as the working medium. However, the widespread use of all types of freon is questioned because of the destruction of the ozone layer in the stratosphere and the accumulation of large amounts of ultraviolet radiation on Earth, as well as the trapping of upward thermal radiation in the Earth's atmosphere, which causes the well-known greenhouse effect. This paper presents cooling and air-conditioning processes that produce artificial cold by using air as a working medium, an inexhaustible ecological resource that exists everywhere in space and time. Using compressed air as the working medium, three types of thermodynamic processes are presented theoretically and experimentally: free flow in the tube, free expansion in a centrifugal field as a proprietary solution, and expansion in a centrifugal field and energy separation/Ranque-Hilsch effect. The paper concludes by summarising the findings and making recommendations for further research.*

Keywords: *Environment and clean energy, artificial cooling, compressed air, thermodynamic cooling processes, expansion in a centrifugal field*

1. Introduction

The need to develop environmentally friendly processes and technologies, in line with the Lisbon Protocol and the EU Green Pact, is justified by the need to drastically reduce greenhouse gas emissions (carbon dioxide, freons, etc.) and limit the devastating consequences of climate change.
Today, most industrial refrigeration, air conditioning and personal comfort processes are carried out using equipment that uses Freon as a refrigerant.
However, despite the quantitative and qualitative growth that has taken place, the general use of all freons (chlorofluorocarbons) is being questioned due to the destruction of the ozone layer in the stratosphere, which allows a large amount of ultraviolet radiation to accumulate on the Earth, with harmful effects on humans, animals and plants. In addition, because of their very long persistence in the stratosphere, freon gases, together with other gases from industrial processes, contribute to the retention of upward thermal radiation in the Earth's atmosphere, causing the well-known greenhouse effect. These serious problems facing our planet are being discussed and analysed in specialised committees and decision-making forums around the world, where measures are being taken to limit the use of freons and find other substitutes.
In this respect, considering the interest of ICMET Craiova in the field of compressed air technology, this paper tries to meet the requirements of ensuring the quality and integrity of the environment, presenting theoretically thermodynamic procedures for the generation of artificial cold and initiating by experiment some applications where the refrigerant is compressed air, an environmentally friendly product for man and the environment.

2. Theoretical research

Despite the fact that air has a low coefficient of thermal conductivity (λ=0,024 W/moC, measured at 25°C), its use as a working medium in thermodynamic cooling and air-conditioning processes is justified by the fact that it is an inexhaustible ecological resource that is ubiquitous in space and time.
Air compression is known to be a costly process and the higher the compression pressure, the more the resulting air overheats. This paper deals with thermodynamic processes for cooling and air conditioning using compressed air from a low pressure source (1.5 ÷ 3 bar), which produces compressed air with an outlet temperature close to the ambient temperature.
The paper presents cooling and air-conditioning processes that produce artificial cold using air as a working medium, an inexhaustible ecological resource that exists everywhere in space and time. Using compressed air as the working medium, we have theoretically and experimentally demonstrated three types of thermodynamic processes, namely: free flow in the tube, multi-jet expansion in a centrifugal field as a proprietary patented solution, and expansion in a centrifugal field with energy separation/Ranque-Hilsch effect.

2.1 Free flow in the tube

Free flow of compressed air from a tube without mechanical work, i.e. free expansion in the atmosphere, causes changes in thermodynamic parameters. The air velocity in a section of tube depends on the value of the upstream pressure, the downstream pressure, the condition of the tube surface, etc. The flow velocity in the tube increases with the pressure variation. For a given value of tube cross section, no matter how much the pressure difference between upstream and downstream increases, the flow velocity cannot increase above the speed of sound. For this maximum value reached, where the speed is equal to the speed of sound, we can say that we have reached the conditions for the so-called critical (sonic) flow.
At the free end of the tube, expansion in the atmosphere can generate air velocities up to the maximum speed of sound. For tube pressure values from a low pressure source (1.5 ÷3 bar), the temperature drop during expansion is moderate ($\Delta T=1\div3^oC$).
At the same time, the release of compressed air into the atmosphere is accompanied by a loud noise that exceeds the level that the human body can tolerate.

2.2 Expansion in a centrifugal field

The pneumatic cooling device for the expansion of compressed air in a centrifugal field, according to its own solution in the patent [12], shown in Figures 1a, 1b, 1c, is constructed without moving parts, i.e. from a body 1.1, a multi-jet injector 1.2, a cover 1.3 and a seal. 1.4. The multi-jet injector 1.2, shown in Figure 1b or Figure 1c, has a number of nozzle holes arranged tangentially to the diameter of the swirl chamber to divide the incoming flow of compressed air. In our approach, convergent nozzle holes of variable cross section were used to accelerate the airflow to increase the outlet velocity.
This pneumatic device has the following functions:
- Dividing the compressed air flow into multiple jets, creating a cold air spray in the swirl chamber.
- Inside the vortex chamber (axial or frontal, Fig. 1b and 1c), the noises corresponding to each jet cancel each other out, resulting in a single background noise due to centrifugation at levels acceptable to the human body.

In the designed cooling device there is a series of orifices with constricted sections (nozzles) arranged tangentially to the diameter of the expansion chamber, in which irreversible thermodynamic turbulent flow phenomena occur, manifested by a sudden drop in pressure (throttling effect), increase in speed and temperature variation (Joule-Thomson effect). The reduction in gas temperature due to throttling - the positive Joule-Thomson effect - is used to achieve moderate refrigeration.
Also from a thermodynamic point of view, in the pneumatic cooling device, the temperature difference ΔT between the inlet temperature at nozzle T_1 and the outlet temperature at nozzle T_2 is:

$$\Delta T = T_2 - T_1 = \frac{w_2^2}{2c_p}, \tag{1}$$

i.e. it is directly proportional to the square of the outlet velocity of the air from the nozzle w_2 and inversely proportional to the specific heat of the air at constant pressure c_p.
The cooling of the expanded air at the nozzle outlet is more significant the higher the flow velocity at the outlet. The value of the flow velocity depends on the shape (conical, truncated, Archimedean spiral, logometric spiral) and the quality of the nozzle geometry (roughness).

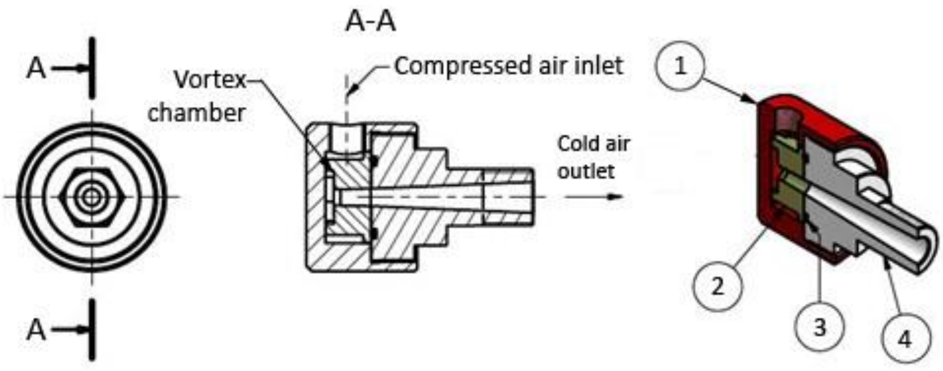

a. Pneumatic cooling device

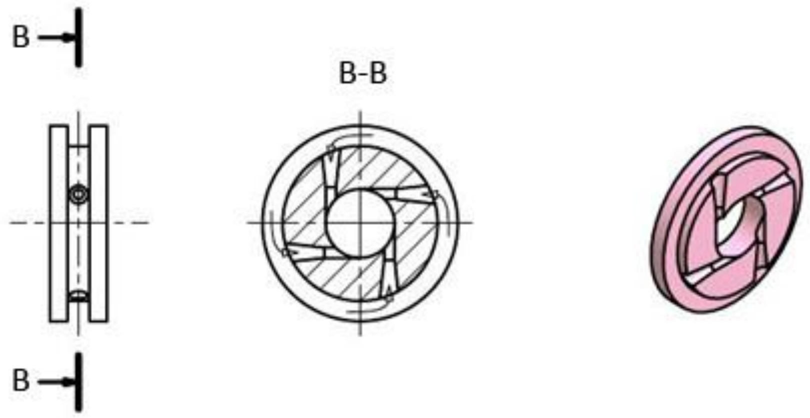

b. Axial swirl chamber

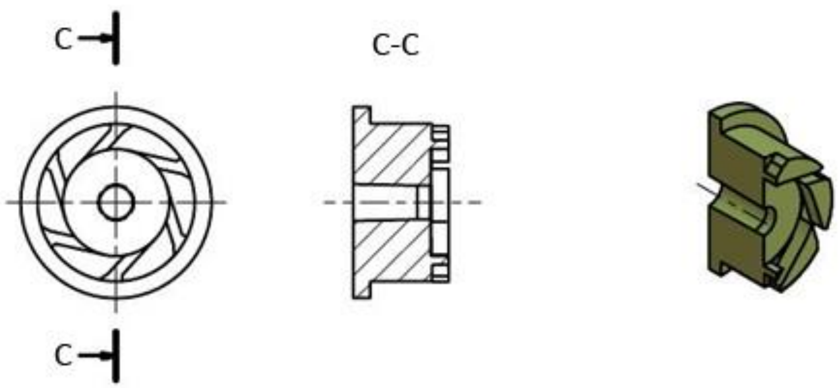

c. Frontal swirl chamber

Fig. 1. Pneumatic cooling device

2.3 Expansion in a centrifugal field with energy separation/Ranque-Hilsch effect

The gas-thermodynamic phenomenon of energy separation in a vortex field of a gas by the Ranque-Hilsch effect is particularly complex and not fully understood, and is described using both known physical-mathematical relationships and a series of quantities and criteria derived from experimental research.
The general scheme of gas flow (gas thermodynamic phenomenon) in a swirl generator (turbulent flow) can be simplified as follows (Fig. 2):

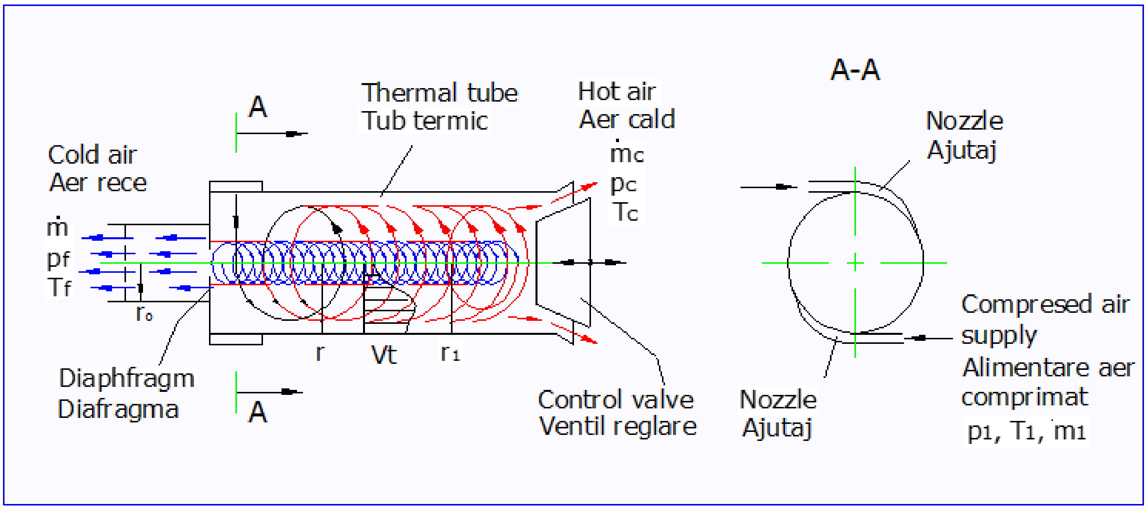

Fig. 2. Gas-dynamic phenomena in the Ranque-Hilsch tube

The compressed gas enters the generator through the nozzle, where it increases its speed due to the reduction in cross-section and is swirled due to the shape of the swirl chamber. When the gas is released into the cylindrical or truncated tube, an intense circular flow is created, characterised by the fact that the gas layers near the axis of the thermal tube cool down and are discharged through the orifice of the diaphragm, while the peripheral gas layers heat up and leave the tube through the semi-open section of the vent. By reducing the cross-sectional area of the valve, the cold gas flow through the diaphragm is increased, with a corresponding reduction in the hot gas flow. These changes are also accompanied by variations in cold and hot gas flow temperatures.
During the described process, a kinetic energy transfer and a turbulent heat exchange take place, in which elementary quantities of gas participate in the realisation of refrigeration cycles (compression-expansion) having the role of pumping energy from the central zone to the peripheral zone of the thermal tube.
In terms of flow and temperature parameters, the phenomenon can also be described as follows: the less cold air, the colder, or the more cold air, the less cold.
The flow rate of compressed gas supplied to the generator " $\dot{m}$" is the sum of the air flows leaving the generator, namely cold air "$\dot{m}_f$" and hot air " $\dot{m}_c$".

$$\dot{m} = \dot{m}_f + \dot{m}_c \ [kg/s] \ ; \ [m_N^3/min] \tag{2}$$

The proportion of cold air exhausted from the generator "μ"

$$\mu = \frac{\dot{m}_f}{\dot{m}} \tag{3}$$

The proportion of hot air exhausted from the generator, the difference is:

$$1 - \mu = \frac{\dot{m}_c}{\dot{m}} \tag{4}$$

The cold air proportion "μ" or the hot air proportion "1-μ" can be changed by operating the control valve.
From the thermal equilibrium equation [6], the thermodynamic temperatures characterising the cold (cooling) air flow T_f and the hot air flow T_c, at the outlet evolve according to the relationship:

$$\mu\Delta T_f = (1-\mu)\Delta T_c \tag{5}$$

where:
$\Delta T_f = T_i - T_f$, is the temperature drop of the cold flow T_f compared to the inlet temperature of the compressed air T_i.
$\Delta T_c = T_c - T_i$, is the drop in temperature of the hot flow T_c compared to the temperature of the compressed air at the inlet of the unit.
The operation of the pneumatic hot and cold air generator can also be expressed as follows: the less cold air ($\dot{m}_f \downarrow$), the colder ($T_f \uparrow$), or the more cold air ($\dot{m}_f \uparrow$), the less cold ($T_f \downarrow$).

3. Experimental research

The theoretical research presented is followed up and confirmed by experimental research in the laboratory, as follows:

a. Compressed air cooling by free flow from the tube

Figure 3a shows a schematic diagram of the circuit components and Figure 3d shows the physical components used during the experiment.

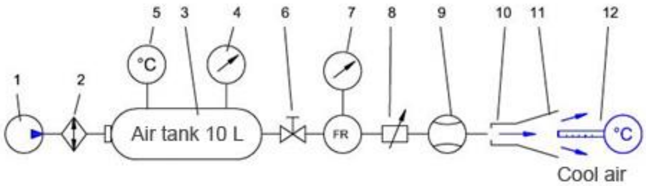

Fig. 3a. Compressed air cooling circuit by free flow from the tube

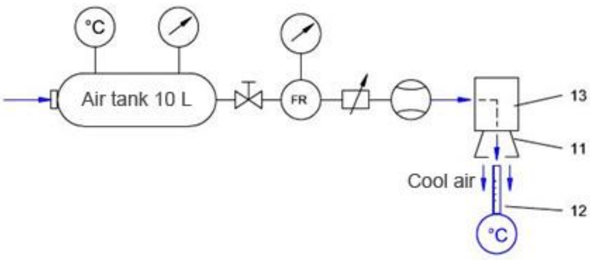

Fig. 3b. Compressed air cooling circuit by expansion in a centrifugal field

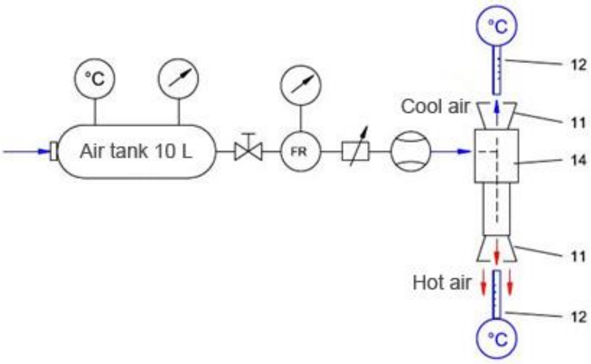

Fig. 3c. Compressed air cooling and heating circuit with vortex tube / Ranque-Hilsch

Fig. 3d. Cooling circuit components overview

Fig. 3. Experimental cooling circuits

Caption:
The equipment in the circuit represents:
1. Electric air compressor AC 1300/Makita; p_{max}=10 bar; q= 240 l/min; P=1.5 kW/230 V
2. Air-to-Air Cooler Type CSL
3. Compressed air tank V=10 litres; p_n=10 bar
4. Pressure gauge p_n=10 bar; G3/8”
5. Digital thermometer with a solid metal probe with a G1/4” thread; T=-25°÷100°C
6. Pass/no pass tap, G3/8”
7. FR pressure reducer-filter unit with pressure gauge G3/8”/SMC
8. Pneumatic throttle valve AS300/SMC; G3/8”
9. Digital calorimetric flowmeter SD6500/ifm D_n=15; p_n=15 bar; q=0.25÷75 m^3/h; Measures flow rate - pressure - temperature - total compressed air consumption
10. Compressed air tube D_n; p_n=10 bar; L=1.5 m
11. Circular diffuser
12. Digital thermometer with metal probe D3.5x120, FM10 Digi Mate; T=-50°÷150°C
13. Pneumatic cooling device by expansion in a centrifugal field DPR-ICMET Craiova
14. Cooling and Heating Vortex Tube, Model 3215 Exair Corporation

The compressed air in the circuit is supplied from a standard AC 1300/Makita source.
The pressure p_1, flow rate q_1 and temperature T_1 in the compressed air circuit and the temperature T_2 in free flow (p_2 = p_{atm}) at the end of the pipe with a nominal diameter of Dn = 6 mm were measured with the instruments shown in Figure 3a.
The working flow value was set by fine-tuning the AS 300/SMC throttle valve to the value set on the SD 6500/IFM digital flow meter.

Table 1

Cooling method	**At the circuit inlet**				**At the circuit outlet**			
	p_1 [bar]	**T_1 [°C]**	**q_1 [l/min]**	**v_1 [m/s]**	**p_2=p_{atm} [bar]**	**T_2 [°C]**	**q_2=q_1 [l/min]**	**v_2 [m/s]**
Free flow of compressed air	1.5	25.8	425	v_{11}	1	24.5	425	v_{21}>v_{11}
	2	25.8	425	v_{12}	1	24	425	v_{22}>v_{12}
	2.5	25.8	425	v_{13}	1	23.5	425	v_{23}>v_{13}
	3	25.8	425	v_{14}	1	23.1	425	v_{24}>v_{14}

By supplying the circuit with compressed air at moderate working pressures (p_1=1.5 ÷ 3 bar), an intense flow of air at a temperature slightly lower than the inlet temperature ($\Delta T=T_2-T_1$=1.3÷2.7ºC) is generated at the outlet, with high flow speeds and loud noises.

b. Compressed air cooling with a device for cooling by expansion in a centrifugal field

The structure of the circuit is shown schematically in Fig. 3b, where, in addition to the structure shown in Fig. 1a, there is the cooling device, item 11.
The compressed air cooling device shown in Fig. 1 is a new and original solution developed by a team of specialists in our institute and protected by patent RO No. 131145/2022. The originality of the solution is that all the compressed air entering the unit is converted into cooling energy by expansion and centrifugation (swirling) and exits as cold air.

Table 2

Cooling method	At the circuit inlet			At the circuit outlet		
	p_1 [bar]	T_1 [ºC]	q_1 [l/min]	$p_2=p_{atm}$ [bar]	T_2 [ºC]	$q_2=q_1$ [l/min]
Expansion and centrifugation (swirling)	1.5	26.5	425	1	23	425
	2	26.5	425	1	21	425
	2.5	26.5	425	1	17.5	425
	3	26.5	425	1	14	425

By supplying the circuit with compressed air at moderate working pressures (1.5 ÷ 3 bar), an air flow at a temperature lower than the inlet temperature ($\Delta T=T_2-T_1$=3.5÷12.5ºC) is generated at the outlet, with moderate flow speeds and noise. The process converts the entire flow of compressed air supplied to the unit into cold air ($q_1=q_2$).

c. Compressed air cooling and heating using a vortex tube/Ranque-Hilsch tube

The structure of the circuit is shown schematically in Fig. 3c where, in addition to the structure shown in Fig. 1b, we have as control element item 14 - vortex tube for cooling and heating, instead of item 13 - pneumatic cooling device.
The vortex tubes can be controlled by a dedicated valve to ensure that 20-80% of the supply flow to the compressed air device is converted to cold air and the 80-20% flow differential is simultaneously converted to hot air. With this type of Vortex Tube Model 3215, the maximum cooling capacity, i.e. the flow rate released at the cold end in conjunction with the temperature of the cooled air, is approximately 70% cold air.
The maximum cooling capacity is obtained with a proportion of 70% cold air, i.e. the product of the cold air flow and its temperature gives the best cooling capacity (P_f=190÷290 W at inlet pressures p_1=1.5 ÷ 7 bar).

Table 3

Cooling method	At the circuit inlet			At the circuit outlet				
	p_1 [bar]	T_1 [ºC]	q_1 [l/min]	$p_f=p_c=p_{atm}$ [bar]	T_2-cold [ºC]	T_3-hot [ºC]	q_2=cold [l/min]	q_3=hot [l/min]
Turbulent flow and energy separation	1.5	31	425	1	+24	+48	297	128
	2	31	425	1	+19	+54	297	128
	2.5	31	425	1	+11	+60	297	128
	3	31	425	1	+7	+67	297	128

By supplying the circuit with compressed air at moderate working pressures (1.5 ÷ 3 bar), a cold air flow is generated at the outlet with a significant temperature drop ($\Delta T=T_1-T_2=8\div24^oC$) in relation to the compressed air inlet temperature, and a hot air flow with a significant temperature rise ($\Delta T=T_3-T_1=17\div36^oC$). At the same time, the processed cold air flow rate (q_1) is approximately 2/3 and the processed hot air flow rate (q_3) is 1/3 of the supply air flow rate (q_1).

4. Interpretations and conclusions

The paper addresses a topical and globally important issue in terms of reducing emissions and finding new technologies and green agents to reduce global pollution. Thus, the use of compressed air as a working fluid in refrigeration and air conditioning systems and equipment can be a solution to replacing climate-changing freons/chlorofluorocarbons.
In industry, pneumatic energy has become the fourth largest source of energy for technological processes, despite its high cost and environmental impact.
In this context, this paper deals theoretically and experimentally with the phenomenon of obtaining moderate refrigeration from compressed air by thermodynamic methods.
It has been shown both theoretically and experimentally that the method of free flow of compressed air from the tube achieves an insignificant reduction in outlet temperature and noise.
The method of compressed air expansion in a pneumatic device (patented solution) by dividing the incoming compressed air flow into a number of jets and centrifuging them in a swirl chamber is an attractive solution for air conditioning in terms of moderate temperature drop ($\Delta T=3.5\div12.5^oC$) in relation to the ambient temperature.
The method of expansion in a centrifugal field and energy separation in the Ranque-Hilsch tube, at moderate compressed air supply pressures (1.5 ÷ 3 bar), produces cold and very cold air flows with temperature differences $\Delta T=8\div24^oC$ and, at the same time, secondary hot air flows with $\Delta T=17\div36^oC$.
To summarise:
- The method of compressed air free flow is of no interest either from an energy point of view or in terms of the noise pollution it produces.
- The method of multi-jet expansion in a centrifugal field of compressed air, converting the entire flow of compressed air into moderately cold air, is of interest for environmentally friendly air conditioning.
- The method of expansion in a centrifugal field and energy separation into hot and cold is already being used in industrial and laboratory applications.

The further development of thermodynamic methods, multi-jet expansion and expansion and energy separation devices may also be of interest to the scientific and technical community and, not least, to applicants.

Acknowledgments

This work was developed with funds from the “Ministry of Research, Innovation and Digitization of Romania” as part of the Nucleu Program: PN 23 33 02 05.

References

[1] Carafoli, Elie, and V.N. Constantinescu. *Compressible fluid dynamic / Dinamica fluidelor compresibile*. Bucharest, Romanian Academy Publishing House, 1984.
[2] Florea, Julieta, and Valeriu Panaitescu. *Fluid Mechanics / Mecanica Fluidelor*. Bucharest, Didactic and Pedagogical Publishing House, 1979.
[3] Christea, Alexandru, and Nicolae Niculescu (coords). *Ventilation and air conditioning / Ventilarea și condiționarea aerului*. Vol. 1, Vol. 2. Bucharest, Technical Publishing House, 1968, 1971.
[4] Chiriac, F., G. Bivol, and D. Hera. *Refrigeration equipment / Instalații frigorifice*. Bucharest, Didactic and Pedagogical Publishing House, 1975.
[5] Voicu, Victor. *Ventilation and air conditioning equipment / Instalații de ventilare și condiționare a aerului*. Bucharest, Technical Publishing House, 1984.

[6] Radcenco, Vsevolod. *Vortex cold and heat generators* / *Generatoare turbionare de frig și căldură*. Bucharest, Technical Publishing House, 1990.
[7] Radcenco, Vsevolod. *Criteria for optimising irreversible thermal processes* / *Criterii de optimizare a proceselor termice ireversibile*. Bucharest, Technical Publishing House, 1977.
[8] Ștefănescu, Dan, Mircea Marinescu, and Ioan Ganea. *Technical thermal-gas dynamics* / *Termogazodinamica tehnică*. Bucharest, Technical Publishing House, 1986.
[9] Nicolae, Dan, Romulus Lungu, and Constantin Cismaru. *Measurement of fluid parameters. Equipment and systems* / *Masurarea parametrilor fluidelor. Echipamente și sisteme*. Craiova, "Scrisul Romanesc" Publishing House, 1986.
[10] Exair Corporation, USA. *Vortex Tubes* / *Tuburi Vortex*. Product leaflet, 2021. Accessed on October 18, 2023. https://www.exair.com/products/vortex-tubes-and-spot-cooling-products.html.
[11] Teișanu, Florin. *Motor vehicle cooling installation* / *Instalație de răcire auto*. Patent No.119869B1/2005, filed with State Office for Inventions and Trademarks OSIM Bucharest.
[12] Teișanu, Florin, et al. *Compressed-air cooling device* / *Dispozitiv de răcire cu aer comprimat*. Patent No. 131145/2022, filed with State Office for Inventions and Trademarks OSIM Bucharest.
[13] Teișanu, Florin, Constantin Chelan, et al. *Applied research for the development of innovative methods, technologies and products in the field of electro-pneumatic equipment with gas-dynamic operation* / *Cercetări aplicative privind dezvoltarea unor metode, tehnologii și produse inovative în domeniul echipamentelor electropneumatice cu funcționare gazodinamică*. PN 19 38 01 02 Project, NUCLEU 2019-2022 Programme.

ISSN 1454 - 8003
Proceedings of 2023 International Conference on Hydraulics and Pneumatics - HERVEX
November 8-10, Băile Govora, Romania

FRUIT AND VEGETABLE DRYING MACHINE WITH ENERGY INDEPENDENCE

Ioan PAVEL[1,*], Gheorghe ŞOVĂIALĂ[1], Gabriela MATACHE[1], Valentin BARBU[1], Kati PAVEL[1], Ana-Maria POPESCU[1]

[1] National Institute of Research & Development for Optoelectronics/INOE 2000, Subsidiary Hydraulics and Pneumatics Research Institute/IHP

* pavel.ihp@fluidas.ro

Abstract: *Drying is one of the ways of long-term preservation of vegetables and fruits for industrialization or direct consumption without added preservatives. Throughout the year, there is a wide availability and diversity of fruits, vegetables, or medicinal plants that can be preserved by drying. To the costs of harvesting and drying one needs to add those of handling and transport, which are sometimes quite high; therefore, it is preferable to move the drying machines to the harvesting site of the products to be dried. Most of the time, these sites are isolated and do not have access to the electricity network; this raises the issue of energy independence of the drying facilities, i.e. the production of thermal and electrical energy from local resources around the harvesting points. The work presents an energy-independent drying machine that uses a Top-Lit-Up-Draft (TLUD) type hot air generator fed with wood chips for the production of thermal energy, and for the automation system the power supply is made from a 12V DC battery charged from photovoltaic panels.*

Keywords: *Energy-independent drying machine, solar PV panel, TLUD module, biomass, gasification*

1. Introduction

Drying is one of the oldest forms of preserving fruits and vegetables. Drying reduces the water content of the product in order to preserve it, but also reduces their mass and volume, which leads to lower packaging, storage and transport costs.

Convective drying is a high energy-consuming technology, which in many situations makes it dependent on cheap, local thermal energy sources.

Because biomass can be stored and used when needed, it remains the most versatile energy source for agricultural farms in various production processes [1,2,3].

By using the Top-Lit-Up-Draft (TLUD) type micro-gasification process, fuel gas and residual vegetable charcoal - commonly called biochar - are produced from biomass. Biochar is a sterile product that can be mixed with compost as an amendment in agricultural soils to increase their production capacity [4,5,6].

Due to the very long half-life of carbon residing in the soil, the incorporation of biochar resulting from the TLUD process achieves a sequestration of atmospheric carbon for very long periods of time and therefore leads to a negative CO_2 balance [4,6].

Compared to the direct combustion or wood gasification processes, the TLUD gasification process is characterized by very low values of the superficial velocity of the gases passing through the pyrolytic front. The slow process maintains a superficial velocity of the produced gas at very low values, which ensures a reduction of free ash being dragged along, as fine particles (PM2.5 - particles less than 2.5 micrometers in diameter), to a maximum value of 5 mg/MJbm at the exit of the burner, value far below the norm imposed in the EU in 2015 for biomass burning processes, which is below 25 mg/MJ [6].

The working principle of the TLUD type gasifier is shown in figure 1. The gas generator consists of a gasifier with an upward gasification air stream, connected to a burner. The biomass is introduced into the reactor and rests on a grate through which the primary air for gasification passes, from bottom to top. The ignition and initiation of the pyrolytic front is done at the upper part of the gas generator, and it advances in the biomass layer. Pyrolysis results in gas, tar and coal. The tars pass through the layer of incandescent coal, are cracked and completely reduced due to the heat radiated by the pyrolysis front and the flame in the upper part. The resulting gas is mixed with the secondary combustion air that is preheated by the reactor wall and is introduced into the combustion zone through the holes located at the top of the reactor. The highly turbulent mixture burns with a flame at temperatures up to 900ºC.

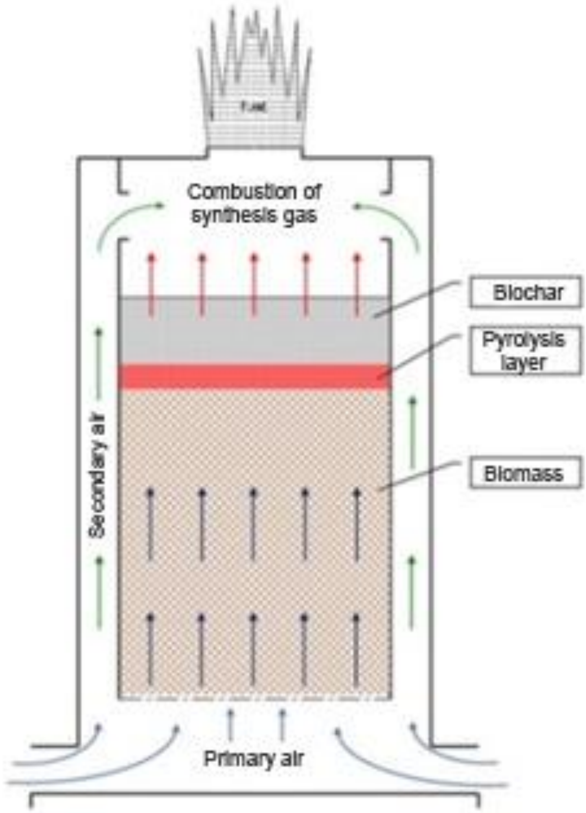

Fig. 1. Functional diagram of the TLUD energy module [7]

Removing excess water from the raw material is conditioned by heat transmission and the state and movement of water vapour. Heat transmission is based on the temperature difference between the material subjected to dehydration (fruits, vegetables, etc.) and the heat carrier (hot air).
During the dehydration of fruits and vegetables in an air stream, the free water is carried away immediately by evaporation. This rapid evaporation depends on the total surface of the fruits (or vegetables), the speed of air circulation and the difference between the surface tension of the vapours on the surface of the material and the surface tension of the vapours in the air stream. During the drying of fruits and vegetables, the water from the cell juice diffuses to the surface, due to internal diffusion, and evaporates. It is important that only the water evaporates during the drying process, not the aromas that give the fruit its taste and flavour.
The movement of water from inside the product to the outside is a result of the internal diffusion process and is the direct consequence of the difference in osmotic pressure determined by a different concentration in soluble substances of the liquid inside and at the periphery of the product particle.
The movement of water takes place from points with a higher water content to those with a lower content, resulting from the evaporation of water through the phenomenon of external diffusion. Thanks to the internal diffusion, the humidity is finally equalized in all the layers of the product subjected to dehydration.
The optimal development of the process (figure 2) occurs when the rate of water evaporation from the surface of fruits and vegetables is equal to the rate of moisture migration from the inside to their surface.

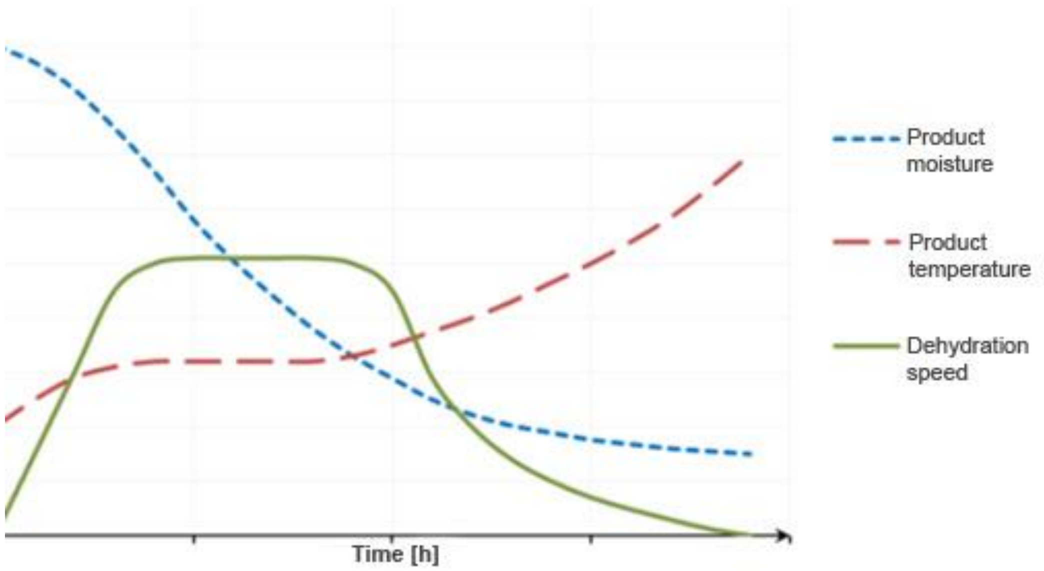

Fig. 2. Theoretical chart of the drying process

2. Materials and methods

2.1 Structure of the drying machine

The fruit and vegetable drying machine has three major subassemblies: a drying chamber with trays, a hot air generator based on the TLUD principle, and a control module.

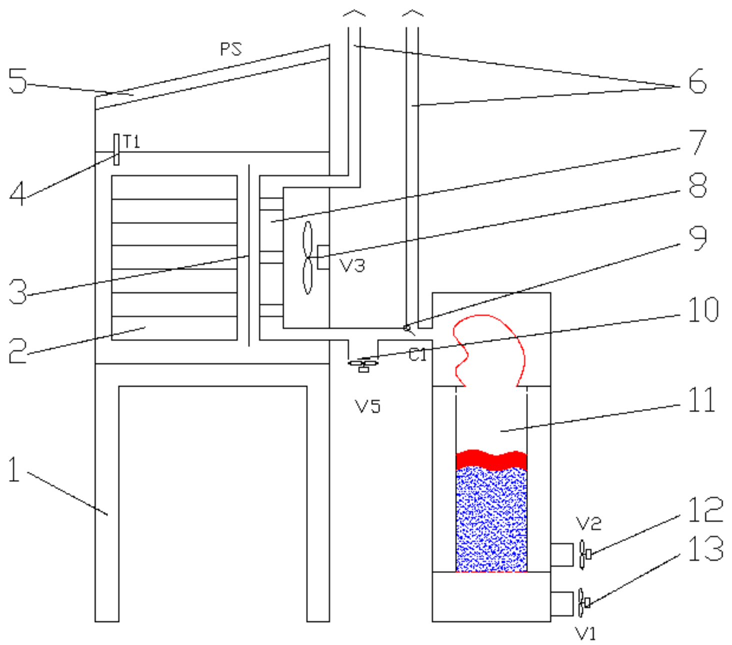

1- Frame
2- Drying trays
3- Deflector
4- Thermometer
5- Solar PV panel
6- Natural draft tubing
7- Heat exchanger
8- Hot air fan
9- Smoke flap valve
10- Cooling fan
11- TLUD hot air generator
12- Combustion air fan
13- Gasification air fan

Fig. 3. Energy-independent vegetable and fruit drying machine - components

The drying machine shown in figure 3 consists of a frame (1) on which a drying chamber is placed, in which there is, next to the drying trays (2), a smoke-to-air heat exchanger (7) that is ventilated by the fan (8) and directs the hot air flow through a deflector (3) - that evens out the temperature and speed of the hot air in the chamber - towards the trays with material to be dried.

The temperature in the chamber is controlled by the thermocouple (4) which controls the flap valve (9) and directs the flow of hot smoke to the exchanger (7) in the chamber or to the atmosphere through the tubing (6) depending on the temperature requirements of the drying program. If the desired temperature is accidentally exceeded or the drying process requires the temperature in the chamber to decrease, the flap valve (9) closes the direction to the exchanger, and the fan (10) introduces cold air from the atmosphere into the exchanger, cooling it. The control signals for running the drying program (figure 4) are generated with the help of a PLC which is supplied with electricity from a battery pack charged from the photovoltaic panel (5). The power of the hot air generator (11) can be controlled by controlling the speed of the fans (12,13), keeping the optimal 1/3 ratio of gasification air/combustion air.

2.2 Sizing of the drying machine

Energy characteristics of energy-independent drying machines [8] are listed in Table 1 below.

Table 1: Energy characteristics of energy-independent drying machines

Parameter	Unit	Value
Positioning surface on trays	m^2	5.00
Specific thermal power	kW/m^2.cas	2.00
Rated thermal power	kW	10.00
Specific drying agent flow rate	$(Nm^3/h)/m^2$.cas	300.00
Drying agent flow rate	Nm^3/h	1500.00
Pressure drop across the drying machine	Pa	80.00
Minimum total fan efficiency		0.40
Fan electric power	W	83.33
PLC supply electric power	W	10.00
Power consumed by a transducer	W	5.00
Power consumed by a servomotor	W	5.00
No. of transducers	-	2.00
No. of servomotors	-	2.00
Automation electric power	W	30.00
Required electric power	W	113.33
Hours of daily use	h	12.00
Daily required electricity	kWh/day	1.36

Parameters related to thermal energy supply to the drying machine [8] are presented in Table 2.

Table 2: Thermal energy supply - related parameters

Parameter	Unit	Value
Positioning surface on trays	m^2	5.00
Specific thermal power	kW/m^2.cas	2.00
Rated thermal power	kW	10.00
Shredded local biomass - dimensions	mm	10...50
Shredded local biomass - moisture	%	<20
Shredded biomass layer medium density	kg/m^3	250

No. of TLUD energy modules	pcs	1
Flue gas/air minimum efficiency	-	0.85
Maximum required thermal power	kW	11.76
TLUD energy module rated power	kW	15
Shredded biomass PCI (Pouvoir Calorifique Inférieur)	MJ/kg	15.00
Share of biochar produced from biomass	%	15
Fully gasified biomass PCI	MJ/kg	14.00
Maximum hourly biomass consumption	kg/h	4.46
Average hourly biomass consumption (75%)	kg/h	3.34
Average drying time/batch	h	6.00
Biomass consumption in one batch	kg/batch	20.06
No. of batches per day	batch/day	2.00
No. of biomass loads/batch		2.00
Mass of fuel loaded into the reactor	kg	10.03
Reactor volume for shredded biomass	dm^3	40.12
Daily biomass consumption	kg/day	40.12
Daily consumed volume of shredded biomass	dm^3/day	160.50
Daily produced biochar mass	kg.ch/day	6.02
CO_2 equivalent mass sequestered in biochar	kg.CO_2/day	22.07

The photovoltaic panel for the production of electricity has a surface area of about 2 m^2 and is connected to a 50 Ah battery pack. This constrictive variant ensures total energy independence, which makes it possible to reside continuously in isolated locations for longer periods of time.
The electricity requirement - related parameters [8] are shown in Table 3 below.

Table 3: Electricity requirement - related parameters

Parameter	Unit	Value
Power supply only from a 12V DC battery		
Charging / discharging energy yield	-	0.87
Battery discharge limit	%	20
Minimum required battery capacity	Ah	**162.84**
Power supply with PV panel + battery		
Lighting hours in an average summer day	h/day	**9.00**
PV panel lighting level	%	66
Specific rated electric power	W/m^2	150
Daily produced electricity	Wh	1469.20
Minimum required PV panel area	m^2	1.649
PV panel area	m^2	2
Power supply safety factor		1.2
Required battery capacity	Ah	**48.85**

The drying machines can be used in stationary mode at the farm premises; the electricity supply is made from the single-phase 220V AC electrical network with a 220V AC/12V DC power supply connected to the battery pack with which the continuity of the drying process can be ensured even during periods of network failure.

2.3 Drying rules

The drying process is considered to be carried out normally when the mass of the product dries uniformly and when, in a dry state, the vegetables meet the qualitative conditions required by the internal standards and norms in force.
The hot air must enter the drying machine at a maximum temperature of 80°C - in principle, as much as the product can withstand - and a relative humidity of about 25%, so that the product can be dried at a minimum of 8% humidity. This air leaves the drying machine at a temperature of 40-45°C (rarely 50°C) with a relative humidity of 60-80% to avoid condensation.
When the product heats up too much and dries unevenly, partial frying or softening occurs, acquiring a foreign smell. Such drying is considered defective.
Drying vegetables and fruits at sub-optimal temperatures inevitably leads to longer drying times, which leads to transient softening of the raw material and a change in its colour.
The softening of the product is also caused by the poor air circulation in the drying machine and is directly caused by the microbiological changes that can occur in this case, changes that consist in the appearance of sour taste, dark colour, loss of nutritional quality.
In order to prevent partial frying or softening of the product, it is necessary to systematically monitor the air temperature variations in the drying machine during the drying process and to adjust in advance both the entry of fresh air and the exit of moist air.
To accelerate the drying process, it is necessary that the relative humidity of the hot air be reduced, and its circulation speed be increased. The decrease in the relative humidity of the thermal agent is obtained by raising its temperature; this decrease translates into an increase in its absorption capacity.
Excessively raising the air temperature above the established limit can adversely influence the process. For example, it is possible that a crust may form on the surface of the product, especially in the case of fruits, which prevents the evaporation of water from the deeper layers.
In the first part of the drying, the air speed has an important influence, since in addition to the function of a heating agent, the air also has the function of taking over and conveying the water vapours resulting from evaporation. The faster the removal of water vapours will be, the better conditions will be created for other quantities of water to migrate to the surface of the products. In the second phase of drying, when vaporization occurs inside the product, the air speed has a much smaller influence on the drying speed.

2.4 Operating principle

To control the temperature of the hot air in the drying machine, a temperature sensor T1 (figure 4) is used, which is fixed in the place where the hot air passes to the products to be dried.
The temperature control is done with a PLC that controls the C1 flap valve for hot air access to the exchanger or its evacuation into the atmosphere. If the temperature in the drying machine is too high, flap valve C1 closes the access of hot air to the exchanger, directing it to the atmosphere, and the cooling fan V5 turns on and introduces cold air from the atmosphere into the heat exchanger, reducing its temperature. The PLC also controls the speed of the V3 fan, obtaining the variation of hot air flow and the variation of the amount of heat extracted from the heat exchanger.

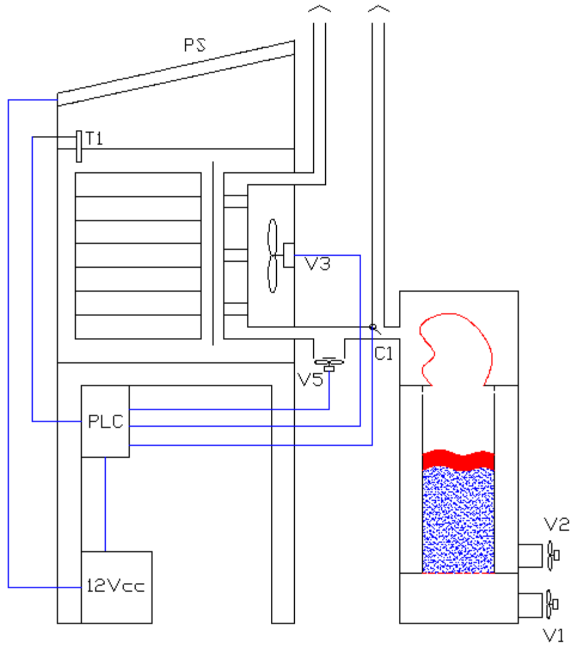

Fig. 4. Control module (wiring diagram)

The power of the TLUD generator can be adjusted manually depending on the requirements of the drying process, from the flow of gasification air and combustion air supplied by the V1 and V2 fans. It should be noted that varying the temperature in the drying machine is done with a relatively large hysteresis, which requires a flexibility of the drying mode programmed in the PLC.

3. Conclusions

This article presents a solution for a convective drying installation with total energy independence intended for isolated areas which uses a mixed system for the production of the necessary energy: thermal energy - produced with a hot air generator based on the TLUD principle, in which shredded local biomass is used, and electricity - produced with photovoltaic panels connected to a battery pack.
The hot air generator on the TLUD principle is characterized by high energy conversion efficiency, biochar production and very low CO and particulate matter (PM) pollutant emissions; it is easy to use and safe in operation; it is tolerant to variations in the properties of the biomass, both chemical and dimensional, which ensures great adaptability to the variety of local biomass resources.
In order to carry out the dehydration process in optimal conditions, the maximum temperature that each product to be dried can withstand must be determined, as well as the temperature entering the drying machine and the temperature at which the moisture-laden air must exit, in order to avoid its condensation.
The automation scheme meets the requirements for temperature control (increase and decrease) and the variation of air speed in the drying machine corresponding to the drying process of vegetables and fruits.

Acknowledgments

This work was supported by a grant of the Ministry of Research, Innovation and Digitization, CCCDI - UEFISCDI, project number PN-III-P2-2.1-PTE-2021-0306, Financial Agreement no. 87PTE/ 21.06.2022, within PNCDI III. It has also received financing under a project funded by the Ministry of Research, Innovation and Digitization through Programme 1- Development of the national research & development system, Sub-programme 1.2 - Institutional performance - Projects financing the R&D&I excellence, Financial Agreement no. 18PFE/30.12.2021.

References

[1] Daugherty, Erik Christian. *Biomass Energy Systems Efficiency: Analyzed through a Life Cycle Assessment*. Master's of Science Thesis. Lund University, February 2001.
[2] Mujumdar, Arun S. (Ed.) *Handbook of Industrial Drying*. 2nd Edition, Revised and Expanded, Volume 2. Boca Raton, CRC Press, 1995.
[3] Murad, Erol, Victor-Viorel Safta, and Georgeta Haraga. "Biomass – a regenerating source of thermal energy for drying installations." Paper presented at ISIRR 2009 – 10th International Symposium "Interdisciplinary Regional Research" – Romania – Hungary – Serbia, Hunedoara, Romania, April 23-24, 2009.
[4] McLaughlin, Hugh, Paul S. Anderson, Frank E. Shields, and Thomas B. Reed. "All Biochars are Not Created Equal, and How to Tell Them Apart." Paper presented at North American Biochar Conference, Boulder, Colorado, USA, August 9-12, 2009.
[5] Mukunda, H.S., S. Dasappa, P. J. Paul, N. K. S. Rajan, Mahesh Yagnaraman, D. Ravi Kumar, and Mukund Deogaonkar. "Gasifier stoves – science, technology and field outreach." *Current Science* 98, no. 5 (March 2010): 627-638.
[6] Murad, E., A. Culamet, and G. Zamfiroiu. "Biochar - economically and ecologically efficient technology for carbon fixing." Paper presented at the 19th International Salon on Hydraulics and Pneumatics HERVEX 2011, Călimăneşti-Căciulata, Romania, November 9-11, 2011.
[7] Maican, Edmond, Iulian Claudiu Duţu, Gabriela Matache, Cătălin Dumitrescu, and Ioan Pavel. "CFD analysis of an improved TLUD based equipment for heating small greenhouses and hothouses." *INMATEH - Agricultural Engineering* 53, no. 3 (December 2017): 5-12.
[8] Murad, E., M. Vintilă, and A. Crăciunescu. "Dryers with low ecological impact for mountainous areas" / "Uscătoare cu impact ecologic redus pentru zone montane." Paper presented at ICDIMPH-HORTING 2012 Annual Session of Scientific Communications, Bucharest, Romania, September 20, 2012.

ISSN 1454 - 8003
Proceedings of 2023 International Conference on Hydraulics and Pneumatics - HERVEX
November 8-10, Băile Govora, Romania

ASPECTS OF THE USE OF AI (ARTIFICIAL INTELLIGENCE) TECHNOLOGY IN CONSTRUCTION EQUIPMENT MANAGEMENT

Mihail Ioan SAVANIU[1], Oana TONCIU[1], Radu PANAITESCU – LIESS[1], Cristina SESCU- GAL[1], Magdalena CULCEA[2], Anca Ruxandra SASU[1]

[1] Technical University of Civil Engineering Bucharest (UTCB) – Faculty of Mechanical Engineering and Robotics in Constructions

mihai.savaniu@utcb.ro; oana.tonciu@utcb.ro; liess.panaitescu@utcb.ro; cristina.sescu-gal@utcb.ro; anca-ruxandra.sasu@utcb.ro

[2] Technical University of Civil Engineering Bucharest (UTCB) – Faculty of Building Services Engineering

magdalena.culcea@utcb.ro

Abstract: *In this paper, the authors want to present some aspects related to the use of AI technology for continuous monitoring of technological processes in a construction site. The authors present preliminary experimental studies undertaken in the implementation of AI technology in the field of construction machinery through the realization of a low-cost hardware platform. The platform allows the development of preliminary tests on the optimization of construction equipment trajectories. The envisaged platform involves the use of affordable equipment such as the Arduino Nano 33 development platform and a small drone for aerial filming. The paper presents the preliminary tests carried out with in defining trajectories for construction equipment.*

Keywords: *Construction equipment, drone, artificial intelligence, optimal trajectory*

1. Introduction

The use of AI technology for continuous monitoring of technological processes on the construction site leads to improved working conditions and thus to higher levels of occupational safety and health on construction sites. At the same time, it increases the productivity of the entire construction process, reduces costs, improves supply chain management, reduces resource consumption and waste generation on construction sites. From a cultural point of view, the introduction of AI technologies on a construction site contributes decisively to raising the technical cultural level of human resources working in the construction sector.

The integration of artificial intelligence (AI) technology into construction equipment management has the potential to significantly improve efficiency, safety, project outcomes. In the case of construction equipment, AI technology can be integrated, for:

- Predictive maintenance: AI can analyze sensor data and equipment performance history to predict when construction equipment is likely to fail. This enables proactive maintenance, reducing downtime and avoiding costly repairs.
- Condition monitoring: Real-time monitoring via AI allows the condition of construction equipment to be assessed. Sensors and data analytics can detect anomalies or the onset of wear, allowing timely intervention before major problems occur.
- Optimized equipment management: AI technology can analyze the work sequences of the adopted construction technology project, check resource availability and equipment capabilities to optimize the layout of construction equipment. This ensures that equipment is used efficiently, reducing downtime and maximizing productivity.
- Automated operation and control: Artificial intelligence can enable autonomous or semi-autonomous operation of construction equipment. This includes technologies such as automated levelling systems, robotic construction equipment and autonomous systems that can increase accuracy, productivity and operational safety.

- Energy efficiency: Artificial intelligence algorithms can be used to optimise the energy consumption of construction equipment. This includes intelligent scheduling of equipment operation and energy efficient use, contributing to cost reduction and environmental sustainability.
- Ensuring personnel safety: AI-driven cameras and sensors can monitor construction sites for safety compliance. This includes detecting potential hazards, ensuring the use of personal protective equipment and alerting operators to unsafe conditions.
- Inventory management and resource management: AI can help manage construction equipment fleets, track equipment location, enforce maintenance schedules. This helps to allocate resources efficiently, reducing the costs associated with over- or under-use of construction equipment.

As the construction industry continues to embrace digital transformation, the integration of AI in equipment management holds the potential to revolutionize how construction projects are planned, executed, and maintained. However, it's essential to address challenges such as data privacy, security, and workforce training when implementing AI technologies in construction [1,2].

According to reference [3] robotics, AI, and the Internet of Things can reduce building costs by up to 20 percent. Companies are using AI to develop safety systems for worksites. AI is being used to track the real-time interactions of workers, machinery, and objects on the site and alert supervisors of potential safety issues, construction errors, and productivity issues. Despite the predictions of massive job losses, AI is unlikely to replace the human workforce. Instead, it will alter business models in the construction industry, reduce expensive errors, reduce worksite injuries, and make building operations more efficient. Leaders at construction companies should prioritize investment based on areas where AI can have the most impact on their company's unique needs. Early movers will set the direction of the industry and benefit in the short and long term.

The research aims to develop a hardware platform for implementing AI technology in the field of low-cost construction machinery. This approach requires the use of low-cost and affordable equipment. Thus for aerial filming of work processes we will use a drone with a mass of less than 250 grams and for the interpretation of images in order to define trajectories we will use a specialized open-source platform such as Arduino Nano 33 BLE. The paper presents how to define trajectories of construction equipment using this type of microcontroller.

Microcontrollers implemented on Arduino development boards, are compact integrated circuits developed to perform a specific operation. They are basically small computers that consist of a processor, memory and input/output (I/O) peripherals, all on a single chip.

Also called MCUs, they are embedded in billions of gadgets such as cars, robots, medical devices, home appliances, drones, 3D printers, toys, smart plugs. These miniature personal computers that have no operating system were developed to control larger entities. In addition, the current trend is to connect these devices, creating what is called the Internet of Things (IoT) [4,5].

Arduino is on the one hand an open-source platform, and on the other a community focused on making microcontroller application development accessible to everyone. There are several practical reasons for wanting to implement Machine Learning ML on microcontrollers. One of these would be that we want a smart device to be able to operate quickly regardless of whether the internet is present or not. Another reason is cost - these hardware devices are simple and low cost. We also want privacy, i.e. not to share all our data outside. Last but not least, these devices are energy efficient.

2. Hardware and software resources used

TinyML (Tiny Machine Learning) is a field of machine learning, dedicated integrated circuits, algorithms and software that have the ability to perform data analysis using sensors (video, audio, IMU, etc.) with extremely low power consumption. [6]. Arduino Nano 33 BLE Sense rev2 with connectors is a board used for Machine Learning from Arduino, having a small form factor and comes equipped with a set of sensors.

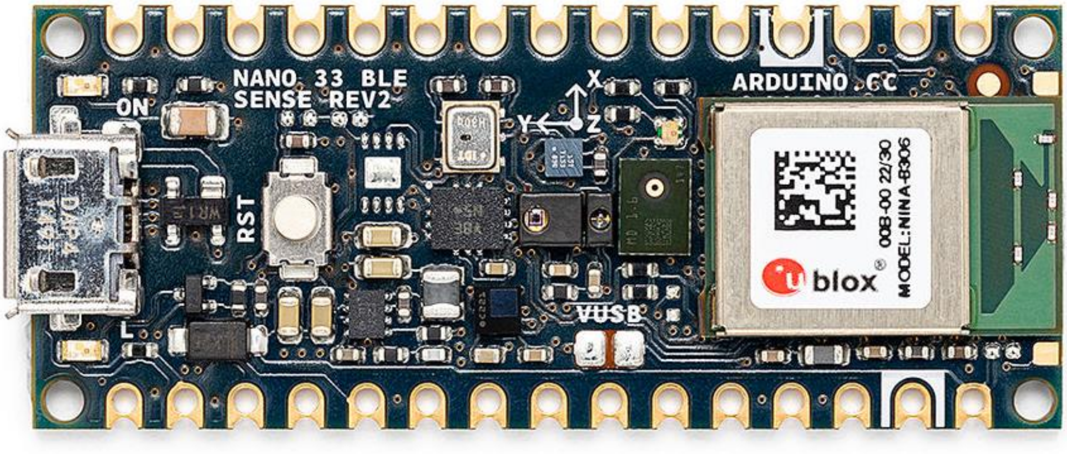

Fig. 1. Arduino Nano 33 BLE Sense Arduino Board [4]

The main feature of this board, in addition to on-board sensors, is the ability to run Edge Computing (AI) applications using TinyML. The features are shown in the table 1.

Table 1

Microcontroller	nRF52840 (Arm Cortex-M4)
Operating voltage	3.3V
Maximum input voltage	21 V
DC current at I/O pins	15 mA
Clock Speed	64MHz
CPU flash memory	1MB (nRF52840)
SRAM	256KB (nRF52840)
Digital Input/Output Pines	14
PWM pins	14
UART	1
SPI	1
I2C	1
Analogue input pines	8 (ADC 12 bit 200 k samples)
Analogue output pines	Only through PWM

External Interrupts	All digital pins
LED_BUILTIN	13
USB	Native in nRF52840 CPU
IMU	BMI270 and BMM150
Microphone	MP34DT06JTR
Motion, vibration and orientation sensor	APDS9960
Pressure sensor	LPS22HB
Temperature and humidity sensor	HS3003

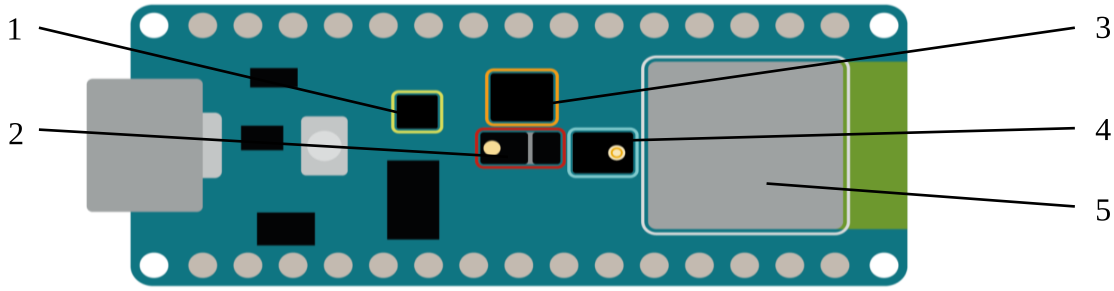

Fig. 2. Arduino Nano 33 BLE Sense board schematic [6]

Figure 2 shows the Arduino Nano 33 BLE, as follows:
1 Temperature, humidity and pressure sensor;
2 Colour, brightness, proximity and gesture sensor;
3 Motion, vibration and orientation sensor;
4 Digital microphone;
5 Arm-Cortex-M4 microcontroller

3. Implementation

The productivity of a construction machine depends, among other things, on the path it takes during the working process. It is clear in this respect that a desideratum is to optimise the mechanisation scheme so that it tends towards a maximum possible value.
For this purpose, we filmed a construction equipment aerial filming a job to move a landfill. The filming was done with a DJI MINI 3 drone which filmed the equipment from a fixed point about 7 meters away during the work process. In fig. We present the drone used and a sequence of the working process of the equipment in an aerial filming.

Fig. 3. Drone used in aerial filming (left). Aerial filming with the equipment (right)

To define the trajectories, we have approached Machine learning technology is a subset of artificial intelligence. Machine learning is an area of artificial intelligence that uses statistical techniques to provide computer systems with the ability to "learn" from previously collected data without being explicitly programmed. An ML becomes more efficient at understanding and providing information as it is exposed to more data-the better trained it is. This can be achieved through ML technology using an Arduino Nano 33 BLE Sense board installed on the shield for ease of use as shown in Fig. 4.

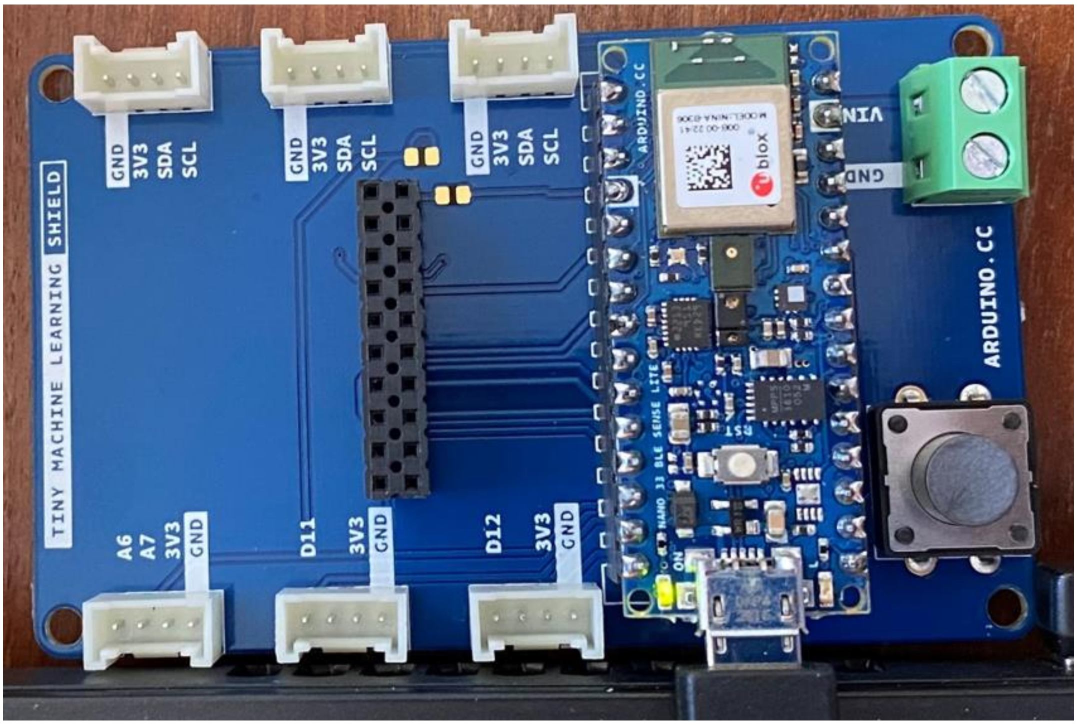

Fig. 4. Shield Arduino Arduino Nano 33 BLE Sense

In order to implement the Ardunino Nano 33 BLE board for our application, there are several steps we plan to take. For example, for the generation of the trajectory we have:

- Install the plate on a mechanized model (mock-up) to generate in the laboratory different trajectories that we will save on https://tinyml.seas.harvard.edu/magic_wand/
- Training the ML model
- Carry out experiments on site

The first step was to generate trajectories via the Arduino Nano 33 BLE Sense board. For this we ran the Magic Wand code (default) from the Arduino IDE examples. After connecting the board via the Bluetooth button in the https://tinyml.seas.harvard.edu/magic_wand/ app, the trajectories were uploaded (an example is shown in Figure 5).

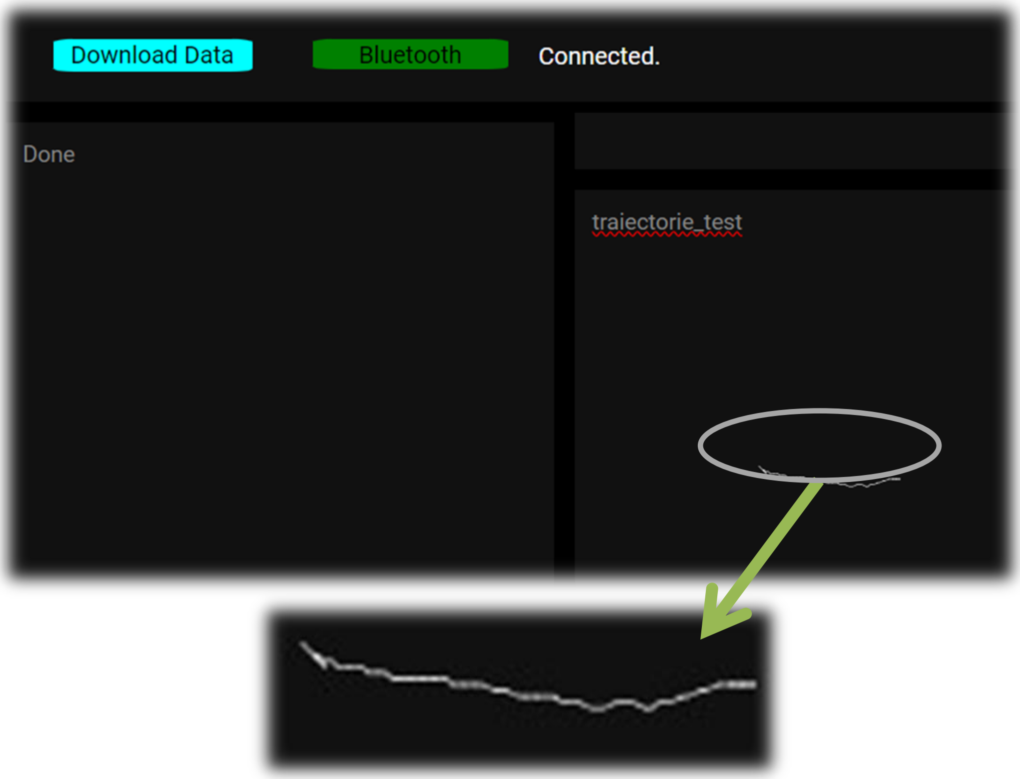

Fig. 5. Recording made by moving the Arduino Nano 33 BLE Sense board

4. Conclusions

Following the aerial drone filming experiment and the tests carried out with the Arduino 33 BLE Sense development board, the possibility of realizing a low-cost hardware platform to be used for implementing AI in construction equipment management is assured.
While early tests are encouraging, one challenge will be to see how the Arduino 33 BLE Sense board performs when generating large trajectories. However, the authors aim to move to the next steps by making multiple trajectories and training the ML model to obtain an optimal trajectory for construction equipment.

Acknowledgments

This work is part of the ARUT Competition Program for the financing of the scientific research in UTCB, project title Optimising mechanisation processes in construction using artificial intelligence project acronym OPTIMEC, code $GnaC_{2023}^{ARUT}$-UTCB-20.

References

[1] Abioye, Sofiat O., Lukumon O. Oyedele, Lukman Akanbi, Anuoluwapo Ajayi, Juan Manuel Davila Delgado, Muhammad Bilal, Olugbenga O. Akinade, and Ashraf Ahmed. "Artificial intelligence in the construction industry: A review of present status, opportunities and future challenges." *Journal of Building Engineering* 44 (December 2021): 103299.

[2] Skycatch, Inc. ″Data Analytics Package (DAP). Our Construction Solution: The only automated drone data solution for construction enterprises.” Accessed October 10, 2023. https://skycatch.com/drone-photogrammetry.

[3] Rao, Sumana. ″The Benefits of AI In Construction.” *Trimble. Construction*, April 6, 2022. Accessed October 10, 2023. https://constructible.trimble.com/construction-industry/the-benefits-of-ai-in-construction.

[4] Mistry, Sandeep, and Dominic Pajak. ″Get Started With Machine Learning on Arduino.” *Arduino Documentation*. Accessed October 10, 2023. https://docs.arduino.cc/tutorials/nano-33-ble-sense/get-started-with-machine-learning.

[5] Lutkevich, Ben. ″microcontroller (MCU).” *TechTarget*. Accessed October 10, 2023. https://www.techtarget.com/iotagenda/definition/microcontroller.

[6] tinyML Foundation. ″About tinyML Foundation.” Accessed October 10, 2023. https://www.tinyml.org/about/.

[7] Arduino S.r.l. ″Arduino Nano 33 BLE Sense Rev2.” Accessed October 10, 2023. https://store.arduino.cc/products/nano-33-ble-sense-rev2.

[8] Ardushop S.R.L. ″Arduino® Nano 33 BLE Sense Rev2 with headers.” / ″Arduino® Nano 33 BLE Sense Rev2 cu pini.” *ArduShop*. Accessed October 10, 2023. https://ardushop.ro/ro/electronica/2730-arduino-nano-33-ble-sense-rev2-with-headers.html.

[9] Ramírez, Lorenzo. ″Physics with Arduino nano 33 BLE Sense and Phyphox: all sensors in one.” / ″Física amb Arduino nano 33 BLE Sense i Phyphox: tots els sensors en un.” *Free experimentation. A resource block for Experimental Sciences / Experimentació lliure. Un bloc de recursos per a les Ciències Experimentals*, May 9, 2021. Accessed October 10, 2023. https://experimentaciolliure.com/2021/05/09/fisica-amb-arduino-nano-33-ble-sense-i-phyphox-tots-els-sensors-en-un/.

ISSN 1454 - 8003
Proceedings of 2023 International Conference on Hydraulics and Pneumatics - HERVEX
November 8-10, Băile Govora, Romania

IMPLEMENTING THE FUNCTIONALITY OF ELECTROHYDRAULIC ACTUATED MACHINES BY PROGRAMMABLE LOGIC CONTROLLER PROGRAMMED USING FINITE-STATE MACHINE

Robert BLEJAN[1,*], Marian BLEJAN[1], Alexandru IONESCU[2]

[1] National Institute of Research & Development for Optoelectronics/INOE 2000, Subsidiary Hydraulics and Pneumatics Research Institute/IHP, Bucharest

[2] National Institute of Research-Development for Machines and Installations Designed to Agriculture and Food Industry INMA

* robertblejan.ihp@fluidas.ro

Abstract: *Electrohydraulic driven machines are widely used due to the high-power density per volume unit as well as due to the high actuation forces and moments. The operation of these machines is managed by a Programmable Logic Controller (PLC). This paper proposes the processing of the operation of the electrohydraulic actuated machine in the operating program of the PLC using finite-state machine. Thus, a state machine developed for the reduction of hydraulic shocks induced by the switching of the electrohydraulic equipment will be presented. Also, the implementation of the movements performed by the hydraulic actuators, imposed by the operation of the machine, is carried out by another state machine.*

Keywords: *Electrohydraulic, finite-state machine, PLC*

1. Introduction

A finite-state machine (FSM) or finite-state automaton (FSA, plural: automata), finite automaton, or simply a state machine, is a mathematical model of computation. It is an abstract machine that can be in exactly one of a finite number of states at any given time. The FSM can change from one state to another in response to some inputs; the change from one state to another is called a transition.
An FSM is defined by a list of its states, its initial state, and the inputs that trigger each transition [1].
In control applications, two types are distinguished:
Moore machine
The FSM uses only entry actions, i.e., output depends only on state. The advantage of the Moore model is a simplification of the behaviour.
Mealy machine
The FSM also uses input actions, i.e., output depends on input and state. The use of a Mealy FSM leads often to a reduction of the number of states.
In this material, Mealy machine are used because they allow representing the process in a smaller number of states. The state diagrams used are of the type represented in fig. 1, the transition between State 1 and State 2 is triggered by the occurrence of an event followed by the execution of an actions list.

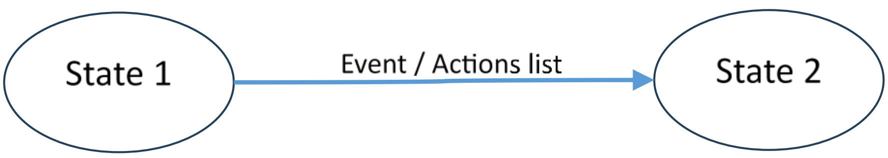

Fig. 1. Finite-State Machine representation as a state diagram

2. State-machine for hydraulic shock reduction

One can notice that if the activation of the valves that distribute the hydraulic fluid to drive is carried out at low pressure values, the hydraulic shock has low values. Taking into account this fact, it is proposed to activate the distribution valves for the hydraulic drive, followed by an adjustable delay of 25...500ms, and then the activation of the working pressure of the drive. When the hydraulic drive stops actuating, the hydraulic pressure to the drive is turned off, followed by an adjustable delay, and then the hydraulic fluid distribution valves to the drive are turned off. The values of these delays are determined experimentally, aiming to obtain the smallest possible shocks when starting and stopping the hydraulic drive.

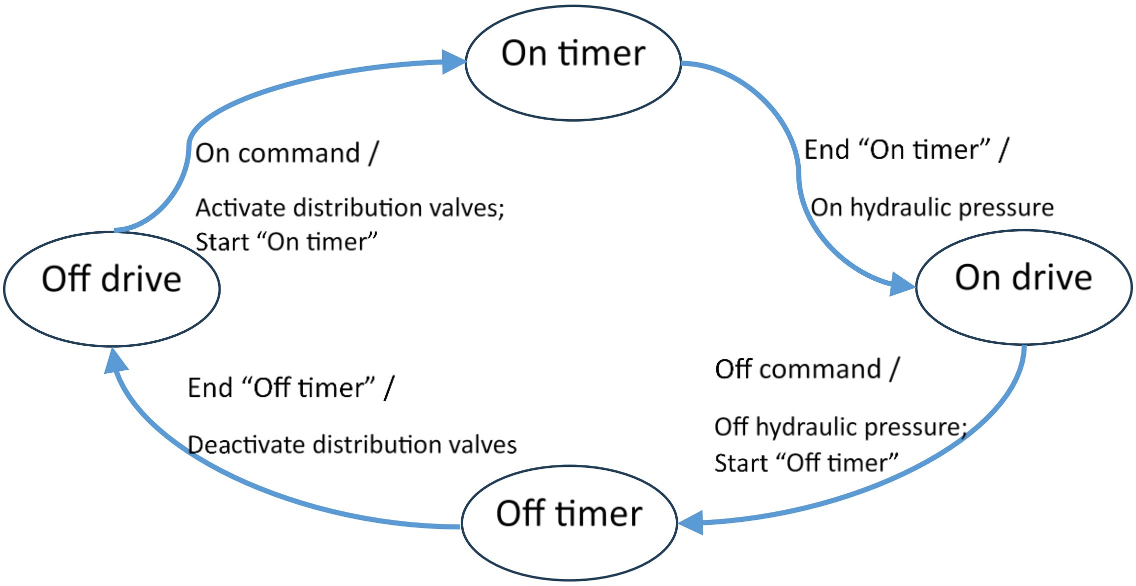

Fig. 2. State diagram for hydraulic shock reduction

3. State-machine for machine operation

State-machine for machine operation runs simultaneously with the state-machine for hydraulic shock reduction. When the operation of the machine requires hydraulic drive, the on or off command is sent, which is executed by the state-machine intended to reduce the hydraulic shocks of the drive.
As an example, the state machine designed to control the hydraulic cylinder used to close the mold and extract the piece, component of a hydraulic press, will be presented in fig. 3.
The following abbreviations have been used:

- INIT → initialization state
- WAIT → wait state
- RETR → retracts state
- INCR → close the mold in retract state
- INCA → close the mold in extend state
- EXTR → extract the piece state
- LE → extract limit switch
- LI → close the mold limit switch
- LR → retract limit switch
- RE → retract button

- IM → close the mold button
- EP → extract the piece button
- MRE → start retract command
- MORE → stop retract command
- MAE → start extend command
- MOAE → stop extend command

The commands MRE, MORE, MAE and MOAE are each implemented through a state machine, as in fig. 2.

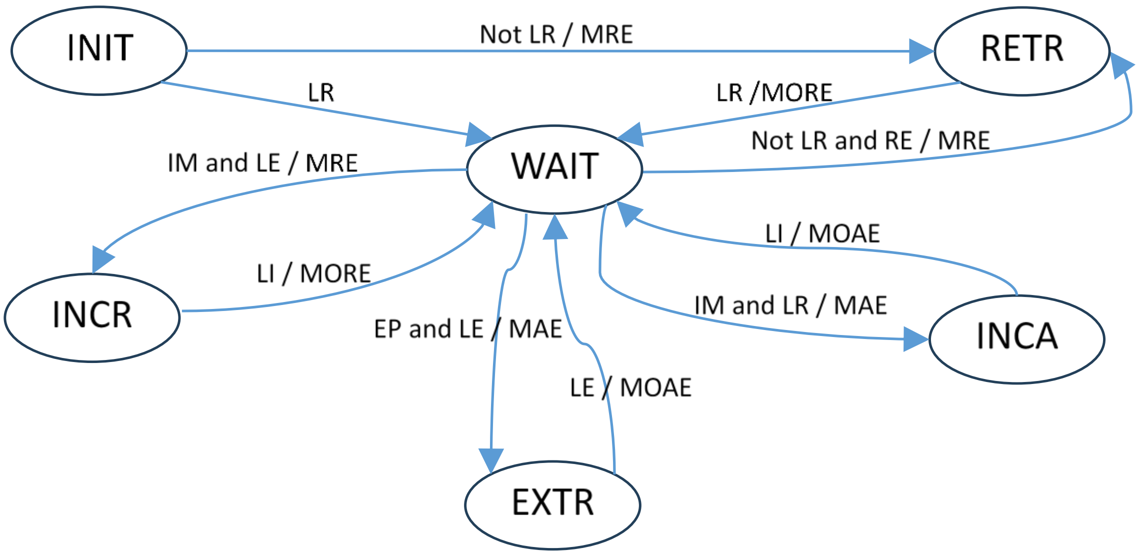

Fig. 3. State-machine for press actuator

4. Implementation of state-machine on PLC

A programmable logic controller (PLC) or programmable controller is an industrial computer that has been specifically designed to operate reliably in harsh usage environments and conditions, such as strong vibrations, extreme temperatures and wet or dusty conditions, and adapted for the control of manufacturing processes, such as assembly lines, machines, robotic devices, or any activity that requires high reliability, ease of programming, and process fault diagnosis. [2]
Programmable logic controllers are intended to be used by engineers without a programming background. For this reason, a graphical programming language called Ladder Diagram (LD, LAD) was first developed. It resembles the schematic diagram of a system built with electromechanical relays and was adopted by many manufacturers and later standardized in the IEC 61131-3 control systems programming standard. As of 2015, it is still widely used, thanks to its simplicity. [3]
A PLC works in a program scan cycle, where it executes its program repeatedly. The simplest scan cycle consists of 3 steps: read inputs, execute the program, write outputs. [4]
The state machine is programmed similarly to the "CASE" or “SWITCH” statement, an instruction common to high-level programming languages such as C, Pascal, Java, etc. In computer programming languages, a switch statement is a type of selection control mechanism used to allow the value of a variable or expression to change the control flow of program execution via search and map. [5]
Fig. 4 shown the ladder diagram implementation of the state-machine for hydraulic press actuator (see fig. 3). The variable used to control flow of program execution is the current state of the state-

machine, "STARE". The "IESIRE" bit is used to finish "CASE" statement after execution of instructions for current state.

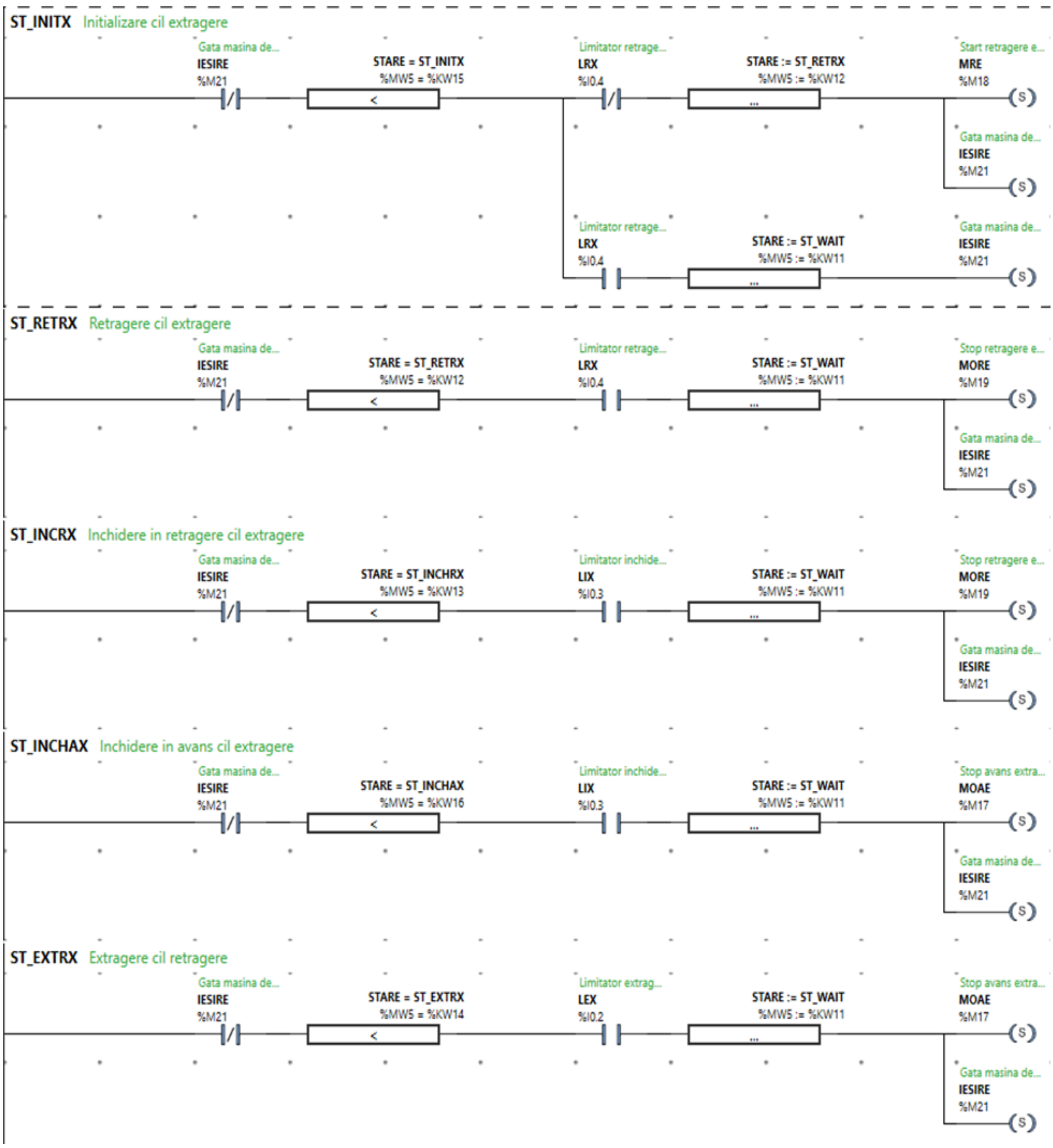

Fig. 4. Partial state-machine ladder diagram

5. Conclusions

The operation of electrohydraulic driven machines can be easily described using state-machines. On the other hand, the software implementation of a state machine to be executed on a PLC is also an easy task. The paper presents the solution of some practical applications, the reduction of hydraulic shocks and the implementation of specific movements for a hydraulic cylinder, using this type of process modelling.

Acknowledgments

This work was supported by a grant of the Ministry of Research, Innovation and Digitization, CCCDI - UEFISCDI, project number PN-III-P2-2.1-PTE-2021-0429, Financial Agreement no. 85PTE/2022, within PNCDI III. It has also received financing under a project funded by the Ministry of Research, Innovation and Digitization through Programme 1- Development of the national research & development system, Sub-programme 1.2 - Institutional performance - Projects financing the R&D&I excellence, Financial Agreement no. 18PFE/30.12.2021.

References

[1] ***. "Finite-state machine." *Wikipedia*. Accessed October 20, 2023. https://en.wikipedia.org/wiki/Finite-state_machine.
[2] ***. "Programmable logic controller." *Wikipedia*. Accessed October 20, 2023. https://en.wikipedia.org/wiki/Programmable_logic_controller.
[3] Bolton, William. *Programmable Logic Controllers*. 6th edition. Oxford, Newnes, 2015.
[4] Parr, E.A. "Computers and industrial control". *Industrial Control Handbook*. 3rd edition. South Norwalk, CT, Industrial Press, Inc., 1998.
[5] ***. "Switch statement." *Wikipedia*. Accessed October 20, 2023. https://en.wikipedia.org/wiki/Switch_statement.

ISSN 1454 - 8003
Proceedings of 2023 International Conference on Hydraulics and Pneumatics - HERVEX
November 8-10, Băile Govora, Romania

DETERMINANT OF THE VARIABILITY OF THE LOAD CYCLE OF A MULTI-SOURCE HYDROSTATIC DRIVE SYSTEM

Krzysztof KĘDZIA[1]

[1] Department of Technical Systems Operation and Maintenance, Faculty of Mechanical Engineering, Wrocław University of Science and Technology, krzysztof.kedzia@pwr.edu.pl

Abstract: *This article, by determining the mathematical relationship called the determinant of the WZ duty cycle variability and the procedure presented therein, gives an engineer who is not a specialist in the field of multi-source drives a tool to assess the impact of a possible modernization of a single-source system to any multi-source system (hydrostatic, electrical or mechanical). Knowing the value of the WZ determinant, the engineer can quickly estimate potential savings in any selected areas (energy or ecological). In this work, the author presented a method for estimating the potential benefits in the energy area resulting from the reduction of fuel consumption after replacing a single-source drive system with a multi-source system used for a selected load cycle.*

Keywords: *Multisource drive system, hydrostatic transmission, modelling and simulation, load cycle, control*

1. Introduction

Nowadays market of machines and devices is regulated by rigorous standards regarding energy consumption, environmental pollution, noise, safety, ergonomics, recycling, etc. The people responsible for implementing the provisions and rules contained in the standards are mainly engineers-designers and constructors. The multitude of regulations, new, more sophisticated technologies and a greater number of physical phenomena considered in machines mean that more is demanded from engineers. For designers and constructors, designing a machine or device with even greater efficiency, lower emissions of harmful or hazardous compounds, faster in operation, more reliable, safer, less noisy or easier to use without additional support in the form of a person (expert), procedure or expert support system them in areas in which they are not specialists is becoming increasingly difficult.
Work is underway in many global research centers to increase the efficiency of drive systems used in machines operating in rapidly changing, repeatable work cycles. One of the reasons for this interest is the possibility of recovering part of the energy usually dissipated in the braking process, by collecting it and storing it in batteries, and then reusing it in the most energy-intensive phases of the machine's work cycle. The use of drive systems with energy accumulation, instead of classic drive systems, is therefore an interesting and promising way to increase the efficiency of the drive system - up to 30%. However, the wide scope of knowledge, the complexity of the issues and the costs associated with the design and construction of this type of drive systems mean that work on them is carried out only in a few, specialized research and development centers.
The paper presents a method for determining the coefficient of variation (WZ) by means of which the designer-engineer, after determining only a few parameters that can be determined on the basis of the machine's operating cycle, can estimate the potential benefits associated with the use of a multi-source drive system instead of a single-source (classic) one to implement a given duty cycle.

2. General information about multi-source drive systems (MDS)

Seven important issues regarding the construction and design of multi-source drive systems is presented in Table 1.

Table 1: Seven important issues regarding the construction and design of multi-source drive systems

No	Description of the issue	State
1	**How to assess the matching of energy and ecological characteristics in drive systems for spectral forms of loads (stochastic)?**	**There are proposed assessment methods for selected types of drive systems.**
2	**Ways to increase the efficiency of individual components and the entire drive system.**	**Constant progress related to the development of technique and technology. The work is still ongoing.**
3	**Appropriate, mutual adjustment of the operating areas of high-performance drive system components.**	**The issue has been solved in many areas of technology. Work is ongoing on optimal solutions in multi-source systems.**
4	**When to use multi-source (hybrid) drive systems, which enable limiting the operating characteristics of the primary energy source to the most favorable areas and recovering part of the kinetic or potential energy that is usually lost?**	**Problem solved. There are many commonly used solutions (mechanical, electrical, hydraulic, etc.).**
5	**Quantitative assessment of energy efficiency of various variants of drive system solutions operating under the same load conditions.**	**There are many theories and assessment methods in this area.**
6	**Answer the question: When is the expansion of a single-source propulsion system to a multi-source one justified?**	**There are general considerations, but there is no method for estimating the potential benefits before deciding whether to expand the system.**
7	**Solving control issues, in particular solving control system synthesis problems (on-line or off-line control).**	**There are solutions in some areas. Work on autonomous systems (FL, NN, AI) is ongoing.**

2.1 Research subject

During the analysis of the results of the research conducted by the author, it was found that it is possible to determine the potential benefits resulting from the use of a multi-source drive system instead of a single-source one at the initial stage of design work. But how to do it? The considerations will be presented on the example of the drive system below (fig. 1).

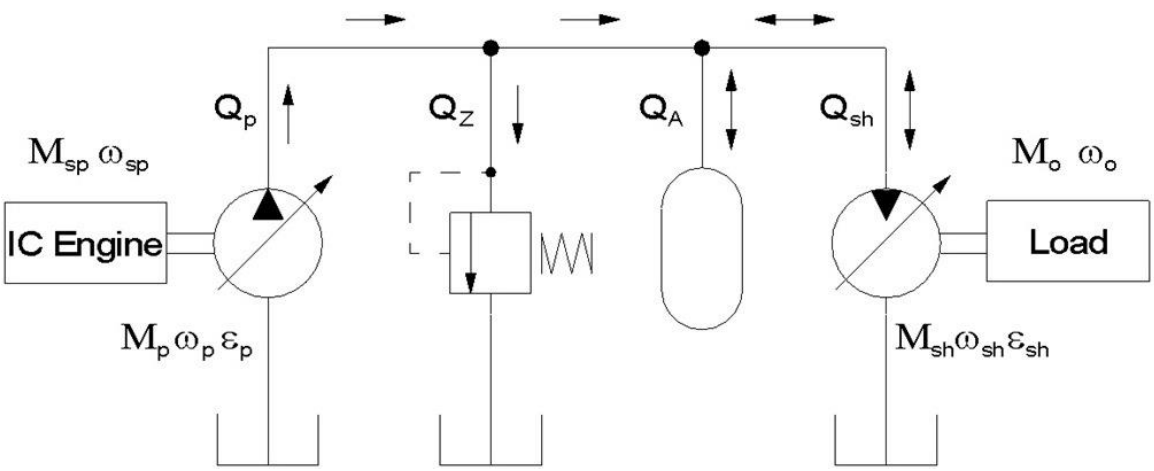

Fig. 1. Schematic diagram of hydrostatic transmission (M: torque; ω: angular velocity; Q: flow ratio; ε: hydrostatic unit control; indexes: sp: IC engine; p: hydrostatic pump; sh: hydrostatic motor; 0: load; z: flow through overflow valve) [1]

2.2 Basic data analysis

The basis for all analyzes of multi-source systems is the machine's work cycle (fig. 2), resulting mainly from the task for which it was built [2], [3], [4], [5].

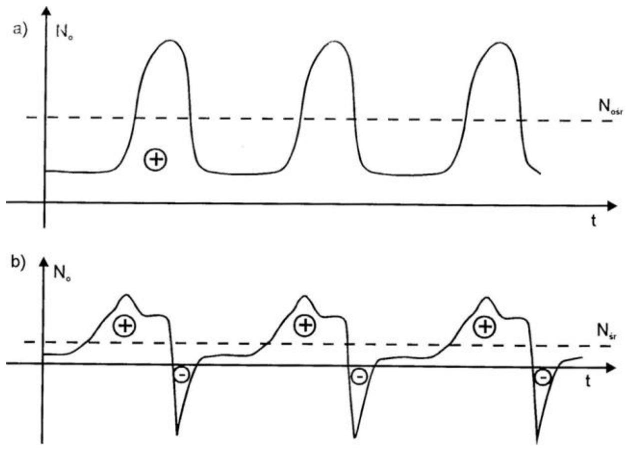

Fig. 2. Variability of energy demand in cyclically operating drives: a) possibility of stabilizing the energy source, b) possibility of stabilization and energy recovery [6], [7]

Most often, when describing the operation of a machine or drive system, the speed is measured and then, based on the energy balance of the working system, a cyclorama of force and power is developed (fig. 3) [8], [9], [10], [11].

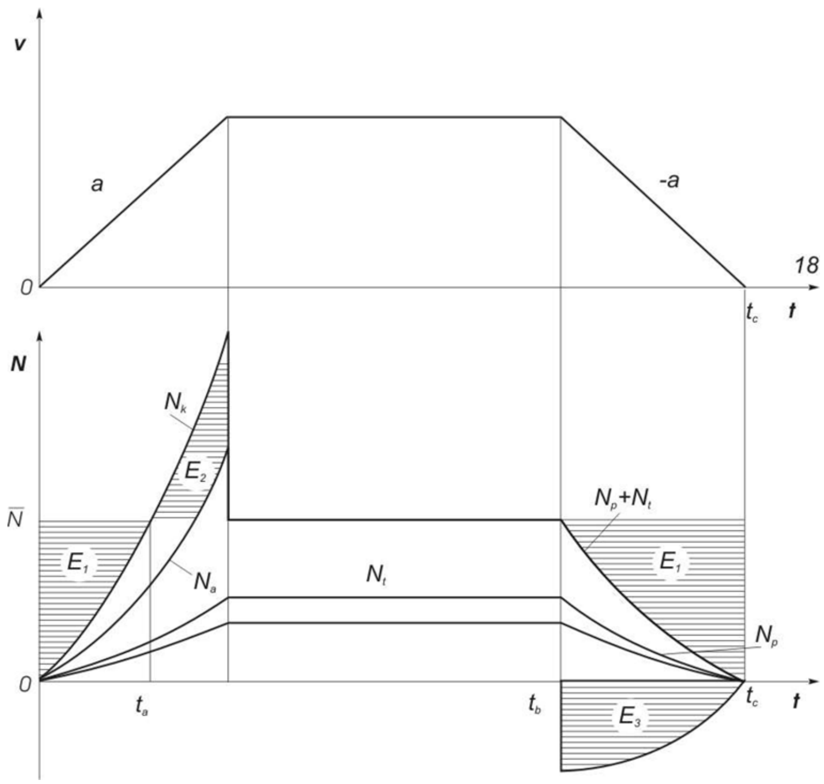

Fig. 3. An example of a simple work cycle [8]

In most working machines and vehicles, changes in the load state are a random process and can be presented in the form of a two-dimensional random variable moment Mo (force F) and angular velocity ωo (linear velocity v) (fig. 4) [12].

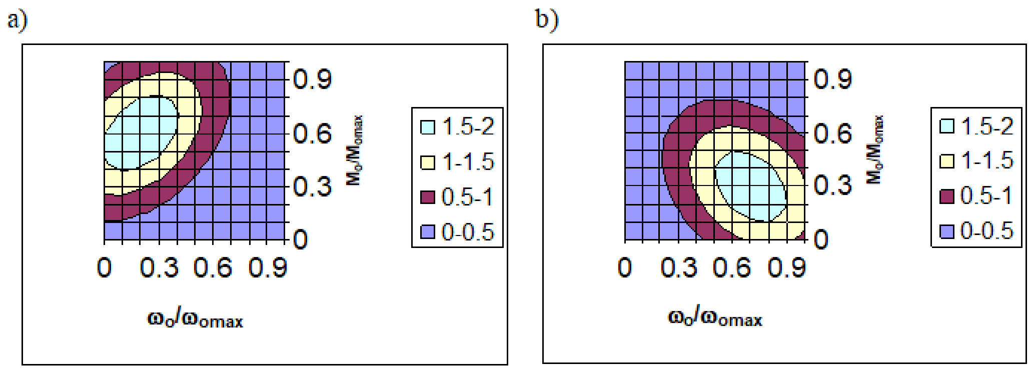

Fig. 4. Examples of load density functions for a bus operating on a) urban and b) intercity routes [12], [13]

3. Determinant of the variability of the load cycle of a multi-source hydrostatic drive system WZ

Discussed in the monograph [14]:
- kinetostatic method,
- method of estimating fuel consumption in a single- and multi-source system (attachment),
- simulation verification of the results obtained using the kinetostatic method,
- proprietary software for determining the settings of drive system components,
- and proprietary software for digitizing universal characteristics,

were used to develop a tool (expert system) on the basis of which an engineer, even if he is not a specialist in the field of multi-source drives, will be able to estimate the difference in energy consumption by a drive system implementing a given duty cycle in the structure of a single-source drive system and its multi-source equivalent. With these estimates, the engineer's decision to upgrade a single-source propulsion system to an equivalent multi-source system will be faster and with less error.

Research and analyzes of single- and multi-source drive systems operating in variable and repeatable work cycles, characteristic of work machines, buses, transport trolleys, etc., resulted in the development of a mathematical formula constituting the basis for the decision to expand the single-source drive system to its multi-source equivalent. Its final form was adopted in the form of relationship (1). It was called the determinant of duty cycle variability - WZ:

$$WZ = \frac{N_{sr\_br}}{N_{sr\_r}} * \frac{1}{n}\sum_{i=1}^{n}\frac{t_{di}}{t_{ci}} \tag{1}$$

wherein:
WZ - determinant of work cycle variability [-],
N_{sr_br} - average power in the work cycle without considering the energy that can be recovered in the recuperation process [W],
N_{sr_r} - average power in the work cycle considering the energy that can be recovered in the recuperation process [W],
t_d - time of energy supply to the drive system in the work cycle (No > 0) [s],
t_c - total duration of the work cycle [s],
n - number of changes in the energy demand in the work cycle from energy supplied to the drive system No > 0 to energy recoverable in the recuperation process No < 0 [-].

The above formula considers only five characteristic parameters. It is the result of a compromise between the quality of the estimate of the potential reduction in fuel consumption ΔG_e in a given work cycle and the time needed to perform this estimate. The WZ determinant in the proposed form will allow for a quick assessment of the potential benefits resulting from replacing a single-source drive system with a multi-source system, based on the characteristics of the machine's work cycle, presented in the form of the course of the effort variable M_o, current ω_o and load power N_o.

3.1 Procedure for determining the fuel consumption difference ΔG_e

To determine the difference in fuel consumption ΔG_e between a single-source drive system and its multi-source equivalent operating in the same duty cycle, follow the procedure presented below (fig. 5) [15]:

The most important elements of the method are:

- Knowledge of the machine's work cycle - the highest priority.
- Analysis and assessment of basic parameters of the machine's work cycle.
- Concluding the continuation of the procedure based on the recuperation coefficient $\chi 20$.
- Calculation of the WZ variability determinant for a given work cycle.
- Using the designated determinant function and determining potential benefits.

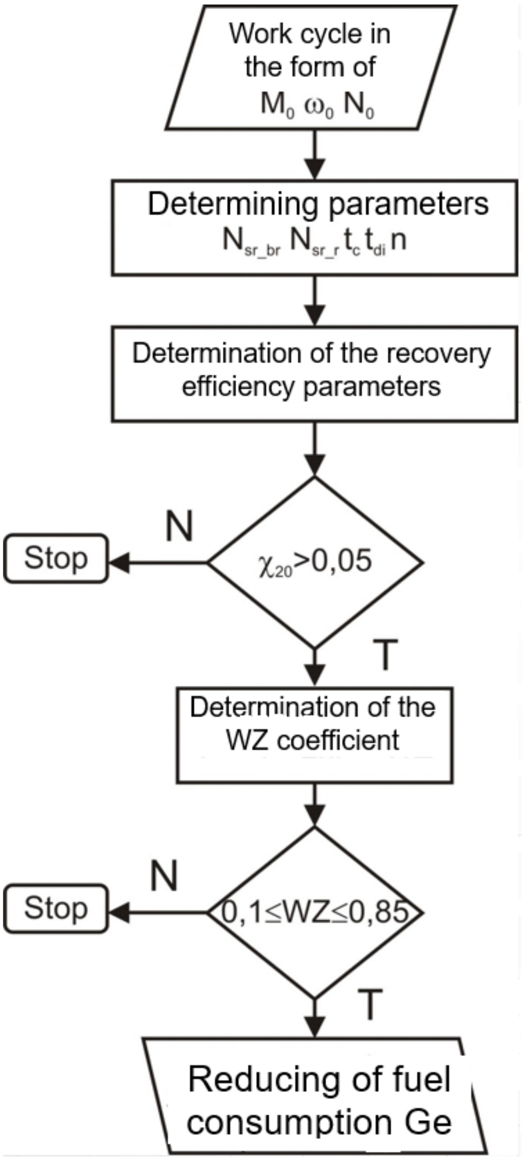

Fig. 5. Scheme of the procedure for determining the WZ duty cycle variability determinant

A description of the procedure is provided below.

- Presentation of the machine's work cycle in the form of waveforms of torque M_o, angular speed ω_o and energy demand (power) N_o during the cycle.
- Determining the parameters of the selected work cycle:

a) N_{sr_br} - average power in the work cycle without considering the energy that can be recovered in the recuperation process,

b) N_{sr_r} - average power in the work cycle, considering the energy that can be recovered in the recuperation process,

c) t_c - duration of the work cycle,

d) t_d - time of energy supply to the drive system in the duty cycle ($N_o>0$),

e) n - number of changes in energy demand in the work cycle from energy supplied (E_d) to the drive system to energy recoverable in the recuperation process (E_o).

- Determination of the heat recovery efficiency factor χ_{20} - eq. (6)
- If the condition $\chi_{20}>0.05$ is met, the next point is passed, otherwise the procedure is interrupted (this method cannot be used).
- Introducing the parameters specified earlier into the relationship describing the coefficient of variation of the WZ duty cycle - eq. (1).
- If the condition 0.1 ≤WZ≤0.85 is met, proceed to the next point of the procedure, i.e. determining the reduction in fuel consumption ΔG_e, otherwise the procedure is interrupted (this method cannot be used).
- Reading from the chart the estimated value of reducing fuel consumption ΔG_e by an internal combustion engine performing a given duty cycle in the structure of a multi-source propulsion system in relation to a single-source propulsion system.

3.2 Determinant of the variability of the load cycle of a multi-source hydrostatic drive system

The WZ determinant. They are calculated using equations (2) to (6). Their graphical interpretations for load are shown in Fig. 6.

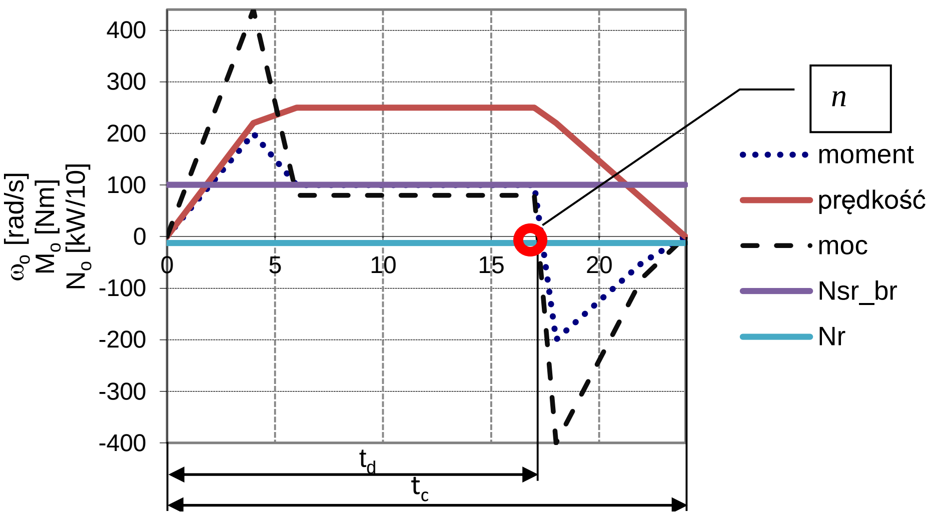

Fig. 6. Graphical interpretation of the parameters used to calculate the WZ determinant for load

Parameters: N_{sr_br} - average power in the work cycle without taking into account the energy that can be recovered in the recuperation process, N_r - average power in the work cycle that can be recovered in the recuperation process and N_{sr_r} - average power in the work cycle including the energy that can be recovered recovery in the recuperation process, were determined from equations (2) to (4):

$$N_{sr\_br} = \frac{1}{t_c}\int_0^{t_c} N_o(t)\,dt \text{ dla } N_o(t) \geq 0 \quad (1)$$

$$N_r = \frac{1}{t_c}\int_0^{t_c} N_o(t)\,dt \text{ dla } N_o(t) < 0 \quad (2)$$

$$N_{sr\_r} = \frac{1}{t_c}\int_0^{t_c} N_o(t)\,dt \quad (3)$$

where:

$$N_{sr\_r} = N_{sr\_br} - N_r \quad (4)$$

The condition that initially verifies the possibility of using the WZ determinant is the heat recovery efficiency coefficient. Knowing the values of the parameters and, the coefficient can be determined from the following relationship (6):

$$\chi_{20} = \frac{N_r}{N_{sr\_br}} \quad (5)$$

For duty cycles for which the indicator χ_{20} reaches values below 0.05 ($\chi_{20} < 0.05$), estimation of the difference in fuel consumption ΔG_e is not possible using this method.
The next parameter is the duration of the work cycle t_c. This is the time from the start to the end of the cycle. Parameter t_d – this is the time of energy supply to the drive system in the work cycle ($N_o>0$).
The last parameter to be determined in this step of the procedure is the n coefficient. This is a number that determines (for a given duty cycle) the number of transitions of the cyclorama from power No > 0 to power No < 0 - which can be recovered in the recuperation process. For load III shown in Figure 6, the number n is 1 (the location is marked with a circle in Figure 6).

A graphical representation of the value of the WZ determinant as a function of the fuel consumption reduction ΔG_e is shown in Figure 7. To determine the reduction in fuel consumption ΔG_e for any duty cycle after replacing the single-source propulsion system with a multi-source one, the obtained value of the WZ determinant should be compared with the function determined on the basis of the approximation of the results obtained in Table 2. The formula of the function in the range of applicability of the method shows the relationship (7) [10]:

$$\Delta G_e = 4.05 \cdot WZ^2 + 18.35 \cdot WZ + 16.57 \quad \text{dla} \quad 0.1 \leq WZ \leq 0.85 \quad (6)$$

where:

ΔG_e - change in fuel consumption,

WZ - coefficient of variation of the duty cycle.

Table 2: List of WZ parameters for the analyzed work cycles

Load	$N_{śr\_br}[kW]$	$N_r[kW]$	$N_{śr\_r}[kW]$	$\Delta G_e[\%]$	n	t_d / t_c [s]	χ	***WZ***
Load III	10.02	1.25	8.77	34.3	1	0.72	0.13	**0.82**
Load IV	5.91	0.69	5.22	25.32	3	0.17	0.12	**0.19**
Load V	11.05	0.75	10.30	16.19	4	0.12	0.07	**0.13**
Load VI	3.15	0.76	2.39	22.09	2	0.27	0.24	**0.35**
Load VII	5.01	0.90	4.11	19.56	4	0.18	0.18	**0.21**

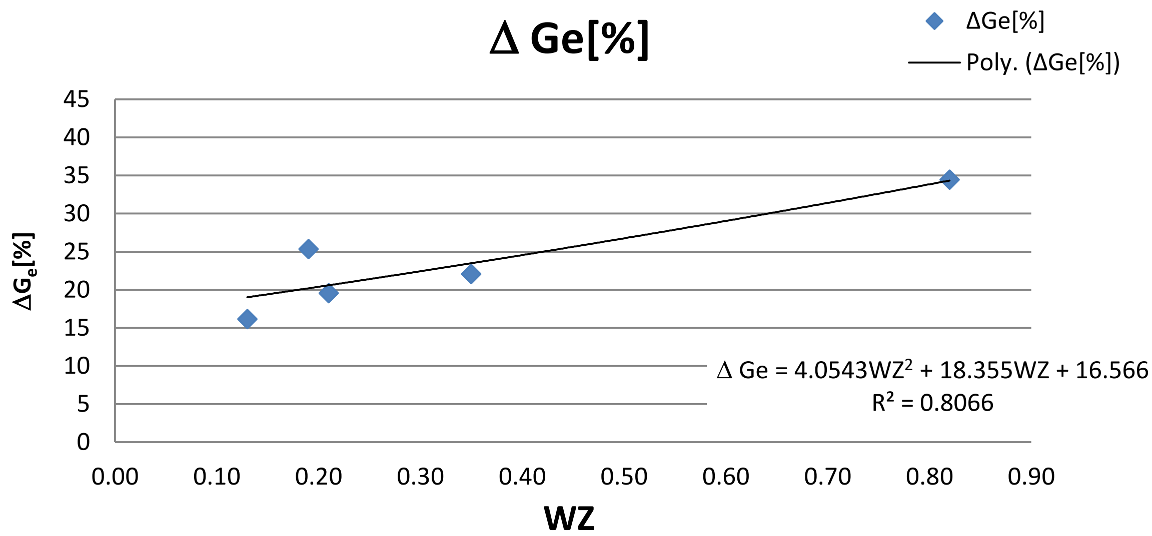

Fig. 7. Determinant of the variability of the WZ duty cycle as a function of the reduction in fuel consumption ΔG_e, approximation with a second-order polynomial

4. Conclusions

The paper, by determining the mathematical relationship called the determinant of the WZ duty cycle variability and the procedure presented therein, gives an engineer who is not a specialist in the field of multi-source drives a tool to assess the impact of a possible modernization of a single-source system to any multi-source system (hydrostatic, electrical or mechanical). Knowing the value of the WZ determinant, the engineer can quickly estimate potential savings in any selected areas (energy or ecological). In this work, the author presented a method for estimating the potential benefits in the energy area resulting from the reduction of fuel consumption after replacing a single-source drive system with a multi-source system used for a selected load cycle.

References

[1] Al-Jadir, T. M., and F. R. Siperstein. "Modeling and simulation of adsorption of methane, ethane, hydrogen sulfide and water from natural gas in (FP)YEu Metal-Organic Framework." *IOP Conference Series Materials Science and Engineering* 579. Paper presented at the 1st International Conference on Petroleum Technology and Petrochemicals, Baghdad, Republic of Iraq, April 10–11, 2019.

[2] Kędzia, K., and M. Pyrc. "Modeling of a multi-source drive system with hydrostatic energy flow conversion." / "Modelowanie wieloźródłowego układu napędowego z hydrostatycznym przetwarzaniem strumienia energii." Paper presented at the 19th International Scientific Symposium of Students and Young Scientists / 19. Międzynarodowe Sympozjum Naukowe Studentów i Młodych Pracowników Nauki, Zielona Góra, Poland, March 28–29, 1997; pp. 168–172.

[3] Kumar, R., and M. Ivantysynova. “An Instantaneous Optimization Based Power Management Strategy to Reduce Fuel Consumption in Hydraulic Hybrids.” *International Journal of Fluid Power* 12, no. 2 (2011): 15 - 25.

[4] Pizoń, A. *Hydraulic and electrohydraulic control and adjustment systems* / *Hydrauliczne i elektrohydrauliczne układy sterowania i regulacji*. Warsaw, Wydawnictwa Naukowo-Techniczne (WNT), 1987.

[5] Chrostowski, H. (ed.). *Basics of the construction of mechano-hydraulic drive systems with energy accumulation* - Technical report on the KBN research project no. 1309/P4/92/02 / Podstawy budowy mechano-hydraulicznych układów napędowych z akumulacją energii - Sprawozdanie merytoryczne z projektu badawczego KBN nr 1309/P4/92/02. Wrocław University of Science and Technology, Wrocław, 1998.

[6] Chrostowski, H. (ed.). *Modeling of power flow in hydrostatic multi-source drive systems* - Scientific Works of the Central Fundamental Research Program 02.05 / *Modelowanie rozpływu mocy w hydrostatycznych wieloźródłowych układach napędowych* - Prace Naukowe Centralnego Programu Badań Podstawowych 02.05. Wrocław University of Science and Technology, Wrocław, 1990.

[7] Dindorf, R.”Reducing energy consumption in compressed air systems.” / ”Zmniejszenie zużycia energii w systemach sprężonego powietrza.” *Pneumatics Industrial Compressed Air Systems* / *Pneumatyka Przemysłowe Systemy Sprężonego Powietrza*, no. 2 (2011): 30-35.

[8] Dindorf, R., J. Takosoglu, and P. Woś. *“*Review of Compressed Air Receiver Tanks for Improved Energy Efficiency of Various Pneumatic Systems.” *Energies* 16, no. 10 (2023): 4153.

[9] Osiecki, A. *Hydrostatic machine drive* / *Hydrostatyczny napęd maszyn*. Warsaw, Wydawnictwa Naukowo-Techniczne (WNT), 1998.

[10] Popławski, E. *Cars with electric drive* / *Samochody z napędem elektrycznym*. Wydawnictwa Komunikacji i Łączności (WKŁ), Warsaw, 1994.

[11] Paszota, Z. “Comparison of the powers of energy losses in a variable capacity displacement pump determined without or with taking into account the power of hydraulic oil compression.” *Polish Maritime Research* 22, no. 2(86) *(*2015): 32-43.

[12] Kędzia, K. *Determinant of the variability of the load cycle of a multi-source hydrostatic drive system*. 2nd edition corrected and supplemented / *Wyznacznik zmienności cyklu obciążenia wieloźródłowego hydrostatycznego układu napędowego*. Wydanie II poprawione i uzupełnione. Wrocław, Publishing House of the Wrocław University of Science and Technology, 2023.

[13] Kędzia, K. *Method of energy and ecological optimization of a hydrostatic multi-source drive system* / *Metoda optymalizacji energetycznej i ekologicznej hydrostatycznego wieloźródłowego układu napędowego*. Doctoral thesis, Wrocław, 2004.

[14] Przystupa, F., M. Sokolski, and P. M. Sokolski. *“*Condition monitoring and diagnostics as important factors for increasing the reliability of machinery components - case study.” *Risk, Reliability and Safety: Innovating Theory and Practice: Proceedings of the 26th European Safety and Reliability Conference, ESREL 2016 Glasgow, Scotland, 25-29 September, 2016*. CRC Press/Balkema, 2017; pp. 2478-2481.

ISSN 1454 - 8003
Proceedings of 2023 International Conference on Hydraulics and Pneumatics - HERVEX
November 8-10, Băile Govora, Romania

HEAT PUMPS. CALCULATION ELEMENTS FOR SOLAR AIR HEATERS

Ioan PAVEL[1,*], Ștefan-Mihai ȘEFU[1], Liliana DUMITRESCU[1]

[1] National Institute of Research & Development for Optoelectronics / INOE 2000 – Subsidiary Hydraulics and Pneumatics Research Institute / IHP, Bucharest, Romania

* pavel.ihp@fluidas.ro

Abstract: *Solar energy is an alternative source of green, free and widely available energy. It can meet all current and future needs of the world respecting the conditions of sustainable development. Heat pumps are devices that convert energy from external heat sources (air, water, etc.) into useful heat, which can then be used to heat premises and/or supply hot water in residential or commercial buildings. In this paper, a classification of heat pumps and several types of solar air heaters are presented. Also presented are some calculations for determining their energy performance to improve the heat transfer rate.*

Keywords: *Heat pumps, solar panels, solar air heaters, renewable energy*

1. Introduction

Heating is the largest final energy consumption, accounting for almost half of total energy consumption in most countries.
Energy efficiency and renewable energy are of paramount importance in the European Union (EU) strategy for sustainable development. The ambitions for low-carbon economies and secure and competitive energy systems were endorsed in Directive (EU) 2018/2001 of the European Parliament [1].
Various factors are demotivating the growth of conventional fuels for power generation, such as limited availability of nuclear power and coal reserves and pollution threats, which harm flora and fauna. It is therefore necessary to meet the energy consumption target by using such energy resources that are abundantly available in nature and create less pollution [2].
Heat pumps are energy recovery systems that use some of the electricity to transfer heat at higher temperatures from external soil or air to a building's heating and hot water circuits. Aerothermal, geothermal and hydrothermal energy are considered renewable energy sources [3].
Heat pumps are becoming an increasingly popular choice for a home's heating and cooling needs. Flexibility, efficiency, long-term return on investment and low environmental impact are just some of the reasons homeowners are looking to replace older heating equipment with heat pumps that use renewable energy. The sun provides the most readily available source of energy available on earth as direct solar irradiation and indirect forms such as wind, agriculture, hydropower, and the sea [4].
The heat pump can be connected to radiators, underfloor heating, fan coils or domestic hot water, in a similar way to how the boiler is currently connected. What differentiates the heat pump from the boiler is how heat is generated, not how it is distributed. Thus, instead of burning fuel to generate heat, a heat pump uses a process of evaporation and condensation of the refrigerant.
The principle of operation of heat pumps is based on the essential element in the process of capturing and yielding energy, on the refrigerant in the inner circuit of the heat pump.
The refrigerant can go from liquid to cold vapor. The liquid refrigerant enters the evaporator, where heat transfer occurs through vaporization, from the energy source to the refrigerant. At the outlet of the evaporator, the refrigerant is in a state of cold vapor.
Cold refrigerant vapors enter the compressor, where with the help of electricity, their pressure and temperature increase occurs. Hot refrigerant vapor enters the condenser, where heat transfer occurs (by condensation) to the thermal agent in the closed circuit of the heating system. At the exit of the condenser, following condensation, the refrigerant is in liquid state. The liquid refrigerant passes through the expansion valve, where its temperature and pressure decrease and from this moment the cycle resumes.

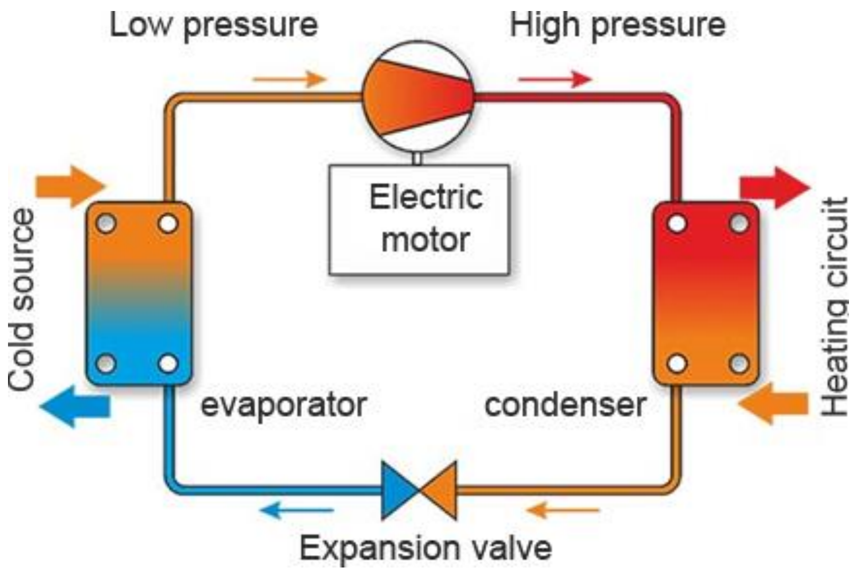

Fig. 1. The principle of operation of heat pumps

Table 1: Types of heat pumps [2]

1.	Air-to-air heat pump	Air-to-air heat pumps, commonly known as air conditioners, are an easy-to-install option with little investment. The heat pump uses energy from the air to provide both heating and cooling capacities in an energy-efficient way.
2.	Air-to-water heat pump	The air-to-water heat pump extracts heat from the outside air to heat the refrigerant (e.g. R32) which in turn passes it on to the water circulating through the heating systems in the home. This pump variant is considered to be the most economical in terms of investment and can operate efficiently up to an outside temperature of up to -28°C.
3.	Ground-to-Water Heat Pump	The ground-to-water heat pump uses ground energy, also known as geothermal energy, to produce heat and chilled water. It works on the basis of a closed circuit, consisting of the heat pump, geothermal drilling (vertical or horizontal collectors depending on the existing land surface and drilling possibilities) and the heating system in the house. By extracting energy from the ground, geothermal heat pumps are extremely reliable, even in the coldest climates. Soil temperatures remain stable throughout the year, making it an ideal renewable energy source.
4.	Ground-to-air heat pump	A dual source heat pump is a solution that combines an air source heat pump and a geothermal heat pump.
5.	Water-Water Heat Pump	It uses groundwater in the groundwater as a source for heat production. Water from lakes or rivers can also be used for heating. Water-to-water heat pump requires vertical well drilling. In order for it to be properly connected to the water source, the direction of groundwater flow must be taken into account. At the same time, it is a suitable solution for houses and dwellings close to a water source.

2. Solar Air Heaters

A solar air heater is a device used to heat air as an energy transfer medium that has several advantages over liquid solutions. Various problems are associated with liquid solar heaters, corrosion problems, fluid leakage and fluid transfer power [5]. All these problems are eliminated by using air instead of liquid in solar heating devices. Solar air heaters collect cooled air from the bottom of the space and distribute it through solar heat exchangers (fig 2). Since these simple methods and direct transfers do not store heat, they are ineffective at night or in gloomy conditions [6].

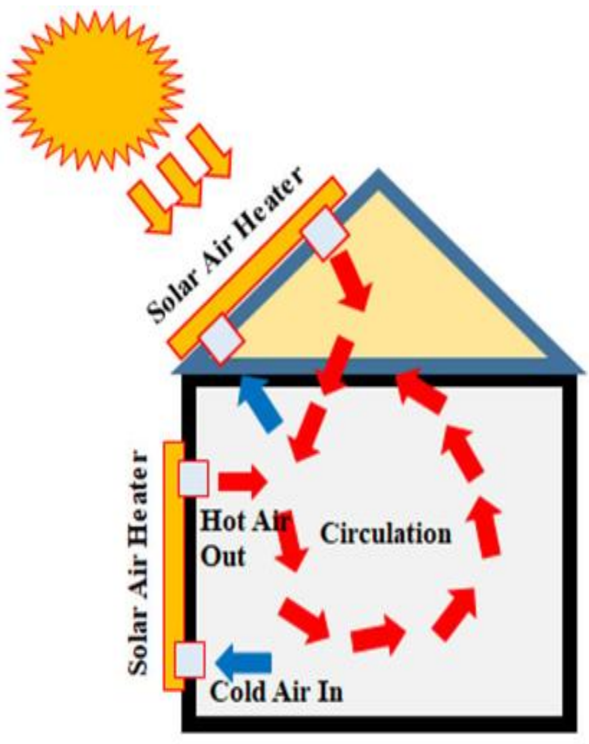

Fig. 2. Air circuit in heating systems with solar air heaters

Solar air heaters are classified according to their glass coatings, absorbent material, flow characteristics, flow types, absorbent surface texture, hybrid systems, and applications.

Table 2: Classifications of solar air heaters

1.	Single-pass	A single-pass solar air heater has air as its working medium. It has a glass cover, a single flow channel, an absorbent plate that has heat absorption capacity due to a dark paint or color, and insulation to cover the back of the channel to reduce thermal losses in the surrounding area. Generally, a blower is attached to the solar air heater to create a forced circulation of working fluid in the system [7].	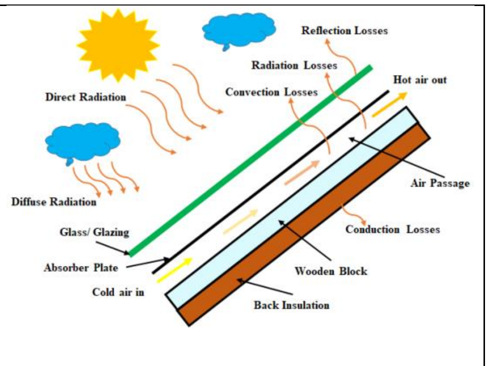

2.	Double-pass			The Double-Pass SAH (DPSAH) concept has been designed to limit heat loss in the surrounding area. Air passes along both sides of the motherboard, extracting heat from the motherboard, and then air blows in both directions of the motherboard in a double-pass configuration [8].	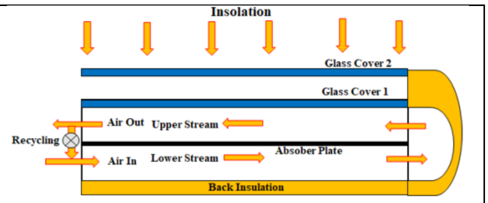
		2.1	Parallel flow	In this type, air passes between the back insulating layer and the motherboard. The second air passage is positioned slightly above the motherboard and between the glass covers and the motherboard.	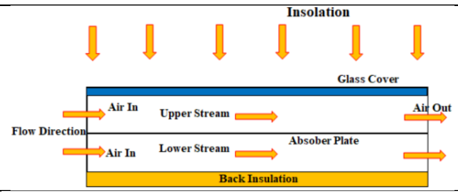
		2.2	Counter current	The counter current model is attractive because it allows additional heat to be extracted, resulting in improved thermal performance.	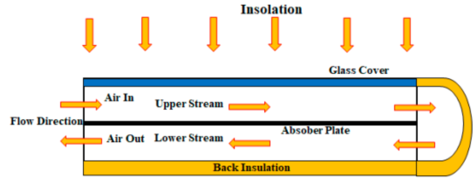
		2.3	Recycling	The mixture of air and the intensity of forced heat convection have recently been shown to play a critical role in increasing heat transfer. Part of the heated output air is redirected to the intake duct and mixed with new inlet air using a blower.	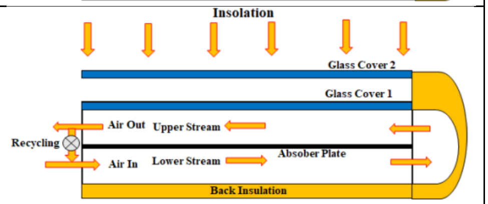
3.	Multi-pass			The use of two or more glass coatings is a common practice when the solar air collector is operating at relatively high temperatures or is exposed to strong winds. This helps prevent convection and heat loss from the collector caused by radiation. Due to the absorption and reflection of sunstroke by the roofs, the amount of solar energy coming into contact with the heated surface is reduced when using many glass caps [9].	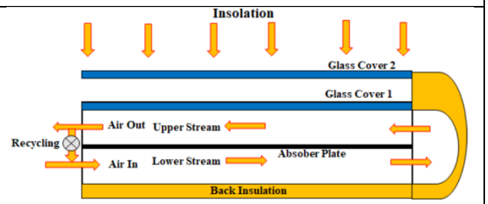

3. Calculation elements for solar air heaters [2]

The thermal performance of a solar air heater refers to its ability to improve heat transmission. The effectiveness of a solar air heater is the energy balance, comprised of the solar-irradiation energy yield to the collectors, the useable energy gained by airflow, and the losses to the environment.
The energy balance under controlled conditions for a collector is given as:

$$Q_u=\left[I(\tau\alpha)-U_t\left(T_{pm}-T_a\right)\right] \tag{1}$$

Where
Q_u = useful heat again, W/m^2;
U_t = total loss coefficient, W/m^{2}K;
T_{pm} = average plate temperature, K;
T_a = ambient temperature, K.

The effective transmittance 0 product (*τα*) is a factor that handles the dynamic interactions of the optical characteristics of the glass and the absorber surface. In reality, the configuration of the absorber, incident solar energy, fluid velocity, and fluid characteristics all influence the mean temperature of the base plate and can be calculated with the formula (2):

$$Q_u=F^{'}[I(\tau\alpha)-U_l(T_{fm}-T_a)] \tag{2}$$

However, the mean absorber-plate temperature, T_{pm}, and average fluid temperature, T_{fm}, are generally unknown. The above equation can be modified for more practical use and is given as follows:

$$Q_u=F_r[I(\tau\alpha)-U_l(T_{fi}-T_a)] \tag{3}$$

Where: the heat-removal factor (F_R) can be calculated as formulas (4):

$$F_r=\frac{\dot{m}C_p}{U_l}\left[1\text{-}\exp\left(\frac{-F^{'}(U_l)}{\dot{m}C_p}\right)\right] \tag{4}$$

The thermal efficiency (η_{th}) of a solar air heater can be calculated as formulas (5):

$$\eta_{th}=\frac{Q_u}{I} \tag{5}$$

From Equations presents the following relationships can be obtained as formulas (6), (7),(8):

$$\eta_{th}=\left[\tau\alpha-U_l\frac{(T_{pm}-T_a)}{I}\right] \tag{6}$$

$$\eta_{th}=F^{'}\left[\tau\alpha-U_l\frac{(T_{fm}-T_a)}{I}\right] \tag{7}$$

$$\eta_{th}=F_R\left[\alpha\tau-U_l\frac{(T_{fi}-T_a)}{I}\right] \tag{8}$$

The above Equations (6)–(8) are recognized as the Hottel–Whillier–Bliss equations. Bondi [10] provided the expression for solar air heater thermal efficiency (η_{th}) that applies to the air-outlet temperature to calculate the η_{th} of solar air heater when pulling air from the atmosphere:

$$\eta_{th}=F_R\left[\tau\alpha-U_l\frac{(T_{f0}-T_{fi})}{I}\right] \tag{9}$$

Where: F_o is the heat-removal factor based on the temperature of the output air and is written as formula (10):

$$F_0=\frac{\dot{m}C_p}{U_l}\left[\exp\left(\frac{F^{'}U_l}{\dot{m}C_p}\right)\text{-}1\right] \tag{10}$$

4. Heat transfer performance of solar air heaters

A solar air heater performance may be determined using this efficiency with the ratio of helpful energy gain to solar radiation during a limiting time. Mathematically, it can be expressed as formula (11):

$$\eta=\frac{\int_0^\theta Q_u d\theta}{A_c\int_0^\theta I d\theta} \tag{11}$$

Where:

η = average collector efficiency over a period of time;
I = intensity of global incident radiation, W/m^2;
Q_u = useful heat gains over a period of time;
A_c = collector-plate area, m^2;
θ = time interval, seconds.

For any short period, the η_{th} of a collector is simply the ratio of the rate of useable energy to the intensity of incoming radiation at that precise moment in time and may be expressed as (12):

$$\eta_{th}=\frac{Q_u}{I} \tag{12}$$

The thermal efficiency η_{th} can be expressed as (13):

$$\eta_{th}=\frac{\dot{m}C_p(T_{f0}-T_a)}{IA_c} \tag{13}$$

The η_{th} evaluations of the solar collector are required to obtain the fundamental design data utilized to develop collector systems. (a) The National Bureau of Standards (NBS) and (b) the American Society of Heating Refrigeration and Air Condition Engineering (ASHRAE) standards 93-77 are the two techniques for solar-collector standard testing.
NBS recommends the following η_{th} equation (14):

$$\eta_{th}=F'\left[\tau\alpha-U_l\frac{(T_{fm}-T_a)}{I}\right] \tag{14}$$

It is recommended [11] the following equation for η_{th}:

$$\eta_{th}=F_R\left[\tau\alpha-U_l\frac{(T_{fi}-T_a)}{I}\right] \tag{15}$$

Where: F_R = receiver heat-removal factor.

Configuration for a solar collector of predefined specifications (η_{th}) can be indicated in the following set of equations (16)-(20).

Case A: with air recycling, i.e., ($T_{fi} > T_a$)

$$\eta_{th}=F'\left[\tau\alpha-U_l\left\{\frac{(T_{f0}-T_a)+(T_{fi}-T_a)}{I}\right\}\right] \tag{16}$$

$$\eta_{th}=2\dot{m}C_p\left[U_l\left\{\frac{(T_{f0}-T_a)+(T_{fi}-T_a)}{I}\right\}\right] \tag{17}$$

Case B: without air recycling, i.e., ($T_{fi} = T_a$)

$$\eta_{th}=F'\left[\tau\alpha-U_l\left\{\frac{(T_{f0}-T_a)}{2I}\right\}\right] \tag{18}$$

$$\eta_{th}=F'\left[\tau\alpha-U_l\left\{\frac{(T_{f0}-T_a)+(T_{fi}-T_a)}{2I}\right\}\right] \tag{19}$$

$$\eta_{th}=2\dot{m}C_p\left[\left\{\frac{(T_{f0}-T_a)}{2I}\right\}\right] \tag{20}$$

These characteristics are shown in Fig. 3, known as design curves [12].

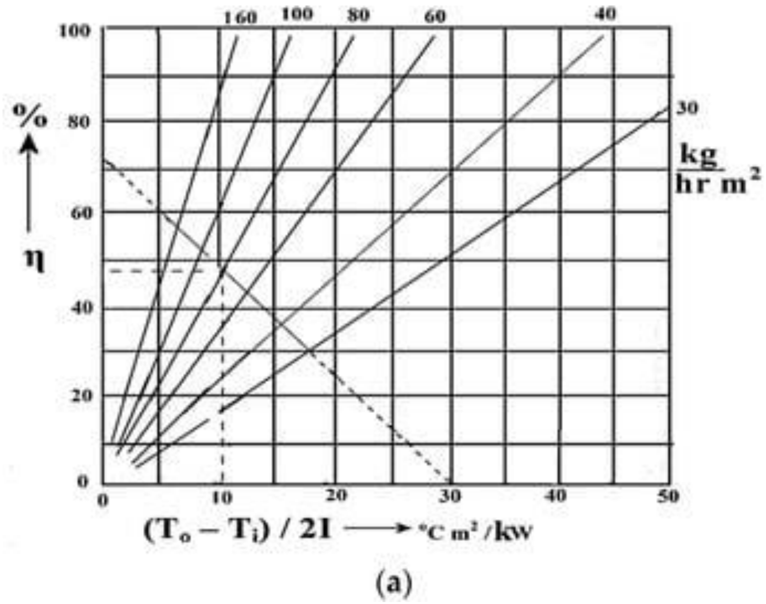

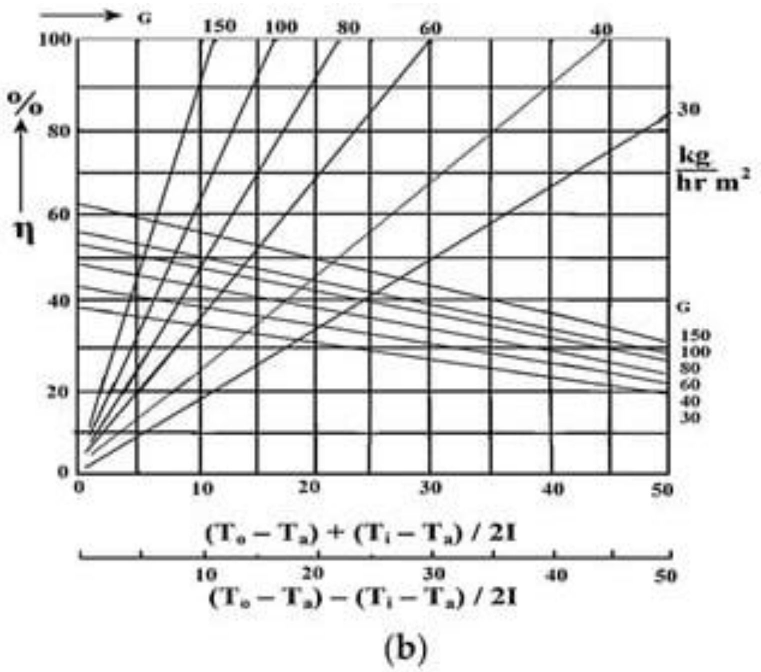

Fig. 3. Design curves (**a**) with air recycling and (**b**) without air recycling.

5. Conclusions

The performance of solar air heaters is greatly influenced by solar irradiance, atmospheric and air temperatures and air velocity, and energy from heated air cannot be stored yet.
Further research into solar air heaters could lead to new, efficient and low-cost hot air generating equipment solutions alone or in combination with other heating systems resulting in simpler, high-efficiency, environmentally friendly heating equipment that contributes to long-term sustainability.

Acknowledgments

This paper has been developed in INOE 2000-IHP, as part of a project co-financed by the European Union through the European Regional Development Fund, under Competitiveness Operational Programme 2014-2020, Priority Axis 1: Research, technological development and innovation (RD&I) to support economic competitiveness and business development, Action 1.2.1 Project type – Innovative Technological Project, project title: Developing an air-to-water heat pump with solar energy input and waste heat recovery, SMIS code: 156488, Financial agreement no. 442/390118/10.03.2023.

References

[1] ***. “Directive (EU) 2018/2001 of the European Parliament and of the Council.” *Official Journal of the European Union*. L 328/82, 21.12.2018. December 11, 2018. Accessed October 19, 2023. https://eur-lex.europa.eu/legal-content/EN/TXT/PDF/?uri=CELEX:32018L2001.
[2] Singh, Varun Pratap, Siddharth Jain, Ashish Karn, Ashwani Kumar, Gaurav Dwivedi, Chandan Swaroop Meena, Nitesh Dutt, and Aritra Ghosh. "Recent Developments and Advancements in Solar Air Heaters: A Detailed Review." *Sustainability* 14, no. 19: (2022): 12149.
[3] ***. "Directive (EU) 2009/28/EC of the European Parliament and of the Council." / “Directiva 2009/28/CE a Parlamentului European și a Consiliului.” *Official Journal of the European Union* / *Jurnalul Oficial al Uniunii Europene*. L 140/60, 5.6.2009. April 23, 2009. Accessed October 20, 2023. https://eur-lex.europa.eu/LexUriServ/LexUriServ.do?uri=OJ:L:2009:140:0016:0062:ro:PDF.
[4] Murthy, Ganti S. “Chapter Ten - Solar energy in India”, pp. 175-194. Murthy, Ganti S., Edgard Gnansounou, Samir Kumar Khanal, and Ashok Pandey (Eds.). *Biomass, Biofuels, Biochemicals*. Amsterdam, Elsevier Inc., 2022.
[5] Lupi, F., C. Borri, R. Harte, W.B. Krätzig, and H.-J. Niemann. “Facing technological challenges of Solar Updraft Power Plants.” *Journal of Sound and Vibration* 334 (January 2015): 57-84.
[6] Alam, T., R.P. Saini, and J.S. Saini. “Heat and flow characteristics of air heater ducts provided with turbulators—A review.” *Renewable and Sustainable Energy Reviews 31* (March 2014): 289–304.
[7] Singh, V.P., S. Jain, and J.M.L. Gupta. “Analysis of the effect of variation in open area ratio in perforated multi-V rib roughened single pass solar air heater - Part A.” *Energy Sources, Part A: Recovery, Utilization, and Environmental Effects* (2022): 1–21.
[8] Aldabbagh, L.B.Y., F. Egelioglu, and M. Ilkan. “Single and double pass solar air heaters with wire mesh as packing bed.” *Energy* 35, no. 9 (September 2010): 3783–3787.
[9] Jin, D., J. Zuo, S. Quan, S. Xu, and H. Gao. “Thermohydraulic performance of solar air heater with staggered multiple V-shaped ribs on the absorber plate.” *Energy* 127 (May 2017): 68–77.
[10] Biondi, P., L. Cicala, and G. Farina. “Performance analysis of solar air heaters of conventional design.” *Solar Energy* 41, no. 1 (1988): 101–107.
[11] Hill, J.E., J.P. Jenkins, and D.E. Jones. “Testing of solar collectors according to ASHRAE standard 93-77.” *ASHRAE Transactions – Technical Papers* 84, no. 2 (1978): 107–125. Paper presented at the 1978 Annual Meeting of the American Society of Heating, Refrigerating and Air-Conditioning Engineers, Inc., Albuquerque, NM, USA, June 25, 1978.
[12] Reddy, T.A., and C.L. Gupta. “Generating application design data for solar air heating systems.” *Solar Energy* 25, no. 6 (1980): 527–530.

ISSN 1454 - 8003
Proceedings of 2023 International Conference on Hydraulics and Pneumatics - HERVEX
November 8-10, Băile Govora, Romania

COLD SPRAYED Ti-6Al-4V COATINGS ON HYDRAULIC COMPONENTS

Wojciech ŻÓRAWSKI[1], Rafał CHATYS[1], Medart MAKRENEK[2], Dominika SOBOŃ[1]

[1] Kielce University of Technology, Faculty of Mechatronics and Mechanical Engineering, e-mail: ktrwz@tu.kielce.pl; chatys@tu.kielce.pl; dsobon@tu.kielce.pl

[2] Kielce University of Technology, Faculty of Management and Computer Modeling, e-mail: fizmm@tu.kielce.pl

Abstract: *Cold Spraying (CS) is a thermal spray process investigated and presented by many authors as an alternative to producing AM freeform parts. It has severe differences from the laser, welding, and other thermal spray processes since CS does not change the properties of the feedstock powder by heating or melting during the AM part fabrication because the powder is kept below its recrystallization temperature during the spraying time. However, CSAM produces parts with a very high density, >99%, due to the very high velocity imposed on the particles, reaching supersonic velocity values. Therefore, the correct selection of feedstock powder, deposition parameters, and strategy are fundamental for achieving high Deposition Efficiency (DE) and good CSAM performance. CS also prevents materials oxidizing during the deposition due to the relatively low temperature that the material absorbs at the spraying time. In addition, CS avoids other harmful effects seen in other AM or thermal spray processes, such as evaporation, melting, recrystallization, tensile residual stresses, debonding, and gas releasing, besides the ability to deposit high-reflective metals such as Cu and Al. A great CSAM advantage is the possibility of the deposition of dissimilar materials, e.g., a sandwich-like structure of Cu and Al or composite components, which is not feasible by welding. The performed statistical analysis of the components determined the complexity of the layered composite structure. And the developed model of the weakest micro-volume presented in this work was the basis for describing not only the predictable strength of the laminate, but also the character of failure, taking into account the stresses in the reinforcement and the distribution of final deformations in the structure of the composite under consideration.*

Keywords**:** *Cold sprayed, the cross-linking process, component of composite, strength*

1. Introduction

The process of depositing metal coatings on polymers or more complex engineering materials such as plastics to obtain good strength properties at the expense of less weight (in many industries) is a topical subject. The process is valuable for depositing materials that are extremely sensitive to the presence of oxygen and readily oxidize at moderately elevated temperatures. Examples of oxygen-sensitive coatings that are typically produced by cold spraying: composites of aluminum, copper, titanium and carbides (e.g., tungsten carbide), as well as coatings made from amorphous alloys.
The wide assortment of composite components (especially those with a polymer matrix) appearing on the market, forces us to develop new models and procedures for molding the strength properties and resin systems, respectively, in the manufacture of laminate.
During the crosslinking of chemically curable compounds such as epoxy resins (with the structure of polar epoxy rings) having the nature of polyaddition (or ionic polymerization), the curing process proceeds without volatile by-products (low-molecular-weight precipitates), based on bisphenol A glycidyl ether (DGBEA - diglycidyl ether of bisphenol A [1-3]. That's why the curing process is so important, determining the quality of the laminate and its adhesion with other materials. And non-uniform curing as a result of failure to meet the reaction parameters (non-linear increase in internal temperature due to exothermic chemical reaction of epoxy), leads to exceeding the so-called "life of the resin system" and may cause incomplete curing or entrapment of volatiles or voids, respectively, and thus degradation of the matrix.
Among other things, cold spraying can be used to repair machine parts to (metal particles, nickel alloys or titanium alloys move in a mixture of nitrogen and helium and are gradually applied to the damaged part) restore the desired surface. That is, in this process, metal powder with relatively small particles (1÷50 µm in diameter) is applied to the coating. Additional heating of the batch powder does

not occur, unlike other thermal spraying processes. Particles of powder carried from powder feeder by separate gas stream are injected into a high velocity stream of the gas (300÷1200 m/s) and accelerated towards substrate. The stream of the pressurised and preheated gas achieves high velocity by flowing through a converging-diverging nozzle. In the diverging part of the nozzle gas is expanded to supersonic velocity with simultaneous fall of pressure and temperature. The particles are first injected in front of the nozzle throat or downstream and after exiting the nozzle impact onto substrate at a very high speed (Fig. 1). Upon impact, the particles in the solid state (opposite to the others thermal spray processes where particles after heating are plastic or molten) deform to the form of the splat and create a bond with the substrate. Subsequent new particles impact onto the substrate and form bonds with previously sprayed and deformed particles. Because of very high speed of powder particles, despite the lack of heating, the degree of particles deformation is very high. As a result, a uniform coating with small number of pores and a very high adhesion and cohesion are formed. The definition “cold spray” has come into being to describe this process due to low temperatures (-100 ÷ 100 °C) of the gas stream at the exit of the nozzle.

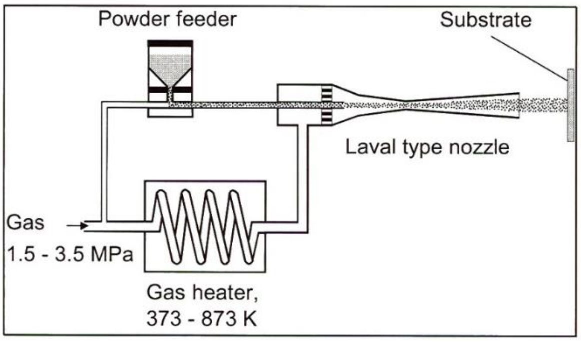

Fig. 1. Schematic of cold spray [4]

The basic characteristic feature of cold spray process is the temperature of the gas stream which is always below the melting point of the sprayed material. As a result, the coating is formed in a solid state. All phenomena accompanying creating of the coating as adhesion to the substrate or cohesion are accomplished in a solid state too, so cold sprayed coatings present unique properties. Firstly, low temperature of the process lets to avoid any phase changes in the feedstock powder, so the sprayed coating presents the same phase composition. Next, as other deleterious phenomena as particle oxidation, evaporation, melting, recrystallisation or gas release are avoided, the obtained coatings are more durable with a better bond strength. Additionally, a very strong adhesion of the coatings to the substrate occurs as result of low temperature of coating deposition.
The objective of the presented studies was to analyze the microstructure and mechanical properties of a cold sprayed Ti-6Al-4V structure for the structure of a composite (laminate) for application in additive manufacturing on hydraulic components.

2. Experimental Data Processing

2.1 Component selection and composite manufacturing technology

In order to carry out the task at hand, that is, spraying a layer of Ti-6Al-4V onto a 4-layer composite molded by the Vacuum Bagging Method at the laboratory of Kielce University of Technology. The flexible vacuum bagging method [5, 6] involves extracting excess resin system and air from a package of percolated composite reinforcement between the mold and the vacuum bag.
In the composite molded by vacuum methods, a 200g/m^3 carbon fabric reinforcement [7] and LH 288 epoxy resin (with H 505 hardener) were selected. The bisphenol A-based epoxy matrix is characterized by very low viscosity, excellent mechanical and chemical properties and thermal strength.

2.2 Vacuum forming process of layered composite

It should be mentioned that at the initial stage of layered composite manufacturing, the mold was degreased by applying a thin layer of a separator (such as Spacewax 300). After the acetone evaporated from the separator (after about 15 - 20min), the surface of the mold was polished (in order to achieve a better quality of the mold surface). After which, double-sided adhesive tape was applied to the edges of the mold, thus defining the field of the prepared mold.
Then, after the appropriate number of layers of carbon cloth were applied and seeped, auxiliary materials were applied (Table 1) and the flexible bag was fixed with clamps on the edges of the mold. An attached spigot (with a vent and optional vacuum reading connector installed), extracted air and possibly excess resin system from the laminate using a vacuum pump.

Table 1: Results of tests of static strength component composites [8]

No	Supporting material	Functions
1	Delamination (peel ply)	acting as a separator of the final product, after tearing off provides a matt laminate surface 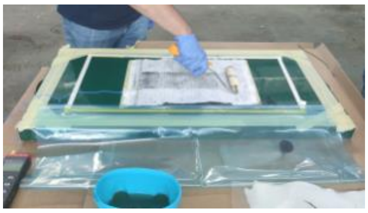
2	suction mat (breathable)	which extracts excess resin system 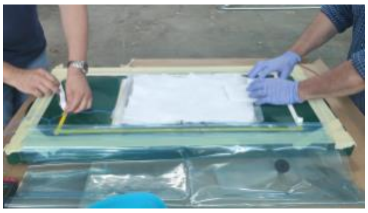
3	perforated foil	which is stuck to the edge of the mould with double-sided tape (Fig. 4), thus creating a vacuum (closed system) 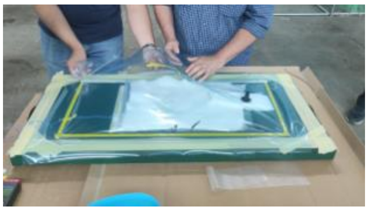

The process of introducing the resin system (injection molding) in a liquid state is carried out through the feed channels into the mold, which were closed after 13 minutes. The technological parameters of the molded laminate with a percentage of 50/50 components are shown in Table 2.

Table 2: Technological parameters of layered composite obtained using vacuum bagging method

Pressure, bar	Hardener	Molding time,h	Gelation time, h	Additional heating, ^{o}C(h)
- 0.6 overpressure	27% H 505	ca. 24	1.5 (T=21-23°C)	50 (10

Then, samples according to PN-EN 10002-1+ACI were cut out of the carbon-epoxy laminate with an average thickness of 1.8 2.0 mm, with dimensions (250 x 25mm) and a 200mm measuring base. The cut specimens were then subjected to a static tensile test on a SHIMADZU AGX-V 20kN machine at a speed of 2 mm/min.

To determine the effect of post-curing, the rest of the specimens were then exposed to UV lamps at 60°C (with 0.76W-m-2 ×nm^{-1} light at 340nm wavelength) and an additional annealing at 50°C for 4h in accordance with ISO 4892-3 and the manufacturer's recommendations.

2.3 Methodology

The coatings were sprayed using the Impact Innovations 5/8 system with the robot Fanuc M-20iA at Kielce University of Technology [9]. The feedstock used for this study was commercial Ti-6Al-4V powder with a "coral-like" morphology (Fig. 2). The working gases used in this process were nitrogen and helium in equal proportions. The coatings sprayed onto the titanium mandrel had a thickness of 15 mm. The microstructure and chemical composition of the powder and the coating were analyzed by means of SEM Jeol JSM-7100. The micromechanical testing of coatings was carried out with the use of the nanoindentation technique (Nanovea) with a Berkovitz indenter (the Olivier and Pharr methodology).

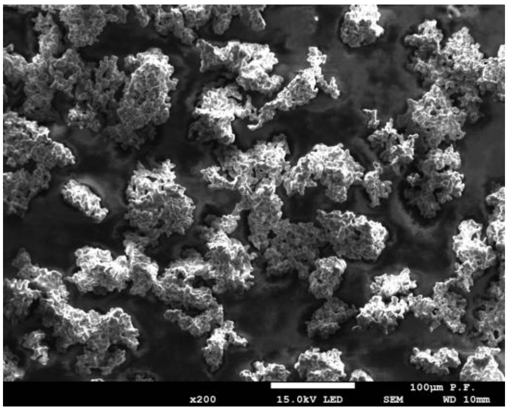

Fig. 2. Morphology of Ti-6Al-4V powder

The high kinetic energy of feedstock particles and their morphology caused significant deformation, and particular splats strongly adhered to the substrate and to each other. Throughout the cross-section, the coating was homogenous and exhibited negligible porosity (Fig. 3).

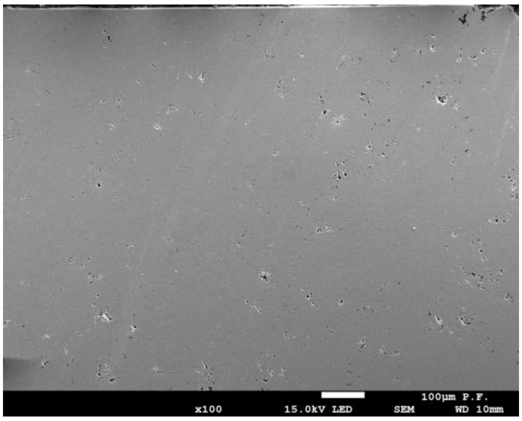

Fig. 3. Microstructure of cold sprayed Ti-6Al-4V coating

On the other hand, histograms and probability distributions of the hardness and Young's modulus of cold sprayed coating showed significant differences (Fig. 4).

ISSN 1454 - 8003
Proceedings of 2023 International Conference on Hydraulics and Pneumatics - HERVEX
November 8-10, Băile Govora, Romania

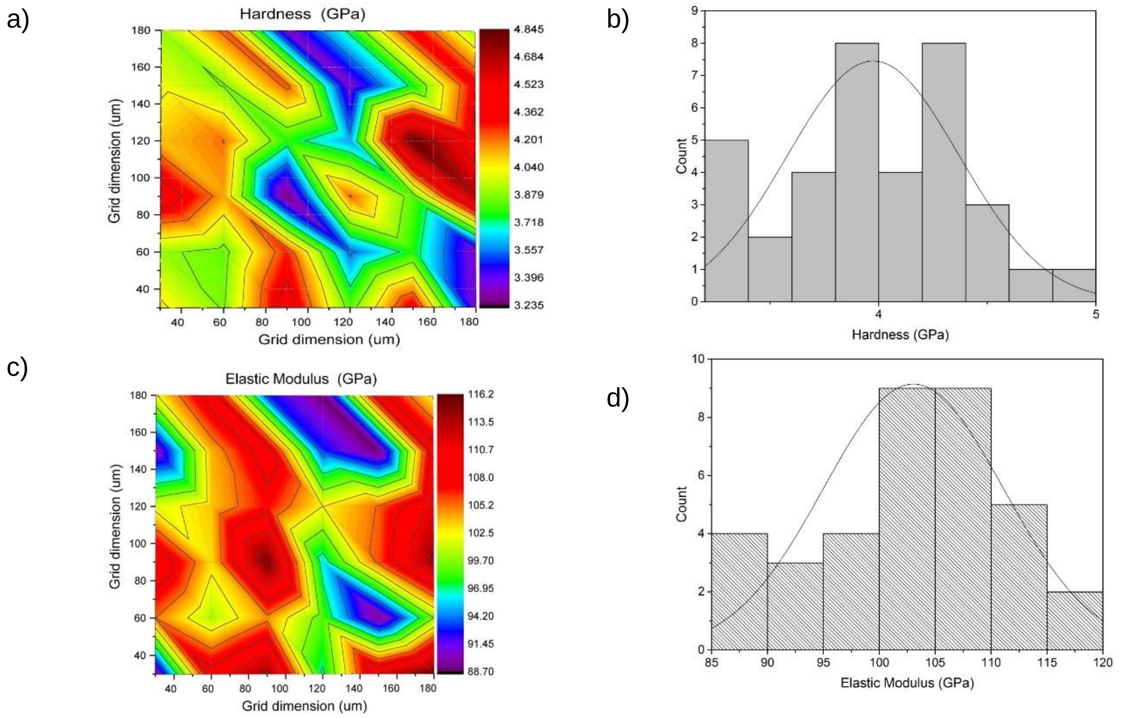

Fig. 4. Distribution of the mechanical properties for a Ti-6Al-4V cold spray coating: (a) hardness map, (b) hardness histogram, (c) elastic modulus map, (d) elastic modulus histogram

2.3.1 Statistical analysis of laminate (sandwich composite) components

The processing of experimental data was based on the assumption that the strength of samples of fibers, bundles of fibers, respectively, decreases as the complexity of the structure increases (which takes into account the strength properties of the components).

$$\sigma_{\text{fibres}} > \sigma_{\text{bundels of fibres}} > \sigma_{\text{sandwich composite (laminate)}} \quad (1)$$

To this end, the distribution function of the glass composite components [10] was investigated as a result of static tensile testing for 12 and 64 samples (Fig. 5) of fibres and an elementary fibre bundle (so-called strands consisting of 10 fibres), respectively. When analysing the experimental data, it is quite important to determine the magnitude of the scatter and to adopt a hypothesis regarding the statistical distributions of the static strength (S_{static}) of the components of the analysed composite structure. Then, the hypothesis of log.-normal strength distribution [19] was adopted for the tested samples through the function:

$$y(x) = x(1 - \Phi_0((\log(x) - \theta_0)/\theta_1)) \quad (2)$$

where $\Phi_0(\cdot)$ - is the standard normal distribution function.

The complexity of the structure of the composite material (from the fibre to the fibre-strand bundle, and then to the laminate itself) causes a deterioration of the average strength and a change in the parameters of the strength probability distribution function (showing a reduction in the value of the statistical parameter which is the standard deviation). Fig. 5 shows classical probability plots of the static strength of the composite components as well as of the composite itself. It can also be seen that the strength range of the fibre bundle specimens is much larger than the strength range for the epoxy composite. This is because no two identical active fibres can ever be obtained, as each bundle has a different number of broken fibres that do not carry the load. Assuming in the model (the main idea of the Daniels model) that the distribution of tensile loads S between n parallel, uninterrupted composite components (strands or fibres) is uniform with the expected fraction of failed strands S_b (the average nominal breaking strength) will be equal to F(s), where F(.) is a function of the cumulative strength distribution of the n strand bundle.

$$s_b = \max_s n \cdot s(1 - F(s)) \tag{3}$$

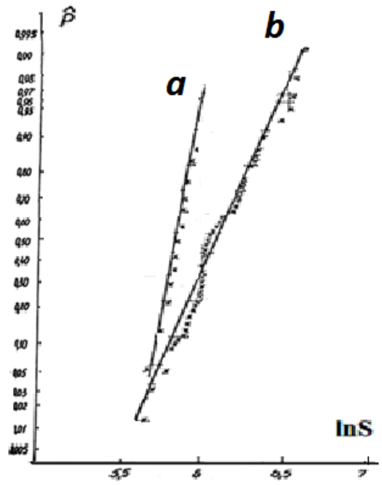

Fig. 5. The normal plot for static strength of a – specimens, b – 10 strands [11]

Making the above assumptions in accordance with the idea of the Daniels model, it can be formulated that: "all fibres have the same load-stress curve and b(S) is the probability of failure of one fibre under load S and (1-b(S)) converges to 0 faster than 1/S, then the strength of a strand S with a sufficiently large number of fibres has a normal distribution with an expectation value, whose parameters are shown in Table 3.

Table 3: Parameters of the probability distribution function of the composite strength

No.	Parameters	Correlations
1	Normal distribution with expected value	$S_r = n \cdot s_r \cdot [1 - b(s_r)]$ (4)
2	Standard deviation (OS)	$\sigma = s_r \cdot \sqrt{n \cdot b(s_r) \cdot [1 - b(s_r)]}$ (5) where: s_r corresponds to the maximum $s \cdot [1 - b(s)]$, which is the average force $\bar{S}_r = s_r \cdot [1 - b(s_r)]$ then OS has the form: $\bar{\sigma} = s_r \cdot \sqrt{b(s_r) \cdot [1 - b(s_r)]} / \sqrt{n}$ (6)

3. A strength model of a fibrous composite with statistical analysis of the properties of polymer matrix components sprayed with Ti-6Al-4V

Assuming a composite consisting of n-fibres embedded in a matrix and the assumptions in Table 4, we observe damage to components within elementary micro-volumes as a result of the development of micro-destruction (elementary volume through the destruction of individual fibres, fibre bundles, matrix cracks up to the avalanche development of macro-cracking).

Table 4: Results of tests of static strength component composites [8]

No	Model objectives
1	The composite consists of fibres (processed into fibre bundles) and matrix, as monolithic joints (Fig. 6).

	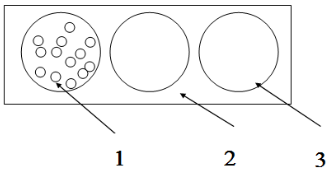 **Fig. 6.** Fiber bundles immersed in a matrix: 1 - fibers, 2 - matrix, 3 - bundles of fibers
2	The fibres (fibre bundles) have random physical-mechanical properties with randomly distributed defects.
3	The deformation in the cross-section is the same in all elements (i.e. the stress in the matrix is less than that in the fibre bundles and the shear deformation in the bundles is negligible compared with the shear deformation in the matrix).
4	When a fibre or a bundle of fibres in a layer (or sandwich composite) breaks, it is transferred to the adjacent fibres (bundles) as a result of shear forces in the matrix (Fig. 7). 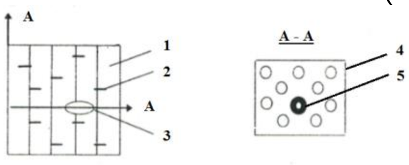 **Fig. 7.** Composite: 1 - bundles, 2 - matrix, 3 - crack bundles, 4 - elementary destruction volume, 5 – destroyed
5	The accumulation of damage cracks in the material structure leads to the appearance of a sufficient number of non-functioning fibre segments (bundles) in the whole volume and the formation of weak segments, which leads to the destruction of the layer (and the laminate) through a critical elementary volume L_{kr} (Fig. 8). $$L_{кр} = d_f \left[\left(\frac{1-V_f^{0.5}}{V_f^{0.5}} \right) \frac{E_f}{G_m} \right]^{0.5} arch \left[\frac{1-(1-\varphi)^2}{2(1-\varphi)} \right], \quad (7)$$ where: L_{kp} - critical ineffective length; j φ - is the relative loading level at which the fiber is considered included in the work (0.97); d_f - is the fiber diameter; E_f - is the elastic modulus of the fiber; G_m - matrix shift modulus; V_f - is the filling factor. 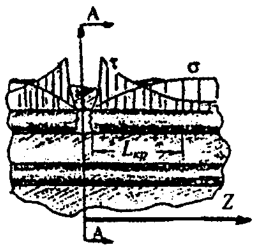 **Fig. 8.** Elementary volume with broken fibre at ineffective length (lkr) at tension (τ, σ)
6	The destruction process takes place in the same way in both the resin bond and the sandwich composite (laminate).

4. Analysis of the results

The obtained values of strength (σ) of the 4-layer composite (from static tensile testing), highlight a slight deviation from the average σ = 126.20MPa (Table 5), related to the plasticization of the matrix. The source of this behavior is their complex microstructure, which makes polymers at the molecular level (i.e. chains, network rings and their crystalline, amorphous and mixed combinations) sensitive to the effects of temperature, visible and ultraviolet light, as well as water (moisture), atmospheric and chemical pollutants.

Table 5: Mechanical properties of the layered composite obtained by the vacuum bagging after accelerated postconditioning of the laminate with fluorescent light in parts of the UVA, UVB and UVC spectrum

Sample No.	ε, mm	σ_{max}, MPa	E, GPa
A–1	1.60	110.47	6.56
A–2	1.84	121.96	6.65
A–3	2.14	146.17	6.76
average	1.85	126.20	6.65

Assuming that the given arrangement of reinforcements works to a greater extent in shear, the glass reinforcement will be destroyed earlier as a result of shearing of the interfacial boundary and the resin layer between the layers, causing significant changes in material constants depending not only on the strength of components (fibres and matrix), but also on the course of the technological process (uneven fibre arrangement in the whole volume, local discontinuities of fibres, lack of adhesion at the fibre - matrix boundary, as well as voids, micro-cracks or gaps) and additional matrix plasticisation. With a view to a uniform stress distribution in the volume.

$$\sigma = \frac{P}{\phi \cdot F_i \cdot n_i} \tag{8}$$

where: n_i - number of fibers, (i = 1, 2, 3,..., n); F_i - cross-sectional surface area pole of the fibre;
P - force (load); Φ - the load level at which the fibre effectively works with the matrix.
The destruction of components (fibres and fibre bundles with individual physical-mechanical properties [12, 13] was based on the critical micro volume.
The location of torn components as fibres, (or bundles of fibres) is random causing an increase of loads between them. At the destruction of the reinforcement in the composite structure the mechanism of stress distribution between the adjacent components (fibers, or fiber bundles) on L_{kr} is activated (under the influence of tangential stresses τ, regroups the stresses on the adjacent fibers - Fig. 3).

$$\tau_{lok} = \frac{\beta\, r}{2} \cdot \varepsilon\, E_i \tanh\left(\frac{\beta\, l}{2}\right) \tag{9}$$

where β – const. ($\beta = \frac{1}{B}$); ε – fibre elongation of the i-th component of the composite;
r – fibre radius, l – fibre length (critical length).
Where:

$$\tanh(x) = \frac{e^x - e^{-x}}{e^x + e^{-x}} \tag{10}$$

The failure process continues, as the load on the fibre is increased by the amount of the redistributed portion of the stress from the broken fibre (or fibre bundle). If the ultimate strength of the laminate (fibre bundle) is exceeded, the redistribution of local stresses (between adjacent components) is not possible.
In such a case the failure of the n^{-th} volume (V_n) with already significant de-lamination takes place in the weakest micro-volume, which is the strength criterion of the whole laminate (Table 6).

$$\sigma = 2\tau/\beta r \tag{11}$$

Table 6: Parameters of the model taking into account the crosslinking process (post-curing) of the laminate

Cross-referencing	L_{kr}, mm	τ_{lok}, MPa	$\sigma_{max.}$, MPa
After curing	1.006	1.3025	104.62

The process of destruction of the composite structure components as well as the composite itself should be complemented by the analysis of the influence not only of the load, but also of the

atmospheric (operational) factors, which complement the sequential accumulation of damage. Having a well-crosslinked (hardened) laminate we can determine the influence [14] of aggressive factors (such as sulphur di- and trioxide SO_2 and SO_3, nitrogen oxides and carbon oxides), which in combination with moisture are inorganic acids.
Also, during aging (which is a process of structural changes that occur in the polymer under the influence of long-term external factors) under natural climatic conditions, it is most often difficult to distinguish which factor has the dominant influence, as they act simultaneously. All the above-mentioned chemical transformations are very complex and often proceed simultaneously.

5. Conclusions

This paper presents the microstructure and mechanical properties of a cold sprayed Ti-6Al-4V structure for the structure of a composite (laminate) for application in additive manufacturing on hydraulic components. A model for estimating the strength of a fibrous composite based on the critical micro-volume, taking into account the distribution of strength properties and the degree of hardening during the laminate curing process using the vacuum bag method is described. The model has been validated with literature examples and experimental data. The non-linear internal heat source and heat transfer process cause non-uniformity in temperature and cure inside the epoxy part. This work is therefore an introduction and at the same time an innovative method that allows further insight into the epoxy resin curing process, which can improve the mechanical and operational properties of the finished element by reducing deformations and residual stresses during the curing process.

References

[1] Lakho, Dildar Ali, Donggang Yao, Kyonghoon Cho, Muhammad Ishaq, and Youjiang Wang. " Study of the Curing Kinetics toward Development of Fast-Curing Epoxy Resins ". *Polymer-Plastics Technology and Engineering* 56, no. 2 (2017): 161-170.
[2] Bereska, Bartłomiej, Jolanta Iłowska, Krystyna Czaja, and Agnieszka Bereska. "Hardeners for epoxy resins." *Przemysł chemiczny* 93, no. 4 (2014): 443-448.
[3] Zhang, J., Y.C. Xu, and P. Huang. “Effect of cure cycle on curing process and hardness for epoxy resin.” *eXPRESS Polymer Letters* 3, no. 9 (2009): 534–541.
[4] Stoltenhoff, T., J. Voyer and H. Kreye. “Cold Spraying - state of the art and applicability.” Paper presented at the International Thermal Spray Conference - ITSC 2002, Essen, Germany, March 4-6, 2002.
[5] Królikowski, Wacław. *Polymer structural composites* / *Polimerowe kompozyty konstrukcyjne*. 1st edition. Warsaw, PWN Publishing House, 2017.
[6] ***. “Composite production method using a vacuum bag.” / "Metoda produkcji kompozytów z użyciem worka próżniowego." April 9, 2012. Accessed February 16, 2020. http://laminaty-trax.blogspot.com/2012/04/metoda-produkcji-kompozytow-z-uzyciem.html.
[7] RYMATEX. Product Catalogue.
[8] Gutans, Juris, Piotr Zagulski, Druvis Verzemnieks, and Martins Kleinhofs. "Failure Model for Unidirectional Composite Element." *Composites the Theory and Practice* 22, no. 2 (2022) 58-61.
[9] Impact Innovations GmbH. Accessed November 6, 2023. https://impact-innovations.com.
[10] Chatys, Rafał, Martins Kleinchofs, Aleksander Panich, and Krzysztof Piernik. "Forecasting the Strength of Reinforced Polymer Composite Using Statistical Analysis Method." Paper presented at the 24th International Conference "Engineering Mechanics 2018", Svratka, Czech Republic, May 14-17, 2018.
[11] Chatys, Rafał, and Łukasz Jan Orman. “Technology and properties of layered composites as coatings for heat transfer enhancement." *Mechanics of Composite Materials* 53, no. 3 (July 2017): 351–360.
[12] Xiong, Xuhai, Rong Ren, Siyang Liu, Shaowei Lu, and Ping Chen. "The curing kinetics and thermal properties of epoxy resins cured by aromatic diamine with hetero-cyclic side chain structure.” *Thermochimica Acta* 595 (November 2014): 22–27.
[13] German, Janusz. *Basics of mechanics of fibrous composites* / *Podstawy mechaniki kompozytów włóknistych*. Cracow, AGH University Press, 1996.
[14] Szumniak, J., Z. Smoczyński, and K. Szcześniak. "Armament and military equipment polymer composite ageing.” / "Starzenie polimerowych kompozytów uzbrojenia i sprzętu wojskowego." *Zeszyty Naukowe WSOWL* 159, no. 1 (2011): 271-285.

ISSN 1454 - 8003
Proceedings of 2023 International Conference on Hydraulics and Pneumatics - HERVEX
November 8-10, Băile Govora, Romania

ANALYSIS OF THE INFLUENCE OF THE CHARACTERISTICS OF WORKING FLUIDS IN HYDRAULIC SYSTEMS ON FUNCTIONAL PERFORMANCE

Adriana Mariana BORȘ[1], Liliana DUMITRESCU[1,*], Ștefan ȘEFU[1], Kamil SZEWERDA[2]

[1] National Institute of Research & Development for Optoelectronics/INOE 2000, Subsidiary Hydraulics and Pneumatics Research Institute/IHP, Bucharest, Romania

[2] KOMAG Institute of Mining Technology, Gliwice, Poland

* lilianad.ihp@fluidas.ro

Abstract: *By following the expression of the binding force of the molecules (resistance of fluid to flow) under controlled pressure and temperature conditions and the influence of the characteristics on the efficiency of the components of the hydraulic mechanism, one can evaluate the compatibility and optimize the potential of the lubricating fluid (subjected to physical-chemical stress) and its impact (toxicity and loading) on the environment after the cycle of use. Phenomena inside the lubricant layer have a great influence on lubrication, as a result of the association of molecules under the action of existing polar substances, but also through intra-molecular friction. The phenomena occurring at the friction surface, at the micro level of the peaks in contact, where the temperature and pressure are significantly increased, can be studied and diminished to reduce energy losses, by creating a protective layer, thus providing better resistance and elasticity of the molecular contact surface. Starting from the aspect of element interactions and the study of chemical transformations between friction surfaces and reaction media, the action of (tribological and rheological) phenomena on the durability of mechanical systems can be analysed and developed. This action can be carried out through mathematical modeling and parameter calculation methods, which define the phenomena that take place at the collision, for the extension and improvement of the experiments at the prototype level. The cumulative influence of the phenomena inside the lubricant layer with those occurring at the lubricant-metal interface is determined by the surface properties of the lubricant but also by the attraction forces from the surface of the metals with which the lubricant is in contact.*

Keywords: *Tribology, durability, lubricant, viscosity, hydraulic systems*

1. Introduction

The development of applications involving friction, wear and lubrication processes at the level of interactions of surfaces in relative motion requires interdisciplinary connections of mechanics, mathematics, physics and chemistry, materials science, biology and engineering sciences. This type of movement between two surfaces highlights specific basic tribological phenomena (lubrication, friction and wear). The methods used for the synthesis of lubricant composite materials aim to ensure certain performance characteristics of the resulting product. Thus, the lubricating oil is recommended for one or more essential properties of a given application: thermal properties, very good chemical resistance, ordered texture on a micro or nanometric scale.
The main aspects of molecular interactions are aimed at:
- geometry, kinematics and dynamics of interactions;
- friction phenomena in the absence and/or presence of the lubricant;
- wear phenomena at the level of interactions between fluid layers;
- lubrication phenomena in limit, mixed, hydrodynamic (HD), elastohydrodynamic (EHD) regime, etc.

The quality of a hydraulic fluid is strongly influenced by the characteristics provided by the finished product. In order to meet the quality criteria of hydraulic oils, lubricating oil compositions have been developed which, among other things, ensure:
- energy transmission and saving;
- provides superior protection against fluid losses (through leaky seals, contaminants, pump wear and irregular operation);

- lubrication, friction protection (between metal components, anti-wear);
- anti-corrosion protection of lubricating circuits;
- increasing both thermal and oxidation stability;
- neutralization of acid products and maintenance of oil characteristics even under conditions of exposure to moisture and extreme temperatures;
- demulsifying properties (for rapid water separation) and good filterability, with high anti-wear and EP characteristics;
- decreasing tendency foaming agents (containing antifoam agents to control the release of entrained air);
- compatibility with non-ferrous metals;
- increasing machine reliability/operating time between lubricant changes;
- maintaining and extending machine lifespan;
- preventing rust and corrosion, etc.

The lubrication and flow characteristics of the oils are represented by:

- unctuousness, a property that depends on the polarity and the length of the molecules in the lubricant,
- fluid viscosity, a property that is strongly influenced by the molecular orientation in the fluid layers and the temperature of the flow. This property can affect power losses in hydraulic systems, hydraulic-mechanical losses (friction losses in pipes) and volumetric losses (leakage losses). These two properties have an influence on the wear of the hydraulic system, namely: the operation of the system in a wide range of temperatures, lower oil consumption, better sealing between the piston, segments and cylinder.

Accidental oil leaks and spills from various hydraulic devices are a medium and long-term environmental polluter. These residual oils have a content of toxic, dangerous particles (metallic and hydrocarbons) with a high migration potential (in soil and groundwater) and complex volatile, hydrophobic, biodegradable, etc. mixtures, which produce damage with a major impact on the soil, with effect on the ecosystem such as:

- the disappearance of some species;
- danger to health and food safety (weaker harvests);
- threatens the well-being of ecosystems and the environment;
- climate change (release of CO_2);
- desertification (arid regions);
- population dislocations (emigration), but also economic (local, zonal, regional) impact.

The pollution aspects as much they are known, they are as much debated, this topic being of real interest also for the Intergovernmental Science-Policy Platform on Biodiversity and Ecosystem Services (IPBES), which dealt with this topic in a Report on soil degradation. Soil pollution is a global threat, extremely serious especially in regions such as Europe, Asia and North Africa, according to the Food and Agriculture Organization of the United Nations (FAO) [1]. Phenomena such as erosion, loss of organic carbon, high salt content, compaction, acidification and chemical pollution are the main causes of current soil degradation. FAO shows that both intense and moderate degradation already affects a third of the planet's soil, and recovery is slow, practically 1000 years would be needed to create a layer of 1 centimeter of arable soil. Therefore, choosing the lubricant for fixed or mobile equipment with hydraulic systems is an extremely important issue, which requires knowledge of the existing working conditions and environment, the required physical-chemical properties, the degree of loading, the special requirements and the compositional content of these hydraulic oils.

2. Analysis methods and hydraulic oils characterization mechanisms

The main characteristics of these oils can be grouped as follows:

- to ensure superior lubrication qualities (viscosity, viscosity index, unctuousness);
- to determine the field of use (viscosity variation with temperature and pressure, volatility);
- to determine the stability under conditions of use (resistant to oxidation, to the formation of deposits);

- for purity and anticorrosiveness (content of mechanical impurities, water, anticorrosive properties),
- various, for oils depending on their field of use.

Therefore, it is very important that the hydraulic oil has the best and long-lasting stability with temperature variation. The specialized literature confirms that the addition of additives with combined effects leads to an increase in the viscosity index [2, 3]. Additives are chemical substances, organic compounds, based on metals or polymers, in a proportion of 25-15%, whose chemical composition must be compatible with the sealing system and which confer the anti-wear, anti-corrosion and maintaining functions of lubricant viscosity.

From the point of view of the type and nature of the additives introduced into the base oil, they can be:

✓viscosity modifiers
✓anticorrosive and antirust
✓defoamers
✓pour point depressants

These additives are used to prevent the formation of crystal networks or to inhibit the growth and solvation of nascent paraffin crystals by adsorption.

✓dispersants (detergents)

Due to the super basic nature of these additives, low operating temperatures, solid impurities are kept in suspension and thus corrosion can be combated.

The action of these additives can be explained by three types of mechanisms:

- adsorption, mechanism by which agglutination is prevented;
- solubilisation, a mechanism leading to the formation of water-in-oil micelles that encapsulate oil-insoluble particles;
- chemical neutralization, a mechanism that can stop the phenomenon of polycondensation.

✓antioxidants (inhibitors of radicals and hydroperoxides)

This type of additives can interfere with the propagation mechanism at different stages of the process through free radicals. These are the most used additives, being practically added in the formulation of all lubricating oils.

✓extreme pressure and anti-wear

These adhesives have as their first role the formation of a protective pellicle layer as a result of the orientation and adsorption of the polar functional groups on the polymer chain. During lubrication, physical or chemical adsorption phenomena occur and the orientation of surfactant molecules from the lubricant at the metal surface takes place. The molecules orientation in the first layer is much more stable than that of the other layers, so the disorder gradually increases in the volume of the lubricant.

The following transformations can occur in the lubricating mechanism system:

- plastic deformations in the metal, without it being destroyed, as a result of the adsorption mechanism at the level of the first layer;
- increasing the contact surface with the formation of compounds with lower mechanical resistance (surfactants with groups of sulfur, chlorine, phosphorus, etc.) as a result of some chemical reactions taking place;
- arching of the chain of oriented molecules as a function of speed, which is stronger the longer its length and stability, but above a certain speed, breakage of hydrocarbon molecules or pairs of molecules in the oriented boundary layer may occur, as a result of the fact that in the hydrocarbon planes the bond energy is lower than in the surfactant planes.

The tendency to break increases with increasing chain length, therefore with the thickness of the lubricant film.

One can expect different phenomena developed by contaminants, especially secondary products resulting from thermal decomposition or oxidation reactions. Numerous compounds (alcohols, aldehydes, ketones, lactones, esters, acids, condensation products - resins) with characteristic effects were identified in the used oils. Thus, acid radicals attack metals, oil-soluble salts favour the formation of emulsions, oxygen compounds lead to colloidal deposits, so through oxidization the volume of molecules increases and blocks the filter and hydraulic valve, water generates emulsions,

causes foaming (aeration increases the compressibility of oils, the cavitation effect appears) and accelerates oil oxidation, suspended solid particles contribute to premature wear of hydraulic oil, the presence of sulfur in oils leads to the appearance of corrosive compounds during use, the increase in hydrogen content leads to a decrease in relative density, oil vaporization leads to the formation of insoluble condensation products, condensation products settle, increase viscosity, form corrosive acidic substances and impede transmission.
To combat phenomena induced by various contaminants, manufacturers resort to specific additives with various effects for the protection of hydraulic drive systems. The best known of these specific additives are:

- Ashless dispersant type additives

From this category, the most commonly used additives contain polyisobutene, where the polar part is an amine and the linking group is maleic anhydride or the phenolic nucleus.

- Additive with depressant effect

From this category, the most frequently used additives are based on polyalkyl acrylates and polyalkyl methacrylates, substances with functional groups that occupy an important place in the production of additives of this type.

- Ameliorating type additives

This type of additives contains copolymers of fumaric esters with vinyl acetate, copolymers of alpha olefins, styrene-butadiene or styrene-isoprene copolymer and polyalkyl-styrenes, as well as naphthalene and phenol derivatives, the best known being a polyalkyl-naphthalene and ditetra alkyl-phenol phthalate or polymers of these copolymeric derivatives. However, too high a content of ameliorate additives is not recommended for closed systems because they reduce the rate of water-oil separation.
Other types of specific additives are also:

- Viscosity index modifiers

These additives have in their composition organic polymers, soluble in oil, such as polyisobutylenes, polymethacrylates, copolymers of methacrylates with alkyl radicals of different lengths, ethylene propylene copolymers, hydrogenated block copolymers of isoprene and styrene as well as polyacrylates, from the range of acrylic copolymers with alkyl radicals of different lengths. Polymer additives are made up of macromolecules with different degree of polymerization; they can be characterized by chromatographic analysis, the most used being the gel permeation method. At high temperatures or at friction between lubricated parts, at high pressures and speeds, macromolecules break. For this reason, shear strength becomes an important characteristic of polymers.

- Antioxidant additives

Like the ameliorate additives, these additives contain phenol derivatives but also aromatic amines such as: di-tert-butyl-paracresol, also known as Topanol, with an antioxidant effect up to 180°C, octyl-diphenyl-amine, alkyl phenyl-beta - naphthylamine. Among the most widely used peroxide removers there is the zinc alkyl dithiophosphate compound that acts as an anti-wear additive, but there are also compounds with sulfur, with selenium, or their combinations, for example compounds with sulfur and nitrogen, with sulfur and phosphorus, etc.

- Additives for extreme pressure and anti-wear

This type of additives forms a film protective, a coating layer that contains several types of polar organic compounds such as: alcohols, esters, amines, fatty acids, sulfur compounds as disulfides, sulfurized olefins, esters of sulfurized unsaturated fatty acids of the dialkyl polysulfide type, dithiophosphate of zinc, and above all, additives with sulfur and phosphorus or sulfur, phosphorus and nitrogen which give appropriate anti-deposition qualities to hydraulic oils.
Filterability is an important characteristic for the good operation of hydraulic equipment. Mixed oils contain constituents of different origins, each type of oil has specific properties in certain amounts and provides a certain contribution, resulting in a beneficial and balanced oil for the hydraulic system. Their composition contains an ideal percentage of polyunsaturated fatty acids such as linoleic and linolenic acids, monounsaturated fatty acids and other constituents. Vegetable oils contain a mixture of technological plants, seeds (sunflower, soybean, corn germ, rapeseed, cotton, sesame) or fruits (walnuts, hazelnuts, coconuts), according to special technologies, the unsaturated fatty acids being

in the form of cis-cis (of the same side of the unsaturated bond). However, a large intake of polyunsaturated fatty acids has negative effects, the most common of which is the peroxidation effect, which favours the accumulation of toluidine and aniline. It is known that the basic effect of aniline is a precursor for obtaining polyurethanes and that it leads to the formation of mineral accumulations (stones), and in extreme cases, through certain peroxidising compounds, it can favour the aging of hydraulic oil.
Hydraulic fluids, depending on their composition and properties, as one can see in the diagram in Figure 1, have an important role in industry.

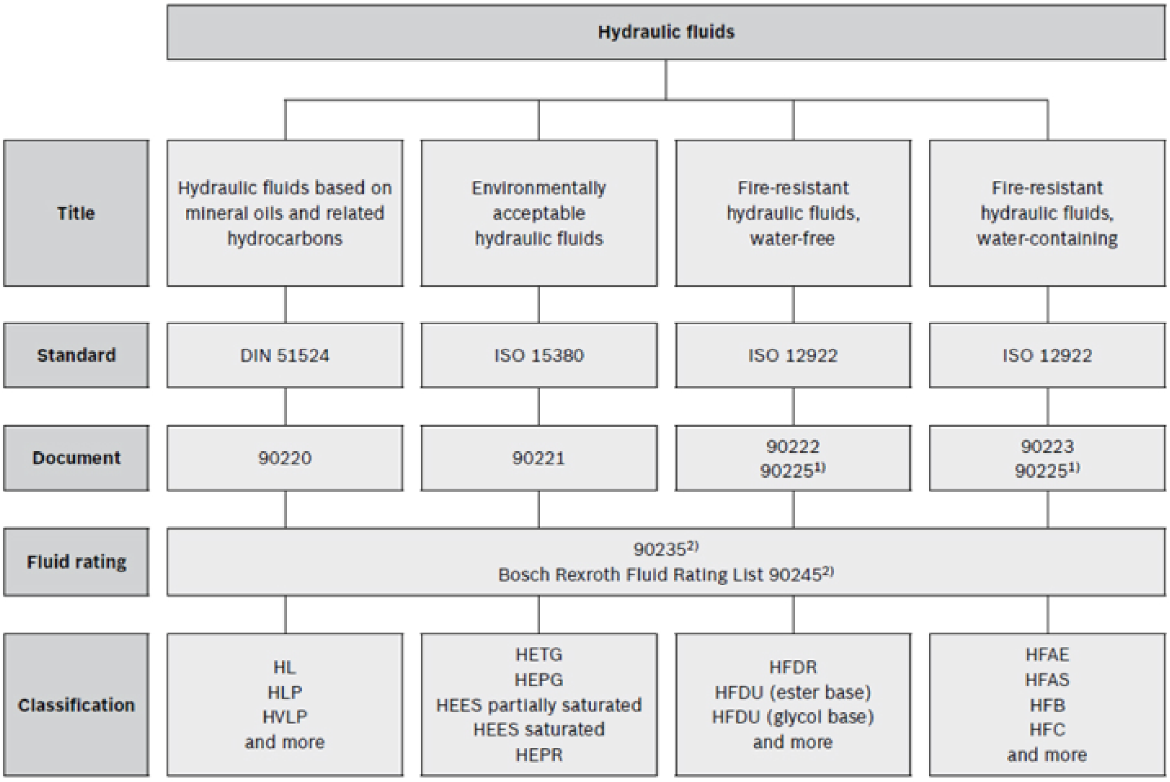

Fig. 1. Classification and properties of hydraulic fluids [4]

Therefore, their demand and the type of use led to their diversification and improvement in the context of the sustainable concept for increasing efficiency.
The German norm DIN 51524 notes them with HL, HLP, HVLP. HL, HLP, HVLP.
- HL: contains active ingredients to reduce aging and protect against corrosion;
- HLP: other active ingredients are added compared to HL to reduce wear, additives that improve particle transport and water dispersibility; it has the largest field of applicability in practice.

As such, the major manufacturers of such products have also developed environmentally friendly hydraulic fluids, so-called biofluids, which must meet the technical requirements of DIN ISO 15380 as environmentally acceptable hydraulic fluids and the classification of fluids used in hydraulic applications defined in ISO 6743-4 [5, 6]. These ecologically acceptable biofluids with a minimum base fluid content for each product group of at least 70% (m/m) are grouped into several categories, namely:
- vegetable oils HETG (Hydraulic Oil Environmental TriGlyceride) whose composition is based on triglycerides, is technically limited by lower resistance to oxidation and temperature stability, as a result of their "double bonds".
- Synthetic Esters - HEES (Hydraulic Oil Environmental Ester Synthetic). Group HEES further splits into 2 sub-categories with different levels of performance properties:

a) Unsaturated (or partially saturated) synthetic esters are products based on vegetable resources or their mixtures. Their technical applicability in high demanding applications individually depends on composition of the mixture;
b) Saturated synthetic esters currently provide the most sophisticated, environmentally acceptable solution for hydraulic systems. Technical advantages of saturated synthetic esters are performance benefits, extreme stability, wide temperature range, compatibility, high levels of biodegradation and renewable resources.
- HEPR (Hydraulic Oil Environmental PAO (polyalphaolefins) and Related products) (and other synthetic hydrocarbons). HEPRs are produced in very low viscosities, limiting their primary applicability. Viscosity modifiers are required to improve their usability in common hydraulic applications. However, their environmental acceptance is often compromised (similar to HEPG).
- HEPG (Hydraulic Oil Environmental PolyGlycol) - in their composition, the majority of compounds are of the polyglycol type. Performance-wise HEPGs are highly sophisticated products. However, their severely limiting factors are incompatibility with sealing materials, hoses, and virtually any other type of hydraulic oil. HEPGs are also questioned for poor biodegradation and not meeting criteria for renewable resources, e.g., unable to obtain Ecolabels. HEPG oils are used only on a small scale.
Environmental compatibility means minimal toxicity, easy biodegradability and no bioaccumulation.
Biodegradable hydraulic oils have favourable rheological properties compared to mineral oils, they have a reduced tendency to degrade, they are coatings materials, carbonation products or resins with good adhesion capacity, which leads to the increase in the efficiency of hydraulic oils, they do not undergo changes in viscosity for large temperature ranges during operation, etc.

Table 1: Classification of Biodegradable Hydraulic Fluids and typical characteristics [7]

Classification of Biodegradable Hydraulic Fluids and typical characteristics

Classification ISO	Composition	Base Fluid	Typical Temperature Range (ISO)	Characteristic Features
HETG	Triglyceride	Vegetable	-20 to +70°C	+ Excellent biodegradation - Lower oxidation resistance
HEES	Synthetic Ester 1) unsaturated 2) saturated	Synthetic	-30 to +90°C	+ Stable, High-performing + Excellent biodegradation
HEPR	Poly alpha olefin (PAO)	Synthetic	-35 to +80°C	+ Good stability - Only available in low viscosities
HEPG	Poly alkyl glycol (PAG)	Glycol	-30 to +90°C	+ Stable, often water-soluble - Incompatible

The most important characteristic features of these biofluids are:
✓ great lubrication performances
✓ outstanding thermal oxidation stability
✓ wide operating temperature range, very low pour point
✓ very long oil-change interval
✓ neutral to seal materials and elastomers
✓ readily biodegradable; non-toxic, with non-foaming additives, CO_2 emissions reduction
✓ EU Ecolabel Certificate of Environmental Excellence.

These types of oils are high performance hydraulic fluids, some have a mixed composition with partial content of saturated and unsaturated synthetic products, some without zinc, easily biodegradable. A special additive package provides excellent extreme pressure properties, thermal oxidation resistance, anti-wear control and non-foaming.
Another characteristic of these hydraulic oils with an important value is the iodine number. This number is a value for the amount of unsaturated organic esters in grease and oil. The value is determined by adding iodine to the grease or oil until the ability of the grease or oil to chemically bind is stopped; essentially, the iodine number is how many grams of iodine were added per 100 grams of substance tested.

A higher iodine number defines the level of unsaturated esters in the liquid, which could combine with other substances to produce a chemical bond. In unfavourable circumstances such as contaminated oil, high temperature or extended drain intervals, high levels of unsaturated organic esters, as found in plant-based industrial oils (e.g., rapeseed), they will react and bind with other substances, e.g., oxygen, and can cause gumming and residues.

Table 2: Typical data for three readily biodegradable fluids in comparison with mineral oil [8]

Typical Available Data	Standard Mineral Oil	HETG (Rapeseed Type Oil)	Unsaturated HEES	Saturated HEES
	ISO VG 32			
Density @ 15°C (g/ml)	0.880	0.922	0.929	0.918
Flash point (°C)	204	255	198	240
Pour point (°C)	-29	-33	-36	-58
Viscosity @ 40°C (mm^2/s)	32.0	34.0	35.0	31.8
Viscosity @ 100°C (mm^2/s)	5.4	8.0	8.1	5.8
TAN (mg KOH/g)	0.96	0.40	0.60	0.70
Viscosity index	103-140	210-250	175-215	140 -150
Iodine value	-	80-120	40-80	<10
Optimum temp range (°C)	<80	<60	<80	>80

The types of fluid available are many and varied; it is therefore essential to evaluate the criteria of a particular environmentally sound hydraulic fluid (ESHF) before use. Table 3 highlights the various properties of the typical fluids available.

Table 3: Properties of typical fluids [8]

Typical Available Data	HETG	HEES (Unsaturated)	HEES (Saturated)	HEPR	HEPG
Flowability at low temp.	-	+/-	++	+	++
Oxidation stability	-,#	+/-	++	+/-	++
Evaporation loss	+	+	++	-	++
Water separation	-	+/-	++	+	Water soluble ##
Anti-rust protection	++	++	++	++	-
Miscibility with mineral oils	Yes* after clarification	Yes* after clarification	Yes* after clarification	Yes* after clarification	No
Compatibility with seals	+	+	+	+	+
Hydrolytic stability	-	+/-	+/-	+	++
Price	+	+/-	+/-	+/-	+
Storage times	-	+	++	+/-	+
++ = Very Good + = Good +/- = Average - = Poor # = Can cause sticking ## = Water content increases corrosion, cavitation * = Mixtures should be avoided, they are not advantageous					

Oxidation, or ageing, of a fluid is caused when a fluid reacts with oxygen.

The result is extreme thickening and gumming of the fluid, producing varnish deposits which can lead to catastrophic system failures. Chemically speaking, vegetable-based and unsaturated ester-based fluids have many open bonds that react with oxygen when exposed to thermal load causing the fluid to age more rapidly. Saturated esters, on the other hand, have significantly fewer open bonds so they do not oxidise rapidly and will last much longer when subjected to high temperatures. Most fluids will have adequate anti-corrosion properties although the chemical structure may differ across the number of functional groups and degree of unsaturation of the polymer chain. The compatibility of the hydraulic fluid with the materials of the cylinder/equipment sealing components is mainly influenced by the chemistry of the respective fluid, parameters such as viscosity or product formulations differ between lubricant manufacturers. It is therefore essential to know detailed seal compatibility data from the supplier for the fluid to be used. Table 4 shows an example in this sense.

Table 4: Detailed data on sealing compatibility according to different viscosity classes of hydraulic oils [8]

Characteristics of Test	Units	Requirements				Test Method or Standard
Viscosity Grade		**22**	**32**	**46**	**68**	**ISO 3448**
Elastomer compatibility after 1,000 h at given test temperature						ISO 6072
NBR I	°C	60	80	80	80	
HNBR	°C	60	80	80	80	
FPM AC 6	°C	60	80	80	80	
AU	°C	60	80	80	80	
Change in Shore-A-hardness, max.	grade	±10	±10	±10	±10	
Change in volume, max.	%	-3 to +10	-3 to +10	-3 to +10	-3 to +10	
Change in elongation, max.	%	30	30	30	30	
Change in tensile strength, max.	%	30	30	30	30	

Consideration should be given to the relationship between the viscosity, temperature and pressure of a fluid. Viscosity index (VI) is an arbitrary measure for the change of viscosity with temperature. Knowledge of the chemistry involved is important in order to ensure the correct choice of fluid. Most fluids will thicken as the pressure exerted on them is increased. Table 4 gives an indication of typical changes of viscosity with pressure. More detailed information can be obtained from the supplier of the product used. The temperature of the oil varies in a wide temperature range (from -40^{o}C to 120^{o}C), so for bio-hydraulic oil the viscosity index is in the range of 150-220, and for mineral oil the viscosity index is around 100. Oil concentrations in test solutions are inherently unstable and sensitive to experimental methods affecting the amount, bioavailability and estimated toxicity of dissolved hydrocarbons. ATIEL (Technical Association of the European Lubricants Industry), together with ATC (Additive Technical Committee) and ACEA (European Automobile Manufacturers' Association), define the limits of the tests and monitor compliance with the declared qualities. One of the most important problems is to establish the chemical nature, structure and composition of the additives and the quantitative ratio in which these additives must be introduced into the oil, so that the resulting lubricating oil composition has specific physical-chemical characteristics.
Mainly these characteristics are: preservation of the viscosity index in operation, dispersing capacity against solid impurities, reduced wear of the device parts by friction, antioxidant properties, prevention of the formation of liquid residues, etc. These aspects must be followed and maintained within the appropriate parameters to ensure the fulfilment of quality norms in the operation of the hydraulic device.

3. The influence of chemical composition on the toxicity of hydraulic oils

The composition of the lubricating oil consists mainly of components such as:
- carboxylic acid derivative, preferably ethylene polyamine, and a substituted succinic acylating agent consisting of a polyalkylene group, preferably polyisobutylene, of medium molecular weight;
- succinic groups with a polydispersity index, preferably in the range of 2...4 [9];
- alkali metal salt of a carboxylic or sulfonic acid, preferably sodium or potassium alkyl benzene sulfonates, with increased basicity;
- dithiophosphate dihydrocarbons, preferably of zinc, calcium, magnesium, or copper, dihydro-dithiophosphoric acid being prepared by the reaction of phosphorus pentasulphide with a mixture of isopropyl or isooctyl alcohol with primary alcohols, containing at least 20% molecules of isopropyl alcohol or sec- butyl, preferably with a mixture of isopropyl and isooctyl alcohol;
- carboxylic acid ester derivative, which is a product of the reaction between a substituted succinic derivative and a polyol, with a polyamine compound, preferably ethylene polyamines, the components being introduced into the oil as such or in the form of a concentrate;
- polymerized hydrocarbons such as polypropylenes, polybutenes, copolymers of propylene and isobutylene;
- alkylbenzene derivatives, such as dodecylbenzene, tetradecylbenzene, dinonylbenzene, di(2-ethylhexyl)-benzene but also products of chemical synthesis;
- polymerized hydrocarbons such as polypropylenes, polybutenes, propylene and isobutylene copolymers;
- their halogenated derivatives, poly(l-hexene), poly(l-octene), poly(l-decene), as well as their mixtures;
- alkylbenzene derivatives, such as dodecylbenzene, tetradecylbenzene, dinonylbenzene, di(2-ethylhexyl)-benzene, etc.;
- polyphenyl compounds, such as diphenyl, terphenyl, alkylated polyphenyl compounds, etc.;
- alkylated diphenyl ethers and alkylated diphenyl sulfides and other synthetic compounds with similar structures and properties, in the form of their derivatives and homologues;
- polymers and copolymers of oxyalkylenes, in which the terminal hydroxyl groups have been etherified or esterified, with alcohols, phenols and respective acids such as polyoxyethylenes or polyoxypropylenes, dimethyl ether of polypropylene glycol, diphenyl ether of polyethylene glycol, diethyl ether of polypropylene glycol;
- esters with monocarboxylic acids with polyols or polyol ethers, such as trimethylolpropane, pentaerythritol, dipentaerythritol, tripentaerythritol, etc.
- esters with monocarboxylic acids or esters of polycarboxylic acids etherified or esterified at the terminal groups such as esters with acetic acid, mixtures of esters with fatty acids, or the diester tetraethylene glycol with an oxoacid with a large number of carbon atoms;
- esters of some dicarboxylic acids (phthalic acid, succinic acid, alkyl succinic acids, maleic acid, fumaric acid, adipic acid, linoleic acid dimer, malonic acid, alkylmalonic acids, alkenylmalonic acids, etc.) with different alcohols (such as butyl alcohol, hexyl alcohol, dodecyl alcohol, 2-ethylhexyl alcohol, ethylene glycol, diethylene glycol monoether, propylene glycol, etc.), such as dioctyl phthalate, dodecyl phthalate, linoleic acid dimer 2-ethylhexyl ester (tetraethylene glycol and 2-ethylhexanoic acid);
- some organic silicon compounds, examples: polyalkylsiloxanes, polyarylsiloxanes, polyalkoxysiloxanes, polyaryloxysiloxanes or organic silicates, such as tetraethylsilicate, tetraisopropylsilicate, tetra(2-ethylhexyl) silicate, tetra(4-methylhexyl) silicate, hexyl (4-methyl-2-pentoxy)disiloxane, polymethylsiloxanes, poly(methylphenyl)siloxanes, etc.;
- some liquid phosphoric acid esters, such as tricresyl phosphate, trioctyl phosphate, or decanephosphonic acid diethyl ester, as well as polymeric tetrahydrofurans can also be used as synthetic oils.

The olefinic monomers from which the polyalkylenes are derived from copolymers having double terminal bonds. They can rarely form polymers due to spherical hindrance [9]. Aliphatic polyalkylenes, those without aromatic or cycloaliphatic substituents, are preferred.

Polyalkylenes with relatively low molecular weights are preferred; they can be obtained starting from the corresponding polymers with high molecular weights by known destruction processes, such as thermal, mechanical, oxidative destruction. Known polymerization and copolymerization techniques include, among others, ways to adjust the molecular parameters by controlling the polymerization temperature, adjusting the concentration and nature of the initiator or catalyst, or introducing chain transfer agents [10]. Obtaining substituted succinic acylating agents is carried out by processes, which usually consist in the direct reaction of one or more polyalkylenes with a maleic or fumaric reactant (maleic acid, fumaric acid, maleic anhydride, fumaric anhydride, as well as mixtures of two or more of these reactants). Acylation reagents are in fact only an intermediate in the process of obtaining carboxylic acid derivatives and consist in the reaction of one or more such substituted succinic acylation reagents (agents) with one or more amino compounds. Amines (alkylene polyamines and polyalkylene polyamines) with primary amino groups (-NH_2 type) and polyamines (two -NH- groups) such as aliphatic, cycloaliphatic, aromatic or heterocyclic amines are preferred. Compositions derived from polyamines have characteristic dispersing properties, superior qualities in terms of the viscosity index of the lubricating oil composition. The compositions of carboxylic acid derivatives resulting from the reaction with amino compounds are complex mixtures containing acylation products of amines, namely amine salts, amides, imines and imides. The ratio between the acylation reactant and the amine one highlights the fact that with the increase in the functionality of polyamines, there is the possibility of using larger amounts of amine, obtaining an additive product with appropriate properties [11]. These compounds can be carboxylic acids, from which alkali metal salts can be derived, usable as an additive agent with the role of dispersant in the compositions of different types of hydraulic oils. As a rule, these compounds are aliphatic, cycloaliphatic or aromatic, without alkylenic unsaturation, mono or polybasic, or naphthenic acids, cyclohexanoic acids, cyclopentanoic acids, alkyl or alkenyl substituted aromatic carboxylic acids [12-14]. Dispersing agents, based on acylated nitrogen, soluble in oil, are characterized by the presence in their structure of a polar group substituted with hydrocarbons selected from the acyl type class, acylimidoyl and acyloxy radicals in which the hydrocarbon substituent contains a large number of carbon atoms aliphatic. In the case of acylated nitrogen compounds with two or more polar groups in one molecule, the hydrocarbon substituent must contain at least half the number of aliphatic carbon atoms per polar functional group. Radicals must be substantially saturated, with saturated carbon-carbon covalent bonds. An excessive percentage of unsaturated bonds makes the molecule susceptible to oxidation, degradation and polymerization resulting in hydrocarbon-based decomposition products that can influence the degree of flammability of hydraulic oils, according to the scheme in Figure 2.

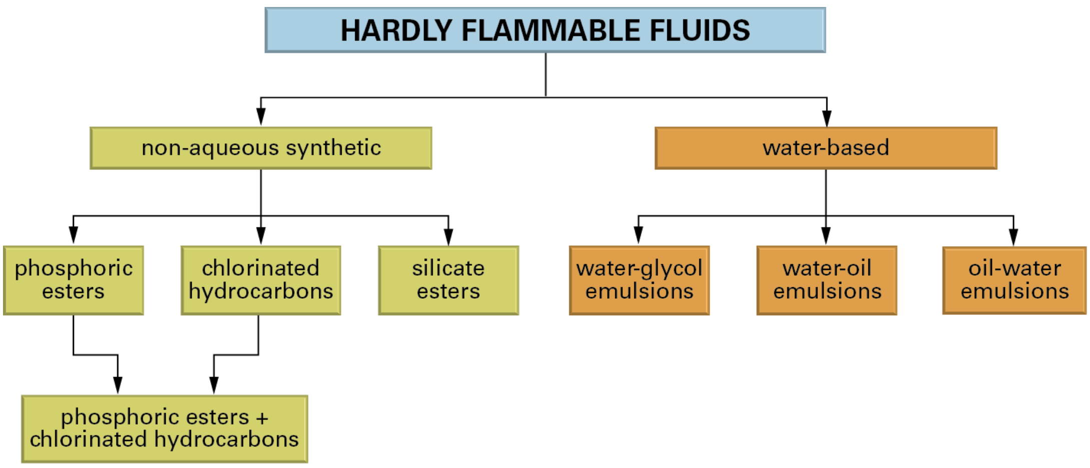

Fig. 2. Scheme of hardly flammable fluids [15]

Reports of toxicity testing methods for different types of hydraulic oil have shown the influence of this characteristic on the composition and stability of oil solutions.

Toxicity tests are essential components of ecological risk and impact assessments of hydraulic oil on the contaminated / affected area (leaks, spills, mishandling, etc.) [16 - 18]. Measured toxicity varies with test methods [19]. The benchmarks are based on the hydrocarbon concentrations measured in the test solutions [20, 21].

4. Conclusions

By measuring toxicity under standard conditions, one can gain insight into the relative hazard of each type of oil. The Organization for Economic Co-operation and Development (OECD, Report 2018) has provided practical strategies to test "difficult substances and mixtures" and to systematically mitigate the effect of test conditions on the stability and toxicity of test solutions before conducting definitive tests.
Standard oil toxicity tests performed in parallel with tests under site-specific conditions can provide an understanding of how test methods and conditions affect measured oil toxicity. The toxicity analyses carried out help to characterize the rapid and varied changes in the concentrations and composition of the oil during the tests, which determines the most accurate estimate of toxicity. Repeating the test under site-specific conditions enables a systematic evaluation of the influence of each condition on the measured toxicity. Improved approaches are needed to generate reliable benchmarks and to understand how site-specific experimental conditions affect oil toxicity. Improved protocols are needed to support reliable and repeatable toxicity estimates and comparisons between oils and test conditions; toxicity is determined by the concentration and composition of dissolved hydrocarbons, which in turn depend on the composition of the test oils and the methods of preparation of the oil solutions [18]. Thus, new combined toxicity testing methods will reduce uncertainty in measured toxicity, calculated reference values and estimated ecological risks.

Acknowledgments

This work was carried out through the Core Program within the National Research Development and Innovation Plan 2022-2027, carried out with the support of the Romanian Ministry of Research, Innovation and Digitalization (MCID), project no. PN 23 05. The research was financially supported by a project funded by MCID through Programme 1 – Development of the national research & development system, Sub-programme 1.2–Institutional performance–Projects financing the R&D&I excellence, Financial Agreement no. 18PFE/30.12.2021.

References

[1] United States Environmental Protection Agency (EPA). "When are You Required to Report an Oil Spill and Hazardous Substance Release?" July 24, 2023. Accessed October 2, 2023. https://www.epa.gov/emergency-response/when-are-you-required-report-oil-spill-and-hazardous-substance-release.
[2] Deuster, S., and K. Schmitz. "Experimental investigation of the influence of fluid viscosity on the efficiency of a crawler excavator." Paper presented at the 17th Scandinavian International Conference on Fluid Power, SICFP'21, Linköping, Sweden, June 1-2, 2021.
[3] Hawe Hydraulik. "Pressure fluids - notes for selection", D 5488/1, February 2007. Accessed October 3, 2023. https://www.hidracomp.com.br/wp-content/uploads/2013/01/Informacoes-sobre-Selecao-de-Fluido.pdf.
[4] Bosch Rexroth Pty Ltd. "Hydraulic fluids." Accessed October 2, 2023. https://www.boschrexroth.com/en/au/products/engineering/hydraulic-fluids/.
[5] German Institute for Standardization / Deutsche Institut für Normung. "DIN ISO 15380:2020. Lubricants, Industrial Oils And Related Products (Class L) - Family H (Hydraulic Systems) - Specifications For Hydraulic Fluids In Categories HETG, HEPG, HEES And HEPR (ISO 15380:2016)." *ANSI webstore*. Accessed October 2, 2023. https://webstore.ansi.org/Standards/ DIN/DINISO153802020.
[6] Forest Stewardship Council (FSC). Deutscher FSC-Standard. Version 3-0, 2018. Accessed October 2, 2023. https://www.fsc-deutschland.de/preview.fsc_x0002_waldstandard-3-0.a-1208.pdf.
[7] Biona Jersín s.r.o. "Technical Topic: Biodegradable Hydraulic Fluids." Accessed October 2, 2023. https://www.biona-oils.com/news/technical-topic-biodegradable-hydraulic-fluids.

[8] International Marine Contractors Association (IMCA). *Understanding Biodegradable Lubricants: An Introduction to 'Green' Oil in Hydraulic Systems Offshore*. IMCA R 019, October 2014.
[9] Ripple, David Eugene, and William Bricker Chamberlin III. "Lubricating oil composition"/ "Compozitie de ulei lubrifiant". RO Patent no. 108801B1. August 30, 1994. Accessed October 3, 2023. https://patents.google.com/patent/RO108801B1/ro.
[10] Le Suer, William M., and George R. Norman. "Lubricating composition containing an acylated nitrogen compound." US Patent no. 3272746A. September 13, 1966. Accessed October 3, 2023. https://patents.google.com/patent/US3272746A/en.
[11] Bera, G., T. Parkerton, A. Redman, N.R. Turner, D.A. Renegar, J.L. Sericano, and A.H. Knap. "Passive dosing yields dissolved aqueous exposures of crude oil comparable to the CROSERF (Chemical Response to Oil Spills: Ecological Effects Research Forum) water accommodated fraction method." *Environmental Toxicology and Chemistry* 37, no. 11: (November 2018): 2810–2819.
[12] Theissen, H. "The German Market Introduction Program for Biobased Lubricants." *Tribology Online* 5, no. 5 (2010): 225-229.
[13] Sivriu, A.M., C.I. Koncsag, G. Jinescu, and A.M. Mareș. "Thermal cracking of waste vegetable oil – A preliminary research." *UPB Scientific Bulletin, series B: Chemistry and Material Sciences* 79, no. 3 (2017): 67-74.
[14] Lenzi, F., G. Campana, A. Lopatriello, M. Mele, and A. Zanotti. "About the Use of mineral and vegetable Oils to improve the Sustainability of Steel Quenching." *Procedia Manufacturing* 33 (2019): 701-708.
[15] Bonanomi, Anna. "Hydraulic Fluids: Risks of fire and toxicity." *Power Transmission World*, July 17, 2018. Accessed October 2, 2023. https://www.powertransmissionworld.com/hydraulic-fluids-risks-of-fire-and-toxicity/.
[16] Hodson, Peter V., Julie Adams, and R. Stephen Brown. "Oil toxicity test methods must be improved." *Environmental Toxicology and Chemistry* 38, no. 2 (February 2019): 302-311.
[17] Aurand, D., and G. Coelho (eds.). "Cooperative aquatic toxicity testing of dispersed oil and the Chemical Response to Oil Spills: Ecological Effects Research Forum (CROSERF)." Technical Report. Ecosystem Management & Associates, Inc., Lusby, MD, USA, 2005.
[18] Redman, A.D., and T.F. Parkerton. "Guidance for improving comparability and relevance of oil toxicity tests." *Marine Pollution Bulletin* 98, no. 1-2 (September 2015): 156–170.
[19] Kobasko, N.I., E. Carvalho de Souza, L.C.F. Canale, and G.E. Totten. "Vegetable Oil Quenchants: Calculation and Comparison of the Cooling Properties of a Series of Vegetable Oils." *Strojniški vestnik - Journal of Mechanical Engineering* 56, no. 2 (2010): 131-142.
[20] Bejarano, A.C., J.R. Clark, and G.M. Coelho. "Issues and challenges with oil toxicity data and implications for their use in decision making: A quantitative review." *Environmental Toxicology and Chemistry* 33, no. 4 (April 2014): 732–742.
[21] Redman, A.D., J.D. Butler, D.J. Letinski, and T.F. Parkerton. "Investigating the role of dissolved and droplet oil on aquatic toxicity using dispersed and passive dosing systems." *Environmental Toxicology and Chemistry* 36, no. 4 (April 2017): 1020–1028.

ISSN 1454 - 8003
Proceedings of 2023 International Conference on Hydraulics and Pneumatics - HERVEX
November 8-10, Băile Govora, Romania

COMPARATIVE THERMAL ANALYSIS OF HYDRAULIC OILS

Andreea Mirela TELEAȘĂ[1], Sorin CĂNĂNĂU[1], Cătălin DUMITRESCU[2], Alexandru Valentin RĂDULESCU[1], Alina Maria STOICA[1], Geanina Mihaela MATEESCU[1]

[1] National University of Science and Technology POLITEHNICA Bucharest, Dept. of Machine Elements & Tribology, Romania, andreea.teleasa@upb.ro

[2] INOE 2000 - IHP, Hydraulics and Pneumatics Research Institute, Bucharest, Romania, dumitrescu.ihp@fluidas.ro

Abstract: *In this work, the experimental and theoretical results of the apparent viscosity for three hydraulic oils are presented. The experimental determinations were made in the laboratory using the Brookfield CAP2000+ experimental equipment. The determination of the apparent viscosity with temperature was made in the temperature range 20...75 ºC, and the theoretical determinations were made with the help of three proposed thermal models, namely, Jarchov and Theissen, Cameron, and Reynolds, using numerical regression.*

Keywords: *Apparent viscosity, hydraulic fluids, temperature, thermal model*

1. Introduction

Rheological characteristics has an important role in understanding heat transfer and in planning, evaluating and modeling continuous treatment processes [1].
It is well recognized that the rheological characteristics of oils depend on a multitude of factors, including temperature, cutting speed, concentration, time, pressure, chemical properties, additives and catalysts. With the maturation of the petrochemical industry, petroleum oils emerged as the preferred choice, supplanting vegetable oils on account of their superior lubricity, stability, and economic feasability [2].
Viscosity is the measure of internal resistance within a fluid. This resistance becomes apparent when layers of fluid move in relation to each other, and the greater the resistance, the more force is needed to initiate this movement, known as shear. One of the most significant factors influencing the rheological behavior of a material is temperature [3]. Apparent viscosity can be described as a macroscopic property that reflects a fluids resistance to high shear rates. It corresponds to the viscosity measured in the experimental setup [4]. Increasing temperature tends to increase molecular interaction, while decreasing the attractive forces between molecules [2].
The purpose of this study is to assess the effects of shear rate and temperature on the apparent viscosity of three hydraulic oils, using three thermal models that will be analyzed through numerical regression. Subsequently, these apparent viscosity results will be compared with the viscosity measured on the experimental stand.

2. Theory

To determine the rheological behavior of the three hydraulic oils, we proposed the Newtonian model, equation (1).

$$\tau = \eta \cdot \dot{\gamma} \tag{1}$$

Where τ is shear stress, η is viscosity, and $\dot{\gamma}$ is shear rate.
From the thermal point of view, three thermal models are proposed with the help of which we determine the variation of the rheological parameters.

- Modelul Jarchov and Theissen

$$\eta = \eta_{50} \cdot e^{B\frac{50-t}{95+t}} \tag{2}$$

Where η is lubricant viscosity, η_{50} is lubricant viscosity at 50 °C, B is non-dimensional parameter, and t is temperature.

- Modelul Cameron

$$\eta = K \cdot e^{\frac{b}{95+t}} \tag{3}$$

Where η is lubricant viscosity, K is viscosity parameter, b is temperature parameter and t is temperature.

- Modelul Reynolds

$$\eta = \eta_{50} \cdot e^{-m(t-50)} \tag{4}$$

Where η is lubricant viscosity, η_{50} is lubricant viscosity at 50 °C, m is coefficient of variation of viscosity with temperature, t is temperature and 50 is reference temperature.
The experimental data were numerically processed using the numerical regression method to obtain the main values of the specific characteristic parameters of the Newtonian model, equation (1) and of the three thermal models, equations (2, 3 and 4).

3. Experimental equipment

The experimental test stand is a Brookfield CAP 2000+ cone and plate rotary viscometer, shown in Fig. 1. This device is ideal for evaluating the rheological behavior of fluids, whether Newtonian or non-Newtonian, and allows the identification of yield strength and thixotropy. It uses as working geometry the cone and plate coupling, shown in Fig. 2. The relevant data is presented on the device screen and the CAPCALC32 software can be used to generate the flow/viscosity graphs [5].

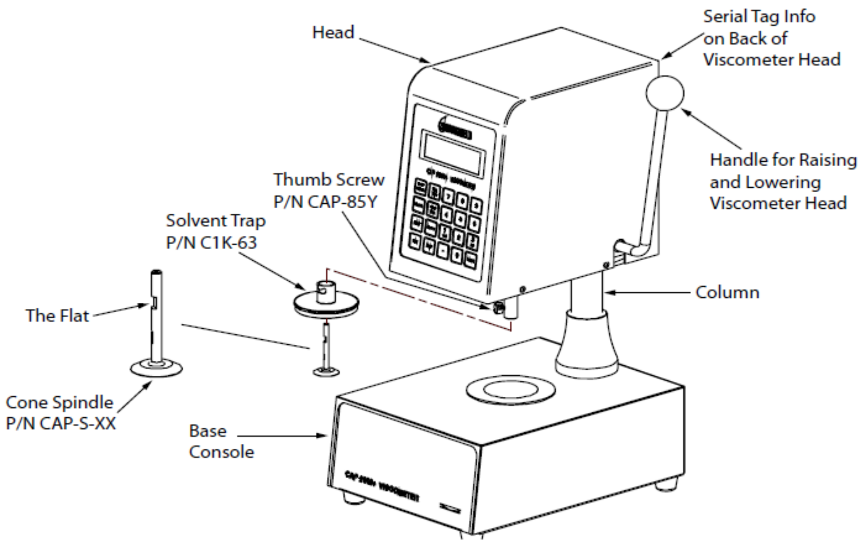

Fig. 1. Viscometer Brookfield CAP2000+ [5]

Fig. 2. Work geometries [5]

ISSN 1454 - 8003
Proceedings of 2023 International Conference on Hydraulics and Pneumatics - HERVEX
November 8-10, Băile Govora, Romania

Tabel 1: Geometry and viscosity range of testing cones

Cone number	**Cone radius, [mm]**	**Cone angle, [°]**	**Viscosity range, [Pa·s]**
3	9.53	0.45	0.083...1.87
5	9.53	1.8	0.333...7.50
6	7.02	1.8	0.833...18.7
8	15.11	3	0.312...3.12

In this work, three hydraulic oils were tested, namely: H46- mineral oil, HETG46-biodegradable oil and HF-E46- non-flammable biodegradable oil. Table 2 shows their properties.

Tabel 2: Physico-chemical properties of tested hydraulic oils [6]-[8]

Oil / **Properties**	**H46**	**HETG46**	**HF-E46**
ISO viscosity class	46	46	46
Density 15 °C, max	0.876	918	921
Viscosity index, min.	98	210	188
Kinematic viscosity at 40°C, cSt	44	-	47.2
Kinematic viscosity at 100°C, cSt	6.6	10	9.41
Flash point, °C, min.	226	>270	320
Pour point, °C, max.	-24	-30	-42
Part of renewable raw materials, %	-	95	76

4. Results

Fig. 3. shows the rheogram of mineral hydraulic oil H46 and the biodegradable ones HETG46 and HF-E46 at a temperature of 20 °C. From this graph it can be seen that the H46 oil has a pronounced thixotropy and a high viscosity, but its thermal stability is low, compared to the other two biodegradable hydraulic oils, where the thixotropy is not so pronounced (thermal stability is high) [9].

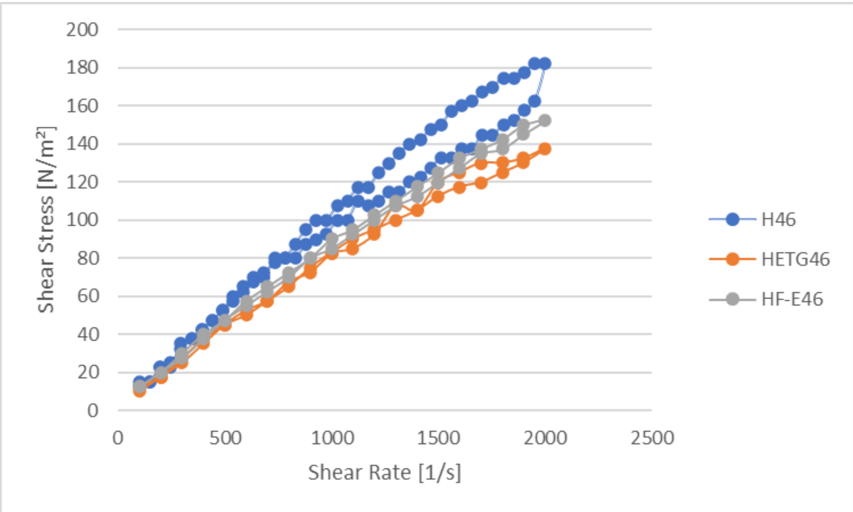

Fig. 3. Rheogram of the three hydraulic oils at a temperature of 20°C [9]

Fig. 4. present the variation of the apparent viscosity with the temperature of the H46 hydraulic oil at four different shear rates (250 s^{-1}, 500 s^{-1}, 750 s^{-1}, 1000 s^{-1}) in the temperature range of 20 ºC...70 ºC, where we can see that the viscosity decrease with the increase of temperature.

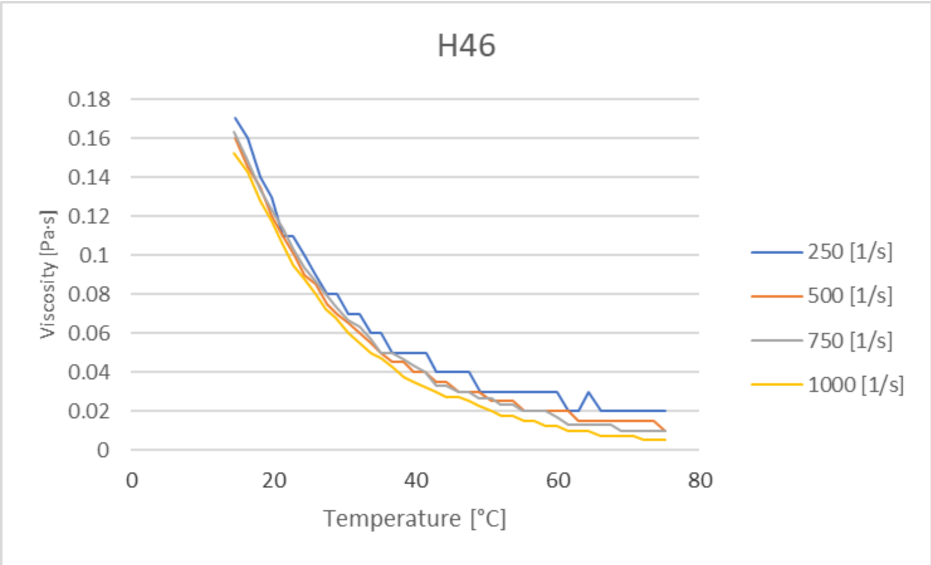

Fig. 4. Variation of the apparent viscosity as a function of the temperature of the H46 mineral hydraulic oil

Fig. 5. and Fig. 6. shows the variation of the apparent viscosity with the temperature of the biodegradable hydraulic oils at four different shear rates. Also, in this graph we can observe the same behavior of biodegradable oils as that of mineral oil, namely decreasing viscosity while the temperature increases. An observation for the biodegradable hydraulic oil HF-E46, is that the viscosity at shear rate of 750 s^{-1} and 1000 s^{-1} tend to have the same shape.

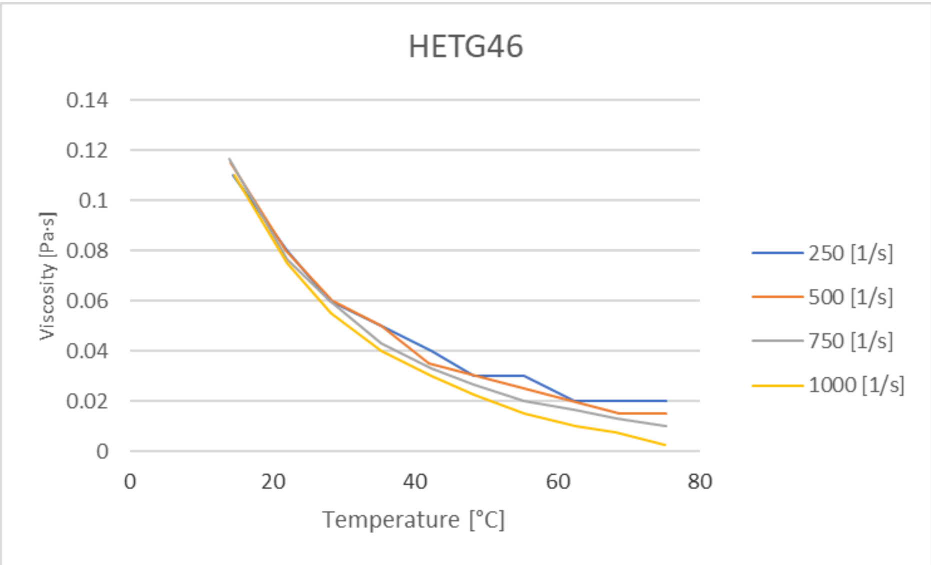

Fig. 5. Variation of apparent viscosity with temperature of HETG46 biodegradable oil

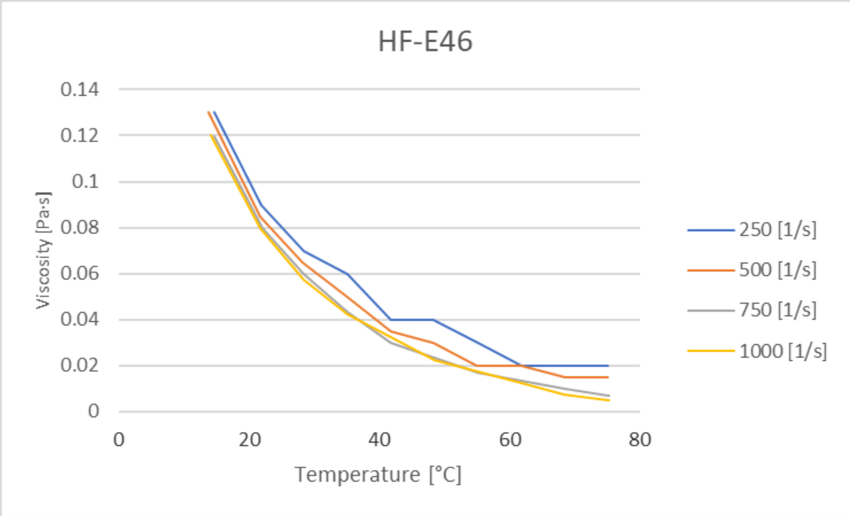

Fig. 6. Variation of apparent viscosity with temperature of HF-E46 biodegradable oil

Table 3, Table 4, and Table 5 shows the results of the thermal rheological parameters of the hydraulic lubricants, according to the Jarchov and Theissen, Cameron and Reynolds thermal models.

Tabel 3: Characteristic parameters of H46 hydraulic oil using the three thermal models

Parameter / Shear rate, s^{-1}	Jarchov and Theissen model			Cameron model			Reynolds model		
	η_{50}, [Pa·s]	*B*	Corr. Coef [%]	*K*, [Pa·s]	*b*, [°C]	Corr. Coef [%]	η_{50}, [Pa·s]	m, [°C^{-1}]	Corr. Coef [%]
250	0.030	4.745	99.17	$3.038 \cdot 10^{-4}$	688.21	99.17	0.030	0.039	96.71
500	0.025	5.549	99.80	$1.061 \cdot 10^{-4}$	804.74	99.80	0.025	0.045	98.41
750	0.027	6.245	99.30	$0.479 \cdot 10^{-4}$	905.55	99.30	0.027	0.048	99.51
1000	0.020	7.319	98.21	$0.480 \cdot 10^{-4}$	905.53	99.31	0.020	0.057	99.89

Tabel 4: Characteristic parameters of HETG46 hydraulic oil using the three thermal models

Parameter / Shear rate, s^{-1}	Jarchov and Theissen model			Cameron model			Reynolds model		
	η_{50}, [Pa·s]	*B*	Corr. Coef [%]	*K*, [Pa·s]	*b*, [°C]	Corr. Coef [%]	η_{50}, [Pa·s]	m, [°C^{-1}]	Corr. Coef [%]
250	0.030	3.832	99.49	$6.808 \cdot 10^{-4}$	555.64	99.49	0.030	0.031	97.62
500	0.025	4.403	99.70	$3.418 \cdot 10^{-4}$	638.38	99.70	0.025	0.036	98.96
750	0.020	5.037	99.65	$1.538 \cdot 10^{-4}$	730.31	99.65	0.020	0.042	99.52
1000	0.015	7.076	96.28	$0.130 \cdot 10^{-4}$	1026.10	96.28	0.015	0.058	99.36

Tabel 5: Characteristic parameters of HF-E46 hydraulic oil using the three thermal models

Parameter / Shear rate, s^{-1}	Jarchov and Theissen model			Cameron model			Reynolds model		
	η_{50}, [Pa·s]	*B*	Corr. Coef [%]	*K*, [Pa·s]	*b*, [°C]	Corr. Coef [%]	η_{50}, [Pa·s]	m, [°C^{-1}]	Corr. Coef [%]
250	0.030	4.219	99.17	$4.950 \cdot 10^{-4}$	611.72	99.19	0.030	0.035	98.18
500	0.020	4.710	99.72	$2.464 \cdot 10^{-4}$	682.96	99.72	0.025	0.041	99.00
750	0.017	6.001	98.99	$0.491 \cdot 10^{-4}$	870.07	99.89	0.017	0.050	99.89
1000	0.018	6.404	98.00	$0.299 \cdot 10^{-4}$	1135.30	99.89	0.018	0.052	99.84

Analyzing the results from the tables, we can observe that all three proposed models are effective in approximating the variation of apparent viscosity as a function of temperature, showing correlation coefficients of over 96%.

Fig. 7. present the comparative results between the viscosity determined experimentally and the theoretical one according to the three thermal models. For this oil, we can observe that there are no noticeable differences between the experimentally determined viscosity and the theoretical ones.

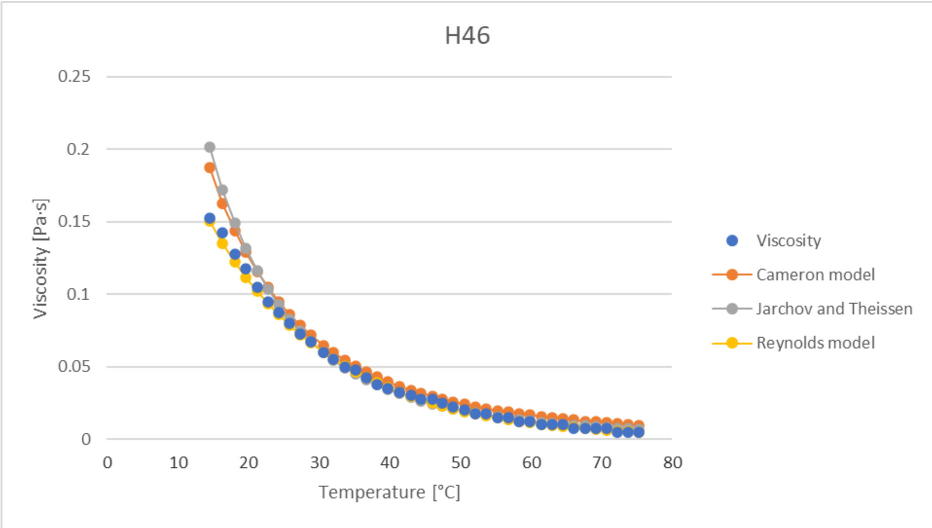

Fig. 7. Comparative results between the theoretical viscosity curves and the experimental ones for H46 mineral hydraulic oil

Fig. 8. and Fig. 9. present the comparative results between the viscosity determined experimentally and the theoretical one according to the three thermal models. For these biodegradable oils, we can observe that there are small differences between the experimentally determined viscosity and the theoretical one, considering the Cameron and Jarchov and Theissen thermal models.

Another observation is that the viscosity determined using the Reynolds thermal model has the same shape as the experimentally determined viscosity.

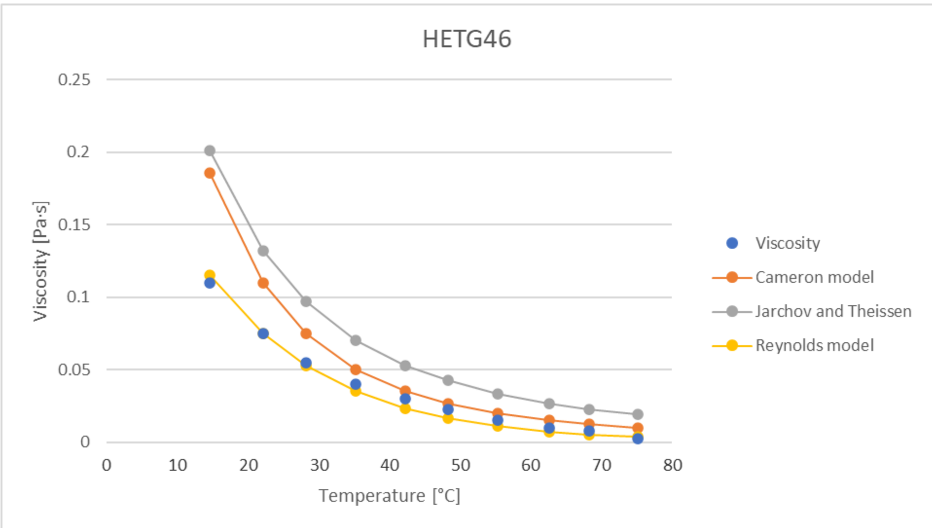

Fig. 8. Comparative results between the theoretical viscosity curves and the experimental ones for the biodegradable hydraulic oil HETG46

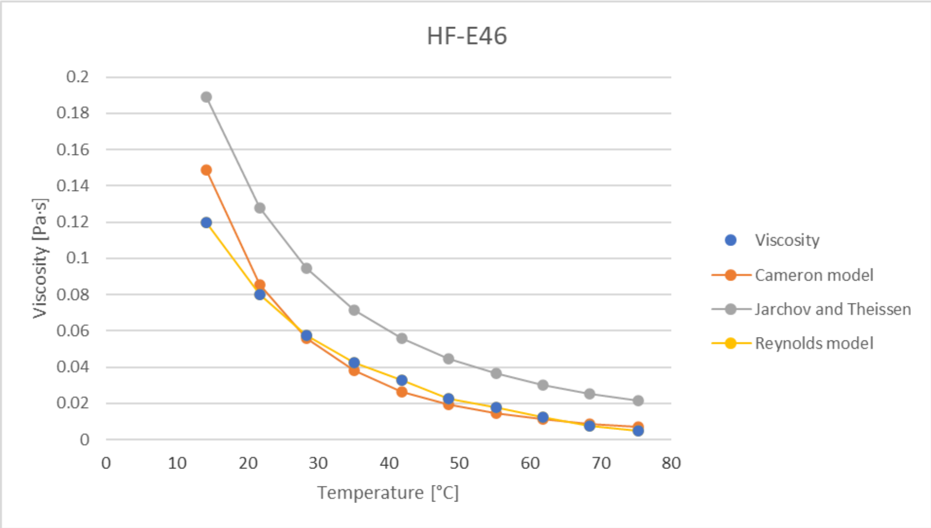

Fig. 9. Comparative results between the theoretical viscosity curves and the experimental ones for the biodegradable hydraulic oil HF-E46

Fig. 10., Fig. 11., Fig. 12. and Fig. 13. show the rheological parameters of the thermal models Reynolds (Fig. 10.), Jarchov and Theissen (Fig. 11.) and Cameron (Fig. 12. and Fig. 13) according to the shear rates at which they were tested hydraulic oils, obtained with the help of numerical regression.
For the Reynolds thermal model, the rheological parameter is "m", for the Jarchov and Theissen thermal model, the rheological parameter is "B", and for the Cameron model the rheological parameter is "b". These are the temperature parameters that indicate us the increase in temperature with the increase in shear rate.
Also, for the Cameron thermal model, we have another rheological parameter noted by "K" and which is a viscosity parameter. As can be observe from Fig. 13., this parameter decreases with the increase of the shear rate.

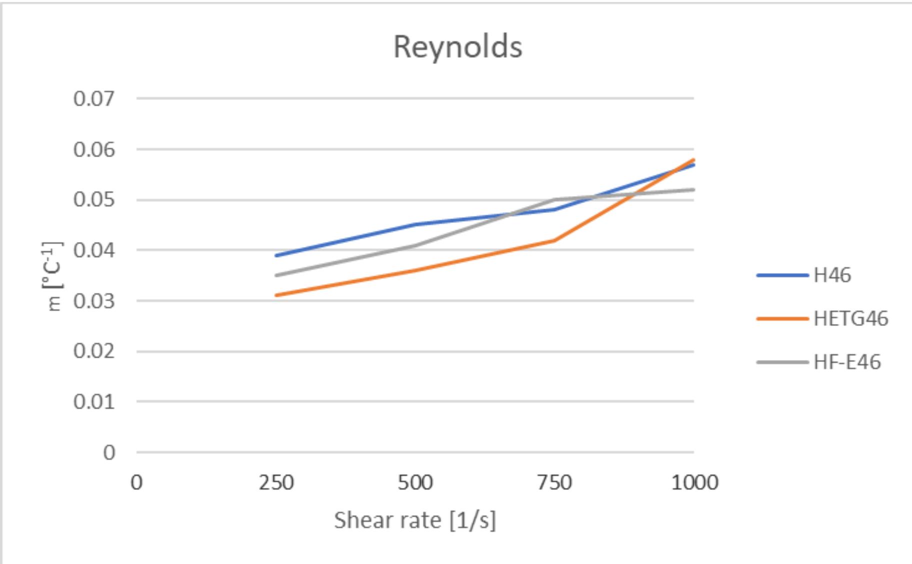

Fig. 10. Variation of the rheological parameter of the Reynolds thermal model depending on the shear rate for the three hydraulic oils

Fig. 11. Variation of the rheological parameter of the Jarchov and Theissen thermal model depending on the shear rate for the three hydraulic oils

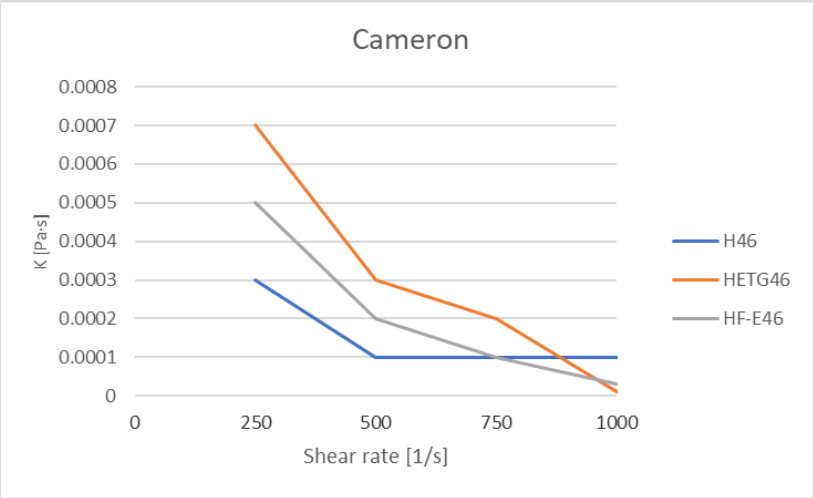

Fig. 12. Variation of the rheological viscosity parameter of the Cameron thermal model as a function of shear rate for the three hydraulic oils

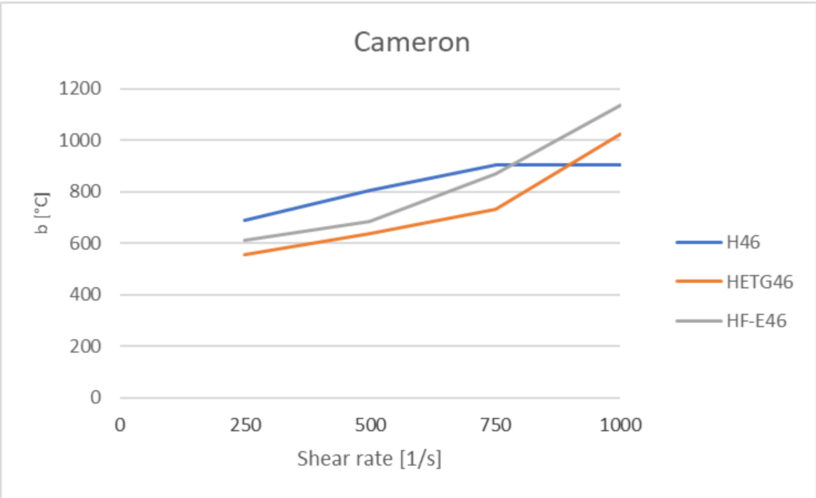

Fig. 13. Variation of the temperature rheological parameter of the Cameron thermal model as a function of shear rate for the three hydraulic oils

5. Conclusion

From a rheological point of view, it was found that:

- Biodegradable oils HF-E46 and HETG46 demonstrate significantly reduced thixotropy when compare with hydraulic oil H46, which exhibits exceptionally high thixotropy.
- The apparent viscosity of the biodegradable oil HF-E46 is higher than that of the biodegradable oil HETG46, and lower than the hydraulic oil H46, where its slope is higher, indicating a higher viscosity;

Analyzing the experimental data presented in table 1, table 2, and table 3 reveals a decrease in the apparent viscosity of hydraulic lubricants concerning the shear rates. For all three lubricants tested, the oil viscosity decreases with the increase of the shear rate, which means that they have a normal behavior.

Regarding the variability of apparent viscosity with temperature, three theoretical models have been proposed to model the experimental results. All these models fit in approximating the viscosity variation, as they have correlation coefficients exceeding the 96% threshold. However, among the three proposed thermal models, the Cameron relation shows correlation coefficients above 99%.

Acknowledgment

The authors are grateful for the financial support by the Romanian Association of Mechanical Transmissions (ROAMET).

References

[1] Marcotte, M., A. R. Taherian, M. Trigui, and H. S. Ramaswamy. “Evaluation of rheological properties of selected salt enriched food hydrocolloids.” *Journal of Food Engineering* 48, no. 2 (May 2001): 157–167.
[2] Wan Nik, W. B., F. N. Ani, H. H. Masjuki, and S. G. Eng Giap. “Rheology of bio-edible oils according to several rheological models and its potential as hydraulic fluid.” *Industrial Crops and Products* 22, no. 3 (November 2005): 249–255.
[3] Rădulescu, Alexandru Valentin, Corneliu Bălan, and Irina Rădulescu. “Thermal regression models for the rheological parameters of lubricants.” Paper presented at International Science Conference of Material Science and Manufacturing Technology (MiTech), Prague, Czech Republic, June 26-27, 2007.
[4] Lefebvre, Aline, and Bertrand Maury. “Apparent viscosity of a mixture of a Newtonian fluid and interacting particles.” *Comptes Rendus Mécanique* 333, no. 12 (December 2005): 923–933.
[5] AMETEK Brookfield.“BROOKFIELD CAP2000+, Viscometer Operating Instructions.” Accessed November 17, 2023. http://www.brookfieldengineering.com.
[6] Nuto™ H Series Mobil. “H46 Hydraulic Oils - Product Data Sheets”. https://www.mobil.com/en/lubricants/for-businesses/industrial/lubricants/products/products/nuto-h-46#lightbox-pdsdatasheet.
[7] Kajo. “Kajo-Bio-Hydrauliköl HETG 46.” https://www.lubricon.com.au/product/biodegradable-lubricants/bio-hydraulic-oil/kajo-bio-hydraulikol-hetg-46/.
[8] Shell plc. “Shell Naturelle HF-E 46.” https://shop.sclubricants.com/pub/media/pds/shell/Shell-Naturelle-Fluid-HF-E-46-datasheet.pdf.
[9] Teleașă, Andreea Mirela, and Alexandru Valentin Rădulescu. “Experimental Analysis of the Rheological Properties of Hydraulic Oils.” *Acta Technica Napocensis* (2023) - publication in progress.

ISSN 1454 - 8003
Proceedings of 2023 International Conference on Hydraulics and Pneumatics - HERVEX
November 8-10, Băile Govora, Romania

NEURAL NETWORK CONTROLLER FOR FAULT DETECTION AND MONITORING OF A CLOSED-LOOP COMPACT HYDRAULIC DIRECT DRIVE SERVOMECHANISM

Alexandru-Polifron CHIRIȚĂ[1,*], Bogdan-Alexandru TUDOR[1]

[1]National Institute of Research & Development for Optoelectronics / INOE 2000 – Subsidiary Hydraulics and Pneumatics Research Institute / IHP, Bucharest, Romania

* chirita.ihp@fluidas.ro

Abstract: *This paper delves into the development and implementation of a neural network controller devised for the purpose of fault detection and monitoring within a compact closed-loop direct-drive hydraulic servomechanism. The primary function of this servomechanism is to swiftly and precisely adjust the force produced by a single-rod double-acting hydraulic cylinder. The monitoring system, integrated with neural networks, is configured to oversee three pressure transducers, the system's command input, and the resultant force output. This configuration enables the generation of continuous error values, specifically adapted to prevalent faults often encountered within such servomechanisms. One notable aspect of this research lies in the ability to generate variable error values that serve as predictive indicators, forecasting potential future system malfunctions in accordance with the principles of predictive maintenance aligned with the paradigm of Industry 4.0. The research and development presented in this paper offer a significant advancement in the field of fault detection and predictive maintenance for hydraulic servomechanisms, catering to the demands of Industry 4.0. By leveraging neural networks to analyze and interpret continuous error values, this approach enables the pre-emptive identification of potential faults, ensuring proactive maintenance interventions. The system's capability to predict potential failures in advance is a pivotal step toward ensuring increased operational efficiency, reduced downtime, and improved reliability within industrial settings adopting compact closed-loop direct-drive hydraulic servomechanisms.*

Keywords: *Neural network, fault detection and monitoring, predictive maintenance, closed-loop, hydraulic direct drive servomechanism, Industry 4.0.*

1. Introduction

Industry 4.0 and predictive maintenance. The spectacular increase in the scientific and technological level of production led to a new form of known development named Industry 4.0, which is the fourth Industrial Revolution (see fig. 1), and was introduced in 2011 by a group of German scientists [1].

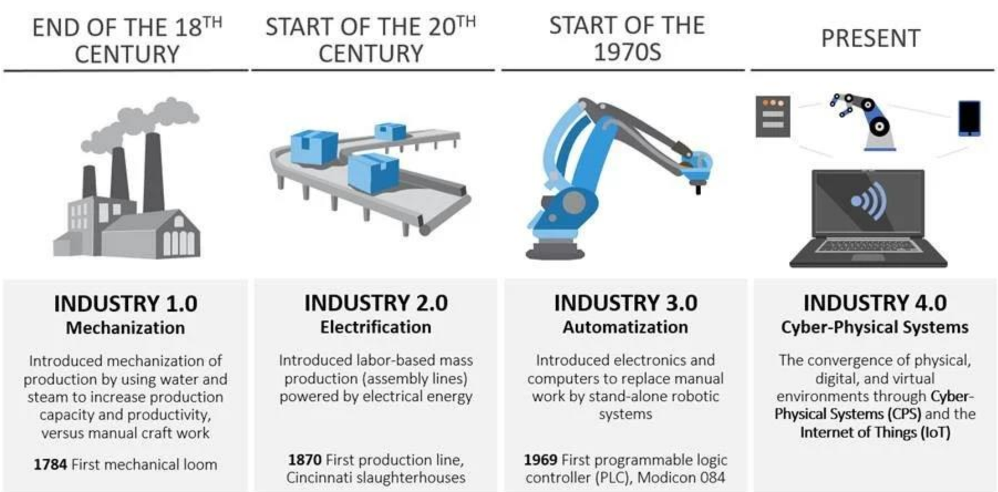

Fig. 1. The 4 major Industrial Revolutions [2]

This industrial revolution also started from the finding that, for several decades, manufacturing was transferred to Asia, so that today the question arises of the reindustrialization of Europe, for a sustainable development. The problem of the technical-economic development of countries is not only in Europe, but is felt in many countries of the world where it has acquired all kinds of names, among which one can mention IIC in the USA, Industrial Value-Chain Initiative in Japan, Industry of the Future in France, but also a similar initiative in China [3].
The main pillars of the Industry 4.0 are (see fig. 2):

- Advance human-machine interface
- Big data
- Internet of things (IoT)
- Data analysis
- Augmented Reality (AR)
- Digital to real life
- Smart sensor

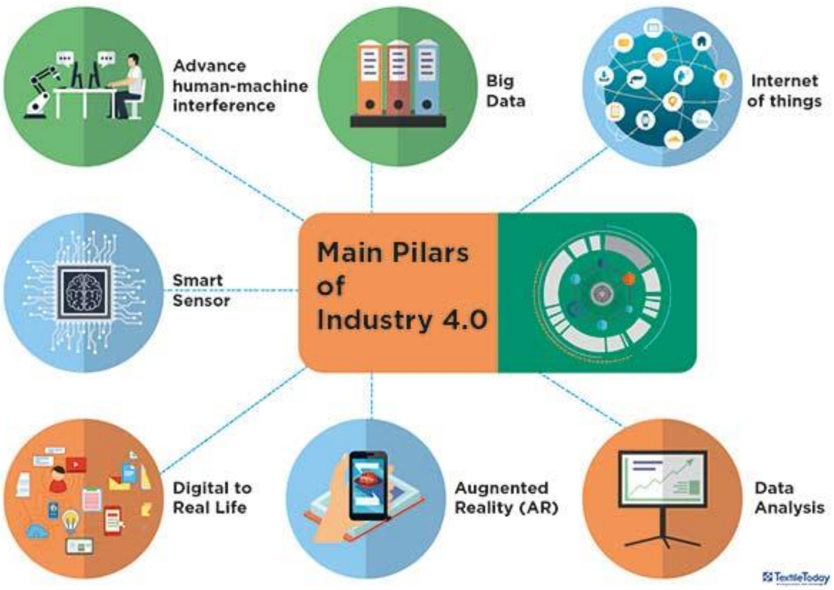

Fig. 2. Main pillars of Industry 4.0 [4]

This concept introduces for the first time the principle of Smart Factory (see fig. 3), where all systems are interconnected with the help of network, and can provide data for all the department in the factory, which reduces time and it is cost efficient. The data provided in the Intelligent Factory can be about a certain process carried out by a system, or about the state of the system itself, and this type of factory comes with a lot of changes compared to the traditional factories.
One of the aspects that changes in the Smart Factory is that of maintenance [5]. In general, the maintenance is calculated for a certain number of operating hours of the equipment and to be able to achieve it, it is necessary to stop work on the equipment in question for the entire maintenance period; even if at the time scheduled for the maintenance the factory urgently needs that equipment to work, it cannot do that.
Therefore, together with this concept of Industry 4.0, the concept of predictive maintenance [6] is also introduced. Predictive maintenance [7] is carried out by introducing into the system some sensors placed on different equipment that can 'tell' the maintenance teams at any time the state of the system and which of the components monitored by the sensors show signs of fatigue or failure, so that the competent department can know in advance when they need to intervene.
Even more, thanks to the continuous harsh surveillance of the system made by the sensors, one can work with the equipment in question until the moment when they are almost at the upper limit

ISSN 1454 - 8003
Proceedings of 2023 International Conference on Hydraulics and Pneumatics - HERVEX
November 8-10, Băile Govora, Romania

of the optimal functioning range before the appearance of a major fault. Of course, this type of operation is only recommended in case of emergencies, when the factory really needs for that equipment to work, otherwise it is recommended that the maintenance be done in advance.

Fig. 3. Smart Factory - Graphic illustration of the concept [8]

A decade after its introduction, the concept of Industry 4.0 has gained global scope and is the dominant concept in the digital transformation of the industry. By combining results-based research and practical industry experience, progress has been made in implementing the concept and new areas of action have been identified from a technological and application-oriented perspective. Industry 4.0 is human-centered and is the basis for innovative business models and agile forms of organization.
At this moment, in industry IoT and cyberphysical production are a reality in newly built factories and the connectivity of machines has been improved in existing factories.
Currently, there are six new megatrends (see fig. 4) that will influence the development of the next 10 years: industrial AI, edge computing up to edge cloud, 5G in the factory, teams of robots, autonomous intralogistics systems and trustworthy data.
These things allow the creation of an innovative digital ecosystem that allows long-term adaptability in a volatile economic and geopolitical environment.

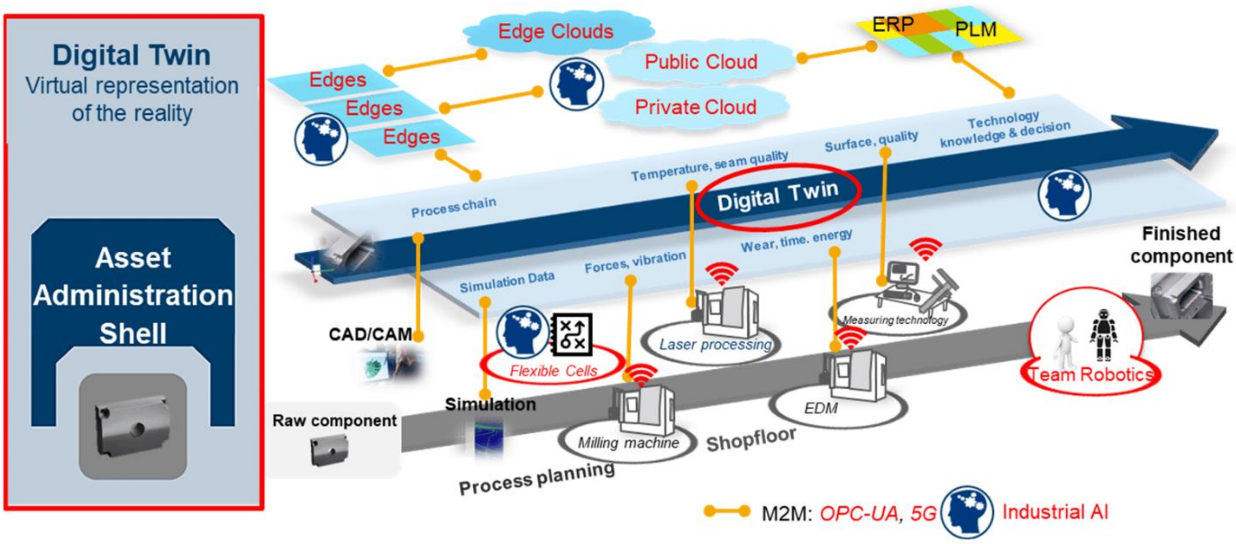

Fig. 4. Megatrends for the next level of Industry 4.0 [8]

Neural network in Industry 4.0. In today's era of Industry 4.0, where automation and smart manufacturing processes are revolutionizing industrial operations, the need for efficient fault detection and predictive maintenance systems has become paramount. The integration of advanced technologies and intelligent systems is no longer a luxury but a necessity to ensure seamless, reliable, and cost-effective industrial processes. In this context, this scientific paper delves into a groundbreaking development that interlaces the power of neural networks [9] with the intricacies of a closed-loop compact hydraulic direct drive servomechanism to create a novel approach for fault detection and monitoring.

This paper paves the path to reshaping the way industries approach maintenance and efficiency in the Smart Factory defined by the Industry 4.0 concept.

The servomechanism at the heart of this research plays a pivotal role in swiftly and precisely adjusting the force generated by a single-rod double-acting hydraulic cylinder, making it indispensable in a variety of industrial applications. However, the very complexity of these systems also renders them susceptible to various faults and malfunctions, leading to reduced operational efficiency and increased downtime.

To address these challenges, the paper introduces an innovative monitoring system that harnesses the capabilities of neural networks [10]. This system is meticulously designed to oversee critical components of the hydraulic servomechanism such as the pump, cylinder or the system filter by including three pressure transducers. The system's command inputs, and the resultant force output, are also collected by the neural network. By continuously monitoring and analyzing data from these components, the neural network-based controller can generate error values that are specifically designed to prevalent faults that often afflict hydraulic servomechanisms. What sets this research apart is its ability to generate variable error values, transforming them into powerful predictive indicators. These indicators, in line with the principles of predictive maintenance, have the potential to forecast future system malfunctions. This proactive approach holds significant promise for industrial settings, as it empowers maintenance teams to address issues before they escalate into critical failures. Consequently, the integration of neural networks into this context paves the way for more efficient, cost-effective, and reliable industrial processes. This research is a clear manifestation of how the interlacing of advanced technology and engineering ingenuity can transform the industrial landscape.

This paper unfolds at the intersection of multiple critical domains. It combines the intricate engineering of a compact hydraulic direct drive servomechanism with the cutting-edge power of neural networks. Furthermore, it aligns itself with the overarching principles of Industry 4.0, where the digitalization of industry is ushering in a new era of intelligent, interconnected manufacturing processes. As we progress further into this digital age, the significance of such research cannot be overstated, as it holds the potential to drive progress and innovation in the industrial sector.

In the following pages, the authors delve deeper into the specific components of the neural network controller, its integration with the servomechanism, the methodologies used for fault detection, and the generation of predictive indicators. This paper represents a significant advancement in the realm of fault detection and predictive maintenance for hydraulic servomechanisms, ultimately catering to the demands and expectations of Industry 4.0. By leveraging the capabilities of neural networks to analyze and interpret continuous error values, this approach not only identifies potential faults but also enables pre-emptive maintenance interventions, a pivotal step toward ensuring increased operational efficiency, reduced downtime, and improved reliability within industrial settings that rely on compact closed-loop direct-drive hydraulic servomechanisms. Below, the authors reveal the intricate details of this groundbreaking research, offering insights that have the potential to reshape the future of industrial maintenance and operation. The utilization of neural networks in Industry 4.0 exemplifies the intersection of cutting-edge technology and the demands of modern industrial processes. This integration not only facilitates efficient fault detection but also aligns with the overarching principles of the fourth industrial revolution, promoting intelligent, interconnected, and agile manufacturing systems. As industries continue to evolve in this digital age, the role of neural networks in optimizing processes and ensuring reliability becomes increasingly indispensable.

2. Material and Method

The present section unveils the foundation of the neural network controller's development for fault detection in a hydraulic servomechanism. Fig. 5 provides a snapshot of training data in both tabular and graphical formats, crucial for the network's learning.

	A	B	C	D	E	F	G	H	I	J	K	L
1	Pressure_P1	Cavitation_B1	Pressure_P2	Cavitation_B2	Pressure_P3	Clogged_filter	Force_1	Overload	P1/P2_ratio	Volumetric_losses_B2_to_B1	P2/P1_ratio	Volumetric_losses_B1_to_B2
2	bar	0 .. -1	bar	0 .. -1	bar	0 .. 200 %	N	+100 .. -100 %	-	0 or 1	-	0 or 1
3	0.00	0.00	0.00	0.00	0.00	0.00	160000.00	100.00	0.00	1.00	6000.00	0.00
4	0.10	0.00	0.10	-1.00	0.02	0.40	159680.00	99.60	0.02	1.00	59.35	0.00
5	0.20	0.00	0.20	-0.90	0.04	0.80	159360.00	99.20	0.03	1.00	29.79	0.00
6	0.30	0.00	0.30	-0.80	0.06	1.20	159040.00	98.80	0.05	1.00	19.87	0.00
7	0.40	0.00	0.40	-0.70	0.08	1.60	158720.00	98.40	0.07	1.00	14.90	0.00
8	0.50	0.00	0.50	-0.60	0.10	2.00	158400.00	98.00	0.08	1.00	11.92	0.00
9	0.60	0.00	0.60	-0.50	0.12	2.40	158080.00	97.60	0.10	1.00	9.92	0.00
10	0.70	0.00	0.70	-0.40	0.14	2.80	157760.00	97.20	0.12	1.00	8.50	0.00
11	0.80	0.00	0.80	-0.30	0.16	3.20	157440.00	96.80	0.13	1.00	7.43	0.00
12	0.90	0.00	0.90	-0.20	0.18	3.60	157120.00	96.40	0.15	1.00	6.60	0.00
13	1.00	0.00	1.00	-0.10	0.20	4.00	156800.00	96.00	0.17	1.00	5.93	0.00
14	1.10	0.00	1.10	0.00	0.22	4.40	156480.00	95.60	0.19	1.00	5.39	0.00
15	1.20	0.00	1.20	0.00	0.24	4.80	156160.00	95.20	0.20	1.00	4.94	0.00
16	1.30	0.00	1.30	0.00	0.26	5.20	155840.00	94.80	0.22	1.00	4.55	0.00
17	1.40	0.00	1.40	0.00	0.28	5.60	155520.00	94.40	0.24	1.00	4.22	0.00
18	1.50	0.00	1.50	0.00	0.30	6.00	155200.00	94.00	0.25	1.00	3.94	0.00
19	1.60	0.00	1.60	0.00	0.32	6.40	154880.00	93.60	0.27	1.00	3.69	0.00
20	1.70	0.00	1.70	0.00	0.34	6.80	154560.00	93.20	0.29	1.00	3.47	0.00
21	1.80	0.00	1.80	0.00	0.36	7.20	154240.00	92.80	0.31	1.00	3.27	0.00
22	1.90	0.00	1.90	0.00	0.38	7.60	153920.00	92.40	0.32	1.00	3.10	0.00
23	2.00	0.00	2.00	0.00	0.40	8.00	153600.00	92.00	0.34	1.00	2.94	0.00
24	2.10	0.00	2.10	0.00	0.42	8.40	153280.00	91.60	0.36	1.00	2.80	0.00
25	2.20	0.00	2.20	0.00	0.44	8.80	152960.00	91.20	0.37	1.00	2.67	0.00
26	2.30	0.00	2.30	0.00	0.46	9.20	152640.00	90.80	0.39	1.00	2.55	0.00
27	2.40	0.00	2.40	0.00	0.48	9.60	152320.00	90.40	0.41	1.00	2.44	0.00
28	2.50	0.00	2.50	0.00	0.50	10.00	152000.00	90.00	0.43	1.00	2.34	0.00
29	2.60	0.00	2.60	0.00	0.52	10.40	151680.00	89.60	0.44	1.00	2.25	0.00
30	2.70	0.00	2.70	0.00	0.54	10.80	151360.00	89.20	0.46	1.00	2.16	0.00

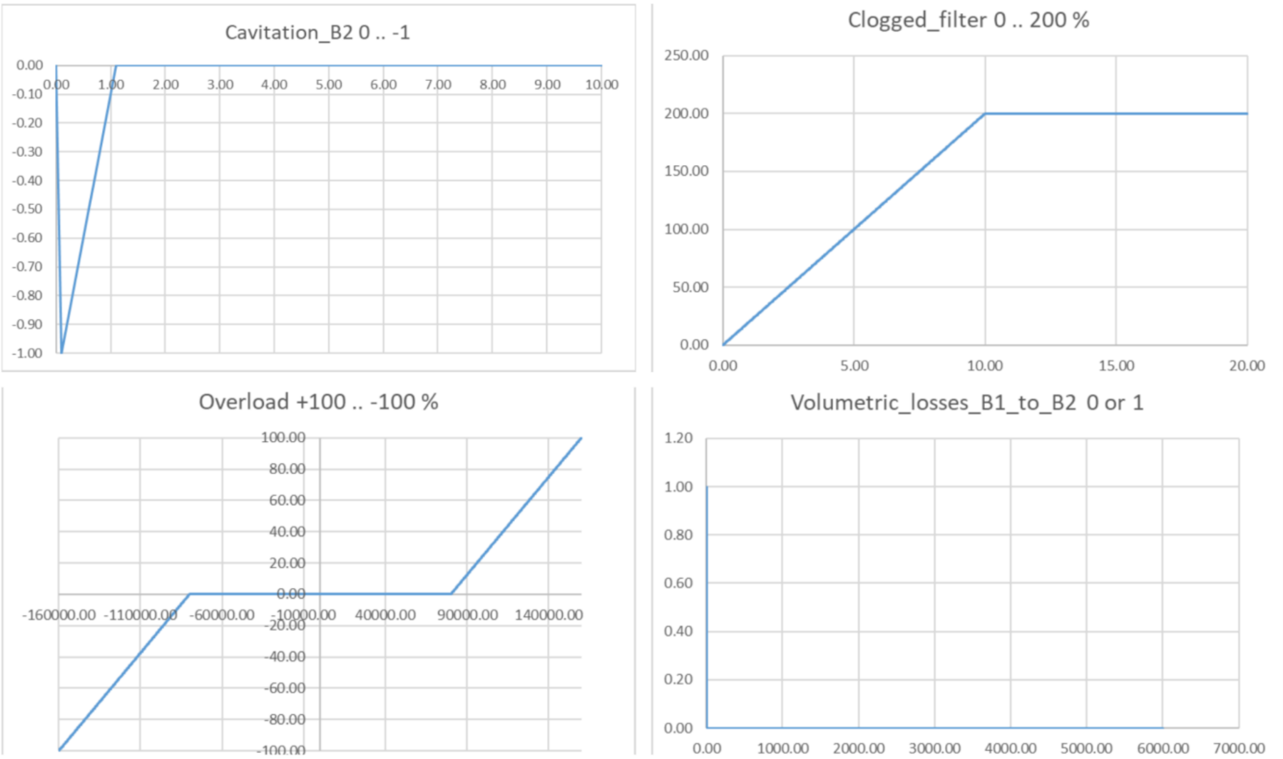

Fig. 5. Sample of data used for training and validation of neural network - tabular and graphical form

Fig. 6 reveals the data headers governing training and validation, offering transparency into the parameters guiding the network's adaptation. These visuals not only anchor the discussion but also emphasize the meticulous approach to training and validation processes, crucial in achieving precision in fault detection within the complexities of Industry 4.0 context.

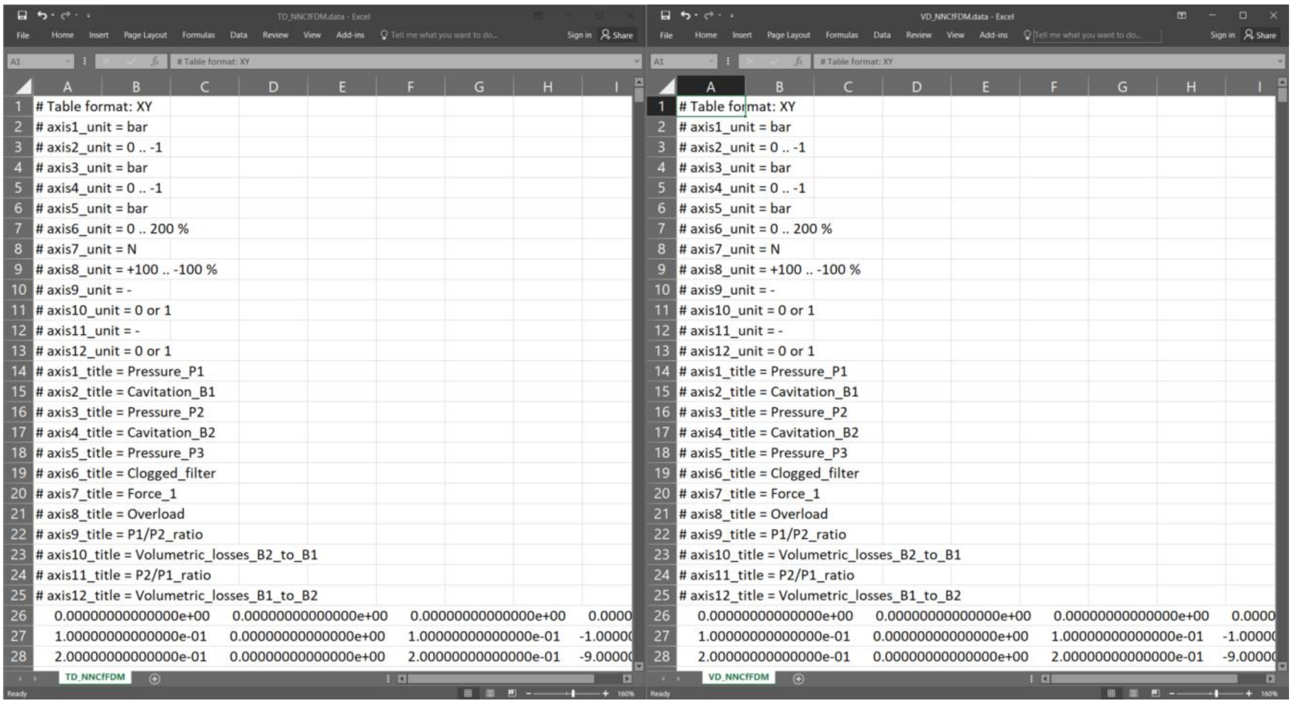

Fig. 6. Data headers of training and validation data

Fig. 7 and Fig. 8 serve as visual representations of the neural network builder, displaying the training and validation data for the newly developed neural network. These figures offer a clear depiction of the two distinct datasets employed in the training process and highlight the 12 variables crucial to the neural network's configuration. The visuals provide a tangible glimpse into the intricacies of the data sets, enabling the identification of key components essential for the network's learning and subsequent application in fault detection within the closed-loop compact hydraulic direct drive servomechanism.

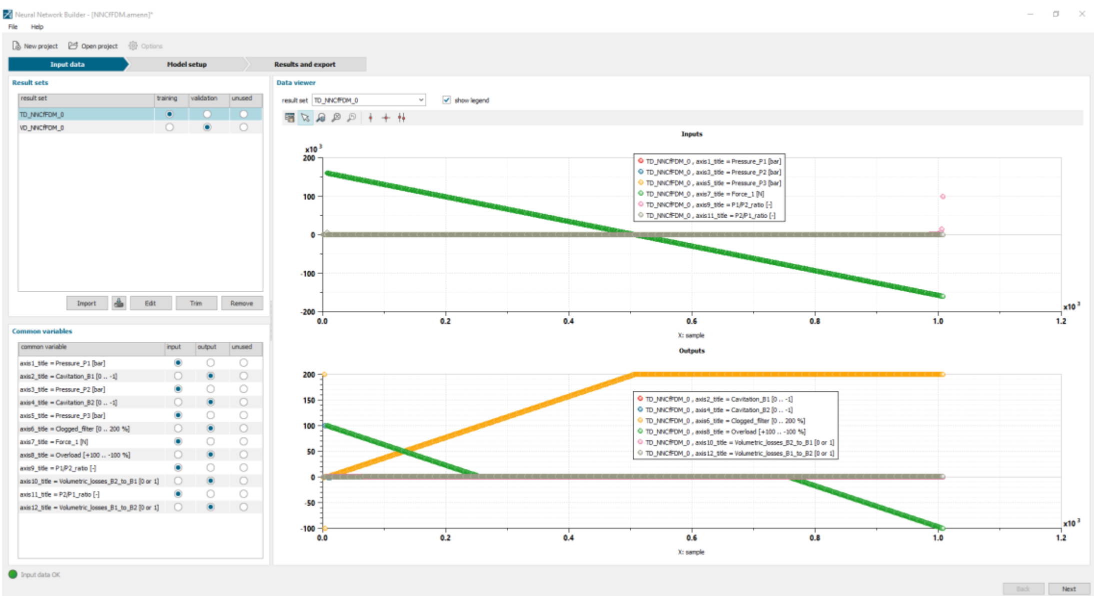

Fig. 7. Input of training data in neural network builder

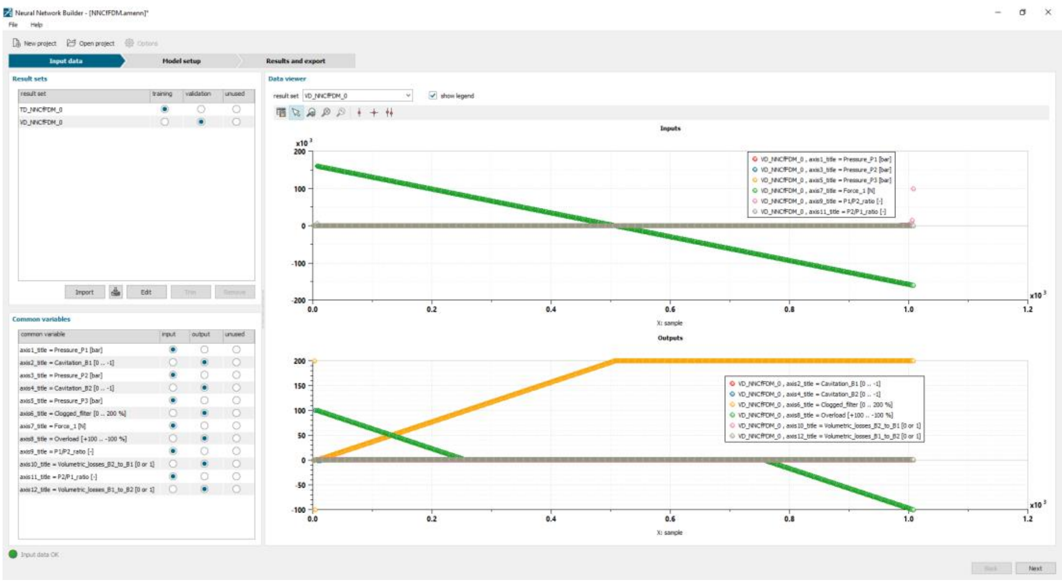

Fig. 8. Input of validation data in neural network builder

Fig. 9 shows the training of the neural network, the training parameters and the variables of the network.

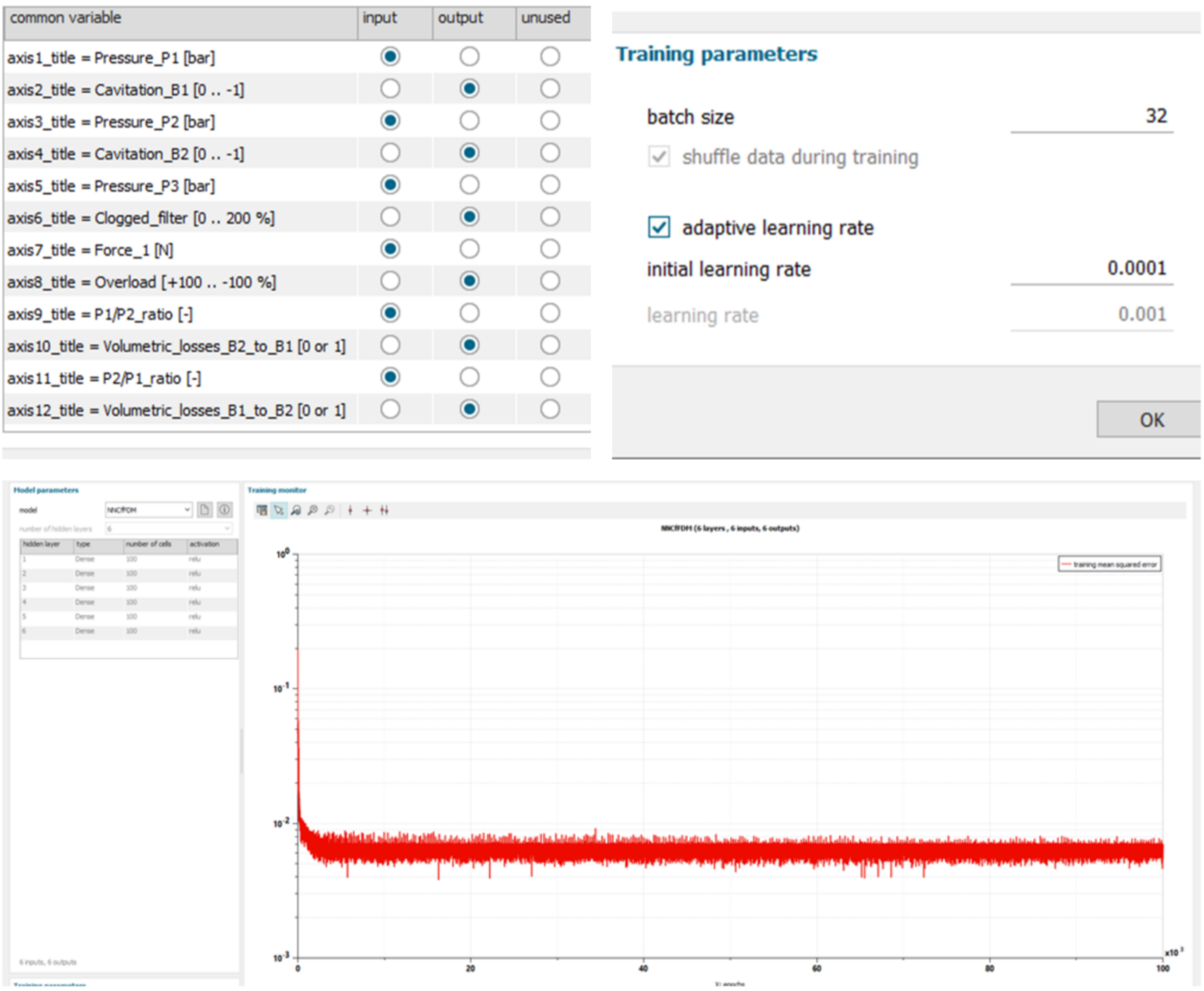

Fig. 9. Neural network training, training parameters and network variables

According to Fig. 10, after the 100000 training epochs the mean square error has a value of 0.007.

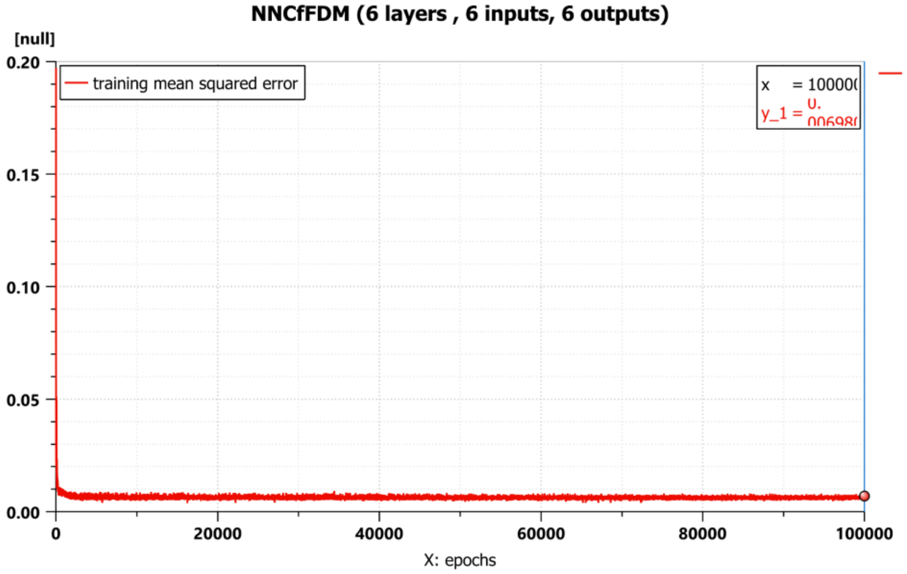

Fig. 10. Training mean square error

The results of the neural network training can be seen in Fig. 11, which shows 4 of the 6 outputs of the neural network.

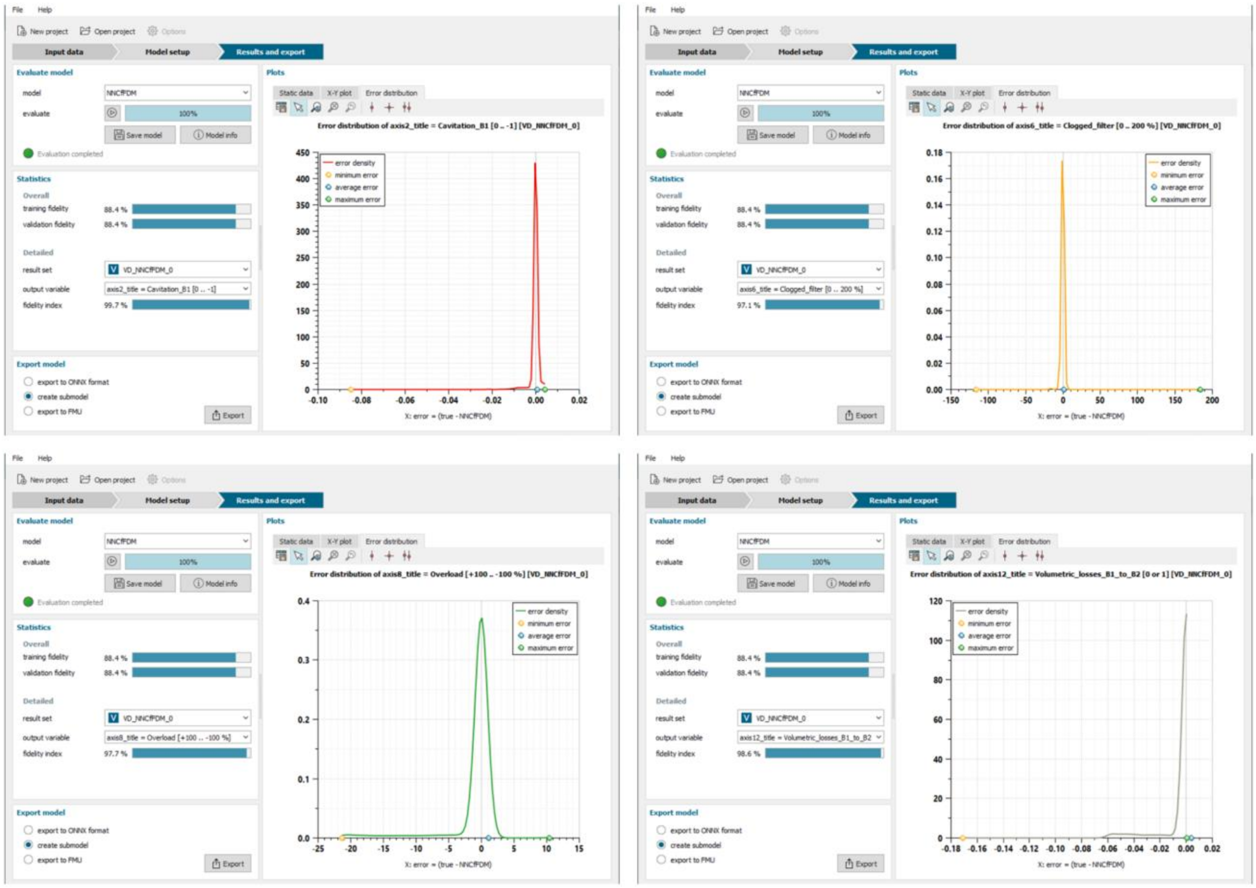

Fig. 11. Results of neural network training

In Fig. 12, the model manager of the neural network discloses, revealing essential parameters and training outcomes. Noteworthy metrics include a training fidelity of 88.4% and a matching validation fidelity. The training process, spanning 5661 seconds, demonstrates the model's robustness. The neural network configuration comprises six deep layers, each containing 100 neurons, using the rectified linear unit (ReLU) type activation. These parameters summarize the neural network's structure and its ability in learning from the provided datasets, crucial for effective fault detection in the closed-loop compact hydraulic direct drive servomechanism.

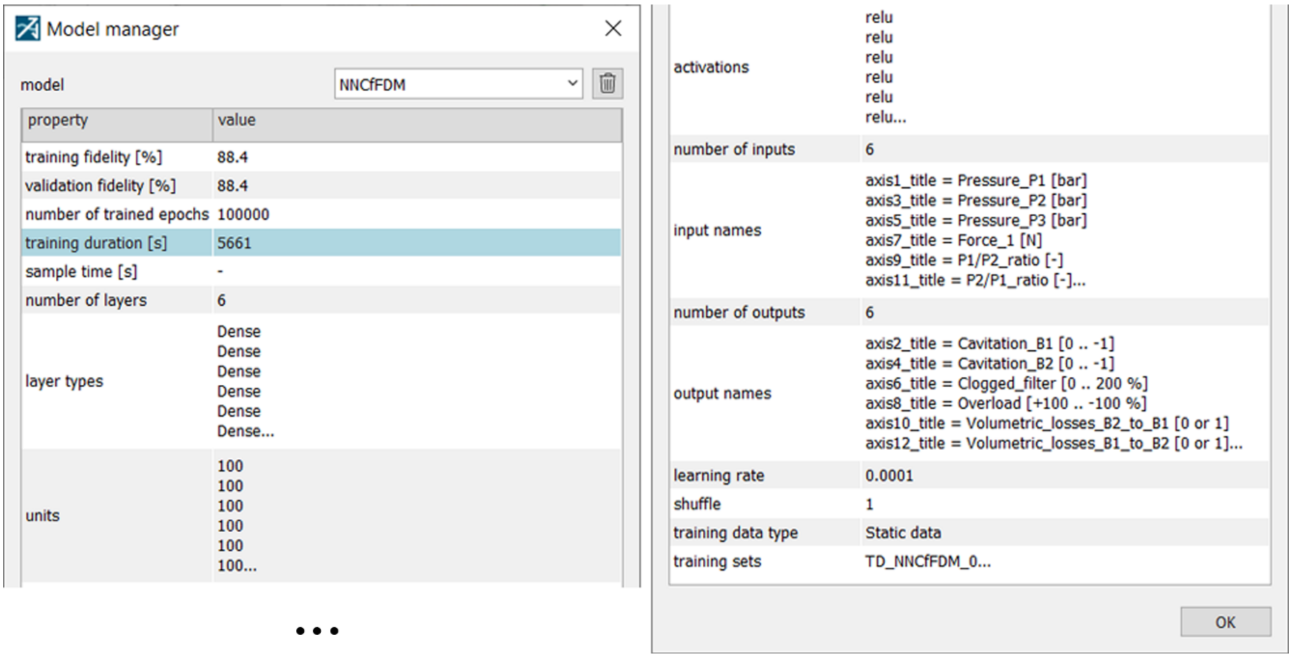

Fig. 12. Model manager of the neural network

At the end of the neural network training and validation process, the network model was saved as a submodel (see Fig. 13) to be used later.

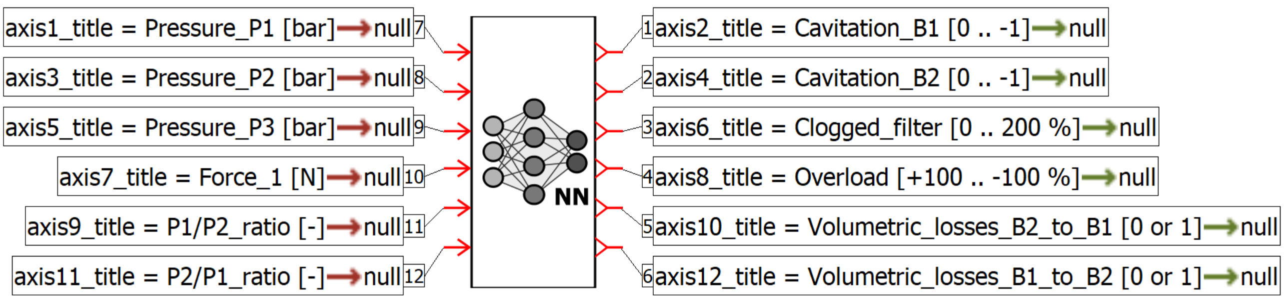

Fig. 13. The neural network submodel

The neural network was integrated into the simulation model shown in Fig. 14, which is composed of a closed-loop compact hydraulic direct drive servomechanism and neural network controller for fault detection and monitoring. The parameters of the components are also presented in the same figure.

System operation: The chirp command signal is sent to the PID controller that continuously adjusts the flow rate of the servopump so that the force generated by the hydraulic cylinder is always as close as possible to the commanded one. The values of the 3 pressure transducers (one of which is differential) and one force transducer are monitored by the neural network that processes them and signals if a malfunction occurs in the system.

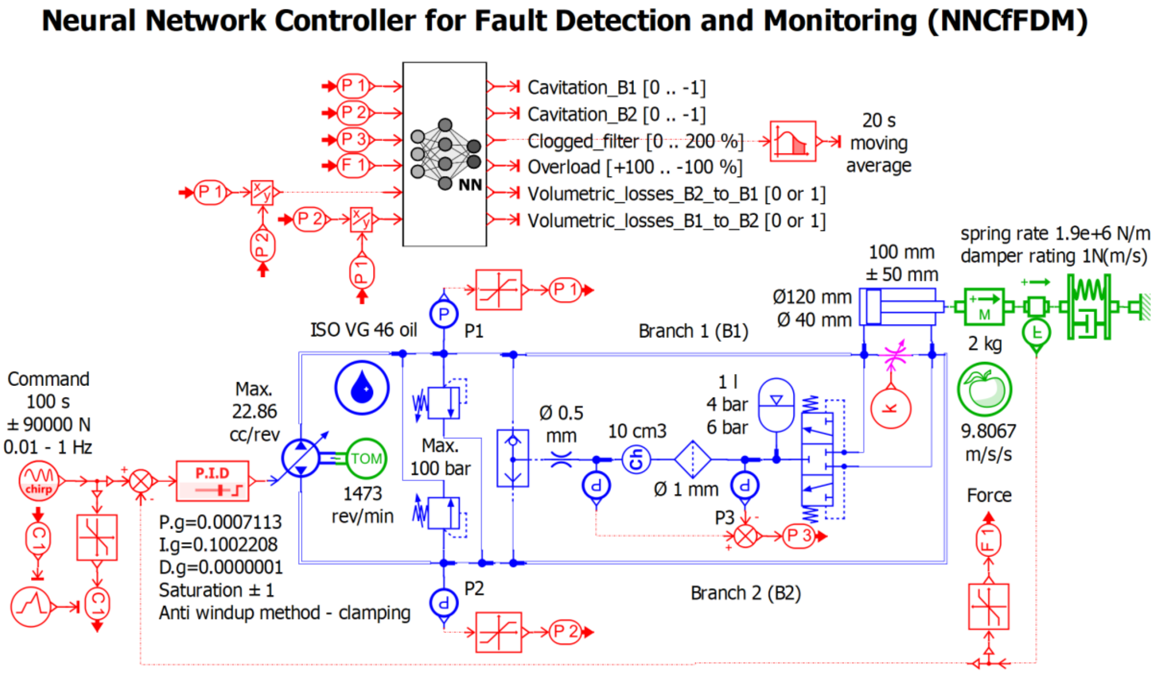

Fig. 14. The simulation network of a closed-loop compact hydraulic direct drive servomechanism

3. Results

In this section, the results of the numerical simulation are presented in three sets (Figs. 15 - 17); the simulation was conducted in the scope of the developing a neural network controller for fault detection and monitoring in the closed-loop compact hydraulic direct drive servomechanism.

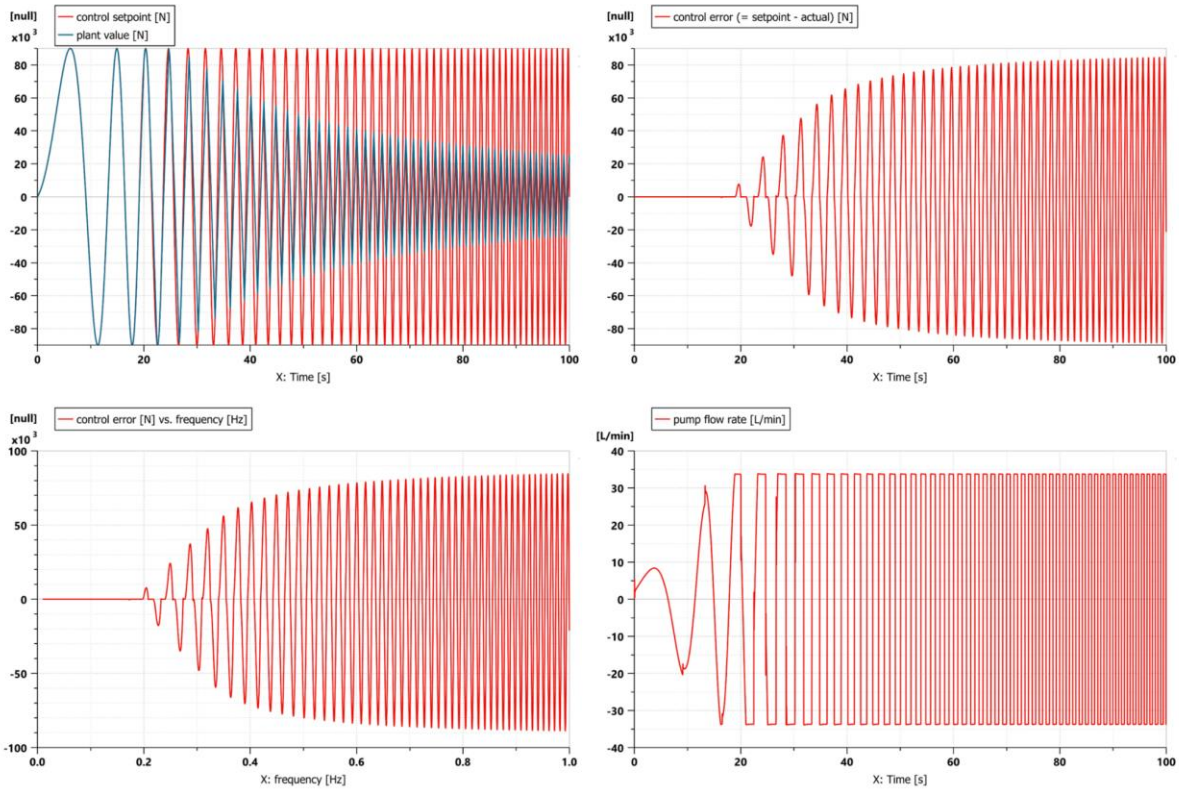

Fig. 15. Results set 1

In Fig. 15, the upper left corner illustrates the control setpoint curve (desired force) alongside the plant value (achieved force). This graphical representation provides a visual comparison between the intended force output and the actual force achieved by the system. On the right side of this graph, the instantaneous variation of the control error is presented, offering insights into how the control error evolves in real-time. Moving to the lower left graph, the instantaneous adjustment control error versus frequency of the control signal is depicted. This section of the figure provides a detailed examination of how quickly and accurately the system responds to changes in the control signal frequency and system limits. The dynamic variation of the servopump flow rate is then showcased on the right side of this graph, shedding light on the real-time adjustments made to the flow rate of the servopump in response to the dynamic requirements of the system; the value of the generated force decreases with the increase of the command frequency.

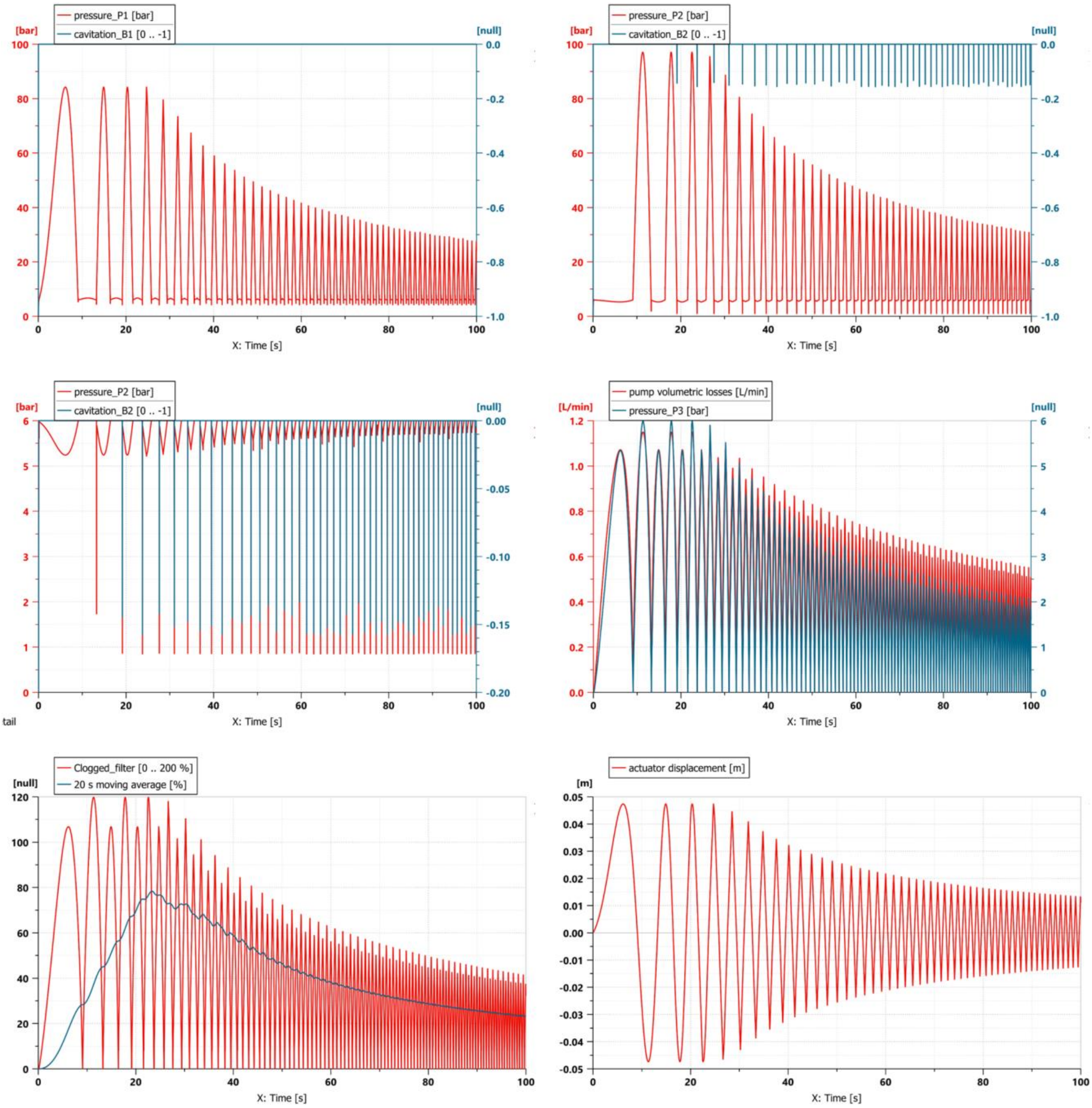

Fig. 16. Results set 2

Fig. 16, the top row of graphs presents an overview of the pressures within the two branches of the transmission. The detailed left-center graph provides a closer view, revealing a drop in pressure below atmospheric pressure specifically on branch B of the transmission; this phenomenon is further corroborated by the neural network's indication, represented by the blue curve, aligning with the observed drop in pressure. The right-center graph in the same row focuses on volumetric losses of the servopump and the resulting pressure drop attributed to these losses on the oil filter. The lower left graph captures the neural network response to this pressure drop (on the oil filter), and an average of these values is also included for a clearer representation. Finally, the graph in the lower right corner shows the movement of the actuator whose movement amplitude decreases with the increase of the command frequency.

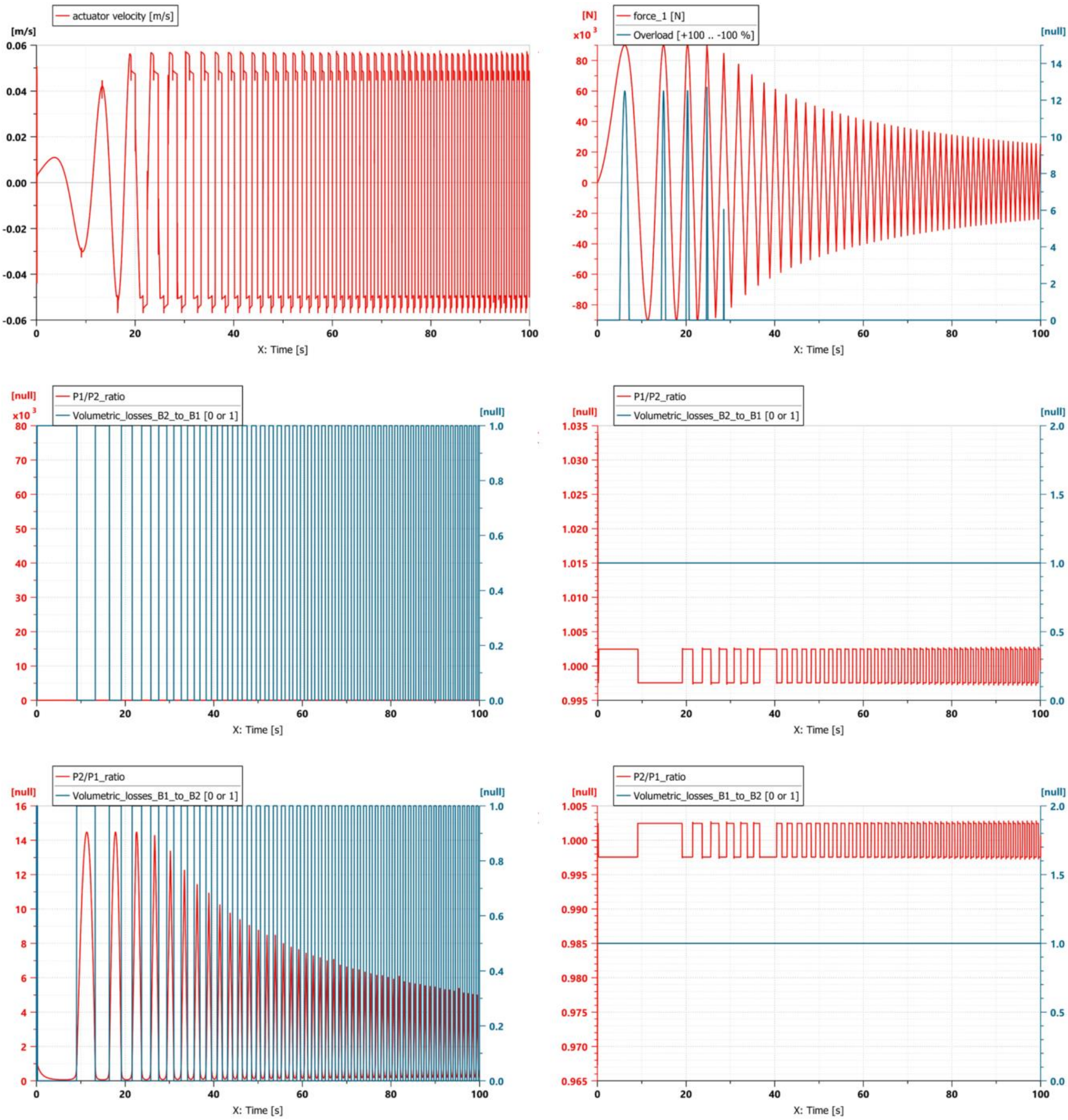

Fig. 17. Results set 3

In Fig. 17, the upper left column features a graph illustrating the time variation of the velocity of the hydraulic actuator. To the right of this graph, the force generated by the hydraulic actuator is presented in red. Additionally, the overload is signaled by the neural network and is represented by a blue curve, indicating a value of 12% of the nominal force, which is 80000 N. The graphs in the center and bottom left further delve into the response of the neural network to small volumetric losses. On the other hand, the graphs in the center and bottom right depict the neural network's response to large volumetric losses, simulated through the use of a throttle that short-circuits the hydraulic cylinder ports.

In summary, the current chapter underscores the effectiveness of the neural network controller in fault detection and monitoring for a closed-loop compact hydraulic direct drive servomechanism. Through meticulous development and numerical simulations, the research demonstrates the controller's robust performance across various scenarios. The ability to generate continuous variable error values, serving as predictive indicators, stands out as a proactive tool for preemptive maintenance interventions. These findings not only present the functioning of hydraulic servomechanisms but also exemplify the integration of cutting-edge technology (neural networks) in addressing the complexities of modern industrial processes within the context of Industry 4.0, setting the stage for further discussion and implications in subsequent research.

4. Conclusions

• The integration of a neural network controller in a closed-loop compact hydraulic direct drive servomechanism marks a substantial advancement in the realm of fault detection and predictive maintenance. This approach addresses the inherent complexities of industrial processes, providing a proactive solution to potential faults.

• The research showcases the meticulous development and training of the neural network controller, with a focus on achieving precision in fault detection within the context of Industry 4.0. The presented results demonstrate the effectiveness of the neural network in monitoring critical components and generating predictive indicators, aligning with the demands of smart manufacturing.

• The ability to generate continuous variable error values and transform them into predictive indicators sets this research apart, offering a valuable tool for preemptive maintenance interventions. The neural network's capacity to forecast future system malfunctions contributes significantly to increased operational efficiency, reduced downtime, and improved reliability in industrial settings.

• The numerical simulations presented in the results section provide a comprehensive overview of the neural network controller's performance in different scenarios, including variations in control error, pressure drops, volumetric losses, and actuator movements. These simulations validate the practical applicability and robustness of the developed neural network.

• As industries continue to evolve in the digital age, the role of neural networks in optimizing processes and ensuring reliability becomes increasingly indispensable. The research not only contributes to the specific domain of hydraulic servomechanisms but also exemplifies the broader intersection of cutting-edge technology and the demands of modern industrial processes, in line with the principles of Industry 4.0.

Acknowledgments

The research in this paper was financially supported by a project funded by the Romanian Ministry of Research, Innovation and Digitalization (MCID) through Programme 1- Development of the national research & development system, Sub-programme 1.2 - Institutional performance - Projects financing the R&D&I excellence, Financial Agreement no. 18PFE/30.12.2021.

References

[1] Gomez, C., A. Guardia, J. L. Mantari, A. M. Coronado, and J. N. Reddy. "A contemporary approach to the MSE paradigm powered by Artificial Intelligence from a review focused on Polymer Matrix Composites." *Mechanics of Advanced Materials and Structures* 29, no. 21 (2022): 3076-3096.
[2] Winter, Jeff. " What Is Industry 4.0?" *International Society of Automation (ISA) blog*. Accessed October 10, 2023. https://blog.isa.org/what-is-industry-40.
[3] Drumea, Petrin, Ana-Maria Popescu, and Cătălin Dumitrescu. "Fluid Power, Industry 4.0 and Circular Economy." Paper presented at the 25th International Conference on Hydraulics and Pneumatics – HERVEX, Baile Govora, Romania, November 13-15, 2019.
[4] Rahman, Arvi. “Introducing ‘Industry 4.0’ to Bangladesh.” *Textile Today Bangladesh. An Innovation Hub*, June 25, 2019. Accessed October 10, 2023. https://www.textiletoday.com.bd/introducing-industry-4-0-bangladesh.
[5] Drumea, Petrin, Ionas Catalin Dumitrescu, Alexandru Hristea, and Constantin Chirita. "Methods of diagnosing malfunctions in hydraulic actuations." Paper presented at the 22th International Conference on Hydraulics and Pneumatics – HERVEX, Baile Govora, Romania, November 9-11, 2016.
[6] Selcuk, S. "Predictive maintenance, its implementation and latest trends." *Proceedings of the Institution of Mechanical Engineers, Part B: Journal of Engineering Manufacture* 231, no. 9 (2017): 1670-1679.
[7] Wang, Lintao, Yuchong Liu, Hang Yin, and Wei Sun. "Fault diagnosis and predictive maintenance for hydraulic system based on digital twin model." *AIP Advances* 12, no. 6 (June 2022): 065213.
[8] Kagermann, Henning, and Wolfgang Wahlster. "Ten Years of Industrie 4.0." *Sci* 4, no. 3 (June 2022): 26.
[9] Islam, Mohaiminul, Guorong Chen, and Shangzhu Jin. "An Overview of Neural Network." *American Journal of Neural Networks and Applications* 5, no. 1 (June 2019): 7-11.
[10] Abiodun, Oludare Isaac, Aman Jantan, Abiodun Esther Omolara, Kemi Victoria Dada, Nachaat AbdElatif Mohamed, and Humaira Arshad. "State-of-the-art in artificial neural network applications: A survey." *Heliyon* 4, no. 11 (November 2018): e00938.

ISSN 1454 - 8003
Proceedings of 2023 International Conference on Hydraulics and Pneumatics - HERVEX
November 8-10, Băile Govora, Romania

INVOLVING FLUID POWER IN ART – A POSSIBILITY TO MATERIALIZE THE ARTISTIC VISION

Adrian CIOCĂNEA[1], Cătălin DUMITRESCU[1,*], Teodor FROLU[2], Dan VEZENTAN[3], Valentin BARBU[1]

[1] National Institute of Research & Development for Optoelectronics INOE 2000 – Subsidiary Hydraulics and Pneumatics Research Institute, Bucharest, Romania; * dumitrescu.ihp@fluidas.ro

[2] Ivan Patzaichin - Mila 23 Association, Bucharest, Romania

[3] Malmaison Studios, Bucharest, Romania

Abstract: *The article presents the materialization of an artistic vision with the help of mechanical engineering, involving the fields of fluid power, mechanics, electricity, and others. In order to create a component of the Ivan Patzaichin Memorial Ensemble from Tulcea, a collaboration was established between an artistic team (artists, architects, etc.) and a design team; the object of the collaboration was the creation of a feasible project for the physical realization of a 'water wheel', inspired by Asian technical achievements in the field of irrigation, but with a symbolism adapted to the purpose of the artistic creation. The final physical realization was very close to the artistic vision.*

Keywords: *Fluid Power, artwork, Ivan Patzaichin Memorial Ensemble, water wheel, hydraulic drive system*

1. Introduction

Most works of art in history or today are static creations; very few add movement to the images or shapes, mainly because this would imply some technical knowledge of the artist or association of the artist with people in the field of exact sciences, such as engineering, mathematics, physics, etc. However, the impact of an artwork with moving elements is much greater, compared to a static one [1]; and when nature is associated with the artistic vision and contributes to the realization of an object in motion, the result is a superior one [2].

Fig. 1. Kinetic Sculpture by Anthony Howe

Waterwheels belong to the category of human achievements that have gone from useful objects to artistic achievements; while in the past they harnessed the energy of running water for the production of energy used for multiple purposes (grain mills, sawmills, pumps for irrigating fields, various small factories, etc.), today they retain their utility only in less developed countries, and in many cases their maintenance is done for tourist purposes.

One such example is the water wheels for irrigation in Vietnam [3]; in some regions, water wheels were adapted for "pumping" water due to the artificially created level difference; the water is raised by means of vessels into a trough at a height, whence it is distributed to the fields to be irrigated by means of bamboo pipes. In addition to their practical utility, they are an attraction for visitors.

a.

b.

Fig. 2. Irrigation water wheel in Vietnam. a. – overview; b. – water collection reservoir

In Romania, at the initiative of the Ivan Patzaichin – Mila 23 Association, a water wheel was created, which is part of the Ivan Patzaichin Memorial Ensemble located on the Ivan Patzaichin seafront in Tulcea. As is well known, Ivan Patzaichin was a famous Romanian sportsman, with a competitive activity of 43 years, of which 18 years as a canoeist and 25 years as a canoe racing coach. Ivan Patzaichin was born in the village of Mila 23 in the commune of Crișan, Tulcea county, and spent his entire career at the Dinamo club in Bucharest. In 2010, together with the architect Teodor Frolu, he founded the Ivan Patzaichin - Mila 23 Association, which aims to promote the nature and traditions of the Danube Delta and the development of this region, but also of other areas in Romania. After the disappearance of Ivan Patzaichin, the association made efforts to create a memorial to remember his activity; this memorial comprises 6 works that highlight his native area and sports activity. Among these works, the one titled “Water Collector” (or “Water Wheel”) is the only dynamic work, and the one with the deepest meanings.

2. The objective of the work. Requirements and possibilities of achievement

2.1 Artistic requirements

Being a work carried out with public funding, the proposal participated in a selection contest; the author of the work, the artist Dan Vezentan, describes it as follows in his proposal:
Kinetic floating installation, attached to a floating pontoon, which will collect and transform water from the Danube into drinking water. Its shape starts from the mill wheel (+ inspirations from Asia – Vietnam) and consists of **24 radially arranged arms** (the 24 hours of the day), which have **enamelled metal buckets** at the end, **paddles** for movement/rotation and on the outside **480 of decorative "wings"**. Inside we will have **a stainless steel double-walled collection basin** to keep the water at a decent temperature + discharge through the inside. It will take the water collected through pipes inside the axle and filter it through an approved system. The principle of operation of the wheel is similar to that of the bicycle fork: the wheel rotates, the fork and the axle are fixed.
To this fixed axis we attached the basin, which will take the water between the movements of the buckets in the interval 10...14 - if we visualize the wheel as a clock.
The author of the proposal has also made various simulations of the object, both in electronic format (artistic drawings or simulations), as well as a 1:5 scale model.

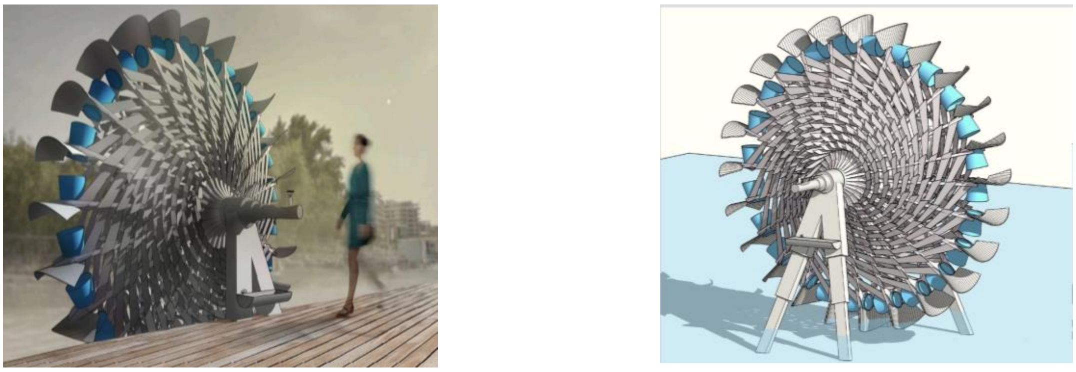

a. b.

Fig. 3. The water collector in artistic vision. a. – artistic sketch; b. – numerical simulation

The biggest challenge for this work was the materialization of the artist's vision in a dynamic object, but which also has utility (provides drinking water), in a structure as close as possible to the artistic one.

In order to obtain the best results, the promoters of the project turned to the Hydraulics and Pneumatics Research Institute from Bucharest, for the development of the layout, and for the actual embodiment a company specialized in metal works was chosen. Since in the artist's vision, the wheel had to be driven in rotation by the Danube, the first stage of the project was to make a dimensioning calculation, to see to what extent it is possible to implement this solution.

2.2 Checking the working condition of the water wheel when driven by the Danube

The water wheel proposed in the project is of the type with lower intake, suitable for floating constructive solutions, with simple construction but which have the lowest efficiency compared to the other types of water wheels [4, 5, 6]. Figure 4 shows a simplified diagram of the water wheel, for which the dimensions necessary for the operation verification calculation are highlighted, and figure 5 shows the proposed site, for which the functional parameters - depth and water speed - have been determined.

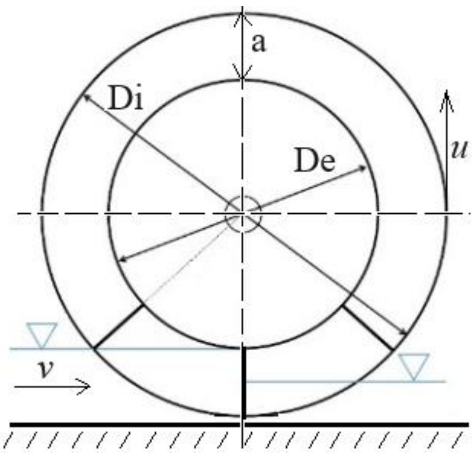

Fig. 4. The dimensions of the water wheel

Fig. 5. Location of Ivan Patzaichin Seafront

The calculation scheme for the water wheel consists in checking the power that it can supply to the shaft so that two conditions are met: that of starting at a low level of water, respectively of the speed of the water current, and the water supply of a water tank coupled to a filter device for providing drinking water.

The water wheel has 24 straight vanes at the end of the arms and works through the effect of hydraulic shock, thus neglecting the relative flow between the blades and therefore the connection

between the absolute velocity *"v"* of water flow, the peripheral velocity *"u"* and the relative velocity "w". Under these conditions, the efficiency of the wheel has values between 0.3 – 0.4.
The impulse force will be:

$$F = \frac{\gamma Q}{g}(v - u) \tag{1}$$

where the flow rate *Q* is calculated taking into account the width *B* of the wheel and the data according to figure 4.

$$Q = B \cdot a \cdot v \tag{2}$$

The wheel power under the above conditions is:

$$P = \frac{Fu}{75} = \frac{\gamma Q}{75g}(vu - u^2) \tag{3}$$

By deriving relation (3) in relation to the peripheral speed *u*, the optimal peripheral speed of the wheel is obtained which is: *u = 0.5 v*, or for practical reasons *u = 0.45 v*. Under these conditions, the maximum hydraulic power will be:

$$P_h = \frac{\gamma Q}{75g}(0.45v^2 - 0.45^2v^2) = 0.336\,Qv^2\ (\mathrm{CP}) \tag{4}$$

If the theoretical power of the river is:

$$P_t = \frac{\gamma Q}{75g} \cdot \frac{\gamma Q v^2}{2g} = 0.68Qv^2 \tag{5}$$

it follows that the theoretical hydraulic efficiency of the water wheel will be:

$$\eta_h = \frac{P_h}{P_t} = 0.495 \tag{6}$$

If it is considered that the mechanical efficiency of the rotating assembly would be η_m = 0.8, the effective power at the turbine shaft can be calculated:

$$P = 0.336\,Qv^2\eta_m = 0.27\,Bav^2 = 0.27\,Sv^2 \tag{7}$$

where S is the surface of the blade immersed in water, having the shape of a rectangle with sides B and a.
The geometric data imposed by the proposed water wheel and the hydraulic parameters of the site are: maximum speed of the water current *v* = 1 m/s; blade width *B* = 0.6 m; blade length *a* = D_e – D_i = 0.55 m. For these data, the power at the turbine shaft will be *P* = 66 W, resulting in a rotation speed *n* = 3 rev/min. Considering that the actual speed of the water in the site will be lower for the period of the warm season, when the demonstration water wheel will be in the public's attention, the average speed of the current was evaluated at the value of 0.4 m/s. Under these conditions the total power available at the shaft will be *P* = 11 W, which shows that, in fact, **the water wheel will not be able to be turned by the Danube**.
After placement, it was found that a number of 3...4 blades are simultaneously in the water, which recommends doubling the power obtained above for a single blade; however, even in the situation of doubling the power, there is not enough energy for the Danube to turn the wheel.

2.3 Presentation of the implemented solution

Because of the insufficient energy that flowing water can provide, the wheel will have to be driven into rotational motion by an external source; the solution to this requirement was to drive the wheel with a hydraulic system (whose diagram is shown in figure 6), hidden inside the support subassembly. It ensures a rotation speed of 1 rpm, as well as safe operation, taking into account that it is located on the Danube.

The power source is a compact pumping unit (1), which generates a flow transmitted through the directional control valve (3) to the low speed orbital motor (4). This motor offers high torque and low rpm, but still too high for the application; for this reason, a planetary reducer was placed after the motor which reduces the revolution in a ratio of 21.6:1, so that the final revolution of the wheel is 1 rpm. In order for the water wheel not to increase its speed due to the increase in water speed, a double overcenter valve (2) was installed in the system. For the maintenance of the wheel - free rotation - a valve (6) was mounted that can link the two connections of the hydraulic motor together, allowing it to rotate freely.

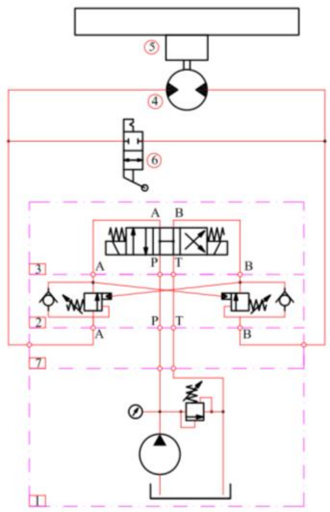

Fig. 6. Hydraulic diagram of the drive system

2.4 Realization of the components

For the mechanical and water circulation parts, solutions were found in time that meet the following requirements:
- to have the artist's consent
- can be manufactured by a company specialized in metal constructions (TEHNOMET SA Buzau)
- to allow the obtaining of drinking water, which can be safely consumed by tourists; this task was assumed and completed by the company Toma Treatment Group SRL [7].

Constructive particularities, taking into account that the artistic work is located on the Danube:
- the spokes of the wheel were galvanized; removable assemblies were made with screws protected against oxidation
- the decorative fins were made of stainless steel
- the tank was made of stainless steel
- the buckets are enamelled and painted in a colour representative of the Danube Delta area (Lipovan blue)
- in the cold season, the assembly is taken out of the water and stored in a special place, so as not to be damaged by ice.

Below are some images (figure 7 and figure 8) of the designed and built components.

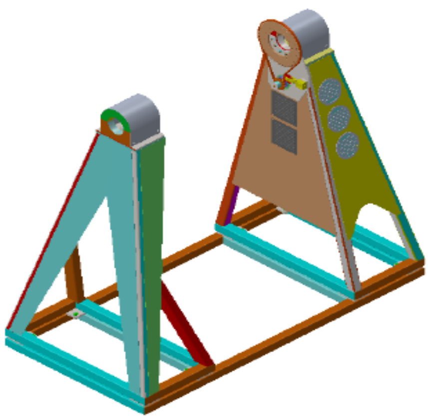

a.

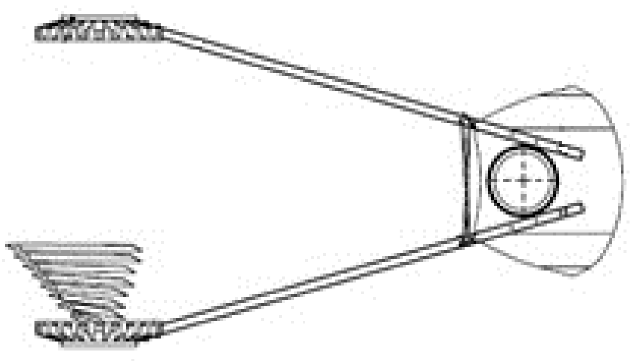

b.

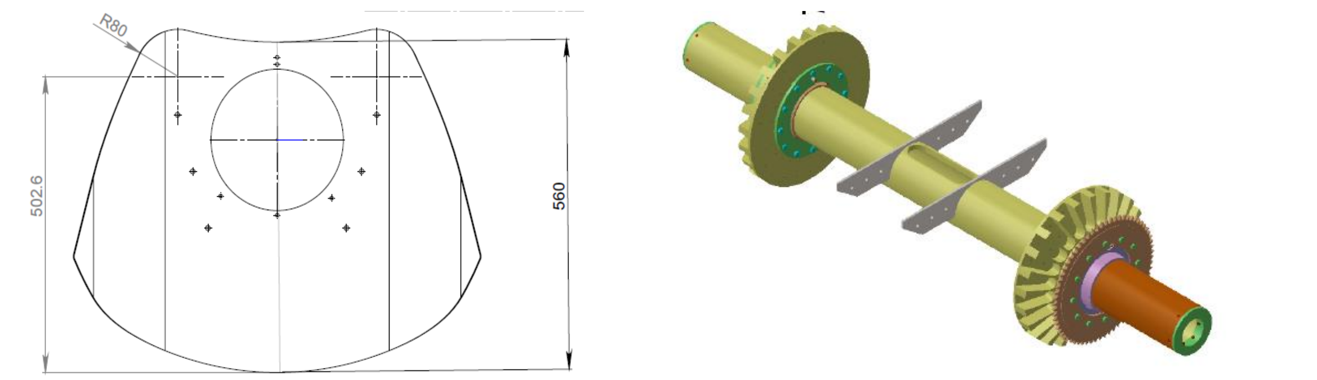

c. d.

Fig. 7. Components designed and built
a. supporting structure; b. arm plus wheel blade; c. blade; d. wheel shaft

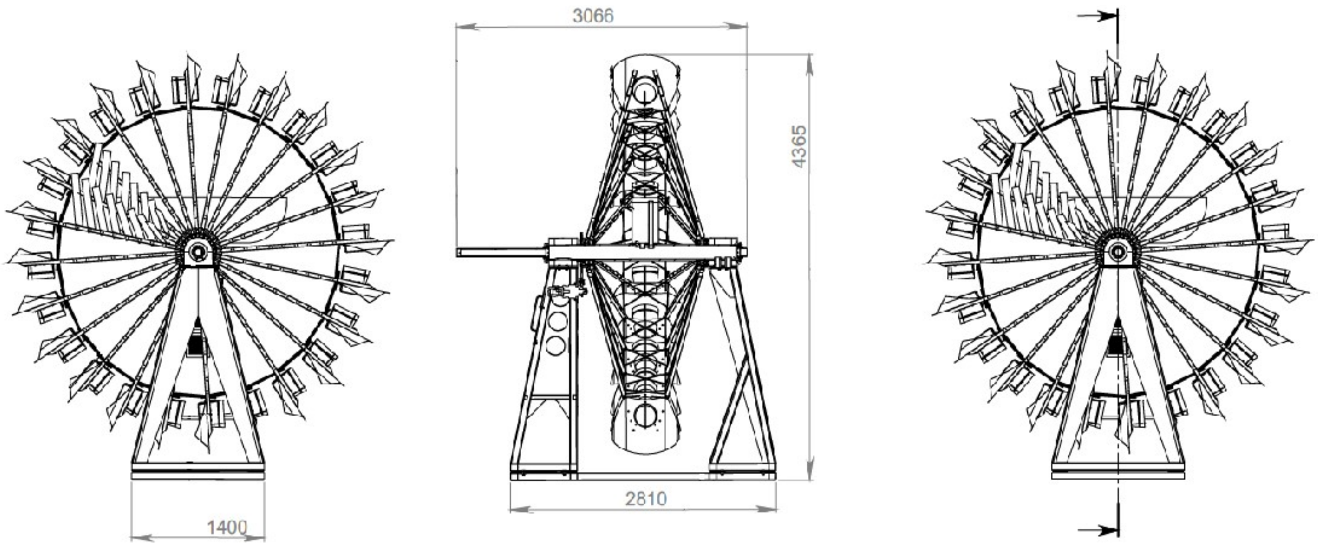

Fig. 8. Overview of the water wheel

The whole assembly is placed on a floating pontoon, so that the blades and buckets enter the water partially. The water collector was made in a form very close to the one proposed by the artist, as one can see in figure 9 below.

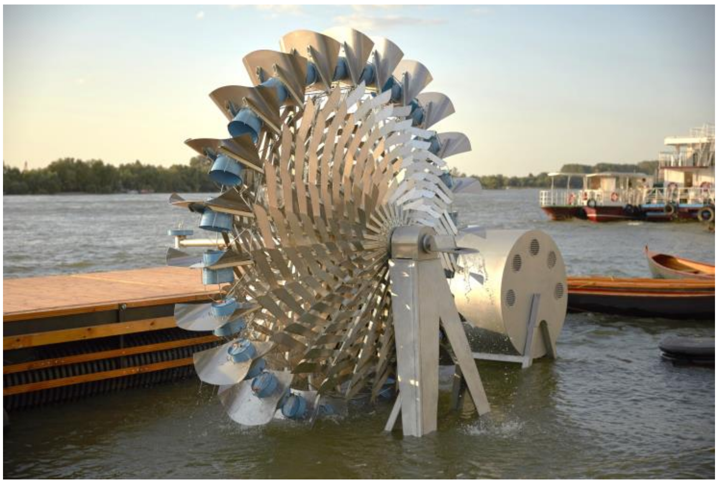

Fig. 9. Waterwheel located on site

3. Conclusions

Starting from the artistic vision, the work was carried out in such a way as to meet all the requirements of design, functionality and security in operation. The chosen solutions took into account the operation in the specific environment of the location area, the Tulcea seafront. For turning the wheel, it was determined in the design phase that the energy provided by the Danube is insufficient; therefore, a solution was implemented for the drive with a rotary hydraulic motor and a speed reducer, which are located in the area of the wheel support structure and are not visible to the public. The rotation speed is 1 rotation/min. The filtration system has also been made to the expected parameters and can provide high quality drinking water.

Acknowledgments

The research in this paper was financially supported by a project funded by the Romanian Ministry of Research, Innovation and Digitalization (MCID) through Programme 1- Development of the national research & development system, Sub-programme 1.2 - Institutional performance - Projects financing the R&D&I excellence, Financial Agreement no. 18PFE/30.12.2021.

References

[1] Chen, Guang-Dah, Chih-Wei Lin, and Hsi-Wen Fan. "The History and Evolution of Kinetic Art." *International Journal of Social Science and Humanity* 5, no. 11 (November 2015): 922-930.
[2] ***. "Anthony Howe. Available works." *Howe Art*. Accessed October 5, 2023. https://www.howeart.net/.
[3] Thien-Viet Cuong, Thong. "Water Wheels in Na Khuong." *Vietnam Pictorial*, September 19, 2017. Accessed October 16, 2023. https://vietnam.vnanet.vn/english/tin-tuc/water-wheels-in-na-khuong-157792.html.
[4] Pavel, Dorin. *Hydraulic machines / Mașini hidraulice*. Vol. I. Bucharest, State Energy Publishing House / Editura Energetică de Stat, 1954.
[5] Budiarso, Budiarso, Dendy Adanta, Warjito, Ahmad Indra Siswantara, Pradhana Saputra, and Reza Dianofitra. "Optimization of the Water Volume in the Buckets of Pico Hydro Overshot Waterwheel by Analytical Method." *IOP Conf. Series: Materials Science and Engineering* 316 (2018): 012056.
[6] Nuernbergk, Dirk M. *Water wheels with goiter channels. Calculation bases and new findings / Wasserräder mit Kropfgerinne. Berechnungsgrundlagen und neue Erkenntnisse*. Verlag Moritz Schäfer GmbH & Co., Detmold, 2013.
[7] Borș, Adriana Mariana, Ștefan Toma, Liliana Dumitrescu, Ștefan-Mihai Șefu, and Gabriel Nae. "Advanced water purification system - contribution to the development and promotion of Romanian cultural and natural heritage." Paper presented at ISB-INMA TEH' 2023 International Symposium, Bucharest, Romania, October 5-6, 2023.

MEASURING CATALASE ACTIVITY IN LI TREATED AQUATIC PLANT TISSUES

Anamaria Iulia TÖRÖK [1], Eniko KOVACS [1,2,*], Erika Andrea LEVEI[1]

[1] INCDO-INOE 2000, Research Institute for Analytical Instrumentation, 67 Donath Street, 400293 Cluj-Napoca, Romania

[2] Faculty of Horticulture, University of Agricultural Sciences and Veterinary Medicine, 3-5 Manastur Street, 400372 Cluj-Napoca, Romania

* eniko.kovacs@icia.ro

Abstract: *Living organism's metabolism can respond to environmental stress through their antioxidant system. The catalase enzyme regulates the H_2O_2 levels protecting the cells against oxidative damage caused by abiotic stress. Lemna minor are ideal test plants for the detection of metal pollution. Therefore, in the present study Lemna minor plant tissue exposed to various lithium concentrations (C_{Li} = 0, 1, 3, 5 mg/L) was used to assess the changes in the catalase enzyme activity. Moreover, a quantification method for Catalase antioxidant activity using a nano UV-Vis spectrophotometer determination was developed. It was observed that high lithium concentrations (5 mg/L) can negatively affect the catalase enzyme activity, decreasing the activity by 71% compared with the control plants (C_{Li} = 0 mg/L). It has been shown that quantification of the catalase enzyme activity can be successfully used as an important signalling biomarker to the induced lithium stress.*

Keywords: *Catalase enzyme, Lemna minor, lithium, enzyme extraction, defense mechanism*

1. Introduction

Catalase (CAT, EC 1.11.1.6) is an antioxidant enzyme found in all living organisms in the cellular peroxisome compartment [1]. Living cells developed several antioxidant mechanisms to regulate the reactive oxygen species (ROS) during various oxidative stress, such as heat, cold, inorganic and organic pollutants [2]. The CAT enzyme plays an essential role in the dissociation of hydrogen peroxide (H_2O_2) into molecular oxygen (O_2) and water (H_2O) [2]. CAT is linked to peroxidases and helps to protect cells from oxidative damage caused by free radicals. Under stress conditions, plants trigger de novo synthesis of H_2O_2 through xanthine and NADPH dependent oxidase, which has been identified as a signalling molecule involved in essential and complex mechanisms of redox homeostasis [3]. Generally, plants, such as peas, beans, rice, and cabbage, show a reduced CAT activity following exposure to Zn, Cr, Cd, As or other metals [1].
The most common CAT activity quantification method is based on the UV-Vis spectrophotometric technique which involves tracking the H_2O_2 consumption in time by measuring the absorbance at 240 nm [4]. The absorbance differences per unit of time define the CAT activity [5].
The nano spectrophotometers are ideal for small volume samples and have capillary-type or sample plate containers to measure low or microvolume samples ranging from 0.5 to 5 µl, as well as the possibility to measure using a quartz cuvette and measure absorbance with a high degree of accuracy and reproductivity
Aquatic plants are emerging biorenewable energy sources due to their aggressive growing and regeneration characteristics, are considered sustainable, have high clean energy potentials, can generate sugar and starch contents can be generated, and the biomass is easily convertible into renewable energy [6]. Duckweed, also known as *Lemna minor* from the Lemnaceae family, is a freshwater aquatic plant highly used for monitoring and toxicity test procedures due to its morphological characteristics and high adaptation capacity to various environmental conditions [7]. Duckweed has a high rate of growth and biomass production, as well as high amino acids and protein content [7, 8]. *Similarly, to other aquatic plants, Lemna minor* have also applications in

phytoremediation (bioaccumulation and biodegradation) of toxic organic and inorganic pollutants, biomass feedstock for biogas, biofuels, biorefineries, and as animal feed [6, 9].

Lithium (Li) is a naturally occurring trace element which can be found in water, soil, rocks and certain minerals (such as amblygonite, petalite, lepidolite, spodumene) [10]. Furthermore, the Li concertation is highly dependent on a region's geology, topography, and hydrogeology. It can be easily washed out after a rainfall and it can be detected in ground water as a result of mineral weathering. Generally, the drinking water Li concentrations can range from <1 to 219 µg/L [10].

Different plant species can absorb a high amount of Li and positively affect growth and development [11]. However, plant species have Li uptake capacities with specific toxicity symptoms [12]. Several studies are focused on the investigation of the role of Li, modifications, and toxicity signalling in the living organism in contact with various Li concentrations. A low level of Li can improve plant productivity by increasing the growth yield, hastening maturation, or increasing disease resistance [13]. This research aimed to optimize and develop a quantification method for CAT antioxidant activity using a nano spectrophotometer in order to assess the changes in the CAT enzyme activity following exposure of *Lemna minor* to various lithium concentrations (Li, C_{Li} = 0, 1, 3, 5 mg/L).

2. Material and methods

2.1 Plant Material and Growth Conditions

Lemna minor aquatic plants were grown in Hoagland's nutrient solution containing 1.25 mM KNO_3, 1.25 mM $Ca(NO_3)_2$, 0.5 mM $MgSO_4$, 0.25 mM KH_2PO_4, 10 µM FeEDTA, 11.6 µM H_3BO_3, 4.5 µM $MnCl_2 \cdot 4H_2O$, 0.19 µM $ZnSO_4 \cdot 7H_2O$, 0.12 µM $Na_2MoO_4 \cdot 2H_2O$, and 0.08 µM $CuSO_4 \cdot 5H_2O$, the pH of the medium was adjusted to 5.5 (±0.05) with 0.01 M KOH. A ten-hour photoperiod and a day/night temperature of 20 ±2°C was used during the experiments. After a growth period of 30 days the plants were transplanted in smaller pots. After two days of adaptation, the nutrient medium was enriched with Li at final concentrations of 0, 1, 3 and 5 mg/L Li (m = 4 g plant, v = 400 mL) prepared from Li_2SO_4. After 7 days of exposure to Li, the plants were harvested and frozen for further analysis.

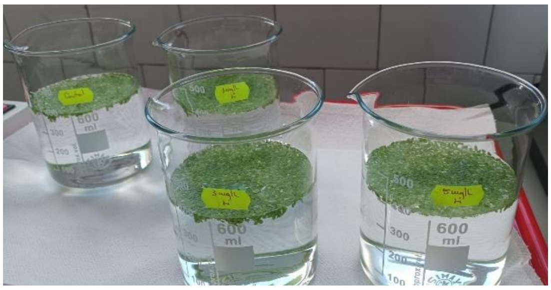

Fig. 1. *Lemna minor* aquatic plant exposed to 0, 1, 3, 5 mg/L Li

2.2 Antioxidant enzyme extraction

The frozen plant tissues were ground, then 0.5 g of ground tissues were homogenized in 5 mL of 100 mM potassium phosphate buffer (pH 7.5), containing 1 mM EDTA. The extract was mixed well, centrifuged for 30 min at 10,000 x g at 4°C, then the supernatant was used as a source of crude enzyme for the assay of CAT activities. The supernatant was stored at -20 °C until the CAT activity assays were performed.

2.3 Antioxidant enzyme activity assay

The plant extracts CAT activity was determined using the Nanodrop One Analyzer (Thermo Fisher Scientific, Waltham, MA, USA) UV-Vis spectrophotometer, at a wavelength of 240 nm by monitoring the variation in H_2O_2 absorption, according to the suggestions of Aebi (1984) [5], Sarker et al. (2018) [14] Barbosa et al. (2019) [15] and Senthilkumar et al. (2021) [16]. A volume of 0.5 mL of 75 mH H_2O_2 with 1.5 ml of 100 mM phosphate buffer (pH 7.00) were used as reaction mixtures for each plant extracts. The reaction mixtures were without the plant extract was used as blank sample. A volume of 1 ml of plant enzyme extract was added to the reaction mixture to obtain a 3 mL final volume. The reaction started after adding the plant extracts to the reaction mixtures, and the absorbance change was monitored for 2 min. The total CAT activities were expressed as μmol min⁻1 mg⁻1 protein, calculated by the following formula Eq (1); where A_0 and A_{180} is the initial and final absorbance, V_t is the final volume of the reaction mixture (3 mL), ε_{240} is the molar extinction coefficient for H_2O_2 (34.9 mol^{-1} cm^{-1}), and d is the optical path of the cuvette (1 cm), V_s is the volume of the sample (1 mL), C_t is the total protein concentration in the samples, and 0.01 is the absorbance change that caused by 1 U (one unit) of enzyme per min at 240 nm.

$$U/mg = (A_0 - A_{180}) \times V_t/\varepsilon_{240} \times d \times V_s \times C_t \times 0.001 \quad (1)$$

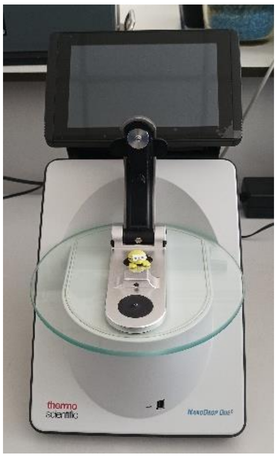

Fig. 2. Nanodrop One Analyzer (Thermo Fisher Scientific, Waltham, MA, USA), UV-Vis Spectrophotometer

3. Results and discussion

In general, the CAT enzyme activity quantification is a low-cost and rapid method used to evaluate the effect of oxidative stress on metal-exposed plants. In the first step, the plant tissues are homogenized in an ice-cold buffer devoid of other antioxidants [17]. The CAT enzyme activity quantification was performed at 20°C in the current study, however, it can be determined between 0-37°C, as the temperature differences in this range do not affect the assay [16]. In the present study, the CAT enzyme assay was optimized for the quantification with a spectrophotometer for aquatic plant tissues. The extraction method was performed with a high repeatability and accuracy rate.

The Li exposure (0, 3, 5 mg/L) induced the decrease of CAT antioxidants (Fig. 1). In the present study, the highest CAT activity was observed in the case of the control plants (0 mg/L Li). By increasing the Li concentrations in the Hoagland's nutrient solution, the exposed plants showed lower CAT activity with 44% in the case of 1 mg/L Li, 61% at 3 mg/L Li and 71% at 5 mg/L Li. In contrast with our results, Zn acts as a biostimulator and activates the CAT enzyme activity as the Zn levels are increased to a maximum 1.5 mg/L concentration [18]. Moreover, Parlack et al. (2012) found that *L. gibba*, *L. minor* and *S. polyrrhiza* plant can adapt to Zn toxicity through the antioxidant defence system [18].

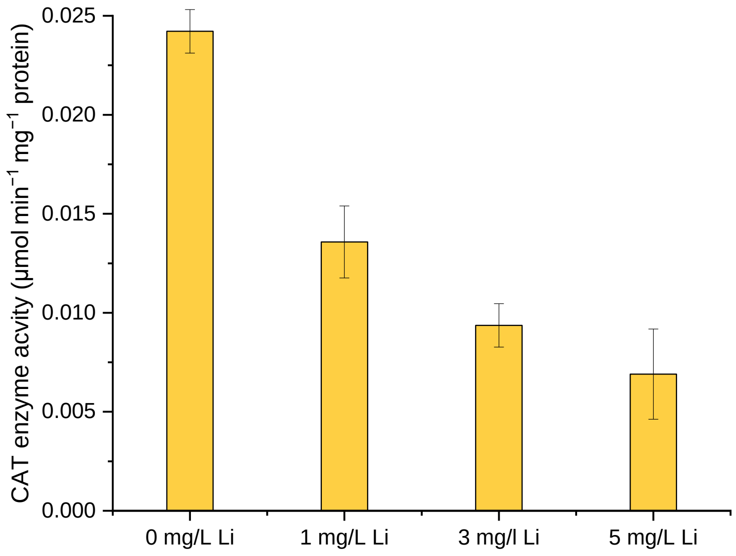

Fig. 3. Catalase enzyme activity of the *Lemna minor* aquatic plants exposed to 0, 1, 3 and 5 mg/L Li

4. Conclusions

Lemna minor aquatic plant tissue was utilized for the catalase enzyme extraction to assess the impact of lithium exposure. The catalase activity was measured after seven days of exposure to concentrations of 0, 1, 3 and 5 mg/L Li. The catalase activity of the plant extracts was measured by a nano UV-Vis spectrophotometer at a wavelength of 240 nm by determining the variation in H_2O_2 absorption. Lithium had a negatively affected the antioxidant defence mechanism of *Lemna minor*.

Acknowledgments

This research was funded by the Ministry of Research, Innovation and Digitization through Program 1—Development of the national research & development system, Subprogram 1.2—Institutional Performance—Projects that finance RDI excellence, Contract No. 18PFE/30.12.2021 and Core Program within the National Research Development and Innovation Plan 2022–2027, carried out with the support of MCID, project No. PN 23 05.

References

[1] Gangwar, Savita, Vijay Pratap Singh, Durgesh Kumar Tripathi, Devendra Kumar Chauhan, Sheo Mohan Prasad, and Jagat Narayan Maurya. "Chapter 10 - Plant Responses to Metal Stress: The Emerging Role of Plant Growth Hormones in Toxicity Alleviation." In *Emerging Technologies and Management of Crop Stress Tolerance*, edited by Parvaiz Ahmad and Saiema Rasool, 215-48. San Diego, Academic Press, 2014.
[2] Olson, K. R., Y. Gao, E. R. DeLeon, M. Arif, F. Arif, N. Arora, and K. D. Straub. "Catalase as a Sulfide-Sulfur Oxido-Reductase: An Ancient (and Modern?) Regulator of Reactive Sulfur Species (Rss)." *Redox Biol* 12 (August 2017): 325-39.
[3] Montavon, P., K. R. Kukic, and K. Bortlik. "A Simple Method to Measure Effective Catalase Activities: Optimization, Validation, and Application in Green Coffee." *Anal Biochem* 360, no. 2 (January 2007): 207-15.
[4] Hadwan, Mahmoud Hussein. "Simple Spectrophotometric Assay for Measuring Catalase Activity in Biological Tissues." *BMC Biochemistry* 19, no. 1 (August 2018): 7.
[5] Aebi, H. "Catalase in Vitro." *Methods Enzymol* 105 (1984): 121-6.
[6] Arefin, Md Arman, Fazlur Rashid, and Amirul Islam. "A Review of Biofuel Production from Floating Aquatic Plants: An Emerging Source of Bio-Renewable Energy." *Biofuels, Bioproducts and Biorefining* 15, no. 2 (2021): 574-91.

[7] Pagliuso, Débora, Adriana Grandis, Janaina S. Fortirer, Plinio Camargo, Eny I. Floh, and Marcos S. Buckeridge. "Duckweeds as Promising Food Feedstocks Globally." *Agronomy* 12, 4 (2022): 796.
[8] Mohedano, Rodrigo A., Rejane H. R. Costa, Flávia A. Tavares, and Paulo Belli Filho. "High Nutrient Removal Rate from Swine Wastes and Protein Biomass Production by Full-Scale Duckweed Ponds." *Bioresource Technology* 112 (May 2012): 98-104.
[9] Krzywonos, Małgorzata, Zdzisława Romanowska-Duda, Przemysław Seruga, Beata Messyasz, and Stanisław Mec. "The Use of Plants from the Lemnaceae Family for Biofuel Production—a Bibliometric and in-Depth Content Analysis." *Energies* 16, no. 4 (2023): 2058.
[10] Barjasteh-Askari, F., M. Davoudi, H. Amini, M. Ghorbani, M. Yaseri, M. Yunesian, A. H. Mahvi, and D. Lester. "Relationship between Suicide Mortality and Lithium in Drinking Water: A Systematic Review and Meta-Analysis." *J Affect Disord* 264 (March 2020): 234-41.
[11] Shahzad, B., M. Tanveer, W. Hassan, A. N. Shah, S. A. Anjum, S. A. Cheema, and I. Ali. "Lithium Toxicity in Plants: Reasons, Mechanisms and Remediation Possibilities - a Review." *Plant Physiol Biochem* 107 (October 2016): 104-15.
[12] Kuloğlu, Selin Sipahi, Emine Yalçin, Kültiğin Çavuşoğlu, and Ali Acar. "Dose-Dependent Toxicity Profile and Genotoxicity Mechanism of Lithium Carbonate." *Sci Rep* 12, no. 1 (August 2022): 13504.
[13] Shahzad, Babar, Mohsin Tanveer, Waseem Hassan, Adnan Noor Shah, Shakeel Ahmad Anjum, Sardar Alam Cheema, and Iftikhar Ali. "Lithium Toxicity in Plants: Reasons, Mechanisms and Remediation Possibilities – a Review." *Plant Physiology and Biochemistry* 107 (October 2016): 104-15.
[14] Sarker, U., and S. Oba. "Catalase, Superoxide Dismutase and Ascorbate-Glutathione Cycle Enzymes Confer Drought Tolerance of Amaranthus Tricolor." *Sci Rep* 8, no. 1 (November 2018): 16496.
[15] Barbosa Neto, A. G., M. B. Morais, E. D. Dutra, and T. Calsa Junior. "Biological Diversity of Lemna Aequinoctialis Welw. Isolates Influences Biomass Production and Wastewater Phytoremediation." *Bioresource Technology Reports* 6 (June 2019): 251-59.
[16] Senthilkumar, M., N. Amaresan, and A. Sankaranarayanan. "Estimation of Catalase." In *Plant-Microbe Interactions: Laboratory Techniques*, edited by M. Senthilkumar, N. Amaresan, and A. Sankaranarayanan, 113-15. New York, Springer US, 2021.
[17] Gagné, François. "Chapter 6 - Oxidative Stress." In *Biochemical Ecotoxicology*, edited by François Gagné, 103-15. Oxford: Academic Press, 2014.
[18] Uruç Parlak, Kadiriye, and Dilek Demirezen Yilmaz. "Response of Antioxidant Defences to Zn Stress in Three Duckweed Species." *Ecotoxicology and Environmental Safety* 85 (November 2012): 52-58.

ISSN 1454 - 8003
Proceedings of 2023 International Conference on Hydraulics and Pneumatics - HERVEX
November 8-10, Băile Govora, Romania

ELECTRIFICATION AND DIGITAL TRANSFORMATION - CHANCES AND CHALLENGES FOR FLUID POWER TECHNOLOGY

Univ.-Prof. Dr.-Ing. **Katharina SCHMITZ**[1]

[1] Institute for Fluid Power Drives and Systems IFAS, Aachen, Germany

sc@ifas.rwth-aachen.de

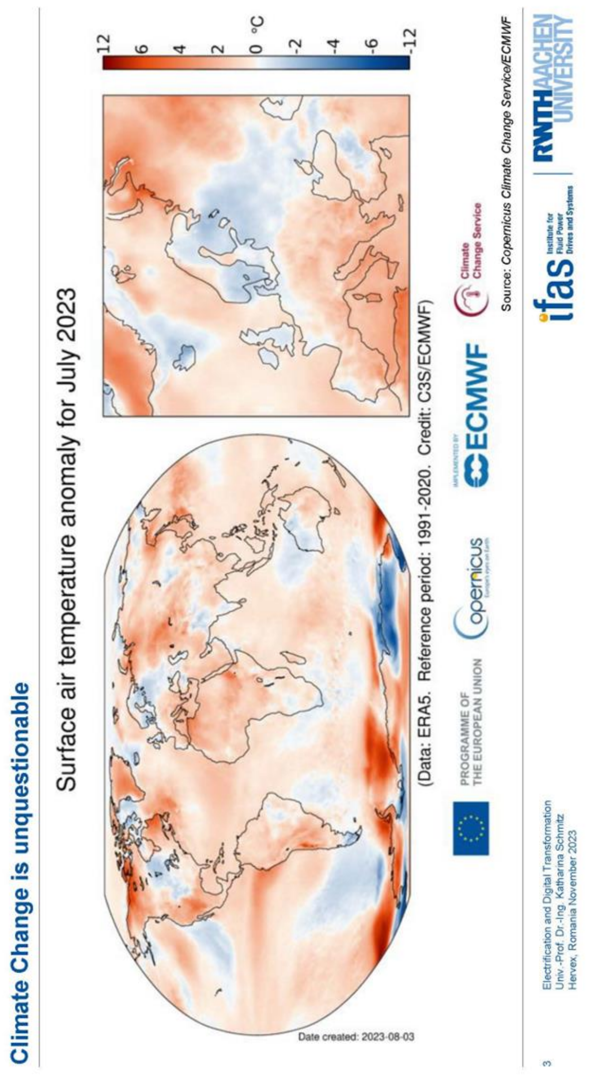

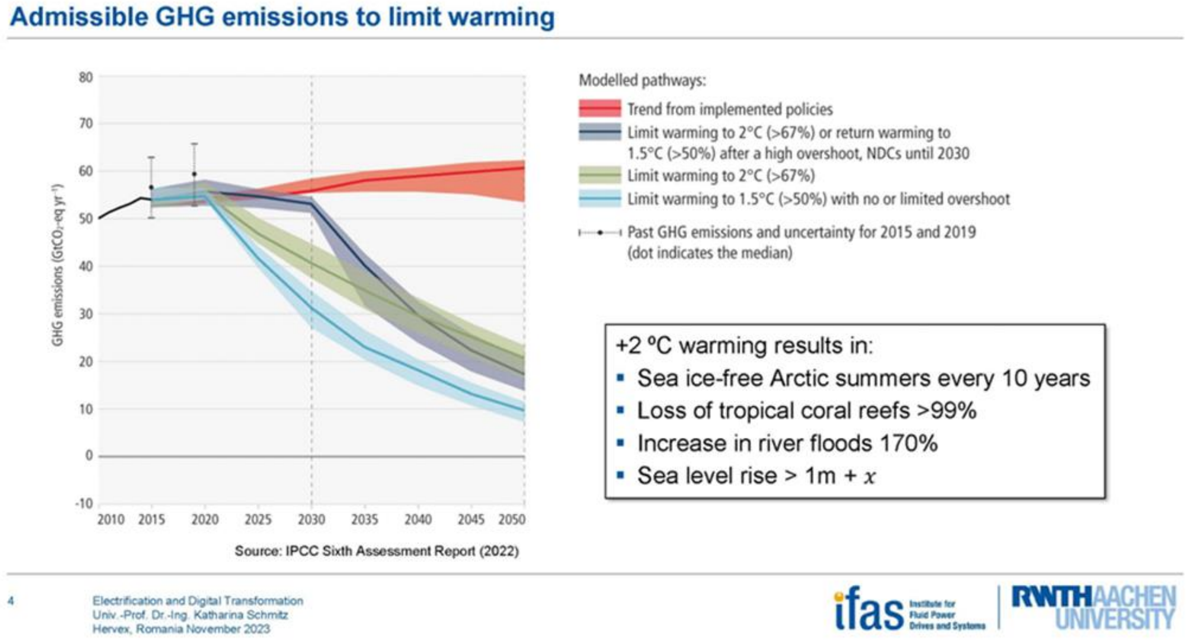
Admissible GHG emissions to limit warming
80
70
60
50
40
30
20
10
0
-10
GHG emissions (GtCO₂-eq yr⁻¹)
2010 2015 2020 2025 2030 2035 2040 2045 2050
Source: IPCC Sixth Assessment Report (2022)
Modelled pathways:
Trend from implemented policies
Limit warming to 2°C (>67%) or return warming to 1.5°C (>50%) after a high overshoot, NDCs until 2030
Limit warming to 2°C (>67%)
Limit warming to 1.5°C (>50%) with no or limited overshoot
Past GHG emissions and uncertainty for 2015 and 2019 (dot indicates the median)
+2 ºC warming results in:
Sea ice-free Arctic summers every 10 years
Loss of tropical coral reefs >99%
Increase in river floods 170%
Sea level rise > 1m + x
4
Electrification and Digital Transformation
Univ.-Prof. Dr.-Ing. Katharina Schmitz
Hervex, Romania November 2023
ifas Institute for Fluid Power Drives and Systems
RWTH AACHEN UNIVERSITY

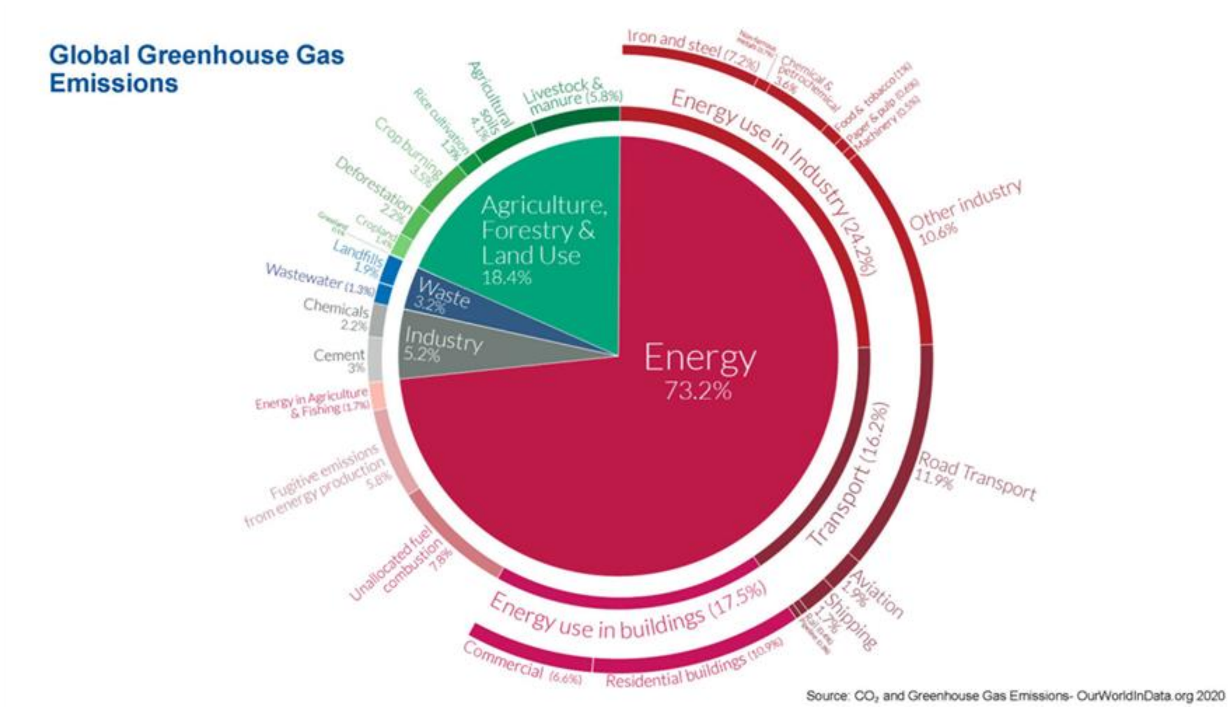
Global Greenhouse Gas Emissions
Energy 73.2%
Agriculture, Forestry & Land Use 18.4%
Waste 3.2%
Industry 5.2%
Energy use in Industry (24.2%)
Iron and steel (7.2%)
Chemical & petrochemical 3.6%
Other industry 10.6%
Transport (16.2%)
Road Transport 11.9%
Aviation 1.9%
Shipping 1.7%
Energy use in buildings (17.5%)
Commercial (6.6%)
Residential buildings (10.9%)
Unallocated fuel combustion 7.8%
Fugitive emissions from energy production 5.8%
Energy in Agriculture & Fishing (1.7%)
Cement 3%
Chemicals 2.2%
Wastewater (1.3%)
Landfills 1.9%
Cropland 1.4%
Deforestation 2.2%
Crop burning 3.5%
Rice cultivation 1.3%
Agricultural soils 4.1%
Livestock & manure (5.8%)
Source: CO₂ and Greenhouse Gas Emissions- OurWorldInData.org 2020

Traditional use of Fluid Power Drives

- High power density
- Robust design
- Good controllability open and closed loop
- Good dynamic behaviour through low inertia

Mobile Machinery

Industrial Hydraulics / Pneumatics

Future of Fluid Power: Modern & Sustainable Motion Technology

6 Electrification and Digital Transformation
Univ.-Prof. Dr.-Ing. Katharina Schmitz
Hervex, Romania November 2023

ifas Institute for Fluid Power Drives and Systems | RWTH AACHEN UNIVERSITY

Electrification and Digitization

	Mobile Machinery	Industrial Hydraulics / Pneumatics
Digitization		
Electrification		

7 Electrification and Digital Transformation
Univ.-Prof. Dr.-Ing. Katharina Schmitz
Hervex, Romania November 2023

ifas Institute for Fluid Power Drives and Systems | RWTH AACHEN UNIVERSITY

Electrification and Digitization

		Mobile Machinery	Industrial Hydraulics / Pneumatics
Digitization	Impact	I	II
	Challenge		
Electrification	Impact	III	
	Challenge		

8 Electrification and Digital Transformation
Univ.-Prof. Dr.-Ing. Katharina Schmitz
Hervex, Romania November 2023

ifas Institute for Fluid Power Drives and Systems | RWTH AACHEN UNIVERSITY

I – Way to an Autonomous Construction Process – Construction Site of the Future

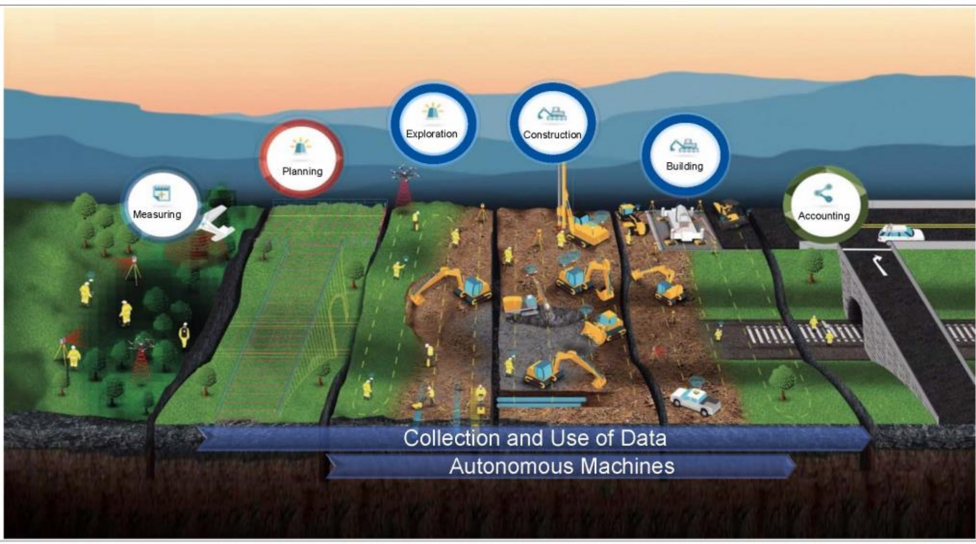

[1]

9 Electrification and Digital Transformation
Univ.-Prof. Dr.-Ing. Katharina Schmitz
Hervex, Romania November 2023

ifas Institute for Fluid Power Drives and Systems | RWTH AACHEN UNIVERSITY


I – Digitization of Mobile Machinery
Motivation
Autonomous construction site, account for lack of (skilled) workers
Safer working environment, more sustainable processes / increase in productivity
Challenges
Consistency of information
Connectivity
Data & algorithm availability
Environment detection
Radar
LIDAR
Camera
Localization
GNSS
Derivation of action
Decision trees
AI
Mapping and modeling
SLAM
Object detection
Legislation
10
Electrification and Digital Transformation
Univ.-Prof. Dr.-Ing. Katharina Schmitz
Hervex, Romania November 2023
ifas Institute for Fluid Power Drives and Systems
RWTH AACHEN UNIVERSITY

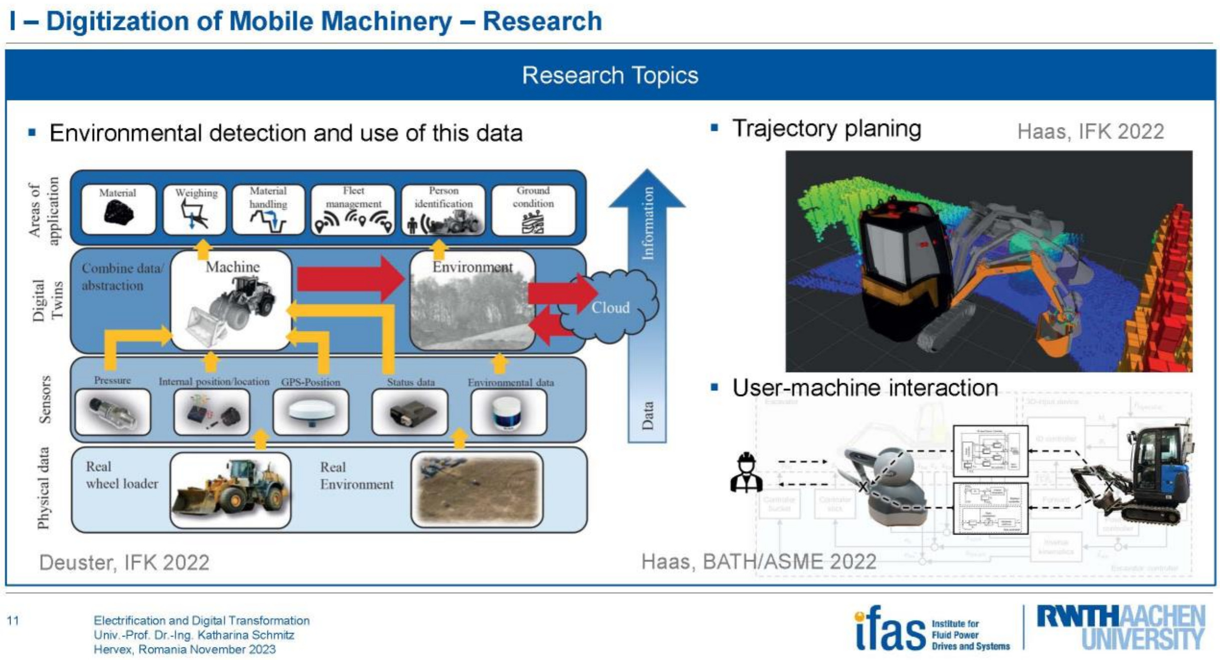
I – Digitization of Mobile Machinery – Research
Research Topics
Environmental detection and use of this data
Areas of application
Material
Weighing
Material handling
Fleet management
Person identification
Ground condition
Digital Twins
Combine data/ abstraction
Machine
Environment
Cloud
Information
Sensors
Pressure
Internal position/location
GPS-Position
Status data
Environmental data
Data
Physical data
Real wheel loader
Real Environment
Deuster, IFK 2022
Trajectory planing
Haas, IFK 2022
User-machine interaction
Haas, BATH/ASME 2022
11
Electrification and Digital Transformation
Univ.-Prof. Dr.-Ing. Katharina Schmitz
Hervex, Romania November 2023
ifas Institute for Fluid Power Drives and Systems
RWTH AACHEN UNIVERSITY

Electrification and Digitization – Summary

		Mobile Machinery	Industry Hydraulics / Pneumatics
Digitization	Impact	Autonomous construction sites Higher efficiency in building / mining	II
	Challenge	Communication, Algorithm, Legislation	
Electrification	Impact	III	
	Challenge		

12 Electrification and Digital Transformation
Univ.-Prof. Dr.-Ing. Katharina Schmitz
Hervex, Romania November 2023

ifas Institute for Fluid Power Drives and Systems | RWTH AACHEN UNIVERSITY

II – Digitization of Industrial Hydraulics / Pneumatics

Motivation & Challenges

- Motivation: Flexible, efficient, reliable manufacturing
- Challenges: Connectivity of components, Data & Algorithm

Industry 4.0 / Connectivity

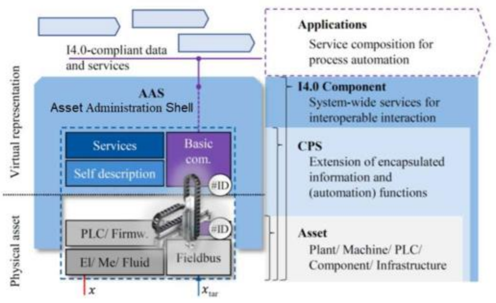

Data & Algorithm

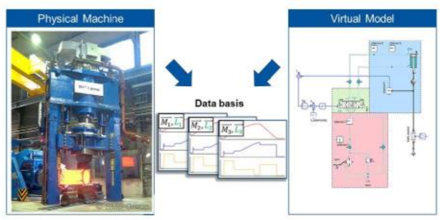

13 Electrification and Digital Transformation
Univ.-Prof. Dr.-Ing. Katharina Schmitz
Hervex, Romania November 2023

AAS: Asset Administration Shell
CPS: Cyber-Physical System

ifas Institute for Fluid Power Drives and Systems | RWTH AACHEN UNIVERSITY

II – Digitization of Industrial Hydraulics / Pneumatics – Research on Industry 4.0 / Connectivity

Industry 4.0 / Connectivity

- Connectivity via Administration Shells

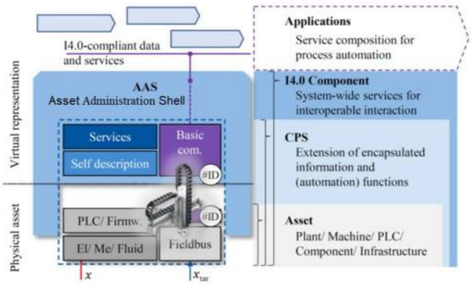

Alt, PhD Thesis, 2023

- Building up Cyber-Physical Systems via Administration Shells

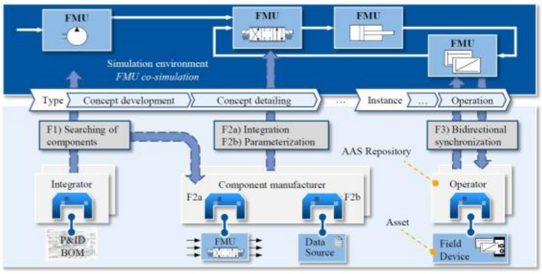

Becker, ASME/FPMC 2023

II – Digitization of Industrial Hydraulics / Pneumatics – Research on Data & Algorithm

Data & Algorithm

- Using data for condition monitoring via Supervised Learning and Neural Networks

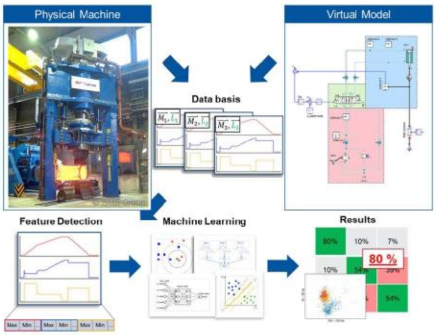

- Using Reinforcement learning for optimizing control performance

- Research on generating „big data“
  - Using simulation models
  - Using virtual sensors

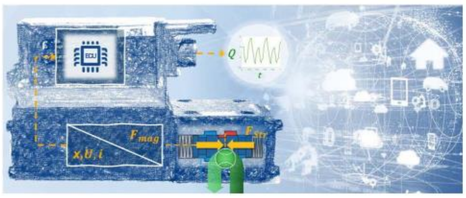

Hucko, ASME/FPMC 2023

Makansi, IFK 2022
Makansi, energies 2022
Makansi, ASME/FPMC 2023

Brumand-Poor, IFK 2022
Brumand-Poor, IJFP 2023

Electrification and Digitization – Summary

		Mobile Machinery	Industry Hydraulics / Pneumatics
Digitization	Impact	Autonomous construction sites Higher efficiency in building / mining	Flexible, efficient, reliable manufacturing
	Challenge	Communication, Algorithm, Legislation	Availability of components and services, Communication
Electrification	Impact	III	
	Challenge		

16 Electrification and Digital Transformation
Univ.-Prof. Dr.-Ing. Katharina Schmitz
Hervex, Romania November 2023

III – Electrification of Mobile Machinery

Motivation & Challenges

- Motivation: Locally reduction of emissions and noise
- Challenges: Cost effectiveness, System integration, Efficient systems, Multiple degrees of freedom

Energy Storage & Supply

- Energy storage: Battery electric, Fuel cell electric, …
- Energy supply: Charging infrastructure, Hydrogen transportation

Option 1: Wait for electric batteries to become cheap, small, available
Option 2: Use less energy / more efficient drive systems

New System Architectures & New Components

- New boundary conditions for hydraulic system and components
- New Components required (lower / higher speeds)

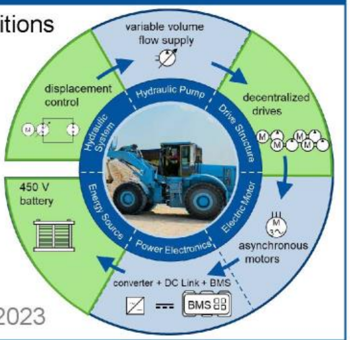

Opgenoorth, SICFP 2023

17 Electrification and Digital Transformation
Univ.-Prof. Dr.-Ing. Katharina Schmitz
Hervex, Romania November 2023

III – Electrification of Mobile Machinery – Research

Drive Train Development

- Multi-pressure systems

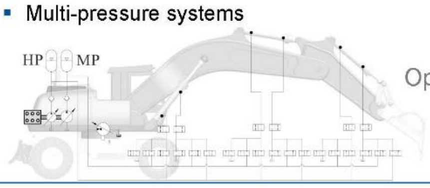

Opgenoorth, IFK 2022

- Displacement controlled actuators

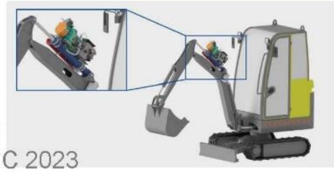

Pietrzyk, IFK 2018
Figge, ASME/FPMC 2023

New / Improved Components

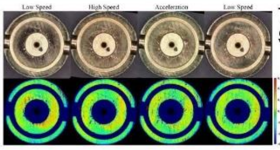

Tribo investigation
Slipper – Swash plate

Internal gear pump for 10.000 rpm

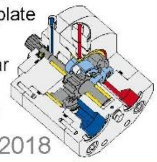

Merkel, IFK 2022
Pietrzyk, IFK 2018

Alternative Fluids

- Improving efficiency by using bio oils / synthetic esters

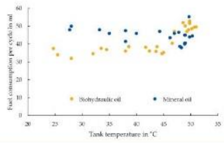

Deuster, Sustainability 2022

18 Electrification and Digital Transformation
Univ.-Prof. Dr.-Ing. Katharina Schmitz
Hervex, Romania November 2023

Electrification and Digitization – Summary

		Mobile Machinery	Industry Hydraulics / Pneumatics
Digitization	Impact	Autonomous construction sites Higher efficiency in building / mining	Flexible, efficient, reliable manufacturing
	Challenge	Communication, Algorithm, Legislation	Availability of components and services, Communication
Electrification	Impact	Local zero emission machines, Noise reduction	
	Challenge	Energy storage and supply, New drive system required	

19 Electrification and Digital Transformation
Univ.-Prof. Dr.-Ing. Katharina Schmitz
Hervex, Romania November 2023

References I/II

- Deuster, S., et.al; Methods of Environmental Information Acquisition by Sensor Data and Digital Twins; 13. International Fluid Power Conference (13. IFK), Aachen, Germany, 2022, Open access version, pp. 206
- Haas, C., et.al.; Environment Detection and Trajectory Planning Concept for an Automated Excavator using Open Source Software; 13. International Fluid Power Conference (13. IFK), Aachen, Germany, 2022, Open access version, pp. 1160
- Haas, C., et.al.; Practical Evaluation of a Control Concept for a Remote Controlled 1.8t Excavator Using a 3D Input Device, Proceedings of BATH/ASME 2022 Symposium on Fluid Power and Motion Control (FPMC 2022)

- Alt, R.; Service-oriented architecture for automated commissioning of fluid power systems; PhD Thesis, Aachen 2023; http://publications.rwth-aachen.de/record/958758/files/958758.pdf
- Makansi, F., et.al.; Feature Generation and Evaluation for Data-Based Condition Monitoring of a Hydraulic Press; 13. International Fluid Power Conference (13. IFK), Aachen, Germany, 2022, Open access version, pp. 794
- Makansi, F., et.al.; Reinforcement Learning-Based Process Optimization and Control of a Hydraulic Press With Multiple Actuators; Proceedings of BATH/ASME 2023 Symposium on Fluid Power and Motion Control (FPMC 2023)
- Makansi, F., et.al; Data-driven Condition Monitoring of a Hydraulic Press Using Supervised Learning and Neural Networks; energies, MDPI, 2022
- Becker, M., et.al.; Improving Fluid Power System Simulation Through an AAS-Based Simulation Framework; Proceedings of BATH/ASME 2023 Symposium on Fluid Power and Motion Control (FPMC 2023)
- Brumand-Poor, F., et.al.; Control of a Hydromechanical Pendulum with a Reinforcement Learning Agent; 13. International Fluid Power Conference (13. IFK), Aachen, Germany, 2022, Open access version, pp. 499
- Brumand-Poor, F. et.al; Application of Deep Reinforcement Learning Control of an Inverted Hydraulic Pendulum, International Journal of Fluid Power, River Publishers, 2023

20 Electrification and Digital Transformation
Univ.-Prof. Dr.-Ing. Katharina Schmitz
Hervex, Romania November 2023

ifas Institute for Fluid Power Drives and Systems | RWTH AACHEN UNIVERSITY

References II/II

- Hucko, S., et.al.; Investigation of Frictional Forces in Hydraulic Spool Valves and Their Effect on the Estimation of Axial Flow Forces; Proceedings of BATH/ASME 2023 Symposium on Fluid Power and Motion Control (FPMC 2023)

- Figge, F., et.al.; Simulative Comparison of Electro-Hydraulic Actuator Circuits for the Application in Excavators; Proceedings of BATH/ASME 2023 Symposium on Fluid Power and Motion Control (FPMC 2023)
- Merkel, A., et.al.; Identification of wear progression due to variating operation modes of small high dynamic piston pumps used in frontline flight control application; 13. International Fluid Power Conference (13. IFK), Aachen, Germany, 2022, Open access version, pp. 242
- Opgenoorth, A., et.al.; Switching procedures of multi-pressure systems for electrified excavators; 13. International Fluid Power Conference (13. IFK), Aachen, Germany, 2022, Open access version, pp. 855
- Opgenoorth, A., et.al.; Algorithm based system synthesis of electrified mobile machines; 18th Scandinavian International Conference on Fluid Power, SICFP'23, Finnland
- Pietrzyk, T., et. al.; Design study of a high speed power unit for electro hydraulic actuators (EHA); 11. International Fluid Power Conference (11. IFK), Aachen, Germany, 2018, pp. 232-245.
- Deuster, S.; et al.; Bio-Based Hydraulic Fluids and the Influence of Hydraulic Oil Viscosity on the Efficiency of Mobile Machinery; Sustainability; MDPI; 2021

21 Electrification and Digital Transformation
Univ.-Prof. Dr.-Ing. Katharina Schmitz
Hervex, Romania November 2023

ifas Institute for Fluid Power Drives and Systems | RWTH AACHEN UNIVERSITY

http://hervex.ro